Photoluminescence-Based Characterization of Charge Extraction and Recombination in Halide-Perovskite Based Solar Cells

Von der Fakultät für Ingenieurwissenschaften,
Abteilung Elektrotechnik und Informationstechnik
der Universität Duisburg-Essen

zur Erlangung des akademischen Grades

Doktor der Naturwissenschaften (Dr. rer. nat.)

genehmigte Dissertation

von

David Adrian Grabowski
aus
Dortmund

Gutachter: Prof. Dr. Thomas Kirchartz
Gutachter: Prof. Dr. Alex Redinger
Tag der mündlichen Prüfung: 13.09.2023

DOI: 10.17185/duepublico/79079
URN: urn:nbn:de:hbz:465-20231024-092250-0

Für meine Eltern.

Contents

Abstract

Halide-perovskite based solar cells have seen a meteoric rise in efficiency since their first introduction in 2009. Today, with reported photovoltaic conversion efficiencies exceeding 25 %, they are closing in on the established silicon technology that is currently dominating the market. In order to further improve upon the progress that has been made it is imperative to understand the losses and limitations still prevalent in devices and the underlying fabrication processes. This thesis examines the limitations of charge carrier extraction in perovskite solar cells and the corresponding implications for charge carrier distribution, recombination and the observed series resistance of a device. In order to gain insight into these properties, fabricated cells are characterized and the obtained sets of data are approximated by drift-diffusion simulations. Specifically the solar cells are investigated with respect to their current-voltage behaviour under illumination and in the dark as well as their voltage-dependent luminescence yield under differing illumination conditions. From these data sets fundamental characteristics of the cells such as the quasi-Fermi level splitting in the absorber, the ideality factor and the series resistance are determined. Subsequently an approximation of all the collected data with simulations gives insight into the inner workings of the cells with respect to charge carrier distribution, elecric field distribution and recombination pathways.

Perovskite solar cells employ markedly different cell architectures than for example silicon-based devices, there are various different structures that are in use. Therefore a number of different types of cell architectures are simulated and the behaviour of the aforementioned data sets are elucidated as well as the band diagrams under differing conditions with respect to illumination and externally applied voltage. Special consideration is given to cells with a field free absorber due to a redistribution of mobile ions as well as to architectures employing symmetric and

asymmetric transport layers respectively.

The findings from the comparisons of simulations are brought into context with a full data set obtained from cells fabricated in the lab. Approaches to replicate the measurement results by means of simulations are introduced and discussed. For a suitable set of simulation data variations to key parameters are introduced and their impact on cell characteristics is demonstrated and interpreted. The observations from these variations may function as a basis for a deeper understanding of the fundamental causes of a perovskite solar cells behaviour and shortcomings in its performance.

The investigation of charge-carrier extraction from the measured and simulated cells is closely tied to resistive effects. These resistive effects may arise from a constant ohmic resistance as well as from finite extraction times in the absorber or the transport layers. The latter part of the macroscopically measurable series resistance is dependent on the externally applied voltage.Thus, from comparisons of current-voltage curves under illumination and in the dark analysed at equal recombination current density a voltage-dependent series resistance is calculated. This is done for measured data and subsequently modelled using simulations. Variations of key parameters in the simulation indicate their influence on the ohmic and the voltage-dependent components of the series resistance. The reported findings may serve as a guide for the optimization of future approaches for perovskite solar cell processing.

Zusammenfassung

Solarzellen auf Basis von Metall-Halogenid Perowskiten haben seit ihrer ersten Einführung im Jahr 2009 einen kometenhaften Effizienzanstieg erlebt. Mit Wirkungsgraden von über 25 % nähern sie sich zunehmend der etablierten Siliziumtechnologie, die den Markt dominiert. Um den erreichten Stand weiter zu verbessern, ist es erforderlich, die Verluste und Einschränkungen zu verstehen, die bei Zellen und den zugrundeliegenden Herstellungsprozessen noch bestehen. Diese Dissertation untersucht die Beschränkungen der Ladungsträgerextraktion in Perowskit-Solarzellen und die entsprechenden Implikationen für die Ladungsträgerverteilung, die Rekombination und den beobachteten Serienwiderstand der Geräte. Um Einblick in diese Eigenschaften zu bekommen, werden hergestellte Zellen vermessen und die erhaltene Messdatensätze werden durch Drift-Diffusions-Simulationen genähert. Konkret werden die Solarzellen hinsichtlich ihres Stom-Spannungsverhaltens unter Beleuchtung und im Dunkeln sowie ihrer spannungsabhängigen Lumineszenz bei unterschiedlichen Beleuchtungsbedingungen untersucht. Aus diesen Datensätzen werden grundlegende Eigenschaften der Zellen wie die Quasi-Fermi-Niveauaufspaltung im Absorber, der Idealitätsfaktor und der Serienwiderstand bestimmt. Anschließend gibt eine Annäherung aller gesammelten Daten mit Simulationen Einblick in das Innenleben der Zellen in Bezug auf Ladungsträgerverteilung, elektrische Feldverteilung und Rekombinationswege.

Perowskit-Solarzellen verwenden deutlich andere Zellarchitekturen als beispielsweise siliziumbasierte Zellen, es gibt unterschiedliche Strukturen, die verwendet werden. Deshalb werden einige verschiedene Arten von Zellarchitekturen simuliert und das Verhalten der oben genannten Datensätze, sowie der Banddiagramme unter verschiedenen Bedingungen bezüglich Beleuchtung und extern angelegter Spannung erläutert. Besondere Aufwerksamkeit wird dabei auf Zellen gelegt, deren Absorber

durch eine Umverteilung beweglicher Ionen feldfrei ist, sowie auf Architekturen mit symmetrischen bzw. asymmetrischen Transportschichten.

Die Erkenntnisse aus dem Vergleich der Simulationen werden mit einem vollständigen Datensatz in Kontext gesetzt, der an im Labor hergestellten Zellen gemessen wurde. Ansätze zur Reproduktion der Messergebnisse mittels Simulationen werden vorgestellt und diskutiert. Für einen geeigneten Satz Simulationsdaten werden Variationen von Schlüsselparametern durchgeführt und deren Einfluss auf die Zelleigenschaften gezeigt und interpretiert. Die Beobachtungen bei diesen Variationen können als Grundlage für ein tieferes Verständnis der grundlegenden Ursachen des Verhaltens einer Perowskit-Solarzelle und ihrer Einschränkungen dienen.

Die Untersuchung der Extraktion von Ladungsträgern aus gemessenen und simulierten Zellen ist eng verknüpft mit resistiven Effekten. Diese Widerstandseffekte können von einem konstanten ohmschen Widerstand sowie durch endliche Extraktionszeiten in den Absorber- oder Transportschichten zustande kommen. Dieser zweite genannte Beitrag zum makroskopisch messbaren Serienwiderstand ist abhängig von der extern angelegten Spannung. Entsprechend wird aus Vergleichen von Strom-Spannungskurven unter Beleuchtung und im Dunkeln bei gleicher Rekombinationsstromdichte ein spannungsabhängiger Serienwiderstand bestimmt. Dies wird für gemessene Daten durchgeführt und anschließend mithilfe von Simulationen modelliert. Variationen von Schlüsselparametern in der Simulation zeigen deren Einfluss auf die ohmschen und spannungsabhängigen Anteile des Serienwiderstands. Die beschriebenen Ergebnisse können als Orientierung für die Optimierung zukünftiger Methoden zur Prozessierung von Perowskit-Solarzellen dienen.

1 Introduction

Since the era of industrialization life in the western world has undergone drastic changes. These changes apply both to the way we live and to the way that we alter our surroundings. We have seen enormous improvements in our life expectancy due to advances in medicine. We have increased our productivity by developing ever more efficient methods and machines. We have developed our means of transportation to the point that we can reach almost every point of the globe within 24 hours. And we have the highest quality of life in the history of mankind.

Unfortunately this unbridled technological progress comes at a cost. Medical advancements have led to an exponential increase of the world population, it has increased from 2 billion in 1927 to 7 billion in 2012 [1, 2].Projections estimate it to increase further without stabilizing this century, potentially reaching over 12 billion humans by the year 2100 [3]. The combination of increasing population and technological progress has led to a similarly extreme increase in resource expenditure. We are depleting the planets fossil resources while simultaneously emitting pollutants like carbon dioxide, methane, soot particles from fossil fuels, nitrous oxides or ozone. These pollutants have adverse health effects for humans and are the primary causes of global warming [4, 5]. The warming of the earth's climate is unequivocal. Since the 1950s changes are being observed that are unprecedented over decades to millennia. Driven by the increase in greenhouse gases, both the atmosphere as well as the oceans have warmed up, the ice caps have shrunk and thereby sea levels have risen. [6] The consequences of these changes are an acidification of the oceans, enhanced severity of tropical storms, droughts and diseases [7–10]. If we continue to emit greenhouse gases at the current or even an increased rate, warming and all associated changes in the climate system will continue and these changes will persist for centuries. Our mission has to be a minimization of these changes, but limiting

them will require sustantial and sustained reductions of greenhouse gas emissions [6].

What mankind needs in order to continue to thrive without simultaneously destroying the planet, are renewable energy sources that generate significantly reduced greenhouse gases. Options in use today are photovoltaics, wind energy and to a lesser extent hydropower, geothermal energy and biomass energy. In 2017 these technologies supplied 36% of the electricity generated in Germany, almost 40% of which came from photovoltaics with about 50% of the production coming from wind energy [11]. Including imports, photovoltaics made up 8.7% of consumed electricity in Germany in 2018 [12]. This market share could be achieved, because progress in photovoltaic research has led to both an increase in efficiency as well as a reduction in production costs. From 2005 to 2015 the price per kWh of photovoltaic electricity has been reduced by 80%, from 1990 to 2018 the reduction has even been 92% [11, 13]. This means that with respect to cost, photovoltaic energy is already competitive with energy from gas, coal or nuclear power plants. It is projected, that photovoltaic power will become the cheapest source of energy in the coming years [13]. This progress has accordingly led to a considerable increase in solar devices being installed worldwide with the global installed capacity increasing from 45 GW in 2010 to 515 GW in 2018 [11].

The first solar cell technology that has been researched since the 1950s are devices made from crystalline silicon [14]. Over the decades since then (poly-)crystalline solar cells have been optimized further and further to be as efficient and price effective as possible. That is why these cells make up about 95% of devices produced today [11]. While crystalline silicon has the advantages of a largely developed and optimized technology with large scale production facilities in place, the energy that is required to produce devices is quite high. A silicon solar module has an energy payback time (EPBT) of 1 - 2.5 years, depending on the technology used and its location on the globe [11]. The EPBT is the time a module needs to be in operation in order to generate the amount of energy that was expended in its production. While this first generation of solar cells uses silicon wafers, in the second generation thin film semiconductors like amorphous silicon, CIGS, CdTe and CdS are used [15]. These second generation absorbers are often applied via vapor deposition techniques and the reduction in thickness from some hundred micrometers to just a few microm-

eters reduced both material and production cost. These cost reductions made them quite competitive in the market despite their lower efficiencies. In recent years solar cell concepts with even thinner absorbers including organic and perovskite solar cells (PSCs) promised to be even more material efficient, reducing absorber thicknesses to a couple hundred nanometers. While organics have struggled to reach high efficiencies until recently [16], PSCs also show remarkably high photovoltaic conversion efficiencies (PCEs) exceeding 25% [17], making them a promising contender to break the dominance of silicon modules on the PV market. For reference, single junction silicon solar cells have achieved efficiencies above 26% [18], while CIGS and CdTe have exceeded 23% and 22% respectively [19].

The advantages of PSCs compared to silicon lie both in the reduced material input due to thinner absorbers and in their low temperature fabrication. These factors lead to a smaller energy investment in production and potentially lower EPBT [20, 21]. Additionally perovskites do not contain any rare materials such as tellurium, gallium or indium, that are used in a lot of second generation solar cells, limiting large scale production. These advantages are of course only relevant, because perovskites also show advantageous optical and electrical characteristics such as a high absorption coefficient [22], high charge carrier mobilities and lifetimes [23, 24].

While the prerequisites of PSCs are promising there are still obstacles keeping them from being ready for mass production. While remarkable efficiencies have been achieved at the laboratory scale (usually < 1 cm^2), up-scaled fabrication has only been done at lower efficiencies [25–27]. Using solution based deposition or evaporation makes it challenging to achieve uniform absorber thickness and morphology [28, 29]. Additionally long-term stability has yet to be proven [30–32] and the toxicity of lead utilized in the most efficient perovskites is considered an issue [33, 34].

In order to resolve the issues the community of researchers working in the field of perovskite photovoltaics are facing, it is obligatory to learn as much as possible about the way a perovskite solar cell functions; insights gathered in that regard can be useful for other fields of solar research as well. That is why in this thesis we will try to gain insights into the inner workings of a perovskite solar cell. Classically a

lot of characteristics of a solar cell can be analyzed by investigating the absorber and its interfaces with the contacts. In this thesis however I will show, that for PSCs the properties of the transport layers are of crucial significance for the behaviour of the cell as a whole. The way the transport layers influence the transport, extraction and recombination of charge carriers is non-trivial and goes beyond the influence of a simple ohmic series resistance. Not only the charge-carrier recombination at the interfaces is influenced but also the distribution of charge carriers and the electric field across the absorber. Understanding these properties is crucial to designing well-functioning PSC architectures.

Chapter 2 presents the background information that is the foundation of the contents of this thesis. First the perovskite solar cells are introduced, followed by a brief introduction into the basic attributes of a solar cell as well as the requirements for a cell to be well-functioning. Subsequently the solar cell is examined from two fundamentally different perspectives. The Shockley-Queisser limit is discussed, which takes into account externally measurable parameters of a solar cell. Then the cell is described with respect to charge-carrier transport and charge-carrier generation and recombination dynamics, all of which are internal processes taking place at the material level and as such are only measurable indirectly. Finally characteristics of the electronic structure in perovskites and its band gap properties are discussed followed by the introduction of a model for currents through the transport layers.

In chapter 3 I introduce the experimental and computational methods utilized in this thesis. First I describe the processing of the cells evaluated for this thesis. Then I introduce the measurement techniques that were utilized, focusing on current-voltage measurements and luminescence measurements. Finally I outline the electrical and optical device simulations that were conducted to replicate the measurements.

Chapter 4 presents device simulations of six idealized device architectures and compares several characteristics exhibited by the different layer stacks. For the six configurations the dark and the illuminated current-voltage curves are contrasted as well as the ideality factor at open circuit $n_{\mathrm{id,OC}}$. Additionally the charge carriers remaining in the absorber of the solar cell are examined yielding a voltage dependent internal voltage V_{int}. This internal voltage is evaluated as a function of the externally

applied voltage V_{ext} which is put into context of the distribution of charge carriers and the electric field within the simulated devices. The internal voltage is then examined specifically at short circuit yielding a novel short-circuit ideality factor $n_{\mathrm{id,SC}}$. The combination of these characteristics yields an overall picture of each cell architecture that can be used to interpret equivalent data sets collected for real solar cells.

In chapter 5 I apply the insights gathered in the previous chapter to measurements conducted on perovskite solar cells. Some additional constraints to the measurement routine are elucidated and the characteristic behaviour of perovskite solar cells in voltage dependent luminescence measurements are shown. Then a full data set corresponding to the simulations in the previous chapter is presented along with a simulation assuming material characteristics taken from literature. This preliminary simulation is unable to mirror the behaviour of the internal voltage V_{in} with respect to the external voltage V_{ext} exhibited by the measured cell. Therefore efforts are made to replicate this behaviour while simultaneously taking into account all other measurement results.

Chapter 6 shows several different methods of calculating the series resistance R_{s} of a solar cell. The concept of a voltage dependent series resistance is introduced along with methods of its determination and corresponding measurement results. A distinguation between a voltage independent ohmic contribution to the series resistance as well as a voltage dependent non-ohmic component is found. The measurement data is matched by a device simulation and key parameters influencing both components of the series resistance are varied to elucidate their role in the behaviour of the series resistance and the cells efficiency as a whole.

2 Fundamentals

This chapter aims to provide the necessary knowledge to follow this thesis. First the basic principles of solar cells are introduced in reference to the specific properties of PSCs. An equivalent circuit model is introduced as well as the band diagram and the series resistance R_s and how it can be calculated. These concepts will be employed in the analysis of measurement and simulation data in the results chapters. Afterwards I discuss the sources of hysteresis that is often encountered in PSCs. This is followed by a summary of requirements the bulk absorber and the contact layers of a PSC should meet in order for the cell to function properly.

After this general overview the fundamentals of charge carrier extraction are first examined from a macroscopic perspective in the Shockley-Queisser Model, followed by the charge carrier transport. Subsequently the processes of generation and recombination of charge carriers are elucidated as these will take a central role in the analyses carried out in this thesis. Since the transport and bulk layers in the measured and simulated solar cells have a strong influence on the charge carrier densities and the electric field distribution within the cells, differing injection characteristics are discussed. Afterwards the influence of these injection characteristics on the charge carrier lifetimes, luminescence measurements and ideality factors are explained. This is important to understand in order to be able to correctly interpret the luminescence measurements and simulations in this thesis.

Finally the electronic structure and band gap characteristics of PSCs are described and an approach to interpret the currents through the transport layers is proposed. This will yield an additional perspective to understand the influence of the transport layer characteristics on charge carrier extraction and will be utilized in chapter 4.

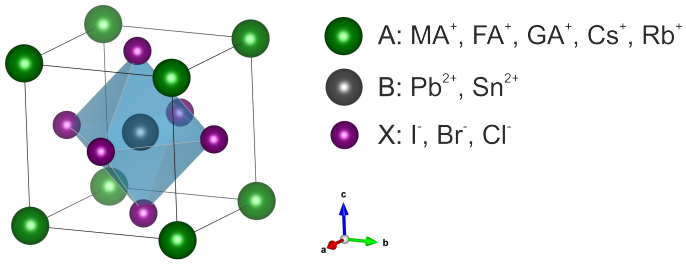

Figure 2.1: Illustration of the cubic perovskite crystal structure ABX_3. In metal halide perovskites used in solar cell applications the A-site is either occupied by an organic or an inorganic cation, the B-site and the X-site are filled with metal anions and halide anions respectively.

2.1 Perovskite Solar Cells

The term "perovskite" does not only refer to semiconductor materials utilized in solar cells but rather to an entire family of materials that crystallize in the ABX_3 structure. The first material of this class was $CaTiO_3$ which was discovered by Gustav Rose in 1939 in the Ural mountains. Rose named it after the Russian mineralogist Lev Perovski [35]. The A, B and X-sites (see fig. 2.1) within the crystal structure can be occupied by a wide range of atoms or molecules thereby producing very different material characteristics. Alongside the semiconducting perovskites that are used in solar cells there are perovskite compositions that show insulating, metallic, superconducting and ferromagnetic properties [36–39]. In this chapter the characteristics of solar cells based on metal halide perovskites will be introduced.

2.1.1 Emergence and Evolution of Perovskite Solar Cells

In 1978 D. Weber was the first to report on the synthesis of methylammonium lead halide perovkites, long before they were being considered for solar cell applications [40]. For the group of semiconducting metal halide perovskites utilized in solar cells the B-site is usually occupied by a heavy cation such as Pb^+ and sometimes Sn^+. The X-site is occupied by halides like Br^-, I^- or Cl^-. The A-site oftentimes contains organic molecules like methylammonium (MA, $CH_3NH_3^+$), formamidinium (FA, $CH(NH_2)_2^+$) or guanidinium (GA, $C(NH_2)_3^+$) but inorganic materials such as

Cs^+ and Rb^+ are used as well. Especially at the A and X-sites it is quite common that a mixture of the mentioned components is used. It is however not possible to use an arbitrary mixture of any of the molecules and elements mentioned above. The compatibility of the components employed is governed by the Goldschmidt tolerance factor

$$t = \frac{r_A + r_X}{\sqrt{2}(r_B + r_X)}, \tag{2.1}$$

which depends on the ionic radii r_A, r_B and r_X [41, 42]. If this tolerance factor is 1 the perovskite crystallizes in an ideal cubic structure whereas variations in the ionic radii change the tolerance factor, adding strain to the crystal lattice. Hybrid perovskites form for compositions exhibiting tolerance factors in the range of $t \approx 0.8 - 1.0$ [43, 44]. Larger A-site cations generate tolerance factors $t > 1$ and lead to compounds with lower dimensionality [43]. While the tolerance factor describes the constraints under which perovskite compositions may be varied, this variation has the potential to yield significantly different electronic properties. It influences stability as well as the band gap energy [45, 46], which can be varied from 1.48 to 2.3 eV for lead-containing perovskites [47] and to even lower values for tin-based perovskites [48]. This tunability makes it possible to adapt metal halide perovkites for various applications.

In the 1990's Mitzi and colleagues investigated charge transport characteristics of organic inorganic hybrid perovskites and used them in field-effect transistors [23, 49, 50]. The first time perovskites were actually employed in the context of a solar cell was in 2009 by the group of T. Miyasaka, achieving a PCE of 3.8% [51]. This first device was a liquid-based dye sensitized solar cell (DSSC) with the perovskite acting as a light-sensitizer forming a thin layer on a mesoporous scaffold of titaniumdioxide (TiO_2). Two groundbreaking works in 2012 demonstrated that halide perovskites were not only capable of absorbing light exceptionally well, but that they also possessed remarkable conducting properties [52, 53]. These publications reported PCEs of 10.9% and 9.7% respectively and sparked an enormous rise in global research activity in the field, giving rise to thousands of research papers being published yearly ever since. The amount of attention paid to PSCs led to an improved control over the perovskite absorber quality and better matching electron

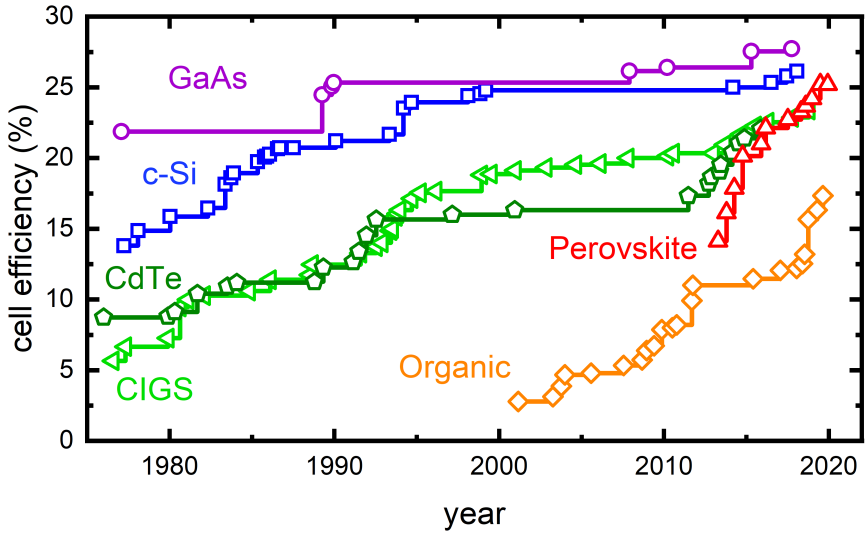

Figure 2.2: Chronological development of the highest confirmed efficiencies of single junction solar cells employing the most successful absorber materials. Adapted from the research-cell efficiency chart published by the National Renewable Energy Laboratory (NREL) [17].

and hole transport layers culminating in an increase of PCE at a speed that no other solar technology had undergone before. In figure 2.2 the evolution of record efficiencies at the laboratory scale of all major single junction solar cell technologies is displayed. PSCs (red curve) have seen the steepest increase in PCE of any technology from 2013 to 2015 and continue to improve, reaching record efficiencies of over 25% today [54], with even higher records to be published.

Research efforts in perovskites have meanwhile also expanded towards other optoelectronic applications, such as light emitting diodes (LEDs) [55, 56] and semiconductor lasers [57, 58]. Perovskites are suitable for these types of devices because they show remarkably high luminescence efficiencies. These luminescence efficiencies are tightly linked to the strong absorbing capabilities of perovskites. Additionally the luminescent properties of perovskites enable the measurements conducted in this thesis.

2.1.2 Photovoltaic Performance

Solar cells are opto-electronic devices that harvest the energy from incoming sunlight and convert it into electrical energy. The energy of photons that enter the solar cell is absorbed by electrons that are lifted to a higher energetic state and leave behind a hole in the space they occupied before. A hole is a quasiparticle representing the lack of an electron at a position where an electron could exist in an atomic lattice. This hole mostly acts like an electron with an opposite sign. The charge carriers - electrons and holes - are extracted at opposite ends of the solar cell generating a current. The reciprocal process to photon absorption is luminescence generated by charge carriers recombining radiatively. The connection between luminescence and the excitation of a semiconductor has been demonstrated both for electroluminescence (EL) generated by an applied voltage [59] and photoluminescence (PL) generated by incident light [60].

The key defining factor of a solar cell is the power conversion efficiency (PCE, η). The PCE is the ratio between the extracted electric power density P_{el} and the power density of incoming light P_{in}. For solar cells the incoming radiation is often defined by the AM1.5g spectrum with $P_{\mathrm{sun}} = \int_0^\infty E\phi_{\mathrm{sun}}(E)\mathrm{d}E = 1000\ \mathrm{Wm}^{-2}$. This corresponds to the power density of the sunlight that passed through 1.5 times the thickness of the earths atmosphere, which is roughly the distance sunlight has to travel to reach the earth's most populated areas because of the zenith angle [61]. The power density that can be extracted with a specific solar cell is usually closely related to its current density-voltage curve (for simplicity and readability I will in the following refer to power density P as "power" and current density J as "current" even though they will usually be normalized to an area). Figure 2.3 shows an example of such a current-voltage curve. The open-circuit voltage V_{OC} is the voltage that builds up within the device, if it is not connected to an external circuit, while the short-circuit current density J_{SC} is the current that flows when the contacts are connected without applying an external voltage. Since the extracted electric power $P_{\mathrm{el}} = J \times V$, there has to be an optimum point on the curve for maximum efficiency. This is the maximum power point (MPP) with the corresponding current J_{MPP} and voltage V_{MPP}. This leads to the definition of the third key characteristic of a solar cell, the fill factor FF, which is defined as

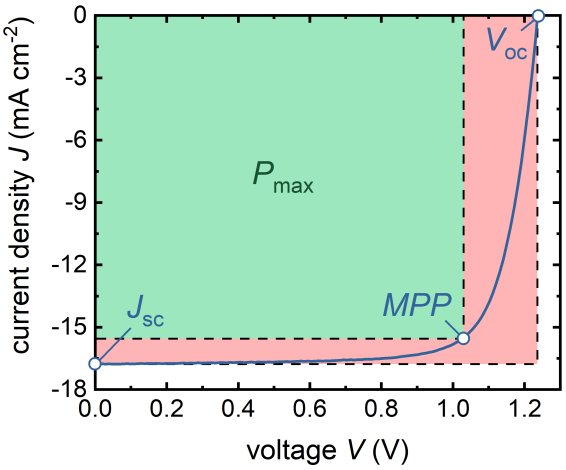

Figure 2.3: Example of a current-voltage curve of an illuminated solar cell. The key characteristics of the cell are indicated. The green area represents the maximum power density P_{max} that can be extracted. The ratio of the green rectangle to the red rectangle is the fill factor FF.

$$FF = \frac{J_{\mathrm{MPP}} V_{\mathrm{MPP}}}{J_{\mathrm{SC}} V_{\mathrm{OC}}}. \tag{2.2}$$

This yields the simple description of the efficiency of a solar cell

$$\eta = \frac{P_{\mathrm{max}}}{P_{\mathrm{sun}}} = \frac{J_{\mathrm{MPP}} V_{\mathrm{MPP}}}{P_{\mathrm{sun}}} = \frac{J_{\mathrm{sc}} V_{\mathrm{oc}} FF}{P_{\mathrm{sun}}}. \tag{2.3}$$

2.1.3 Diode Equation and Equivalent Circuit Model

In the previous chapter the defining parameters for the efficiency of a solar cell were introduced and explained. Now it is necessary to understand how these parameters interact and how they may be limited by advantageous or disadvantageous characteristics of a solar cell. Assuming a solar cell functions as an idealized diode, its current-voltage characteristic is described by the ideal diode equation

$$J = J_0 \left[\exp\left(\frac{qV}{n_{\mathrm{id}} k_{\mathrm{B}} T} \right) - 1 \right] - J_{\mathrm{SC}}, \tag{2.4}$$

with the Boltzmann constant k_B, the temperature T and the ideality factor n_{id}. The ideality factor n_{id} can be assumed to be 1 in this ideal representation of the diode; how it behaves in other situations is elaborated in chapter 2.5.7. This diode equation relies on the superposition of two currents, the photogenerated current that is in this case equal to the short-circuit current density J_{SC} and the recombination current J_{rec} at the diode that is modulated by the externally applied voltage V. The recombination current or diode current is defined by the saturation current J_0, which contains the voltage independent prefactors of the recombination current density, multiplied by a rectifying term varying exponentially with the external voltage V. The superposition of the two currents can be visualized in an equivalent-circuit model as is presented in fig. 2.4 (a). The recombination current, signified by J_{rec} runs in the opposite direction to the photogenerated short-circuit current J_{SC}, reducing the collected current J (which is negative in the signature convention used here). If the applied voltage $V = 0$, the diode term in equation 2.4 vanishes and the collected current $J = J_{SC}$.

This simplified model does not take into account any resistive effects that are present in any real world solar cell. In fig. 2.4 (b) an equivalent circuit is illustrated including both a series resistance R_s and a parallel resistance R_p which are in series and in parallel to the diode respectively. The series resistance R_s usually reflects ohmic losses at the contacts or in other layers of a solar cell. It may however also include resistive effects arising from limited mobilities of charge carriers in the absorber of a solar cell. A high series resistance in a solar cell will lead to a reduction of its fill factor FF. The parallel resistance R_p is often referred to as the shunt resistance of a cell. In a solar cell a shunt is typically a manufacturing defect creating an area of the cell where current can flow from one contact to the other with low resistance. Thus a shunt provides an alternate current path for the photogenerated current J_{ph} reducing the current collected at the contacts. This means a good solar cell should have a high parallel resistance in order to reduce these losses. If the shunt resistance is reduced however, it will lead to a reduction of the fill factor FF of the cell as well as the open-circuit voltage. If we want to include the new elements in the equivalent-circuit model as depicted in fig. 2.4 (b) in the diode equation we get [62]

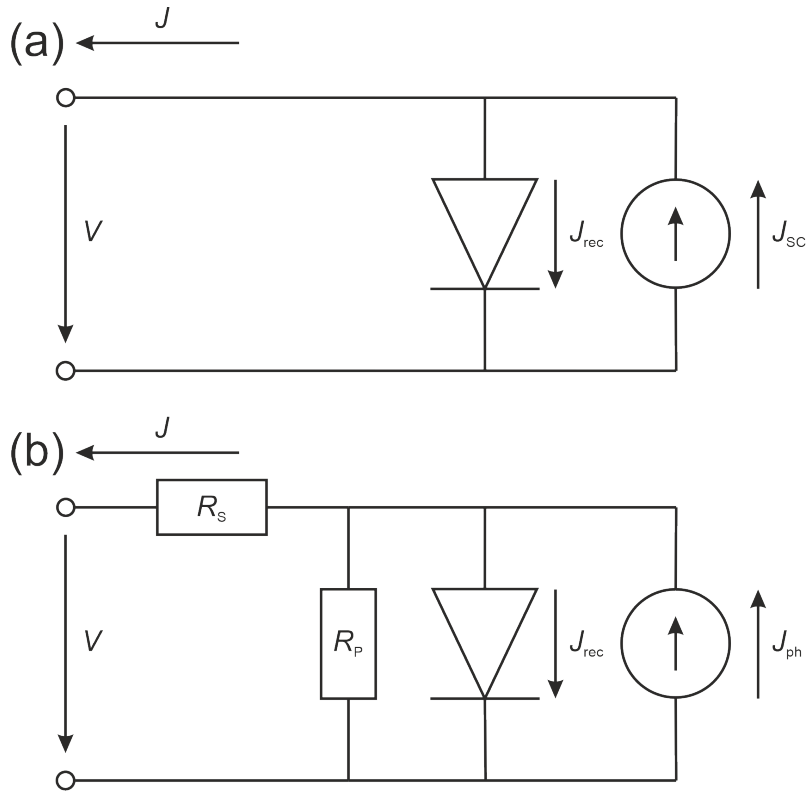

Figure 2.4: One-diode equivalent-circuit model of (a) an ideal solar cell consisting of a rectifying diode element with recombination current density J_{rec} and a current source supplying the photogenerated short current density J_{SC} and (b) a more realistic solar cell including a series resistance R_{s}, a parallel resistance R_{p} with the photogenerated current density J_{ph}. In both cases the external voltage V is applied at the contacts and the current density J is extracted.

$$J = J_0 \left[\exp\left(\frac{q(V - JR_{\mathrm{s}})}{n_{\mathrm{id}} k_{\mathrm{B}} T} \right) - 1 \right] + \frac{V - JR_{\mathrm{s}}}{R_{\mathrm{p}}} - J_{\mathrm{ph}}. \tag{2.5}$$

Note that this equation reduces to equation 2.4 for the case that $R_{\mathrm{s}} = 0$ and $R_{\mathrm{p}} = \infty$. The photogenerated current J_{ph} in equation 2.5 and fig. 2.4 (b) is not represented by the short-circuit current density J_{SC} anymore since they are not equal at $V = 0$. This shows that while the current loss across the parallel resistance R_{p} can be regarded as a seperate term in the diode equation, considering the series resistance R_{s} in the ideal diode equation violates the assumption of superposition. The current J that is extracted from the cell is no longer solely determined by the applied voltage V but

additionally influenced by the current flowing in the cell and accordingly dependent on the illumination intensity ϕ impinging on the cell. The recombination current J_{rec} in short circuit at the diode is no longer zero and can be measured. The measurement of the series resistance R_{s} as well as the measurement of the recombination current J_{rec} in short circuit can give valuable insights into the characteristics of a solar cell and its components and will be central aspects of this thesis.

2.1.4 Structure of Perovskite Solar Cells

As established in chapter 2.1.2, the two main functions of a solar cell are to first absorb light generating charge carriers and then separate and extract them. While the prerequisite for the former step is mainly a high absorptance of the absorber layer, the second step can be a bit more complicated to achieve. In order to understand the strategies employed to efficiently extract charge carriers an understanding of the structure of semiconductors is necessary. In order for a material to be semiconducting it needs to have a band gap E_{g} distinguishing it from metals, which do not possess one. This band gap is an energy space in the crystal lattice that does not offer any energetic states for charge carriers to reside in, it is illustrated in fig. 2.5. In a defect free semiconductor charge carriers may only reside at energy levels above or below the band gap. It is defined as the energetic difference between the highest occupiable state on the lower end of the gap (maximum of the valence band E_{V}) and the lowest occupiable state on higher end (minimum of the conduction band E_{C}). The edges of the valence band E_{V} and the conduction band E_{C} are also illustrated in fig. 2.5. Their energetic positions are defined relative to the vacuum energy E_{vac}, which represents the state of a free electron not bound to an atom or lattice. In the center of the band gap the energy of the Fermi-level is illustrated by a dashed line. The Fermi-energy is the anchor point for the Fermi-Dirac distribution analytically describing the charge carrier densities within the respective bands. If the charge carrier densities in both bands are equal the Fermi-level is situated in the middle of the band gap as illustrated in fig. 2.5. If the density of electrons n in the conduction band exceeds the density of holes p in the valence band the Fermi-level moves towards the conduction band, if it is the other way around it gets closer to the valence band.

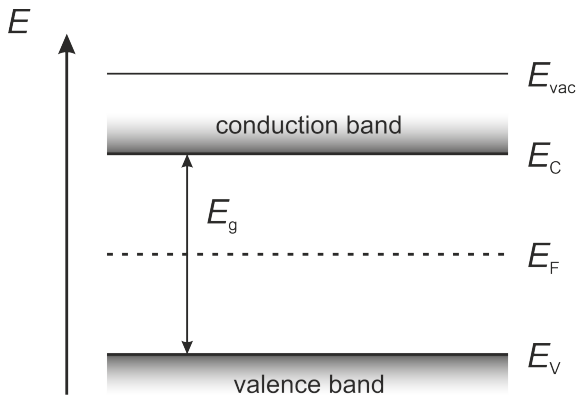

Figure 2.5: Schematic depiction of the key energy levels in the band diagram of a semiconductor. E_{vac} is the vacuum level energy, E_{C} and E_{V} are the energy levels of the conduction band edge and the valence band edge respectively and E_{F} is the energy of the Fermi-level. E_{g} denotes the band gap which describes the difference between the band edges $E_{\mathrm{C}} - E_{\mathrm{V}}$.

In wafer based crystalline silicon solar cells charge separation - the spatial separation of electrons and holes for extraction - is achieved by creating a so called *pn*-junction by doping the wafer and creating an electric field. Doping of a layer is achieved by introducing atoms (dopants) into the crystal lattice that either add an additional valence electron (donators with the donator density N_{D}) or lack a valence electron (acceptors with the acceptor density N_{A}) leaving a positively charged hole. These dopants asymmetrically increase the density of electrons n and holes p within the semiconductor, shifting the Fermi-level E_{F} towards the conduction band E_{C} and the valence band E_{V} respectively. The *pn*-junction is located where a positively doped *p*-layer comes into contact with a negatively doped *n*-layer. In contact the Fermi-levels align because the asymmetric charge carrier concentrations equilibrate at the interface. This results in a bending of the valence and conduction bands creating an electric field. Along this electric field the oppositely charged carriers are separated and can subsequently be extracted.

Like most thin film solar cells, PSCs follow a different architecture. Additionally to the p and n layers, there is a third intrinsic i-layer sandwiched between those two. Thin film amorphous silicon solar cells are early predecessors of this kind of structure [63, 64]. Figure 2.6 (a) shows a schematic drawing of the layer stack of a typical *p-i-n*-type solar cell. The stack is situated on a glass substrate beginning

with a transparent conducting oxide (TCO), which acts as the front contact for charge extraction. The TCO is followed by a *p*-type layer that acts as a hole transport layer (HTL), the absorber, which is denoted as the *i*-type layer and an *n*-type layer also referred to as an electron transport layer (ETL). At the back the stack of layers is concluded by a metal contact for efficient charge extraction.

The description of the *p*-*i*-*n*-structure can be understood in different ways, it could be seen as the order the layers in a solar cell stack are manufactured or the order layers are traversed by incident light. In perovskite solar cells these two are often the same because cells are fabricated on a glass substrate and illuminated through this glass. In this work I will be using the latter definition of the layer stack along the incident light axis. Anologously to the *p*-*i*-*n*-structure there is also the inverted *n*-*i*-*p*-structure, where the contact layers are switched. Historically for PSCs this is indeed the initially used architecture as it was derived from DSSCs employing mesoporous TiO_2 as a scaffold. Aside from using materials adjusted for this structure the functionality of these *n*-*i*-*p*-type cells is similar, here I will focus on the *p*-*i*-*n* archetype.

Figure 2.6 (b) shows the band diagram of the three *p*-*i*-*n*-layers in isolation from each other. They are characterized by the positions of their conduction and valence band energies E_C and E_V with respect to the vacuum energy E_{vac} as described above.

The position of the Fermi level in the band gap between the two bands differs according to the doping conditions. In the conventional *p*-*i*-*n*-structure the function of the doped layers is to create an electric field across the absorber. The build-up of this field comes about when the three layers are brought into contact as illustrated in figure 2.6 (c). In equilibrium, the Fermi levels need to align once again bending the bands, mainly in the absorber. The high doping densities in the transport layers keep their bands from bending, at least this is the case in a lot of classical thin film solar cells employing this architecture. Fig. 2.6 (d) shows a situation that more closely resembles the situation in perovskite solar cells as they have been investigated in this thesis. The ETL and HTL are not as highly doped and therefore bend as well as they are in contact with the absorber.

The equilibration of the Fermi level E_F and the subsequent bending of the

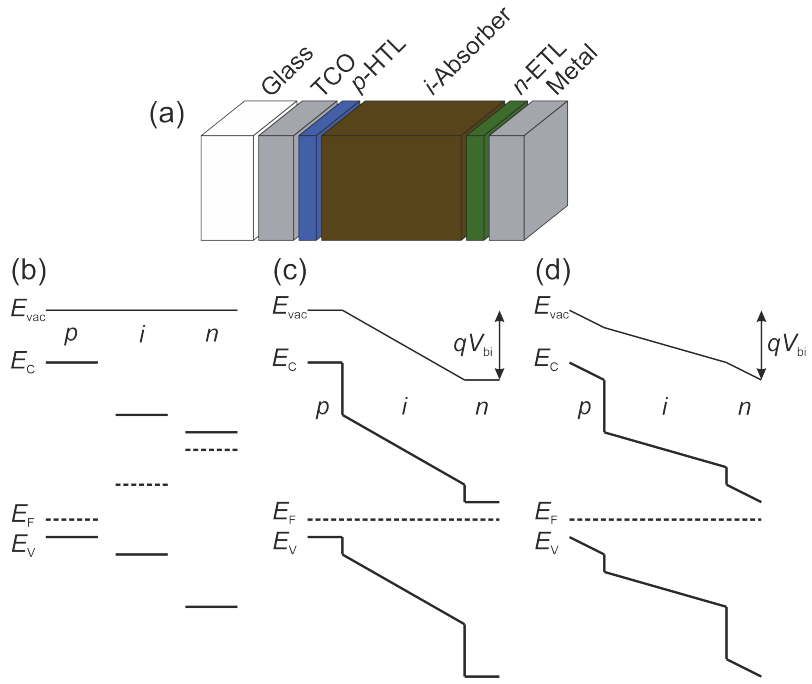

Figure 2.6: (a) Typical layer stack of a *p-i-n*-type thin film solar cell. (b) Schematic energy diagram of the intrinsic absorber layer (i), electron transport layer (n) and the the hole transporting layer (p) seperate from each other. The conduction and valence band energies (E_C and E_V), as well as the Fermi energy E_F are shown in relation to the vacuum energy E_{vac}. (c) The energy diagram of the *p-i-n* layers in contact, the Fermi levels are equilibrated and generate the built-in voltage V_{bi}. (d) More realistic band diagram for perovskite solar cells in this work without highly doped n- and p-layers. Energy levels in ETL and HTL are not necessarily fixed and part of the built in voltage V_{bi} can drop off across them.

bands and the vacuum energy lead to the formation of an electric field across the stack. In the more "classical" picture in fig. 2.6 (c) this field forms across the i-layer entirely, it is signified by the built-in voltage V_{bi}. In fig. 2.6 (d), which is closer to the situation covered in this thesis, the built-in field stretches across all three layers. This field aids in the separation and extraction of photogenerated charge carriers, especially when the charge carrier diffusion lengths are small compared to the device thickness [65]. At any given point in the device the electric field

$$F = \frac{1}{q}\frac{\mathrm{d}E_{vac}}{\mathrm{d}x} \tag{2.6}$$

is given by the gradient of either the conduction and valence band energies E_C and E_V or by the gradient of the vacuum energy E_{vac}.

It is important to note, that the denotation of a *p*-*i*-*n*-type cell structure, while easily comprehensible, may be a bit misleading or not entirely accurate at times. In contrast to the *p* and *n*-layers the absorber is described as intrinsic meaning no doping and essentially a Fermi level in the middle of the band gap. Especially for perovskites that may not necessarily be true [66, 67] and it is oftentimes not immediately evident how the multitude of crystal components may influence the charge carrier concentrations in a complex perovskite material.

At the same time the *p*- and *n*-materials are not necessarily heavily doped either. The task of the ETL and the HTL is to extract one kind of charge carrier while keeping the other out. There are however means to achieve this aside from doping. In the case of an undoped or lightly doped ETL/HTL the adjacent layers such as a TCO, metal or dipole layer may define the position of the Fermi level, effectively pinning it in place at the respective interface. On the other hand the alignment of the conduction and valence band energies of the *p*- and *n*-layers with respect to the absorber is of great importance. As can be seen in figure 2.6 (b), there are some smaller and some larger band offsets. For the valence bands of the *p*- and the *i*-layer, as well as for the conduction bands of the *n*- and the *i*-layer the offsets are rather small. These small offsets aid the respective charge carriers in entering the transport layer that they are meant to go into. It is however crucial, that these offsets are kept as small as possible, because they reduce the field across the absorber, thereby impairing charge carrier collection and ultimately reducing V_{OC} and PCE of the solar cell. Opposed to these ideally smooth transitions for the "desired" type of charge carrier, the offsets of the conduction bands of the *p*- and *i*-layers as well as the valence bands of the *n*- and *i*-layers are rather large. They act as an energetic barrier for the respective "undesired" type of charge carrier, preventing them from entering the layer and effectively reducing surface recombination. Consequently making electrons the majority carriers in the ETL and holes in the HTL can be facilitated by a sensible choice of contact materials and band alignments of the transport layers themselves without a necessity for doping. The *p*- and *n*-layers act as blocking layers for the minority carriers while transporting the majority carriers,

hence their denotation as ETL and HTL.

Undoped transport layers in a *p*-*i*-*n*-structure have implications for the band diagram as well. The diagram in figure 2.6 (c) assumes highly doped *p*- and *n*-layers. This means that their bands are flat and the entire built-in voltage V_{bi} drops off across the absorber. For undoped or lightly doped transport layers this is not necessarily the case and the situation in figure 2.6 (d) is more realistic. Here nonzero amounts of the built-in electric field are present in all layers, crucially influencing charge extraction and device performance. The implications of this will be an important part of this thesis and will be discussed in more detail in chapter 5.

2.1.5 Series Resistance

As mentioned in chapter 2.1.3 it is vital to the understanding of the functionality of a solar cell to be able to measure the resistive effects taking place both in the contacting framework as well as the absorber and the transport layers. Before we start discussing measurement techniques for the series resistance R_{s} however, we first have to understand what phenomena it is comprised of. Figure 2.7 shows an equivalent-circuit model modified with respect to the ones shown in figure 2.4 [68,69]. Here the series resistance R_{s} is no longer illustrated as a singular ohmic resistance but as two seperate resistances with different properties [70]

$$R_{\mathrm{s}}(V) = R_{\mathrm{s,ext}} + R_{\mathrm{s,int}}(V). \tag{2.7}$$

The external series resistance $R_{\mathrm{s,ext}}$ best corresponds to a sort of textbook description of a solar cell where the series resistance R_{s} is comprised of all the ohmic resistances of a solar cell system caused by the contacts or other external components of a measurement setup. In reality this is oftentimes not the case, because there is an internal contribution to the series resistance. This new aspect to the model is described as the internal series resistance $R_{\mathrm{s,int}}(V)$, which is dependent on the voltage V applied to the cell. This contribution stems from non-ohmic resistive effects within the absorber and the transport layers of a solar cells caused by finite charge carrier mobilites μ and insufficient electrical fields driving the charge carriers out of the cell. These limitations will lead to a reduction of the externally

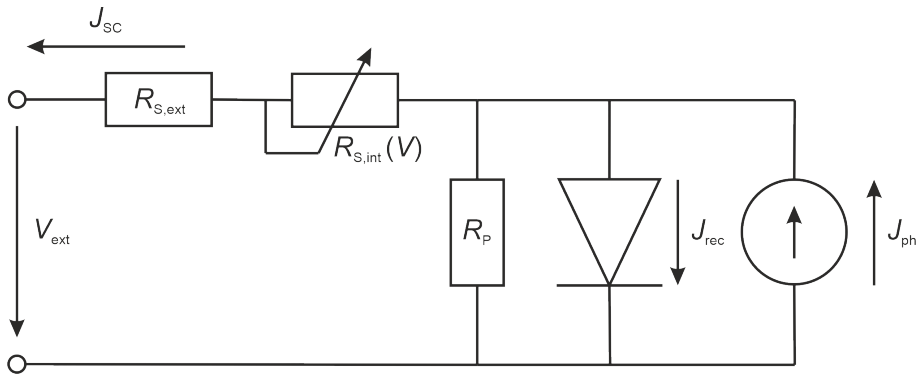

Figure 2.7: One-diode equivalent circuit of a solar cell including a parallel resistance R_p as well as a series resistance consisting of an external component $R_\mathrm{s,ext}$ and a voltage dependent internal component $R_\mathrm{s,int}$. J_ph signifies the photogeneretad current density, while J_rec is the total current density caused by recombination.

measureable current density J without ohmic losses in the classical sense. Additional non-linear resistive effects can stem from the spatial dimension of a solar cell. Since the distance to a current-extracting contact can strongly vary spatially, charge carriers have to traverse differing proportions of contacting layers acting as ohmic resistors [71].

The limitation of charge extraction from the absorber of a solar cell can be modulated by the application of an external voltage V_ext as well as an introduction of additional charge carriers into the system by changing the illumination intensity ϕ impinging on the cell. It is therefore not a fixed value like the external series resistance $R_\mathrm{s,ext}$ but rather a characteristic that is strongly dependent on the conditions the solar cell is put under. This is why measuring the internal series resistance $R_\mathrm{s,int}$ while varying these conditions can grant valuable insights into the mechanisms causing it. So naturally the next question is, how the voltage dependent series resistance $R_\mathrm{s}(V)$ can be determined.

A classical method to determine the series resistance R_s was introduced by Wolf and Rauschenbach and involves the comparison of dark and illuminated current-voltage characteristics [72]. In figure 2.8 we see a dark current-voltage curve $J_\mathrm{d}(V)$ in comparison to a current voltage curve under one-sun illumination $J_\mathrm{i}(V)$ as well as a curve generated by measuring the short-circuit current density J_SC and the open-circuit voltage V_OC at varied illumination intensities ϕ. The latter will in the

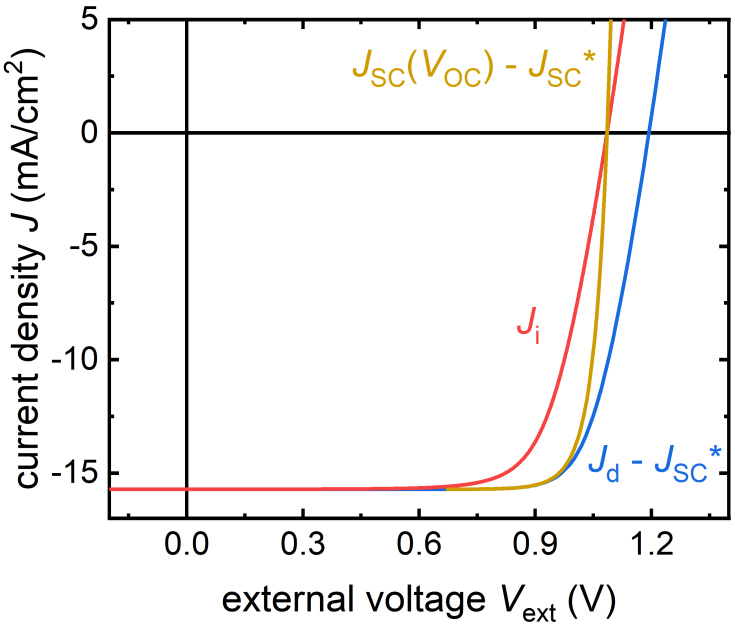

Figure 2.8: Three current-voltage characteristics in comparison in the fourth quadrant of the coordinate system. $J_\mathrm{d} - J_\mathrm{SC}^*$ denotes the dark current-voltage curve, J_i denotes the current-voltage curve under illumination of one sun and $J_\mathrm{SC}(V_\mathrm{OC}) - J_\mathrm{SC}^*$ describes a suns-V_OC curve of short-circuit current densities J_SC and open-circuit voltages V_OC measured at varied illumination intensities. The $J_\mathrm{d}(V)$ curve and the suns-V_OC curve were moved to the fourth quadrant of the graph by subtracting the short-circuit current density J_SC^* taken from the $J_\mathrm{i}(V)$ curve.

following be referred to as the suns-V_OC characteristic of a cell due to its dependency on illumination intensity. All curves are plotted in the fourth quadrant of the coordinate system. To facilitate this the short-circuit current density J_SC^* taken from the illuminated current-voltage curve has to be subtracted from the other two. Upon inspection of the curves we see that while they per definition share the same J_SC, their behaviour at high external voltages V_ext differs quite substantially. This difference is caused by the series resistance R_s of the cell. In order to show this we will use equation 2.5 while assuming that the parallel resistance R_p is sufficiently high for the second term of the equation to become insignificant. This yields three equations

$$J_\mathrm{d} - J_\mathrm{SC}^* = J_0 \left[\exp\left(\frac{q\left(V_\mathrm{d} - J_\mathrm{d} R_\mathrm{s}\right)}{n_\mathrm{id} k_\mathrm{B} T} \right) - 1 \right] - J_\mathrm{SC}^*, \tag{2.8a}$$

$$J_\mathrm{i} = J_0 \left[\exp\left(\frac{q\left(V_\mathrm{i} - J_\mathrm{i} R_\mathrm{s}\right)}{n_\mathrm{id} k_\mathrm{B} T} \right) - 1 \right] - J_\mathrm{SC}^*, \tag{2.8b}$$

$$J_\mathrm{SC} - J_\mathrm{SC}^* = J_0 \left[\exp\left(\frac{q V_\mathrm{OC}}{n_\mathrm{id} k_\mathrm{B} T} \right) - 1 \right] - J_\mathrm{SC}^*, \tag{2.8c}$$

for the three curves shown in figure 2.8, where J_SC^* is the short-circuit current density taken from the illuminated current-voltage curve as opposed to J_SC, which is the short-circuit current density measured at varying ϕ for the suns-V_OC curve. Note that the series resistance R_s has no influence on the suns-V_OC curve since there is no current flow at open circuit that can be impeded. These equations can now be evaluated for equal current densities J which correspond to equal recombination currents J_rec. If we do this for the dark current-voltage curve in comparison to the illuminated curve, $J_\mathrm{d} - J_\mathrm{SC}^* = J_\mathrm{i}$ means we can equate the right hand sides of equations 2.8a and 2.8b leading to

$$V_\mathrm{d} - J_\mathrm{d} R_\mathrm{s} = V_\mathrm{i} - J_\mathrm{i} R_\mathrm{s}, \tag{2.9}$$

which can subsequently be resolved for the series resistance R_s. The same can be done for any combination of the three equations 2.8, yielding three equations

$$R_\mathrm{s} = \frac{V_\mathrm{d} - V_\mathrm{i}}{J_\mathrm{SC}^*}, \tag{2.10a}$$

$$R_\mathrm{s} = \frac{V_\mathrm{d} - V_\mathrm{OC}}{J_\mathrm{SC}}, \tag{2.10b}$$

$$R_\mathrm{s} = \frac{V_\mathrm{i} - V_\mathrm{OC}}{J_\mathrm{SC} - J_\mathrm{SC}^*}, \tag{2.10c}$$

for the determination of the series resistance R_s. Thus we have found expressions to calculate the series resistance of a solar cell from the difference in voltage exhibited by these three different current-voltage characteristics. In case of a voltage independent series resistance R_s, all three methods should yield the same result and it should not depend on the voltage or current density at which the differences defined

by equations 2.10a - 2.10c are evaluated. If, however, there is a voltage dependent component to the series resistance it can still be determined by application of equations 2.10a - 2.10c. These methods will be used in the calculation of the R_s of perovskite solar cells in chapter 6.

2.1.6 Hysteresis

The characteristic values introduced in chapter 2.1.2 are some of the most essential and readily available information about a solar cell and have been used to characterize a wide array of solar cell types with silicon based solar cells as the most prominent examples. Unlike these silicon based cells however the current-voltage characteristic of PSCs often exhibits strong dependencies to prior optical and electrical conditioning [73–75]. While this has led to research on perovskite-based artificial synapses that rely on their electrical response to depend on electrical pre-conditioning [76], it creates challenges for characterization and application of photovoltaic devices based on these materials. This means that the result of a current-voltage measurement depends on the measurement history of the cell and very close attention has to be paid to the measurement parameters, specifically the sweep direction and the sweep speed. In figure 2.9 we see current-voltage curves of the same perovskite solar cell, one measured in forward direction and one measured in reverse. The cell exhibits moderate hysteresis, which leads to the two curves not overlapping but showing different values for both the fill factor FF and the short-circuit current density J_{SC}, as well as a slight change in open-circuit voltage V_{OC}. These changes lead to a differing estimation of the cells efficiency η depending on the measurement direction. A transient change of the PSC's characteristics has also been observed for the photocurrent J_{ph}, open-circuit voltage V_{OC} and photoluminescence intensity ϕ_{PL} on the timescale of up to hundreds of seconds [46, 77–79]. The extent to which these effects take place tends to get exacerbated by deagradation or aging of the devices [80]. In order to properly measure the characteristics of a perovskite solar cell it is therefore crucial to understand the origin of hysteretic effects in order to rule out any distorting influence on the measurement data.

The most widely accepted explanatory approach is that time-varying quantities of charge-carrying ions accumulate at the interfaces of the perovskite absorber

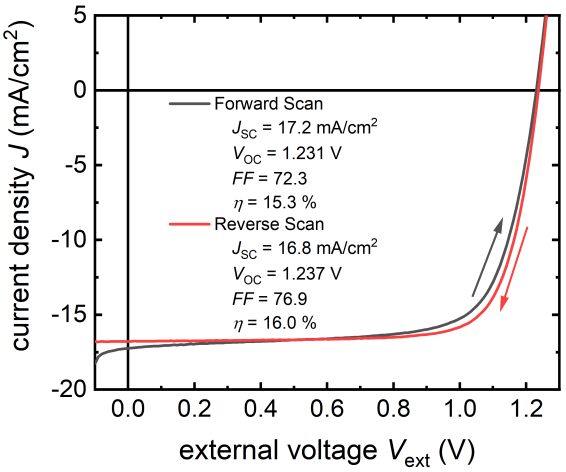

Figure 2.9: Current-voltage characteristic of the same solar cell measured in forward (grey curve) and reverse direction (red curve) together with the characteristic values taken from the measurements. The scan speed was 75 mV/s for both curves.

and partially or even entirely screen the electric field within, effectively reducing the photocurrent [74, 81–83]. While several different theories for the origin of this accumulation of charge carriers have been discussed there is strong evidence that it is caused by the drift or diffusion of mobile ionic defects within the perovskite absorber [84–86]. Note that these ionic defects are not extrinsic defects caused by impurities externally introduced into the perovskite crystal lattice but intrisic defects such as iodine or methyllamonium ions or vacancies. While there have been reports on extrinsic defects influencing the functionality of PSCs, they are associated with compositions that are not used in the cells evaluated in this thesis [87].

When an external voltage V_{ext} is applied to a PSC an electric field forms in the absorber which leads to a drift of ions towards the contacts. Since these ionic defects can usually not leave the perovskite layer they accumulate at the interface with the magnitude of the accumulation being dependent on the externally applied voltage. Among others this phenomenon was studied by Tessler and Vaynzof and can be understood by the graphs adapted from their work seen in figure 2.10 [88]. Panels (a) and (b) show the distribution of charge carrier densities in a device roughly at V_{OC} taken from simulations with and without the inclusion of mobile ions, respectively. For panel (a) including ionic movement the dashed lines show a

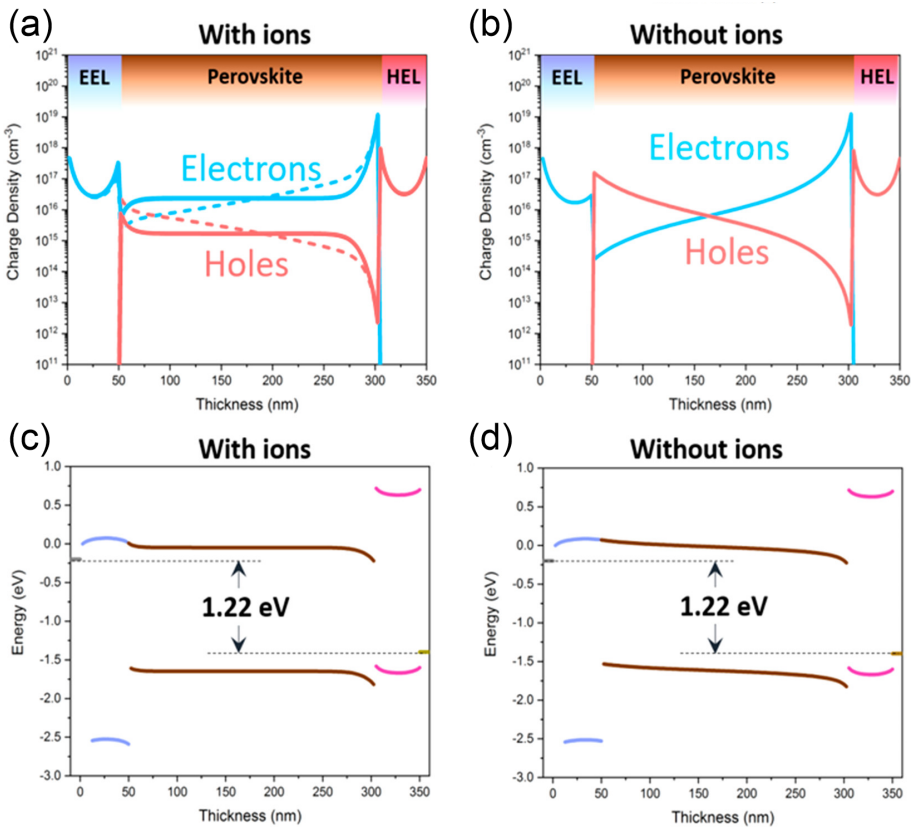

Figure 2.10: Spatial charge carrier density distribution at $V \approx V_{OC}$ (a) with and (b) without the inclusion of ions. In (a) dashed and solid lines refer to forward and reverse scans respectively (50 mV/s). Band diagrams at $V \approx V_{OC}$ in a reverse scan (c) with ions and (d) without the influence of ions. Adapted with permission from [88]. Copyright 2020 American Chemical Society.

markedly different distribution for a forward scan than the solid lines exhibit for a measurement in reverse direction. The field screening effect of ions accumulating at the contacts can be illustrated by considering a cell at V_{OC} in a reverse scan. The band diagram for such a cell is displayed in figure 2.10 (c) and (d) with and without the inclusion of ionic movement, respectively. We can observe strongly flattened bands for the simulation including mobile ionic defects while a mostly unifom electric field is present in the simulation that does not take it into account.

These observations mean, that the cell can be 'preconditioned' by applying a voltage or illuminating the cell before a measurement since this preconditioning defines the extent to which ionic charges can accumulate at the interfaces. Further-

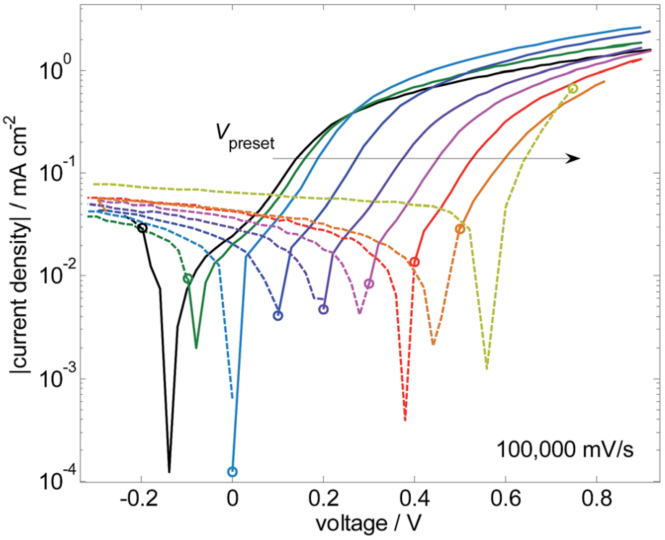

Figure 2.11: Dark current-voltage curves vor a device previously equilibrated at a voltage V_{preset} marked by circles. Solid lines relate to forward scans and dashed lines to reverse scans. The scan-speed was 100000 mV/s. Reproduced from [74] with permission from the Royal Society of Chemistry.

more the timescales for the charges to diffuse through the film and screen the field or reequilibrate can be quite long (1-100s) and depend on e.g. illumination and temperature. This elucidates the significance of the sweep speed when measuring current-voltage curves, the slower the measurement is conducted, the longer the charges are given time to either accumulate or equilibrate. Overall the hysteresis phenomena in PSCs lead to a high importance of sample prebiasing for most of the measurements in this thesis and the taken precautions will be discussed in the respective chapters focusing on these measurements.

The preconditioning of samples can not only be observed in illuminated current-voltage curves but also for curves measured in the dark. In these curves the hysteretic effects can lead to a shift of the minimum of the semilogarithmic plot as can be seen in figure 2.11. The scans in these curves were measured at an extremely high scan-speed of 100000 mV/s, however we will see similar behaviour in my data in this thesis. The shift can be explained by capacitive effects in the cell, however usually the effect is reduced by slower scanning of the dark current-voltage curve [89, 90]. The curves measured for this thesis nevertheless show a behaviour

comparable to figure 2.11 due to a preconditioning of the cells cause by previous illuminated measurements.

2.1.7 Requirements for Bulk Absorbers and Contact Layers

When trying to design the concept for a well-performing solar cell it is important to first consider the requirements for the employed components. The starting point for a new solar cell concept is usually the absorber, which has to fullfil a number of requirements in order for the solar cell to function well. These prerequisites will be briefly discussed now while a more in depth illustration will be given in the following chapters.

1. Suitable band gap

   In the most basic interpretation the band gap energy E_g defines the energy an incoming photon must possess to potentially be absorbed by a material. That means such an idealized band gap represents a cut-off point: photons with lower energy will not be absorbed, their energy can not be harnessed. Therefore a lower band gap of an absorber material leads to a higher absorptance, more charge carriers generated and subsequently to a higher short-circuit current density J_{SC}. Having said that the drawback of low band gaps is energy loss through thermalization. High energy photons will excite electrons from below the valence band and lift them above the conduction band - they are given excess potential energy. This energy is released to the crystal lattice in small steps as phonons (vibrational modes of the lattice, macroscopically heating up the absorber), until the charge carriers have reached the respective band edges. This thermalization also constitutes a loss of energy, the lower dissociation of the charge carriers leads to a lower achievable open-circuit voltage V_{OC}. As equation 2.3 shows, both J_{SC} and V_{OC} are crucial factors for the efficiency of a solar cell. Choosing the band gap of the absorber material is to strike a compromise between the two and there is a maximum to the theoretically achievable efficiency depending on the band gap. The highest efficiencies above 32% can be achieved at band gaps of 1.1-1.4 eV, the band gap of crystalline silicon of 1.12 eV falls into this window. The most efficient

perovskites usually have band gaps of 1.5-1.6 eV and therefore have a slightly lower maximum efficiency. The influence of the band gap on cell performance limits is described by the Shockley-Queisser theory [91]. This theory and its relation to real solar cells are discussed in chapter 2.3.

2. High absorptance

   Why a high absorptance is important for a solar cell is easily understood. It is defined as the ratio between the number of absorbed photons to incoming photons, therefore a higher absorptance is synonymous with a higher amount of charge carriers generated. These charge carriers contribute to the photocurrent J_{ph}, which is essential for a well-performing solar cell. Aside from reflection and light trapping effects the absorptance of a solar cell mainly depends on two parameters: the absorption coefficient α and the thickness of the absorber d. The thickness of the absorber layer has to be tuned to the absorption coefficient in order to absorb a maximum of incoming photons. If the absorber is too thick, the result may be insufficient charge extraction. For most solar cell absorbers a sufficiently high absorptance and consequently a high photocurrent are not a big issue, it is usually one of the first requirements considered.

3. Low non-radiative recombination

   Once charge carriers have been introduced into the absorber either by light absorption or electrical current via the contacts, they may recombine. Naturally this is undesirable since this implies a reduction in short-circuit current density J_{SC}. The charge carriers can recombine radiatively emitting a photon with the energy of the band gap E_{g} or non-radiatively giving their energy off to the crystal lattice. Radiative recombination can not be avoided, because it is thermodynamically coupled to absorption according to the principle of detailed balance and Kirchhoff's law [92, 93]. The higher the absorptivity, the higher the emissivity of the absorber. Non-radiative recombination on the other hand can be controlled and needs to be reduced as much as possible. There are several non-radiative recombination paths that are usually caused by defects or impurities of some sort. Controlling these defects is crucial since the faster recombination occurs, the less time there is for the extraction of charge carriers. The different recombination mechanisms will be discussed

more closely in chapters 2.5.2 and 2.5.3.

4. Efficient charge carrier extraction

   As mentioned above, charge carrier extraction is a process that is competing with recombination. The extraction needs to take place sufficiently quickly in order to avoid significant recombination losses. In solar cells there are two different ways charge carriers can reach the contacts to be extracted, drift and diffusion. If there is a significant electrical field across the absorber transport will be dominated by charge carriers drifting along the field lines to their respective contacts. If there is no or little electric field across the absorber, charge carriers have to diffuse towards the contacts. Both processes depend heavily on the conduction properties of the absorber material, the consequences of limitations in that characteristic will be a central part of this thesis. Charge carrier transport will be explained more closely in chapter 2.4 and resistive effects hindering extraction will be further elucidated in chapter 6.

A suitable absorber is the foundation that a well-performing solar cell can be developed from. It is usually the first part of a concept to be optimized and defines the upper limit of the device performance. A full solar cell also needs properly matched contact layers, otherwise the efficiency of the device may be considerably reduced. The design criteria for the contact layers will be discussed in the following.

1. Suitable band offsets

   As mentioned before the energetic alignment of bands for the contact materials is important for the device performance. The offsets should be designed in such a way that one species of charge carriers can enter the contact layer losing a minimal amount of energy in the process while the other species is being repelled by an energetic barrier. The band offsets between the i-layer (absorber) and the n-layer (ETL) have been illustrated in fig. 2.12 in different cases. The first case in fig. 2.12 (a) is rather suitable for a solar cell. For the ETL the energetic offset for the conduction band (ΔE_{C}) is rather small, for electrons the transfer to the slightly lower band is energetically favourable. This offset enables the electrons to enter the ETL and then poses a small barrier deterring them from reentering the absorber. At the same time holes

in the valence band will not be able to enter the ETL, because of the high barrier ΔE_{V} (due to their inverse polarity for them "higher" energy levels are energetically favourable). Fig. 2.12 (b) shows both bands in the ETL being shifted upwards. This leads to an energetic barrier for the electrons we actually wanted to have in the ETL which is unwanted. On the other hand the barrier for the holes is reduced allowing some of them to penetrate into the ETL where they can recombine with electrons reducing the cell current. Fig. 2.12 (c) shows the bands in the ETL being shifted down. The barrier for the holes is large keeping them out of the ETL, but the offset ΔE_{C} is quite large. Electrons passing this offset will lose energy equivalent to the difference reducing V_{OC} and subsequently the PCE of the device. All these considerations can be applied to the interface between *i*- and *p*-layer as well with reversed roles of the charge carriers. Therefore, designing the contact materials to properly align with the energy levels of the absorber can greatly enhance device performance. Unfavourable band alignment can be detrimental to the electric field distribution within the cell and subsequently hinder the charge carrier extraction process [94–97].

2. Low surface recombination

   At the interface between two heterogeneous crystal structures the crystal lattice is disrupted. This disruption leads to defects like dangling bonds and other vacancies that facilitate recombination. In suboptimal circumstances the recombination at the interfaces can significantly hamper device performance by reducing J_{SC} and V_{OC}. Therefore it is important that the contact layer and the absorber form an interface with slow surface recombination. The surface recombination can be inhibited by passivating vacancies (i.e. filling them with atoms) and by designing the cell architecture in such a way, that low amounts of charge carriers are present at the interface.

3. Sufficient conductivity

   As mentioned above, surface recombination depends on the amount of defects at the surface as well as the amount of charge carriers available to recombine. While a high barrier for minority carriers can help reduce the amount of one species of charge carriers available for recombination, a high conductivity of

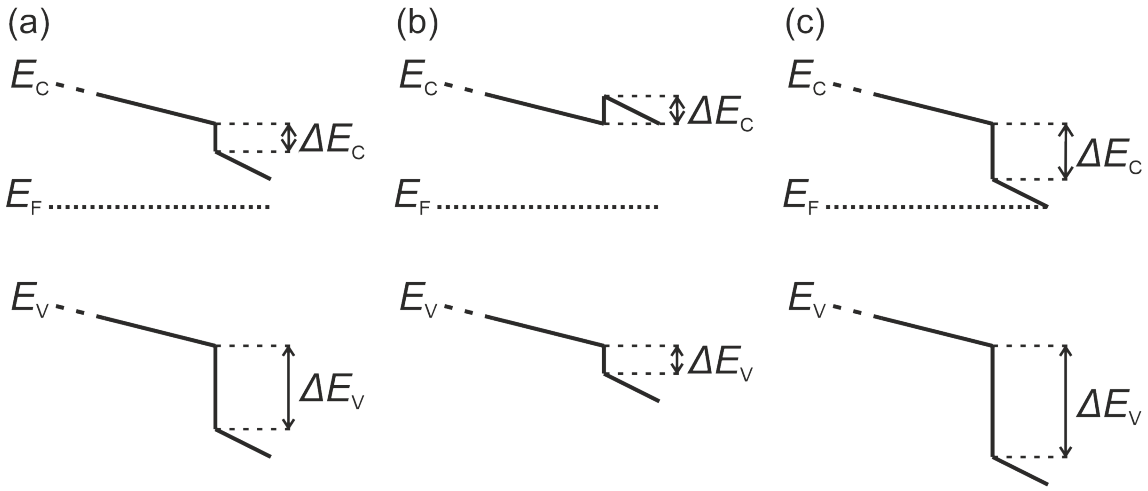

Figure 2.12: Schematic band diagram of an intrinsic absorber layer i together with an n-contact layer in multiple cases. The band offsets between the i- and the n-layer are designated for the conduction band (ΔE_C) and for the valence band (ΔE_V). Sketch (a) shows rather suitable offsets with a small ΔE_C for the electrons and a large barrier ΔE_V for the holes. Sketch (b) shows bad offsets leading to a barrier for the electrons and an insufficient barrier for the holes. Sketch (c) shows an offset ΔE_C which is too large leading to losses in V_{OC}.

the contact layer will ensure that the other species - the majority in the contact layer - are transported off efficiently. If the conductivity is too low, a resistive effect will reduce the efficiency of the device, potentially impairing the FF, J_{SC} and V_{OC}. The influences of conductivity and series resistance on cell performance are a major part of this thesis and will be discussed in chapters 5 and 6.

2.2 Internal versus External Perspective

There are two fundamental ways to approach the characterization of a solar cell - internally, considering parameters at the material level, and externally, characterizing the cell as a full device. The most important aspect however is to be able to connect both perspectives and to understand the assumptions that have to be made to do so. A lack of understanding at this crucial junction can lead to confusion and errors in the evaluation of measurements and simulations. Since most of this thesis

is dedicated to simulations modelling the externally measurable photoluminescence signal and the current-voltage characteristic of a cell from internal parameters this understanding is of particular importance.

When examining a solar absorber from the internal perspective, material parameters like the absorption coefficient α, the refractive index n_r or the recombination rates have to be considered. All of these values are characteristic of the absorber material and are independent of the geometry of the solar cell. The theoretical foundations for an internal description of a solar absorber will be introduced in chapter 2.5.

The external perspective however deals with parameters such as the absorptance A, the short-circuit current density J_SC and the saturation current J_0. These are macroscopic characteristics of the full solar cell device and can be used to calculate the efficiency of the cell. In this external view, the solar cell is treated like a black box with inputs and outputs. Light is coupled into the system and a current density or a luminescence signal are coupled out. Some basics of the external perspective to characterizing a solar cell have been introduced in chapter 2.1.2 and further introductions will be given in chapter 2.3.

In order to connect the internal and the external perspective we have to understand the optical qualities of the system. The way light couples into and out of a solar cell governs the interdependence of the internal and the external picture. The relevant optical processes and the resulting equations are introduced in chapters 2.5.6 and 3.3.1.

2.3 Shockley-Queisser Model and Radiative Limit

The Shockley-Queisser (SQ) model [91] is one of the most important theoretical approaches of describing the limits of an idealized single junction solar cell and offers a way to analyze real solar cells based on their divergence from the model. It is based on the thermodynamic principle of detailed balance [93] and makes some substantially simplifying assumptions. These assumptions yield an upper limit for the efficiency of a solar cell which is usually referred to as the Shockley-Queisser limit. Fig. 2.14 (a) shows the highest possible power conversion efficiency η_SQ in

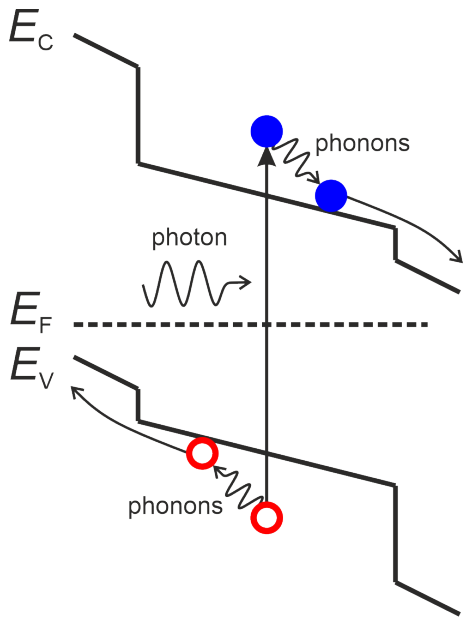

Figure 2.13: Basic process of photovoltaic power conversion. Incoming photons create an electron-hole pair, both charge carriers thermalize towards the band edges and are subsequently collected at their respective contacts.

the SQ limit in relation to the band gap energy E_g of the absorber material. The assumptions that are made to calculate the upper limit for efficiency and other solar cell parameters in the SQ model are relevant at different stages during the energy harvesting process. In the following these assumptions will be explained and departures of real-world solar cells from these rules will be mentioned. Fig. 2.13 illustrates the processes during the photovoltaic power conversion.

In order for a solar cell to function it needs to be illuminated with light of some sort of spectrum describing its distribution of photon energies. While the SQ model can be applied to any illumination spectra I will focus on solar illumination represented by the AM1.5g spectrum introduced in chapter 2.1.2. When this light is entering the absorber layer of a solar cell, photons with a sufficient energy exceeding the band gap energy E_g can be absorbed. This leads to assumption 1: The absorptance is a step-function, which means all incident photons with energy $h\nu \geq E_g$ are absorbed while all photons with lower energies will pass through the absorber without interacting with it. The absorption edge of any real solar cell however will always be broadened by tail states of the bands or structural disorder and will not a

show the characteristics of a step function. Additionally finite absorber thicknesses and absorption coefficients will always leave some photons unabsorbed.

When a photon is absorbed it lifts an electron from the valence band into the conduction band leaving behind a hole. The creation of an electron-hole pair yields assumption 2 in the SQ model: Every photon with energy $h\nu \geq E_\mathrm{g}$ generates precisely one pair. This assumption ignores parasitic absorption of photons in the contact layers or by free carriers in the absorber itself. Photons absorbed this way do not generate an electron-hole pair and and reduce the ratio of electron-hole pair per incident photon above the band gap energy E_g to below 1.

Since most photons that are absorbed have an energy that is higher than the band gap E_g, they can and will generate electrons and holes deeper within their respective bands meaning they have excess energy compared to the band edges. This energy is subsequently released to the lattice of the semiconductor in the form of phonons and the charge carriers move to the band edges. This process is known as thermaliziation, leading to assumption 3: Every electron-hole pair thermalizes to the same average energy in thermal equilibrium with the cell. The cells temperature T_cell is equal to the ambient temperature T_amb (thermal equilibrium). This assumes an immediate heat transfer from the cell to the ambient, in a real solar cell that is not the case and the operation temperatures of a cell under sunlight are significantly higher than the ambient temperature, reducing the cells efficiency.

After the generation and thermalization of the electron-hole pairs the charge carriers need to be extracted at opposite sides of the solar cell. During this process real solar cells exhibit a number of different kinds of recombination (see chapters 2.5.2 and 2.5.3). Assumption 4 in the SQ model concerns this recombination: All recombination pathways except for the radiative recombination necessary to satisfy detailed balance are suppressed, no charge carriers recombine non-radiatively. In a real solar cell suppression of non-radiative recombination is desirable but is never fully achieved.

Lastly for every solar cell to function it needs two different external contacts to extract the generated and separated charge carriers. These contacts satisfy assumption 5: The external contacts only exchange one type of charge carrier and ther resistance is negligibly small. In a real solar cell the contacts would have ohmic

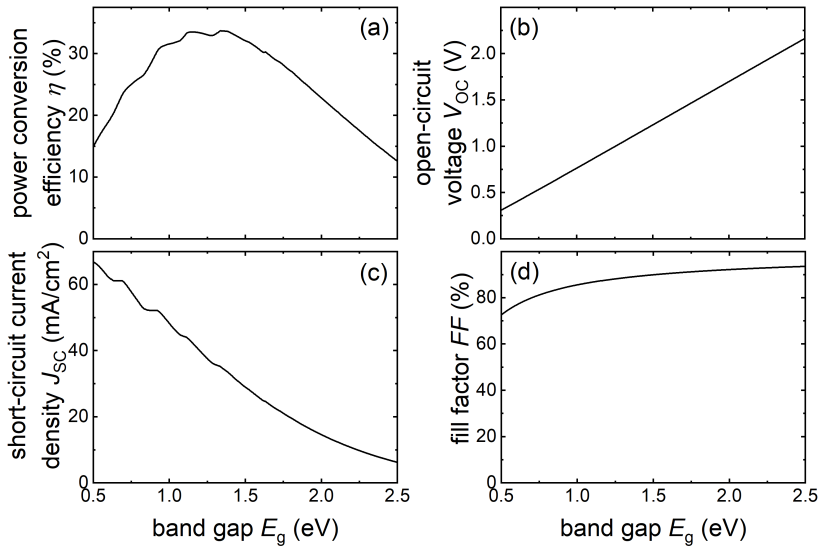

Figure 2.14: Performance limits in the Shockley-Queisser theory for a single junction solar cell with regards to (a) efficiency η, (b) open-circuit voltage V_{OC}, (c) short-circuit current density J_{SC} and (d) fill factor FF depending only on the band gap E_{g}

losses and the wrong charge carrier type can enter these contacts and would be lost for the generated current J.

Together, the five assumptions outlined above create an idealized model of a solar cell that is fully parametrized by a single characteristic of the absorber - its band gap energy E_{g}. The full current-voltage characteristic of any cell employing an absorber with band gap E_{g} including the most important characteristic values can be calculated. The current-voltage curve is described by the ideal diode equation as it was discussed in chapter 2.1.3 and in equation 2.4. The short-circuit current density in the SQ limit is given by

$$J_{\mathrm{SC,SQ}} = q \int_{E_{\mathrm{g}}}^{\infty} \phi_{\mathrm{sun}}(E) dE, \tag{2.11}$$

since the absorptance is a step function and all absorbed charge carriers contribute to the extracted current. The dark saturation current or the solar cell's thermal emission at temperature T (usually assumed to be room temperature or $T = 300\mathrm{K}$) is

$$J_{0,\mathrm{SQ}} = q \int_{E_\mathrm{g}}^{\infty} \phi_\mathrm{bb}(E,T) dE, \tag{2.12}$$

with the black body radiation

$$\phi_\mathrm{bb}(E,T) = \frac{2\pi E^2}{h^3 c^2} \frac{1}{[\exp(E/k_\mathrm{B}T) - 1]} \approx \frac{2\pi E^2}{h^3 c^2} \exp\left(-\frac{E}{k_\mathrm{B}T}\right) \tag{2.13}$$

according to Planck's law. Here h is Planck's constant and c is the speed of light. Resolving eq. 2.4 for V with $J = 0$ yields the open-circuit voltage

$$V_{\mathrm{OC,SQ}} = \frac{n_\mathrm{id} k_\mathrm{B} T}{q} \ln\left(\frac{J_{\mathrm{SC,SQ}}}{J_{0,\mathrm{SQ}}} + 1\right). \tag{2.14}$$

While there is no analytic solution for the fill factor FF, there are very precise approximations for the idealized case, resulting in Green's formula [98]

$$FF_\mathrm{SQ} = \frac{v_\mathrm{OC} - \ln(v_\mathrm{OC} + 0.72)}{v_\mathrm{OC} + 1}, v_\mathrm{OC} = \frac{q V_{\mathrm{OC,SQ}}}{n_\mathrm{id} k_\mathrm{B} T}. \tag{2.15}$$

Finally the efficiency limit in the SQ model can be calculated analogously to eq. 2.3 as

$$\eta_\mathrm{SQ} = \frac{J_{\mathrm{SC,SQ}} V_{\mathrm{OC,SQ}} FF_\mathrm{SQ}}{P_\mathrm{sun}}. \tag{2.16}$$

The graphs in figures 2.14 (a)-(d) show the maximum attainable values attainable in the SQ model for the PCE η, the open-circuit voltage V_OC, the short-circuit current density J_SC and the fill factor FF respectively. The values for all are shown in relation to the band gap energy E_g. The V_OC increases linearly with E_g, whereas the J_SC is reduced monotonously. The waves in the J_SC-curve stem from the variations within the solar spectrum that is used to calculate it. The FF sees a slight increase for higher band gaps E_g, only dropping off significantly for values uninteresting for solar cell applications. The opposing trends for V_OC and J_SC with respect to the band gap E_g signals that an optimum band gap for the highest PCE can be found. Fig. 2.14 (a) shows that this is indeed the case, the highest attainable efficiencies η are in the range between 1.1-1.4 eV.

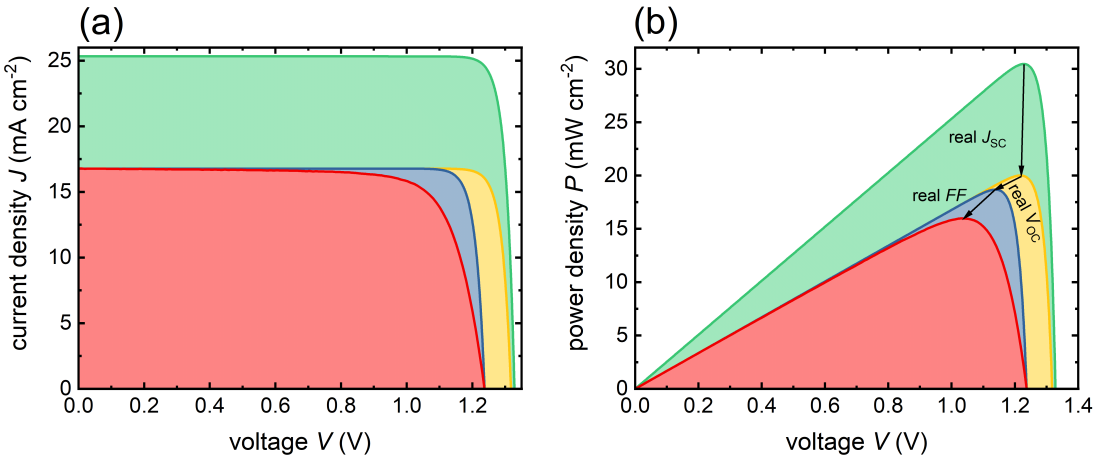

Figure 2.15: a) Current density versus voltage and b) power density versus voltage of a real-world solar cell as compared to more idealized scenarios. Curves are depicted in the Shockley-Queisser limit (green) and consecutively with real J_{SC} (yellow), real V_{OC} (blue) and real FF (red).

In order to illustrate the deviations from the SQ model that the perovskite solar cells discussed in this thesis show, they have been illustrated in fig. 2.15. Fig. 2.15 (a) shows the current voltage behaviour of a real perovskite solar cell (red curve) and the SQ limit for a cell with the same band gap energy (green curve). The yellow and blue curves illustrate intermediate degrees of idealization and fig. 2.15 (b) shows the same scenarios for the power density P with respect to the voltage V.

As discussed above, both assumption 1 and 2 imply an absorption behaviour of the idealized cell that is not found in real-world cells. The limitations in absorption and losses through parasitic absorption reduce the short-circuit current density J_{SC} and subsequently the power that can be extracted from the cell. This change of J_{SC} from the SQ case to the real value is marked by the transition from the green to the yellow curves in fig. 2.15. The yellow curve still retains all other idealizations however. It must be noted, that a reduction of J_{SC} also reduces the saturation current J_0 und thereby the open-circuit voltage V_{OC} is also slightly decreased.

Since assumption 4 requires the non-radiative recombination in the solar cell to be zero, the difference to the real-world cell will be in the recombination current J_0. Since the non-radiative recombination is usually orders of magnitude higher than the radiative recombination the change in J_0 significantly reduces the open-circuit

voltage V_{OC}, this change is signified by the transition from the yellow to the blue curves, which employs the V_{OC} from the real perovskite solar cell. The deviation from assumption 3 is usually an increased temperature of the solar cell as compared to that assumed in the SQ model. Since all recombination mechanisms are thermally activated and the corresponding losses increase exponentially with temperature this deviation from the model also increases the saturation current J_0 and subsequently reduces V_{OC} with some small effects on other parameters.

Finally assumption 5 can mainly be simplified as assuming zero resistive losses for charge carriers moving in the absorber. The reductions in solar cell efficiency can therefore be described easiest as additional resistive effects, which will be more closely examined in chapter 2.1.5. These resistive effects reduce the fill factor FF of the idealized cell to a lower value in the real cell which is illustrated by the transition from the blue to the red curves.

Having understood the foundations for the reduction in efficiency from the ideal case to the real case, fig. 2.15 can be examined quantitatively. It is apparent that the leading cause in efficiency reduction are losses in light absorption, followed by resistive effects. The smallest contribution in terms of losses stems from non-radiative recombination.

Note that the Shockley-Queisser limit is derived for a single absorber layer and can be exceeded by stacking multiple absorbers of different band gaps on top of one another in order to reduce losses due to thermalization and below band gap transmission. These multi-junction or tandem (employing two different absorber layers) solar cells thereby violate some of the assumptions made by Shockley and Queisser and allow us to reach even higher efficiencies. These multi-junction solar cells also increased interest in semiconductors with bandgaps E_g outside of the maximum of the SQ model. Tandem solar cells employing crystalline silicon as one absorber require a second layer with a band gap E_g of approximately 1.75 eV, a requirement perovskites can fulfill due to the tunability of band gaps [47].

2.4 Charge Carrier Transport

The movement or transport of charge carriers in a semiconductor or any number of different material layers within a solar cell can be described in a drift-diffusion model. This semi-classical description is based on the density of free charge carriers in the bands and the electrostatic potential. The mathematical basis for the description of charge carrier transport in the drift-diffusion model are three coupled partial differential equations - the Poisson equation and the continuity equations for both electrons and holes. The one-dimensional Poisson equation perpendicular to the layers within the solar cell stack

$$\frac{\partial^2 \varphi}{\partial x^2} = -\frac{\partial E}{\partial x} = -\frac{\rho}{\epsilon_0 \epsilon} \tag{2.17}$$

describes the electrostatic potential φ in relation to the vacuum level, as it is induced by the net space charge density ρ. The space charge density ρ is normalized by the dielectric constant of vacuum ϵ_0 and a relative dielectric constant ϵ, which is dependent on the semiconductor. The resulting electrical field is denoted as E. The net space charge density

$$\rho = q(p - n + p_{\mathrm{loc}} - n_{\mathrm{loc}} + N_{\mathrm{D}} - N_{\mathrm{A}}) \tag{2.18}$$

is the sum of free electrons n and holes p, localized charges n_{loc} and p_{loc} trapped in defects or tail states and ionized donors N_{D} and acceptors N_{A}. The continuity equations

$$\frac{\partial n}{\partial t} = G - R - \frac{1}{q}\frac{\partial J_{\mathrm{n}}}{\partial x} \tag{2.19a}$$

$$\frac{\partial p}{\partial t} = G - R - \frac{1}{q}\frac{\partial J_{\mathrm{p}}}{\partial x} \tag{2.19b}$$

for free charge carriers n and p are a direct result from the conservation of charge. The change over time in free charge carrier density in a given volume is the sum of the processes adding charge carriers to the volume or removing them. The generation rate G and the recombination rate R are connected to the charge currents for

electrons J_n and holes J_p. These charge currents can be described by the current equations

$$J_\mathrm{n} = qD_\mathrm{n}\frac{\partial n}{\partial x} + qF\mu_\mathrm{n}n \tag{2.20a}$$

$$J_\mathrm{p} = qD_\mathrm{p}\frac{\partial p}{\partial x} + qF\mu_\mathrm{p}p \tag{2.20b}$$

for electrons and holes respectively. Both equations are comprised of two terms, the first describing a diffusive current component obeying Fick's law and the second concerning the drift component described by Ohm's law. D_n and D_p are the diffusion constants for electrons and holes respectively which relate to the mobilities $\mu_\mathrm{n/p}$ via the Einstein relation $D_\mathrm{n/p} = \mu_\mathrm{n/p}k_\mathrm{B}T$. The drift current stems from the electric field $F = \partial\varphi/\partial x$.
The relations above form a set of differential equations that only have the electrostatic potential φ and the free charge carrier densities n and p as independent variables. If these parameters are known or simulated they enable us to calculate a vast array of characteristics of a material or a solar cell stack such as the current voltage curve or spatially resolved recombination rates. The model forms the basis for the simulations more thoroughly explained in chapter 3.3.

2.5 Generation and Recombination

2.5.1 Charge Carrier Concentrations in Equilibrium and Non-Equilibrium

A solar absorber at a constant temperature T is in thermal equilibrium. If no light is incident onto the absorber and no voltage is applied it is also in chemical equilibrium which means no charge carriers are lifted from the valence band into the conduction band by non-thermal processes. Additionally the charge carrier concentrations do not change with time. For such an absorber at room temperature most electrons will reside in the valence band with only a few in the conduction band due to thermal activation. Correspondingly only few holes will be found in the valence band. The

occupation probability of these charge carriers can be described by the Fermi-Dirac distribution [99, 100]

$$f(E,T) = \frac{1}{\exp\left(\frac{E-E_\mathrm{F}}{k_\mathrm{B}T}\right)+1} \approx \exp\left(-\frac{E-E_\mathrm{F}}{k_\mathrm{B}T}\right), \tag{2.21}$$

with the Fermi-energy E_F as a material specific value. The right hand side of equation 2.21 uses the Boltzmann-approximation which is valid for $E - E_\mathrm{F} \gg k_\mathrm{B}T$ which is usually the case at room temperature. Utilizing the Fermi-Dirac distribution and the Boltzmann-approximation the charge carrier densities in thermal equilibrium can be calculated as the integral

$$n_0 = \int_{E_\mathrm{C}}^{\infty} N_\mathrm{Cb} f(E,T) dE \approx N_\mathrm{C} \exp\left(\frac{E_\mathrm{F}-E_\mathrm{C}}{k_\mathrm{B}T}\right), \tag{2.22a}$$

$$p_0 = \int_{-\infty}^{E_\mathrm{V}} N_\mathrm{Vb} f(E,T) dE \approx N_\mathrm{V} \exp\left(\frac{E_\mathrm{V}-E_\mathrm{F}}{k_\mathrm{B}T}\right), \tag{2.22b}$$

with the density of states near the bottom of the conduction band $N_\mathrm{Cb} = \frac{2}{\sqrt{\pi}(kT)^{3/2}} N_\mathrm{C}\sqrt{E-E_\mathrm{C}}$ and the density of states near the top of the valence band $N_\mathrm{Vb} = \frac{2}{\sqrt{\pi}(kT)^{3/2}} N_\mathrm{V}\sqrt{E_\mathrm{V}-E}$ [101]. N_C and N_V are the effective densities of states at the band edge energies E_C and E_V respectively. Both N_C and N_V are temperature dependent via [101]

$$N_\mathrm{C,V}(T,T_0) = N_\mathrm{C,V}(T_0)\left(\frac{T}{T_0}\right)^{\frac{3}{2}}, \tag{2.23}$$

with T_0 as the initial temperature. The product of the charge carrier densities in equilibrium is defined as

$$n_0 p_0 = n_\mathrm{i}^2 = N_\mathrm{C} N_\mathrm{V} \exp\left(-\frac{E_\mathrm{g}}{k_\mathrm{B}T}\right), \tag{2.24}$$

which is the definition of the intrinsic charge carrier density n_i. If the semiconductor that acts as the absorber is indeed intrinsic meaning it is not intentionally or unintentionally doped, $n_\mathrm{i} = n_0 = p_0$.

Once a semiconductor is illuminated, charge carriers are generated and the chemical equilibrium is disturbed. The generation of charge carriers leads to a

splitting of the Fermi-level into two, one for the electrons and one for the holes. This is necessary in order to be able to accurately describe the charge carrier densities in the respective bands. These new Fermi-levels in non-thermal equilibrium are typically referred to as quasi Fermi-levels (QFLs). With E_{Fn} as the QFL for electrons and E_{Fp} as the QFL for holes the charge carrier densities are defined as

$$n = N_{\mathrm{C}} \exp\left(\frac{E_{\mathrm{Fn}} - E_{\mathrm{C}}}{k_{\mathrm{B}}T}\right), \tag{2.25a}$$

$$p = N_{\mathrm{V}} \exp\left(\frac{E_{\mathrm{V}} - E_{\mathrm{Fp}}}{k_{\mathrm{B}}T}\right). \tag{2.25b}$$

If we combine these two equations we arrive at

$$np = N_{\mathrm{C}}N_{\mathrm{V}} \exp\left(\frac{E_{\mathrm{V}} - E_{\mathrm{C}}}{k_{\mathrm{B}}T}\right) \exp\left(\frac{E_{\mathrm{Fn}} - E_{\mathrm{Fp}}}{k_{\mathrm{B}}T}\right) = N_{\mathrm{C}}N_{\mathrm{V}} \exp\left(-\frac{E_{\mathrm{g}}}{k_{\mathrm{B}}T}\right) \exp\left(\frac{\Delta E_{\mathrm{F}}}{k_{\mathrm{B}}T}\right), \tag{2.26}$$

where ΔE_{F} is the quasi-Fermi level splitting. This QFL splitting corresponds to a voltage that is built up within the absorber of a solar cell, in this work this will be called the internal voltage $V_{\mathrm{int}} = q\Delta E_{\mathrm{F}}$. The internal voltage describes the chemical potential that is building up inside the absorber of the solar cell under illumination and that can ideally be extracted to be used for electricity. In thermal and chemical equilibrium it is zero.

Note that the charge carriers that lead to the splitting of the quasi-Fermi levels ΔE_{F} can not only be introduced into the absorber via incoming photons but analogously via applying an external voltage V_{ext} to the solar cell. In an idealized case with negligible resistances in the contact layers and high lifetimes and mobilities in the absorber the internal voltage will be equal to the externally applied voltage ($V_{\mathrm{int}} = V_{\mathrm{ext}}$). In a real solar cell however that is not the case, the deviations of real world solar cells from this ideal will be a central aspect of this thesis.

2.5.2 Radiative Recombination

Recombination is the reciprocal process of the generation of electron-hole pairs, it plays a central role in this thesis because it is the basis for photoluminescence

measurements. Fundamentally there are two different kinds of charge carrier recombination in solar cells, radiative and non-radiative recombination. The process of recombination sees an electron and a hole annihilate. While radiative recombination sees a photon being generated and possibly emitted from the absorber, non-radiative recombination deposits the energy, that was stored in the charge carriers, into the crystal lattice in the form of phonons.
Radiative recombination is the dominant recombination process in direct semiconductors, a depiction of the absorption, thermalization and subsequent radiative recombination can be seen in fig. 2.16 (a). Generation and thermalization have been discussed in depth in chapter 2.3. The rate at which the charge carriers recombine is proportional to the carrier densities of electrons n and holes p. Additionally the radiative recombination rate

$$R_{\mathrm{rad}} = k_{\mathrm{rad}} \left(np - n_{\mathrm{i}}^2 \right) \tag{2.27}$$

is described by the radiative recombination constant k_{rad}. Note that the radiative recombination rate of an absorber in a solar cell is usually not the rate that will be externally measurable. The probability p_{e} of photons to be emitted from the absorber is usually reduced by the probability of them being reabsorbed creating new electron-hole pairs (p_{r}) and the probability of them being parasitically absorbed in one of the contact layers (p_{a}). These loss mechanisms and their impact on the interpretation of photoluminescence measurements will be discussed in chapter 2.5.6.

2.5.3 Non-Radiative Recombination

Non-radiative recombination describes all manners of transitions where the the energy of the elevated state of an electron is emitted into the lattice in form of phonons. While radiative recombination can not be avoided for thermodynamic reasons, suppressing non-radiative recombination is one of the central goals in solar cell design. An important recombination mechanism is recombination that takes place at a trap such as impurities, foreign atoms or structural defects. This process is depicted schematically in fig. 2.16 (b), the trap energy E_{T} defines the position of the trap within the band gap. Charge carriers can be captured by the trap emitting phonons

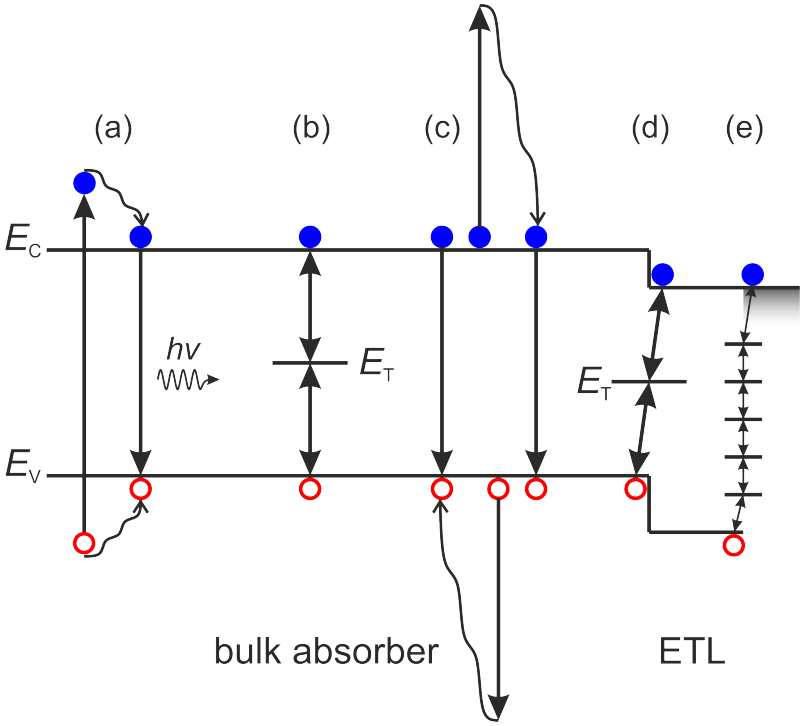

Figure 2.16: Recombination processes in semiconductors. (a) Generation, thermalization and radiative recombination. (b) Shockley-Read-Hall recombination through a trap level at the energy E_T. (c) Auger recombination. (d) Interface recombination between two semiconductors of differing band gap E_g and electron affinity χ through a trap level at the energy E_T. (e) Surface recombination at an interface between a semiconductor and a metal or metal-oxide.

in the process. The probability of such a capture event is dependent on the energetic distance between the band the charge carrier resides in and the trap, as well as the phonon energies within the semiconductor. Both low phonon energies as well as a high distance between the energetic levels lead to a high amount of phonons being necessary for a transition and thus reduce its probability [102]. The rate for this trap assisted recombination, also referred to as Shockley-Read-Hall recombination (SRH recombination) is given by

$$R_{\mathrm{srh}} = N_{\mathrm{T}}\beta_{\mathrm{n}}\beta_{\mathrm{p}}\frac{np - n_i^2}{n\beta_{\mathrm{n}} + p\beta_{\mathrm{p}} + e_{\mathrm{n}} + e_{\mathrm{p}}}, \tag{2.28}$$

where N_{T} is the trap density, $\beta_{\mathrm{n/p}}$ are the traps capture coefficients and $e_{\mathrm{n/p}}$ are the emission coefficients for electrons and holes respectively. These values correspond

to one specific trap energy, in case of more different types of traps being relevant, multiple equivalent terms will be added increasing recombination. The recombination rate is greatest towards the middle of the band gap (assuming $\beta_\mathrm{n} N_\mathrm{C} = \beta_\mathrm{p} N_\mathrm{V}$). These deep traps have negligible emission coefficients $e_\mathrm{n/p}$ and the capture coefficients $\beta_\mathrm{n/p}$ are similar due to the amount of phonons involved in each transition. Shallow defects close to the bands usually capture one type of charge carrier easily while the amount of phonons required for the other is so high that capture rates are insignificant. This slower transition consequently limits the total recombination rate for shallow traps. For a deep trap with insignificant emission coefficients $e_\mathrm{n/p}$, eq. 2.28 simplifies to

$$R_\mathrm{srh} = \frac{np - n_\mathrm{i}^2}{n\tau_\mathrm{p} + p\tau_\mathrm{n}}, \tag{2.29}$$

with lifetimes for electrons and holes defined as $\tau_\mathrm{n/p} = 1/(N_\mathrm{T}\beta_\mathrm{n/p})$. The capture coefficients $\beta_\mathrm{n/p} = v_\mathrm{th}\sigma_\mathrm{n/p}$ can also be expressed in terms of the capture cross section $\sigma_\mathrm{n/p}$, $v_\mathrm{th} \propto \sqrt{k_\mathrm{B}T}$ is the thermal velocity.
Another non-radiative recombination process in semiconductors is Auger recombination, which is illustrated in fig. 2.16 (c). This process requires three charge carriers and functions similar to radiative band-to-band recombination. An electron and a hole recombine but the resulting energy is not emitted in form of a photon but is instead transferred to a third electron or hole. This third charge carrier is activated deep into the band it resided in and subsequently thermalizes back to the band edge, releasing its energy to the lattice in the form of phonons. The recombination rate for this process is given by

$$R_\mathrm{aug} = \left(C_\mathrm{n} n + C_\mathrm{p} p\right)\left(np - n_\mathrm{i}^2\right), \tag{2.30}$$

where C_n and C_p are the Auger recombination coefficients for electrons and holes respectively. Auger recombination is prevalent at high charge carrier concentrations and in highly doped absorber materials. Like radiative recombination it is an intrinsic process also present in high quality semiconductors.

While all of the aforementioned recombination processes take place in the bulk of a semiconductor it is also crucial to take recombination at interfaces into account

since this process is one of the most important loss mechanisms in perovskite solar cells. There are two types of interfaces that have to be taken into account, the interface between two semiconductors and the interface of a semiconductor with a metal or metal-oxide like ITO. First we will consider the two different semiconductors in contact, the process of recombination at such a contact is sketched in figure 2.16 (d). In the figure we see an interface between an absorber on the left and an ETL on the right which is marked by an offset in both the conduction band energy E_C and the valence band energy E_V caused by differences in band gap E_g and electron affinity χ between the two materials. These differences lead to a reduced energy difference between the holes situated in the valence band of the absorber and the electrons in the conduction band of the ETL effectively increasing the probability of one of the charge carriers being captured by a trap situated at an energy level E_T at the interface. Just as was the case for SRH recombination the recombination rate depends on the densities of charge carriers in their respective bands as well as the trap density and the efficiency of charge carrier capture in these traps. In analogy to equation 2.29 this allows us to calculate the recombination rate per surface area at the interface as

$$R_\mathrm{int} = \frac{n_\mathrm{ETL} p_\mathrm{abs} - n_\mathrm{i,int}^2}{n_\mathrm{ETL}/S_\mathrm{p} + p_\mathrm{abs}/S_\mathrm{n}}, \tag{2.31}$$

with n_ETL as the density of electrons in the ETL, p_abs as the density of holes in the absorber and $n_\mathrm{i,int}^2 = n_\mathrm{0,ETL} p_\mathrm{0,abs} \propto \exp\left(-\frac{E_\mathrm{int}}{k_\mathrm{B}T}\right)$. $E_\mathrm{int} = E_\mathrm{V,abs} - E_\mathrm{C,ETL}$ is the interfacial band gap which is defined as the difference between the valence band energy of the absorber and the conduction band energy of the ETL. S_n and S_p are the interface-recombination velocites. Just like the charge carrier lifetimes $\tau_\mathrm{n/p}$ in the bulk SRH recombination model these recombination velocities are a parameter that reflects the kinetic element of the recombination process. The higher the trap density at the interface and the higher the probability of charge carrier capture at these trap sites, the faster surface recombination will take place. In order to suppress this kind of interface recombination both the density of charge carriers at the interface (n_ETL and p_abs) as well as the interface recombination velocities $S_\mathrm{n/p}$ have to be kept as low as possible.

Finally we have to take into account recombination at a semiconductor-metal

interface. As was mentioned in chapter 2.1.7, these kinds of interfaces often exhibit a high density of trap states due to the disruption of the crystal structure of the semiconductor. Therefore, unless the material was properly passivated (i.e. filling vacancies with atoms), surface recombination velocities $S_{\mathrm{n/p}}$ may be quite high. The recombination path across multiple trap levels is depicted in figure 2.16 (e). Since in the case shown in the figure the density of electrons in the metal can be assumed as arbitrarily high the recombination rate per surface area at these interfaces is only determined by the concentration of the minority carriers - in this case holes - and their respective surface-recombination velocity. This leaves us with a rather simple description of the recombination rate at the surface

$$R_{\mathrm{surf}} = S_{\mathrm{n}} n \tag{2.32}$$

for electrons as minority carriers with an analogous relation for holes as minority carriers. In the simulations of solar cells that were conducted for this thesis the surface recombination usually functions as a boundary condition to determine charge carrier concentrations at the surfaces.

2.5.4 Injection Characteristics

When trying to probe the recombination characteristics of a solar absorber or a full cell there are a couple of possible situations to consider in which the equations for recombination rates presented above can be simplified substantially. In the following I am going to characterize the most important situations and how the equations for the recombination rates change accordingly. To understand the dependency on various parameters of luminescence intensities under steady state excitation it is crucial to understand the influence of the ratio of electron and hole densities and to know the involved recombination processes. The ratio of charge carrier densities can be described by two common situations, low level injection (LLI) and high level injection (HLI). These two conditions and their corresponding recombination rates will be elucidated in the following.

2.5.4.1 Low Level Injection

Whether a semiconductor under illumination is in low level injection or high level injection depends on the doping concentration and the intensity of the incoming light. Most established semiconductor materials are doped when utilized in solar cell applications. As mentioned before, the doping of a semiconductor leads to an imbalance in free charge carriers. In an unilluminated p-doped semiconductor the amount of free holes will be many orders of magnitude larger than the amount of free electrons ($p \gg n$). This imbalance of charge carrier concentrations is called low level injection. While the imbalance is most extreme in the unilluminated absorber, given sufficient doping it can also be relevant at moderate to high illumination intensities. In the following we will always assume a semiconductor in LLI to be p-doped with a doping density N_A making electrons the minority carriers and holes the majority carriers. If we assume the doping density to be much higher than the density of photogenerated charge carriers ($N_\mathrm{A} \gg \Delta n = \Delta p$ with $\Delta n = n - n_0$ and $\Delta p = p - p_0$) then $p \approx N_\mathrm{A}$ and equations 2.27, 2.29, 2.30 and 2.31 simplify to

$$R_\mathrm{rad} = k_\mathrm{rad}\left(nN_\mathrm{A} - n_\mathrm{i}^2\right), \tag{2.33a}$$

$$R_\mathrm{srh} = \frac{\Delta n}{\tau_\mathrm{n}}, \tag{2.33b}$$

$$R_\mathrm{aug} = C_\mathrm{p} n N_\mathrm{A}^2 - C_\mathrm{p} N_\mathrm{A} n_\mathrm{i}^2, \tag{2.33c}$$

$$R_\mathrm{int} = nS_\mathrm{n} = R_\mathrm{surf}. \tag{2.33d}$$

A look at equations 2.33 reveals that in LLI all of these recombination rates are linear in the minority carrier density which in this case is the density of electrons n. Furthermore according to equation 2.26 the QFL splitting can be determined as

$$\Delta E_\mathrm{F} = k_\mathrm{B} T \ln\left(\frac{np}{n_\mathrm{i}^2}\right), \tag{2.34}$$

in dependence on the charge carrier concentrations. In the LLI case this simplifies to

$$\Delta E_\mathrm{F} = k_\mathrm{B} T \ln\left(\frac{n}{n_0}\right), \tag{2.35}$$

utilizing the same assumptions as above. The term in the logarithm exhibits a linear dependence on the electron carrier density n.

2.5.4.2 High Level Injection

In contrast to LLI, if a semiconductor is not doped or has a low density of dopants, a low amount of incoming light will be enough to generate more charge carriers in the absorber than there are charge carriers from doping. In this case the density of free electrons will equal the density of free holes ($n = p$). This situation is called high level injection and the condition of equal charge carrier densities together with the assumption of $np > n_\mathrm{i}^2$ leads to a corresponding simplification of the equations for the recombination rates to

$$R_\mathrm{rad} = k_\mathrm{rad} n^2, \tag{2.36a}$$

$$R_\mathrm{srh} = \frac{n}{\tau_\mathrm{p} + \tau_\mathrm{n}}, \tag{2.36b}$$

$$R_\mathrm{aug} = (C_\mathrm{n} + C_\mathrm{p})\, n^3, \tag{2.36c}$$

$$R_\mathrm{int} = \frac{n}{1/S_\mathrm{n} + 1/S_\mathrm{p}}. \tag{2.36d}$$

Looking at equations 2.36 we note that unlike the LLI setting, the recombination rates have varying dependencies on the electron density (or the hole density for that matter since they are equal). While the Shockley-Read Hall recombination rate still exhibits a linear dependency on n, the characteristic of the radiative recombination is quadratic in n with the Auger recombination even being cubic in n. These so-called recombination orders of charge carrier concentrations are crucial for understanding the ideality factors n_id characterizing the slope of the total recombination currents in a semiconductor diode. Ideality factors will be further discussed in chapter 2.5.7. Of similar importance is the dependency of the QFL splitting on the charge carrier densities. In HLI equation 2.34 simplifies to

$$\Delta E_\mathrm{F} = k_\mathrm{B} T \ln\left(\frac{n^2}{n_\mathrm{i}^2}\right), \tag{2.37}$$

which implies a quadratic dependency of the logarithm on electron density.

2.5.5 Charge Carrier Lifetimes

A important concept when describing the charge carrier dynamics and the recombination rates within a solar cell is the charge carrier lifetime τ, which is defined as the average time it takes for an excited electron or hole to recombine. If we consider a semiconductor in the dark with a previously generated electron density n and no additional generation G, the change in electron density will be

$$\frac{dn}{dt} = -\frac{\Delta n}{\tau_{\text{eff}}}. \tag{2.38}$$

Here Δn is again the electron density exceeding the intrinsic electron density n_0 and τ_{eff} is the effective lifetime of the electrons taking into account all recombination mechanisms. If we now consider the simple case that SRH recombination is the only recombination mechanism impacting the semiconductor, the lifetimes can easily be concluded depending on the injection characteristic. In LLI with electrons as the minority carriers the lifetime will be $\tau_{\text{eff}} = \tau_{\text{SRH}}^{\text{LLI}} = \tau_{\text{n}}$ according to equation 2.33b, while in HLI the lifetime will be $\tau_{\text{SRH}}^{\text{HLI}} = \tau_{\text{n}} + \tau_{\text{p}}$ according to equation 2.36b.

If we move away from the simplified situation of a single relevant recombination mechanism it becomes more difficult to analytically describe the effective lifetime τ_{eff} of electrons or holes. In order to attempt to do so we will define a total recombination rate

$$R_{\text{tot}} = \left[k_{\text{rad}} + \frac{1}{n\tau_{\text{p}} + p\tau_{\text{n}}} + C_{\text{n}}n + C_{\text{p}}p\right]\left(np - n_{\text{i}}^2\right) \tag{2.39}$$

in terms of the charge carrier densities. The first term in the square brackets relates to the radiative recombination, the second represents Shockley-Read Hall recombination at a deep defect and the last two describe the Auger recombination. In LLI, applying the same assumptions from chapter 2.5.4.1 for a p-type semiconductor, equation 2.39 simplifies to

$$R_{\text{tot}} = \left[k_{\text{rad}}N_{\text{A}} + \frac{1}{\tau_{\text{n}}} + C_{\text{p}}N_{\text{A}}^2\right](n - n_0) \coloneqq \left[\frac{1}{\tau_{\text{rad}}} + \frac{1}{\tau_{\text{srh}}} + \frac{1}{\tau_{\text{aug}}}\right](n - n_0) \coloneqq \frac{\Delta n}{\tau_{\text{eff}}}. \tag{2.40}$$

Here we are able to find a simple way to calculate the effective lifetime τ_{eff}, since all recombination rates have a linear dependency on the electron density. As each term in the square brackets on the left hand side in equation 2.40 corresponds to a recombination mechanism, each of them can be assigned a lifetime that is the inverse of the respective term. The effective lifetime τ_{eff} can be calculated from the recombination lifetimes of the discrete recombination processes. It can be observed as an external characteristic of the semiconductor or solar cell (taking into account reabsorption and parasitic absorption), for example using transient photoluminescence measurements [103,104]. Since under HLI conditions the recombination mechanisms adhere to differing recombination orders, the total charge carrier lifetime cannot be calculated as easily. One of the key objectives however is to discern which recombination pathway dominates and thereby shapes the recombination lifetime a sample exhibits. In order to learn more in this regard it can be a viable strategy to examine the ideality factor of a diode which will be discussed in chapter 2.5.7.

2.5.6 Luminescence Measurements

In chapter 2.5.1 I described an absorber in thermal and chemical equilibrium. Thermal equilibrium means that the temperature T of the semiconductor is constant whereas we take chemical equilibrium to mean that the quasi-Fermi levels are not split up by incoming light or an applied voltage. In this state any incoming radiation will be equalled by the outgoing radiation. In a given energy interval E the emissivity $\zeta(E)$ of the cell is equal to its absorptance $a(E)$ as described by Kirchhoff's law [92]. Kirchhoff describes the thermal emission $\phi_{\text{em}}(E)$ of this black body as

$$\phi_{\text{em}}(E) = \zeta(E)\phi_{\text{bb}}(E) = a(E)\phi_{\text{bb}}(E), \tag{2.41}$$

here ϕ_{bb} is the black body spectrum according to Planck's law as introduced in eq. 2.13.

Both Kirchhoff's and Planck's laws were established to be valid in thermal and chemical equilibrium. Luminescence however describes the emission of light from a solid arising from deviations from these equilibria. While the disturbance of the thermal equilibrium has a considerable impact according to equation 2.23, the

divergernce from chemical equilibrium is what mostly governs luminescence. This means the emitted radiation exceeds the black body radiation and new equations have to be found to describe emission. There are mutliple ways this disturbance can be introduced into a semiconductor [105], but in this thesis I will focus on the most commonly encountered, voltage and illumination. According to Würfel the electron-hole pairs generated by absorbed photons or an applied external voltage V_{ext} lead to a difference in chemical potential building up within the device [106]. Both the electrons within the conduction band and the holes in the valence band develop a local chemical equilibrium with differing chemical potentials. Utilizing the chemical potentials for the valence band μ_{V} and the conduction band μ_{C} Würfel developed a generalized version of Planck's law for non-chemical equilibrium [106]

$$\phi_{\mathrm{em}}(E) = a(E)\phi_{\mathrm{bb}}(E)\exp\left(\frac{\mu_{\mathrm{C}} - \mu_{\mathrm{V}}}{k_{\mathrm{B}}T}\right). \tag{2.42}$$

Note that this equation assumes that the difference in chemical potential is constant across the semiconductor. Additionally this equation will still hold in thermal equilibrium as the difference in chemical potential does not influence temperature. In a real solar cell however both applying a voltage and illumination will disturb thermal equilibrium as well. The difference in chemical potential considered in equation 2.42 corresponds to the splitting of quasi-Fermi levels introduced in chapter 2.5.1 and can be represented as an internal voltage V_{int} building up in the device via

$$\phi_{\mathrm{em}}(E) = a(E)\phi_{\mathrm{bb}}(E)\exp\left(\frac{V_{\mathrm{int}}}{k_{\mathrm{B}}T}\right). \tag{2.43}$$

The photons created by radiative recombination according to the above formula carry the chemical potential that was lost in the semiconductor as part of the recombination process.

The flux of these emitted photons ϕ_{em} can now be measured. If it arises from an applied voltage the characteristic is called electroluminescence (EL), if it stems from illumination it is called photoluminescence (PL). As mentioned both EL and PL are results of radiative recombination, however since non-radiative recombination modulates the amount of charge carriers available to radiatively recombine, measuring the luminescence can give crucial insight into both processes. In this thesis

measurements will be referred to as photoluminescence even though applying voltages to samples leads to a mixture of EL and PL. Ultimately the amount of charge carriers within the absorber will determine the luminescence intensity regardless of how they were generated.

In order to properly understand and interpret PL measurements it is important to again consider an external and an internal perspective. The externally measured luminescence may be very different from the amount of recombination occurring within the cell. The luminescence signal functions like an integral disregarding positional changes of internal parameters within the absorber volume. The properties of luminescence can be characterized by the external and the internal luminescence quantum efficiency. The external quantum efficiency [59, 107]

$$Q_{\mathrm{e}}^{\mathrm{lum}} = \frac{J_{\mathrm{em}}}{J_{\mathrm{rec}}}, \tag{2.44}$$

is defined as the ratio between the emission current density J_{em} and the recombination current density J_{rec}. While J_{rec} is the total recombination current density taking into account all recombination mechanisms, J_{em} describes the externally measurable current density of photons that were generated by radiative recombination and were coupled out of the cell or absorber. The external luminescence quantum efficiency $Q_{\mathrm{e}}^{\mathrm{lum}}$ is tied closely to the open-circuit voltage V_{OC} of a cell since both depend on recombiation currents as was mentioned in chapter 2.3. In open circuit the photogeneration and recombination currents of an illuminated solar cell are equal, leading to zero net current flow. This enables us to express the deviation of the open-circuit voltage from the radiative limit in terms of the $Q_{\mathrm{e}}^{\mathrm{lum}}$ via [59, 108, 109]

$$qV_{\mathrm{OC}}^{\mathrm{rad}} - qV_{\mathrm{OC}} = -k_{\mathrm{B}}T \ln\left(Q_{\mathrm{e}}^{\mathrm{lum}}\right) > 0, \tag{2.45}$$

with the open-circuit voltage in the radiative limit $V_{\mathrm{OC}}^{\mathrm{rad}}$. In the radiative limit the only recombination losses are the outcoupled photons of the emission current density J_{em}, leading to $Q_{\mathrm{e}}^{\mathrm{lum}} = 1$ and both terms being equal on the left hand side of equation 2.45. Additional non-radiative recombination will reduce the value of $Q_{\mathrm{e}}^{\mathrm{lum}}$, consequently also reducing the open-circuit voltage V_{OC}. For every order of magnitude that the recombination current increases in relation to the emission

current, the open-circuit voltage will decrease by $k_{\mathrm{B}}T\ln(10) \approx 60$ meV (at room temperature).

When describing luminescence at the material level the internal luminescence quantum efficiency is considered, which is defined as

$$Q_{\mathrm{i}}^{\mathrm{lum}} = \frac{R_{\mathrm{rad}}}{R_{\mathrm{tot}}} = \frac{R_{\mathrm{rad}}}{R_{\mathrm{rad}} + R_{\mathrm{nrad}}}. \tag{2.46}$$

Unlike the definition of $Q_{\mathrm{e}}^{\mathrm{lum}}$, which utilizes currents, $Q_{\mathrm{i}}^{\mathrm{lum}}$ is defined as the ratio of recombination rates, the rate of radiative recombination R_{rad} and the rate of non-radiative recombination R_{nrad}. These rates have been introduced for various scenarios in the previous chapters. While photoluminescence measurements will only detect photons created by radiative recombination the definition of the internal luminescence quantum efficiency reflects its dependency on non-radiative recombination processes as well. Since all recombination processes depend on the density of charge carriers in a semiconductor the photoluminescence does not only reflect the radiative recombination characteristics of an absorber. If a device is dominated by non-radiative recombination its photoluminescence signal will reflect that.

After finding definitions for the external and the internal luminescence quantum efficiency to describe luminescence the next step is of course to try and put these two parameters into context with each other. The most important leap from the internal picture to the external picture is the definition of the emitted current density J_{em} in equation 2.44. It is defined as the current of photons that are created by radiative recombination and subsequently coupled out of the device. So far in this thesis we have assumed that all of the radiatively generated photons leave the solar cell, in reality however that is not the case. In a real solar cell a photon that is generated within the bulk of an absorber has a probability p_{e} to be emitted, then it could be detected as part of a luminescence signal. It may alternatively with a probability p_{r} be reabsorbed by the absorber layer itself, generating a new electron-hole pair. This process of reabsorption is identical to the absorption of photons of incident light, it is often referred to as photon recycling. While photons that are recycled within the absorber create electron-hole pairs that can again contribute to recombination or the cells current, photons may also be reabsorbed in one of the other layers of the cell such as the ETL, HTL or the contacts.In this case

they can not create additional recombination events. This process is called parasitic absorption and happens with a probability of p_a. Since these are all the possible outcomes of a radiative recombination event $p_\mathrm{e}+p_\mathrm{r}+p_\mathrm{a}=1$ must hold. All possible interactions of a photon created by radiative recombination have been illustrated in fig- 2.17. While the probabilities for reabsorption p_r and parasitic absorption p_a are not easily calculated the probability for emission p_e can be calculated as the ratio of the outgoing photon flux ϕem and the integral over the internal radiative recombination. While the former is defined by Kirchhoff's law in equation 2.41 the latter is described in the van Roosbroeck-Shockley equation [110]

$$k_\mathrm{rad} n_\mathrm{i}^2 = \int_0^\infty 4\alpha n_\mathrm{r}^2 \phi_\mathrm{bb} dE \tag{2.47}$$

with the refractive index n_r. Using these two relations the emission probability can be calculated as [111]

$$p_\mathrm{e} = \frac{\phi_\mathrm{em}}{\int_0^d k_\mathrm{rad} n_\mathrm{i}^2 dx} = \frac{\int_0^\infty a\phi_\mathrm{bb} dE}{d\int_0^\infty 4\alpha n_\mathrm{r}^2 \phi_\mathrm{bb} dE}. \tag{2.48}$$

This equation assumes light outcoupling out of a single surface of the absorber volume. While it calculates the emission probability for an absorber in thermal and chemical equilibrium we assume these purely optical characteristics not to change when these equilibria are disturbed.

Ignoring all spacial dependencies of the charge carrier concentrations and consequently the recombination rates, the different probabilites allow us to find rather simple equations connecting the external and the internal luminescence quantum efficiency. The emission current density $J_\mathrm{em} = qdp_\mathrm{e}R_\mathrm{rad}$ with the thickness d of the absorber layer and the recombination current density $J_\mathrm{rec} = qd[R_\mathrm{nrad} + (1-p_\mathrm{r})R_\mathrm{rad}]$, where the probability of photon recycling p_r reduces the effective radiative recombination rate. Using these relations the luminescence quantum efficiencies can be put into context via [107, 111, 112]

$$Q_\mathrm{e}^\mathrm{lum} = \frac{J_\mathrm{em}}{J_\mathrm{rec}} = \frac{p_\mathrm{e}R_\mathrm{rad}}{(1-p_\mathrm{r})R_\mathrm{rad}+R_\mathrm{nrad}} = \frac{p_\mathrm{e}Q_\mathrm{i}^\mathrm{lum}}{1-p_\mathrm{r}Q_\mathrm{i}^\mathrm{lum}} = \frac{p_\mathrm{e}Q_\mathrm{i}^\mathrm{lum}}{\left(1-Q_\mathrm{i}^\mathrm{lum}\right)+\left(p_\mathrm{e}+p_\mathrm{a}\right)Q_\mathrm{i}^\mathrm{lum}}. \tag{2.49}$$

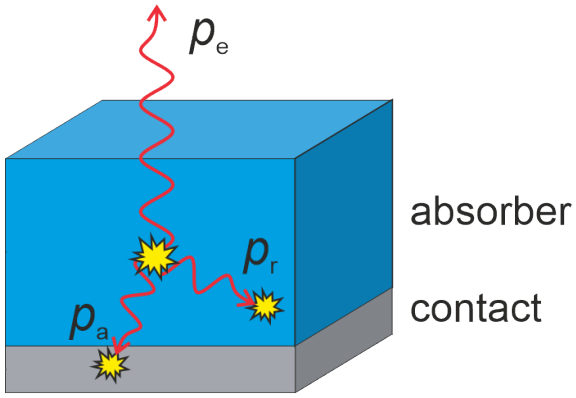

Figure 2.17: Schematic depiction of the possible interactions of a photon after it has been created by radiative recombination. It can either be emitted from the absorber or solar cell with a probability p_e, it can be reabsorbed withing the absorber with a probability p_r or it can be parasitically absorbed in one of the contact layers of the cell with a probability p_a. For simplicity only one contact layer has been illustrated representing all contact layers that may contribute to parasitic absorption.

2.5.7 Ideality Factors

I have first briefly mentioned an ideality factor n_{id} in chapter 2.3 as part of the diode equation 2.4. It is a dimensionless factor with values that are usually in the range of $1 < n_{id} < 2$ and which can be used to gather insights into the recobination mechanisms governing the diode behaviour of a solar cell. There have been multiple approaches identified to measure ideality factors. As will be shown in chapter 4 these approaches can lead to differing results, even though they fundamentally probe a similar characteristic. All of the ideality factors introduced in the following are measures of the dependency of the voltage dependency of the recombination current density $J_{rec}(V)$.

The most commonly used method to determine an ideality factor n_{id} is presumably via a dark current voltage measurement because these measurements are easily and routinely performed. When applying this method, what I will be calling the dark ideality factor $n_{id,d}$ is measured as the slope of the semilogarithmic dark current-voltage curve. It can be calculated as

$$n_{\mathrm{id,d}} = \frac{q}{k_{\mathrm{B}}T}\frac{dV_{\mathrm{ext}}}{d\ln(J_{\mathrm{d}})}, \tag{2.50}$$

with the externally applied voltage V_{ext} and the dark current density J_{d}. While this rather simple method can give a broad idea about the recombination mechanisms governing the behaviour of the current-voltage curve, it does have significant drawbacks. The issue are resistive effects first mentioned in chapter 2.1.3 influencing the dependency of J_{d} on V_{ext}. Both an external series resistance R_{s} stemming from the contact layers, as well as the parallel shunt-resistance R_{p} can alter the dark ideality factor characteristics. Additionally finite mobilities in the absorber layer can lead to an internal contribution to the series resistance R_{s}, further distorting the current behaviour. All of these influences make it difficult to distinguish between recombination and resistive effects determining the dark ideality factor at a given external voltage V_{ext}, limiting the insights that can be taken from it.

A second common method to access an ideality factor n_{id} is the so called suns-V_{OC} measurement [113–115]. Here the open-circuit voltage V_{OC} is probed at varying illumination intensities ϕ, enabling the determination of the ideality factor via

$$n_{\mathrm{id,OC}} = \frac{q}{k_{\mathrm{B}}T}\frac{dV_{\mathrm{OC}}}{d\ln(\phi)}. \tag{2.51}$$

The main advantage of this method is that at V_{OC} no net current is flowing across the series resistance R_{s}, thereby eliminating its influence. However, influences of the parallel resistance R_{p} can not be excluded this way. A third option to access an n_{id} is employing electroluminescence or photoluminescence. The PL approach utilizes the exponential dependency of the radiative recombination flux ϕ_{rad} on the quasi-Fermi level splitting ΔE_{F} via

$$\phi_{\mathrm{rad}} \propto \exp\left(\frac{\Delta E_{\mathrm{F}}}{k_{\mathrm{B}}T}\right). \tag{2.52}$$

Hence this ideality factor $n_{\mathrm{id,PL}}$ can be determined by variation of the incident light intensity ϕ according to

$$n_{\mathrm{id,PL}} = \frac{q}{k_{\mathrm{B}}T}\frac{d\ln(\phi_{\mathrm{PL}})}{d\ln(\phi)}. \tag{2.53}$$

Ideally two or more of these methods are combined in order to attain the most insight into the QFL splitting and the recombination characteristics of a solar cell. As mentioned at the beginning of this chapter, recombination is indeed the basis of the ideality factor n_{id}, as it can be defined looking at a solar cell or a solar absorber internally. It describes the exponential dependence of the recombination rate R on the voltage according to

$$R = R_0 \exp\left(\frac{\Delta E_{\mathrm{F}}}{n_{\mathrm{id}} k_{\mathrm{B}} T}\right), \tag{2.54}$$

where R_0 is the recombination rate in equilibrium and the QFL splitting ΔE_{F} represents the internal voltage V_{int} as I introduced it in chapter 2.5.1. This enables us to find an expression for the ideality factor

$$n_{\mathrm{id}} = \frac{1}{k_{\mathrm{B}} T} \frac{d\Delta E_{\mathrm{F}}}{d\ln(R)}, \tag{2.55}$$

that is an internal description of the recombination properties of the absorber of a solar cell, unaffected by resistive effects. Note that this calculation of an ideality factor does not take into account spatial inhomegeneities of a real solar cell. In order to calculate the recombination current density J_{rec}, we have to integrate over the volume of the cell. This can lead to ideality factor values between 1 and 2, due to a superposition of recombination characteristics varying across the cell [115]. This superposition will be relevant for the interpretation of simulations in chapter 4 and measurements in chapter 5.

From equation 2.55 we can determine the ideality factor n_{id} for any recombination mechanism in LLI and HLI on the basis of the equations shown in chapter 2.5.4. We will use two values describing the specific situation. The relationship of the charge carrier density to the QFL splitting is characterized by the exponent β in the equation $\Delta E_{\mathrm{F}} = k_{\mathrm{B}} T \ln\left(n^{\beta}/n_{\mathrm{i}}^2\right)$. In LLI $\beta = 1$ and in HLI $\beta = 2$. The second value γ is the reaction order of the recombination mechanism involved so that $R = k n^{\gamma}$. With these two values, that can be extracted from the equations in chapter 2.5.4 via the simple equation

$$n_{\mathrm{id}} = \frac{\beta}{\gamma}, \tag{2.56}$$

as proposed by Calado et al. [116,117]. The β and γ values as well as the resuliting n_{id} are displayed in table 2.1 for the relevant recombination mechanisms in LLI as well as HLI. When looking at the resulting values it is quickly understood, that there is only a single case that generates an ideality factor larger than 1, SRH recombination at a deep trap in high level injection. Therefore an ideality factor $n_{\mathrm{id}} > 1$ is a strong indicator that traps are involved in non-radiative recombination [118]. A more in depth discussion of ideality factors in PSCs and simulations of the absorber can be found in chapter 4.

Table 2.1: The values β, describing the ratio of charge carriers, and the recombination order γ, together with the resulting ideality factors n_{id} for different recombination and injection scenarios. In low level injection (LLI) $p \gg n$ and in high level injection (HLI) $n = p$. Here Shockley-Read Hall recombination refers to the case of a deep defect.

Recombination Mechanism	**Injection Type**	β	γ	$n_{\mathbf{id}}$
Radiative	LLI	1	1	1
	HLI	2	2	1
Shockley-Read Hall	LLI	1	1	1
	HLI	2	1	2
Auger	LLI	1	1	1
	HLI	2	3	2/3
Interface	LLI	1	1	1
	HLI	2	1	2

2.6 Electronic Structure

As mentioned in sec. 2.1.7, long charge carrier lifetimes corresponding to a suppression of non-radiative recombination is a key characteristic of a well functioning solar cell. Metal halide perovskite absorber layers show remarkably long charge carrier lifetimes despite their polycrystalline structure. This property is usually credited to the specific electronic structure of the metal halide perovskite material. The band structure is mostly defined the larger components of the crystal structure, the lead Pb^{2+} and the halide component (Cl^-, Br^-, I^-). The Pb^{2+} ion has the electron configuration $6s^2 6p^0$ ($[\mathrm{Xe}]4f^{14}5d^{10}6s^2 6p^0$), while the electron configuration of the

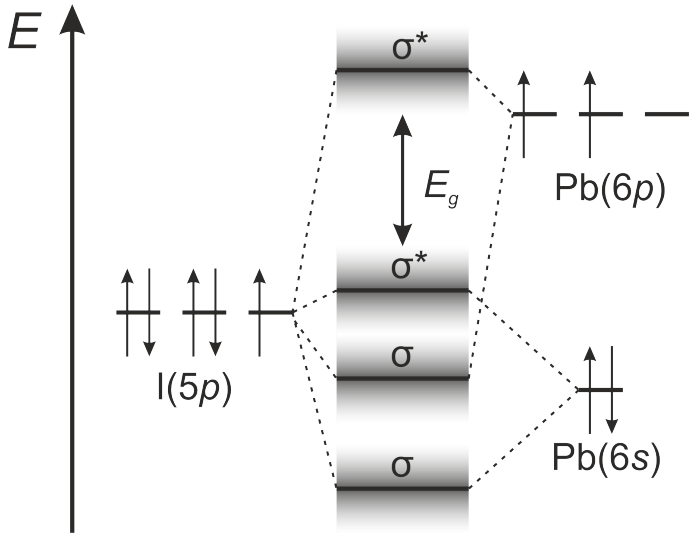

Figure 2.18: Bonding diagram of lead and iodine orbitals in $MAPbI_3$ adapted from [121]. The hybridized bonding (σ) and the anti-bonding ($\sigma*$) orbitals are shown relative to the energies of the p and s orbital energies of isolated lead and iodine respectively. The hybridized orbitals form the energy bands and accordingly the band gap E_g.

halides is xp^6 with x=3,4,5 for Cl^-, Br^- and I^- respectively. Since both lead and iodine are heavy elements, they exhibit very large spin-orbit coupling, therefore these relativistic effects need to be taken into account when describing the nature of the valence and conduction bands [119,120]. In fig. 2.18 the bonding (σ) and anti-bonding ($\sigma*$) hybrid orbitals formed between lead and iodine are illustrated [121]. The valence band maximum is formed by the anti-bonding state between the 6s-orbital of Pb^{2+} and the I^- 5p-orbital, while the conduction band minimum is formed by the anti-bonding hybrid state between the lead 6p-orbital and the iodine 5p-orbital [122]. The electronic levels of the organic cation are situated deep withing the valence and conduction bands [120, 123], thus the impact on the perovskite band structure is insignificant.

As shown by Zakutayev et al., an anti-bonding electronic state at the valence band maximum likely relates to an increased defect tolerance due to defects being shallower than for bonding states in the same position [124]. In order to figure out whether this is the case for perovskites, more specifically $MAPbI_3$, as well, energy levels of potential defects in a semiconductor are theoretically calculated, usually using density functional theory (DFT). There are three different types of

intrinsic defects to be taken into account, vacancies (ions missing in the lattice, in $MAPbI_3$ denoted as V_{MA}, V_{Pb} and V_I), interstitials (ions in positions usually not occupied in the lattice, MA_i, V_{Pb} and I_i) and ion substitutions (one ion in the lattice position of another, MA_I, MA_{Pb}, Pb_{MA}, Pb_I, I_{MA} and I_{Pbi}). So overall there are twelve different defects to be taken into consideration for $MAPbI_3$. While several works striving to calculate the energy levels of the intrinsic defects have found an agreement as to which defects are shallow, there are conflicting results concerning defects situated deep within the band gap [107]. This incongruency was resolved by Du et al. by comparing results of DFT calculations investing different levels of theory [125]. They found that the inclusion of spin-orbit coupling into the calculations is of particular importance as well as the self-interaction error that is high for the generalized gradient approximation but can be reduced using hybrid density functional calculations [125]. In figure 2.19 the defect levels calculated by Yin et al. [126, 127] are shown in comparison to the results of Du et al. [125] for two representative defects.

For the results on the left, calculated without spin-orbit coupling, it is readily seen, that most of the point defects have energy levels that are either within the valence or conduction band respectively or less than 0.05 eV from the band edges. These shallow defects do not make a major contribution towards recombination and therefore do not diminish the quality of the material significantly. To the right we see the calculations for two defects that do form deep traps, the iodine interstitial (I_i) and the related iodine ion occupying a methylammonium position (I_{MA}). Their respective trap levels were calculated using the generalized gradient approximation without and then with spin-orbit coupling. The inclusion of spin-orbit coupling leads to a substantial reduction of the band gap, using a hybrid functional with spin-orbit coupling once again yielded a realistic band gap showing deep trap levels for the two defects evaluated [125]. In summary, DFT calculations show, that most defects in $MAPbI_3$ absorbers are shallow, but there are some that form deeper traps. These however do not heavily impact the functionality of the material and yield remarkably high carrier lifetimes for a polycrystalline material.

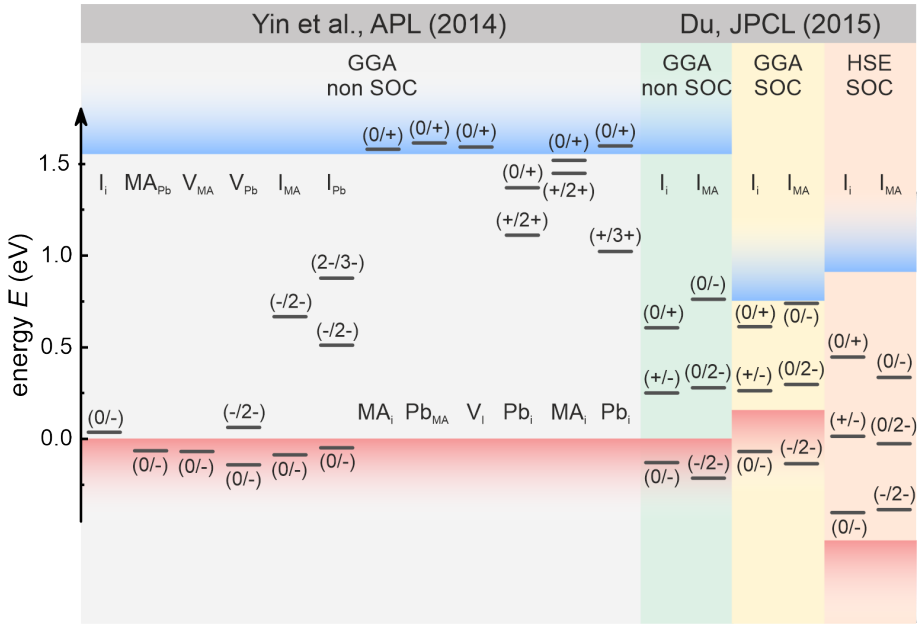

Figure 2.19: Transition energy levels of point defects in $CH_3NH_3PbI_3$ calculated using density functional theory. The data on the left (grey background) are calculated with the generalized gradient approximation without spin-orbit coupling (GGA non-SOC) in [126,127]. The data on the right are calculated using GGA non-SOC (green background), GGA with SOC (yellow background) and a hybric functional with spin-orbit coupling (HSE SOC, HSE for Heyd-Scuseria-Ernzerhof) (orange background) in [125]. The X_Y-notation refers to a lattice position usually occupied by ion Y that is occupied by the defect ion X. V and i represent vacancies and interstitial sites respectively. Reproduced from figure 8 in the publication by Kirchartz, KrÃ¼ckemeier and Unger [107].

2.7 Band Gap Characteristics

As mentioned in chapter 2.1.4 the defining characteristic of a semiconductor is its band gap. The band gap defines the minimum energy that is required for an electron to be lifted from the valence band into the conduction band and the energy a photon produced by a radiative recombination event possesses. However the charge carriers present in the semiconductor also carry a momentum described by the wave vector k. This can lead to the extrema of the bands being in different positions in momentum space, altering the characteristics of recombination in the semiconductor. In direct semiconductors both extrema are in the same position in momentum space ($\Delta k = 0$) whereas indirect semiconductors feature a momentum shift of the extrema ($\Delta k >$

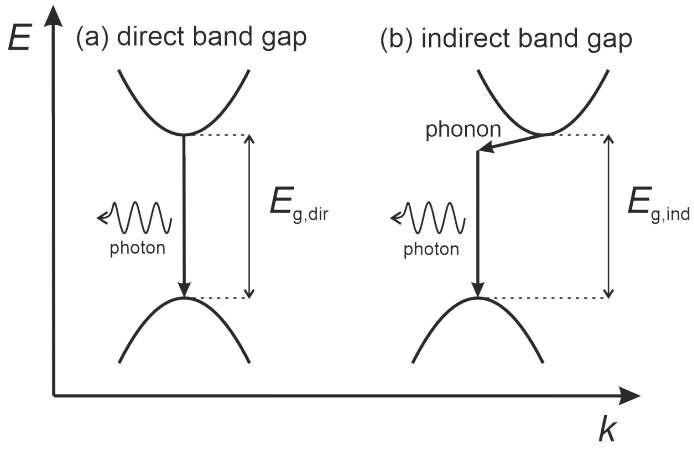

Figure 2.20: Illustration of a recombination process in a semiconductor with (a) a direct band gap and (b) an indirect band gap. While the direct band gap only requires an electron and a hole for the recombination process, in the indirect semiconductor it additionally requires a phonon to satisfy the conservation of momentum. The same constraints apply to generation processes.

0). The two types of semiconductors and their respective recombination paths are illustrated in fig. 2.20.

Recombination in a direct semiconductor simply requires an electron and a hole to coincide and is therefore only limited by the amount of charge carriers present in the semiconductor. Recombination in an indirect semiconductor additionally requires a phonon (a quasiparticle quantifying vibrational modes of the crystal lattice) in order to satisfy conservation of momentum. This additional requirement makes the transition from conduction band to valence band a lot less likely in an indirect semiconductor and thereby slower than direct recombination processes.

Since recombination is the reciprocal process of generation the same restrictions apply to the generation of charge carriers. In order for a photon to be absorbed in an indirect semiconductor it either needs to coincide with a phonon or possess significantly more energy in order to overcome the band gap E_g at a fixed point in momentum space. While the slow recombination present in indirect semiconductors is desirable these restrictions also usually limit their absorption. Direct semiconductors on the other hand often yield very good absorbing properties while also being highly luminescent due to fast radiative recombination. Consequently direct

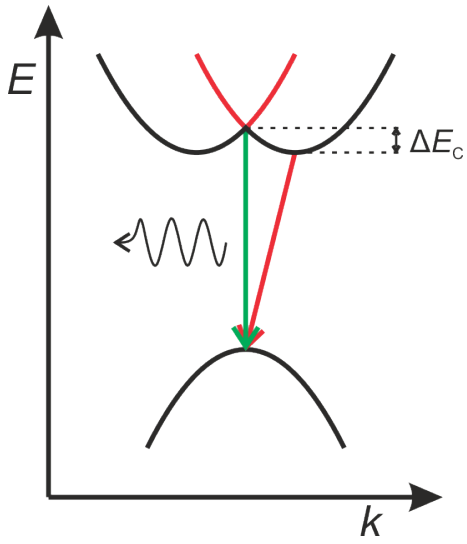

Figure 2.21: Schematic depiction of the Rashba effect on optical transitions in metal halide perovskites. The conduction band is split into two bands in momentum space, while the splitting of the valence band is assumed to be negligible. The band gap allows for both indirect transitions (red arrow) as well as direct transitions (green arrow), the latter requiring higher photon energies (ΔE_C).

semiconductors are both well suited for solar cell applications as well as active materials in light emitting devices (LEDs).

As mentioned in section 2.6 the heavy lead and halide ions in metal halide perovskites lead to a strong spin-orbit coupling. The spin-orbit coupling in combination with the breaking of the crystal inversion symmetry lifts the spin degeneracy in momentum space [128, 129]. As a consequence the extrema of the valence band and the conduction band are shifted in momentum space, this phenomenon is known as the Rashba effect. The resulting band gap characteristic is shown in fig. 2.21, the lowest conduction band is split into two subbands which are symmetric in k-space. The highest valence band undergoes a similar splitting, however this effect is significantly smaller and was therefore not included in the illustration [130, 131]. This Rashba splitting of the valence band directly influences recombination [132]. The lowest bandgap energy now corresponds to an indirect transition, direct transitions however are still possible. The energy difference ΔE_C between the valence band minimum that is shifted in k-space and the valence band at $\Delta k = 0$ is low

enough to be overcome via thermal activation ($\approx 25-75$ meV [132–134]). The indirect transition however seems to be dominating luminescence [135], recombination for this transition is slowed due to the momentum mismatch as explained before. Metal halide perovskites therefore exhibit advantageous characteristics of both a direct and an indirect semiconductor. The direct band gap facilitates the strong absorption capabilities exhibited by perovskites while the indirect bandgap slows charge carrier recombination resulting in long charge carrier lifetimes [128].

2.8 Transport Layer Currents

In most solar cells the quality of the absorber is the first consideration taken when thinking about improving the system as a whole. Thus, most absorbers are quite well suited for the task they are expected to perform within the framework of the cell. This often leaves the contacts as limiting factors within the architecture; the same can be argued to be true for PSCs. The materials employed as transport layers in PSCs often have low charge carrier mobilities μ impacting the cell's operation. If we want to quantify the losses associated with contacts, it makes sense to take a look at the currents flowing through these contacts. The current density $J_{\mathrm{n/p}}$ through the transport layer of a PSC can be described by the concentration of charge carriers present in the layer, the charge carrier mobility $\mu_{\mathrm{n/p}}$, and the gradient of the QFL of electrons and holes respectively. For electrons this yields the current equation

$$J_{\mathrm{n}} = \mu_{\mathrm{n}} n(x) \frac{dE_{\mathrm{Fn}}(x)}{dx}, \tag{2.57}$$

which can be established analogously for holes. The significance of this equation can be elucidated by figure 2.22. Here we see the band diagram of a generic solar cell including the absorber, ETL, HTL and the metal contacts. Neither the transport layers nor the absorber are significantly doped leading to an electric field being present in all of these layers. The cell is at an externally applied bias V_{ext} which results in a corresponding splitting of the energy levels of the metal contacts and contributes to the splitting of the QFLs in the cell. In the sketch V_{ext} is marked between the extensions of the metal contact energy levels. The internal voltage V_{int} marks the splitting of the quasi Fermi-levels E_{Fn} and E_{Fp} of electrons and holes in the

absorber, respectively, as introduced in chapter 2.5.1. In figure 2.22 the difference between the internal and the external voltage can clearly be seen. It is reduced by a decline of the QFL splitting across the transport layers. We define the voltages $V_{\mathrm{int,n}}$ and $V_{\mathrm{int,p}}$ as the energy difference between the energy level E_{mid} situated in the middle between the metal contact energy levels and the respective QFL at the interface between the absorber and the transport layer. These voltages are the sum of the loss across one of the transport layers plus half of the external voltage V_{ext} and $V_{\mathrm{int}} = V_{\mathrm{int,n}} + V_{\mathrm{int,p}}$. The difference of the QFL energy at the edges of a transport layer describes the loss of electrochemical potential between the absorber and the external contacts of the solar cell, caused by suboptimal transport characteristics of the transport layers. Note that figure 2.22 is based on a few underlying assumptions. In this idealized scenario the QFLs in the absorber are completely flat and - more importantly - parallel to each other. This is relevant for the calculation of V_{int}, which is otherwise an average value across the absorber and it may signal a loss of V_{int} already taking place in the absorber itself. In a real solar cell this is the case but parallel QFLs can often be a valid approximation.

In order to find an expression to describe the current across a transport layer in terms of the internal and the external voltage of a cell we substitute equation 2.25a for the concentration of electrons into equation 2.57. We arrive at

$$J_{\mathrm{n}} = \mu_{\mathrm{n}} N_{\mathrm{C}} \exp\left(\frac{E_{\mathrm{Fn}}(x) - E_{\mathrm{C}}(x)}{k_{\mathrm{B}} T}\right) \frac{dE_{\mathrm{Fn}}(x)}{dx}, \tag{2.58}$$

with the electron current density J_{n} assumed to be constant in the contact layer, showing no dependency on x. This assumption is valid as long as no significant amount of charge carriers is created through absorption of photons or is lost due to recombination. Both of these characteristics are usually facilitated by large band gaps in the transport layers. Furthermore we assume the conduction band within the contact layer to be linearly dependent on the spatial coordinate x and can therefore express it as $E_{\mathrm{C}} = E_{\mathrm{C}}^{0} + qFx$, where E_{C}^{0} is the conduction band energy at the edge of the contact layer ($x = 0$) and F denotes the electric field throughout the contact layer. This assumption holds up very well for PSCs at low to medium voltages, towards high voltages the bands may bend leading to errors in the model. When we plug the linear relation above into equation 2.58 we obtain a differential equation

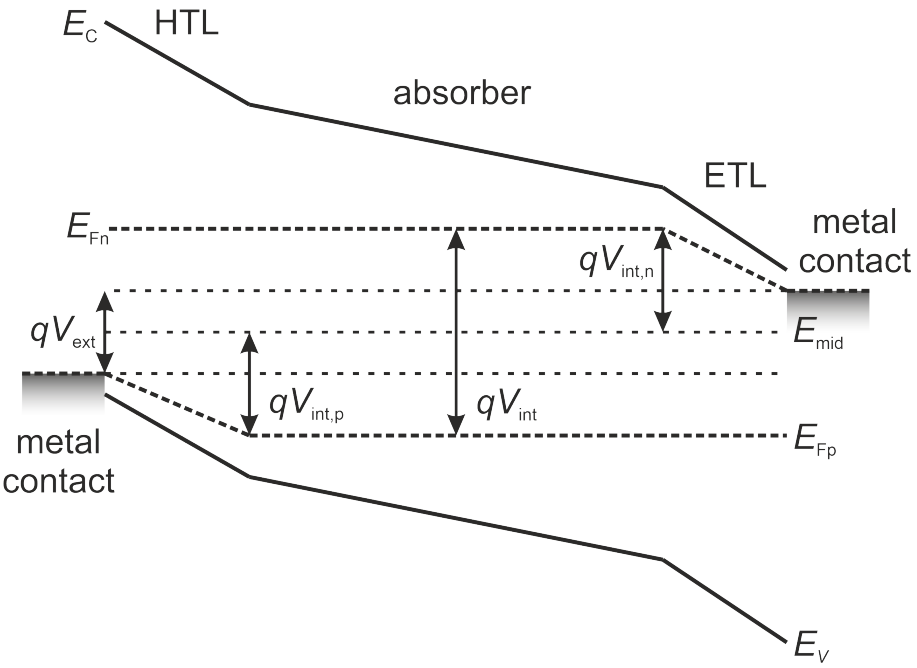

Figure 2.22: Schematic depiction of the contributions to the internal voltage V_{int} within a generic solar cell. The internal voltage V_{int} is depicted as the splitting of the QFLs in the absorber, the external voltage V_{ext} describes the potential difference between the external metal contacts and $V_{\mathrm{int,n}}$ and $V_{\mathrm{int,p}}$ represent the portion of the internal voltage that is lost at the ETL and the HTL respectively.

for the QFL E_{Fn}

$$\exp\left(\frac{E_{\mathrm{Fn}}(x)}{k_{\mathrm{B}}T}\right) dE_{\mathrm{Fn}}(x) = \frac{J_{\mathrm{n}}}{\mu_{\mathrm{n}} N_{\mathrm{C}}} \exp\left(\frac{E_{\mathrm{C}}^{0} + qFx}{k_{\mathrm{B}}T}\right) dx. \tag{2.59}$$

Integration of equation 2.59 with integration limits of $x = 0..d$ and $E_{\mathrm{Fn}} = E_{\mathrm{Fn}}^{0}..E_{\mathrm{Fn}}^{d}$, where d is the thickness of the contact layer and E_{Fn}^{0} and E_{Fn}^{d} are the values for the electron quasi Fermi level at either edge of the contact layer, yields

$$k_{\mathrm{B}}T\left[\exp\left(\frac{E_{\mathrm{Fn}}^{d}}{k_{\mathrm{B}}T}\right) - \exp\left(\frac{E_{\mathrm{Fn}}^{0}}{k_{\mathrm{B}}T}\right)\right] = \frac{J_{\mathrm{n}}}{\mu_{\mathrm{n}} N_{\mathrm{C}}} \exp\left(\frac{E_{\mathrm{C}}^{0}}{k_{\mathrm{B}}T}\right) \frac{k_{\mathrm{B}}T}{qF}\left[\exp\left(\frac{qFd}{k_{\mathrm{B}}T}\right) - 1\right]. \tag{2.60}$$

This can be simplified to

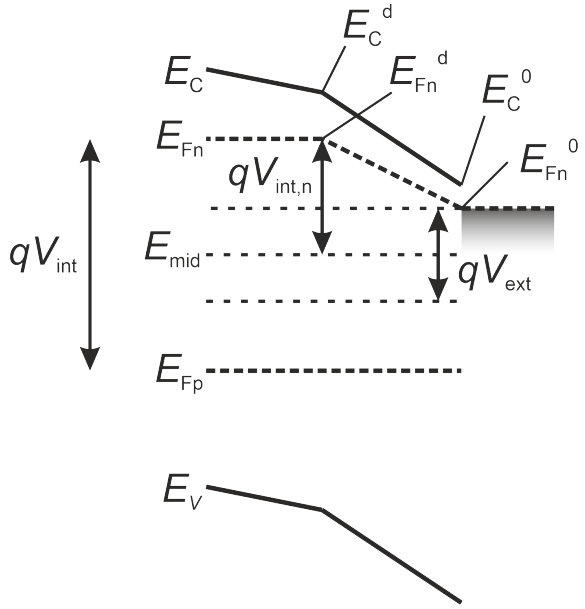

Figure 2.23: Closeup of the electron transport layer from figure 2.22 with additional depiction of the energies at the edges of the transport layer of the conduction band E_{C}^{0} and E_{C}^{d} as well as the quasi Fermi-level for electrons E_{Fn}^{0} and E_{Fn}^{d}.

$$\exp\left(\frac{E_{\mathrm{Fn}}^{d}}{k_{\mathrm{B}}T}\right)-\exp\left(\frac{E_{\mathrm{Fn}}^{0}}{k_{\mathrm{B}}T}\right)=\frac{J_{\mathrm{n}}}{q\mu_{\mathrm{n}}N_{\mathrm{C}}F}\exp\left(\frac{E_{\mathrm{C}}^{0}}{k_{\mathrm{B}}T}\right)\left[\exp\left(\frac{qFd}{k_{\mathrm{B}}T}\right)-1\right] \tag{2.61}$$

and subsequently resolved for the electron current

$$J_{\mathrm{n}}=q\mu_{\mathrm{n}}N_{\mathrm{C}}F\exp\left(-\frac{E_{\mathrm{C}}^{0}}{k_{\mathrm{B}}T}\right)\frac{\exp\left(\frac{E_{\mathrm{Fn}}^{d}}{k_{\mathrm{B}}T}\right)-\exp\left(\frac{E_{\mathrm{Fn}}^{0}}{k_{\mathrm{B}}T}\right)}{\exp\left(\frac{qFd}{k_{\mathrm{B}}T}\right)-1}. \tag{2.62}$$

All energy levels utilized in equation 2.62 are marked in a closeup of the ETL in figure 2.23. Considering the relation of V_{ext} and $V_{\mathrm{int,n}}$ to the energy level in the center between the metal contacts E_{mid} we arrive at

$$J_{\mathrm{n}}=q\mu_{\mathrm{n}}N_{\mathrm{C}}F\exp\left(\frac{E_{\mathrm{mid}}-E_{\mathrm{C}}^{0}}{k_{\mathrm{B}}T}\right)\frac{\exp\left(\frac{E_{\mathrm{Fn}}^{d}-E_{\mathrm{mid}}}{k_{\mathrm{B}}T}\right)-\exp\left(\frac{E_{\mathrm{Fn}}^{0}-E_{\mathrm{mid}}}{k_{\mathrm{B}}T}\right)}{\exp\left(\frac{qFd}{k_{\mathrm{B}}T}\right)-1}, \tag{2.63}$$

which yields

$$J_\mathrm{n} = q\mu_\mathrm{n} N_\mathrm{C} F \exp\left(-\frac{\frac{1}{2}qV_\mathrm{ext} + \varphi_\mathrm{b,b}}{k_\mathrm{B}T}\right) \frac{\exp\left(\frac{qV_\mathrm{int,n}}{k_\mathrm{B}T}\right) - \exp\left(\frac{qV_\mathrm{ext}}{2k_\mathrm{B}T}\right)}{\exp\left(\frac{qFd}{k_\mathrm{B}T}\right) - 1}. \tag{2.64}$$

With this we have an expression for the majority carrier current through the ETL which is only dependent on $V_\mathrm{int,n}$, V_ext and the electric field F across the absorber, which is in turn dependent on the external voltage. The same expression can anologously be found for the hole current J_p^d through the HTL. Equation 2.64 can be written as

$$J_\mathrm{n} = J_\mathrm{extr,n}(V_\mathrm{ext}) \left[\exp\left(\frac{qV_\mathrm{int,n}}{k_\mathrm{B}T}\right) - \exp\left(\frac{qV_\mathrm{ext}}{2k_\mathrm{B}T}\right)\right], \tag{2.65}$$

with the prefactor, which we will define as the extraction current

$$J_\mathrm{extr,n}(V_\mathrm{ext}) = q\mu_\mathrm{n} N_\mathrm{C} F \frac{\exp\left(-\frac{\frac{1}{2}qV_\mathrm{ext} + \varphi_\mathrm{b,b}}{k_\mathrm{B}T}\right)}{\exp\left(\frac{qFd}{k_\mathrm{B}T}\right) - 1}. \tag{2.66}$$

This prefactor characterizes the extent to which a transport layer enables charge carrier extraction. A high value of $J_\mathrm{extr,n}$ means that only a low gradient of the QFL is necessary to drive out charge carriers whereas a low $J_\mathrm{extr,n}$ necessitates a higher gradient leading to a higher discrepancy between V_int and V_ext. Note the dependency of $J_\mathrm{extr,n}$ on V_ext incorporating the reduction of the extraction barrier with an applied voltage.

With this model we have found a rather elegant way of quantifying the influence of the transport layers on charge carrier extraction processes. The internal voltage V_int will play a prominent role in interpreting the efficiency of charge extraction in simulated solar cells (chapter 4) and real solar cells (chapter 5). In chapter 6 it is utilized to calculate the series resistance R_s. In chapter 4 I will use this model to rationalize the behaviour of the ideality factors of simulated solar cells at short circuit. There it allows us to understand how the transport layers and their corresponding values of J_extr could be adjusted to facilitate any kind of ideality factor at short circuit.

3 Materials and Methods

This chapter presents the experimental and simulation methods utilized in this thesis. Chapter 3.1 covers the processing steps of the solar cells measured for this thesis. Subsequently in chapter 3.2 the performed measurements will be introduced. Finally in chapter 3.3 the simulation tools used to interpret the measurements are described.

3.1 Processing of Perovskite Solar Cells

The basic architecture of a perovskite solar cell was introduced in chapter 2.1.4. In figure 3.1 (a) the architecture of the cells utilized in this thesis is displayed. The perovskite material used as the absorber is a simple methylammoniumlead-triiodide ($CH_3NH_3PbI_3$). It is bordered by [6,6]-phenyl-C_{61}-butyric acid methyl ester (PCBM) and poly[bis(4-phenyl)(2,4,6-trimethylphenyl)amine] (PTAA) serving as the ETL and HTL respectively. The contacts are made up of transparent indium tin oxide (ITO) at the front and silver (Ag) at the back. Situated between the PCBM and the Ag layer is a layer of bathocuproine (BCP) which reduces the work function at the Ag interface [136, 137] and reduces charge accumulation and accordingly recombination at the interface [138].

The cells are manufactured on 20 mm × 20 mm glass substrates that were commercially bought with pre-patterned ITO (PsiOTec Ltd). The layout of a fully processed cell on this scaffolding can be seen in figure 3.1 (b). The light grey vertical stripes represent the ITO pattern as it is prepared on the glass substrate. This substrate is successively cleaned in an ultrasonic bath with soap (Hellmanex III), acetone and isopropyl alcohol (IPA, purity of 99.5 %) for 10 minutes at a time. The cleaned substrates are dried and subsequently treated with oxygen plasma for

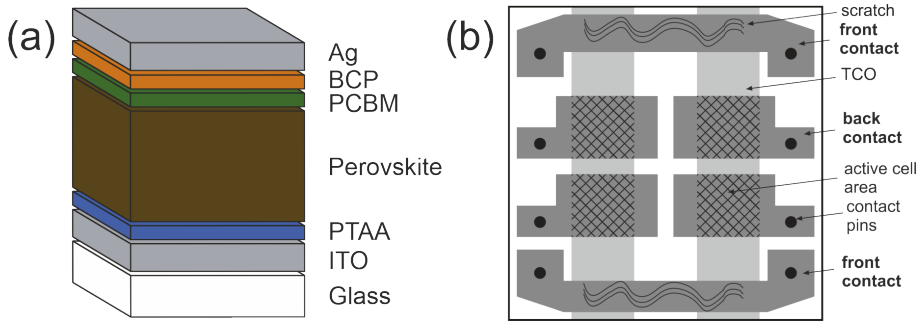

Figure 3.1: (a) Layer stack of processed and measured PSCs employing PTAA and PCBM as HTL and ETL respectively as well as ITO and Ag as contacts. BCP acts as a buffer layer reducing interfacial recombination. (b) Schematic depiction of a substrate and the cell configuration viewed from the back. The area of the cells is defined by the overlap of the front and back contacts, four cells with an area of 4 mm × 4 mm are formed.

12 minutes and transferred to a glovebox filled with nitrogen (N_2).

Within the glovebox all layers except for the silver contacts are produced by spincoating. Spincoating describes a technique for which the materials that are supposed to make up a layer are first dissolved in a solvent. The solution containing the precursor for a layer may have to be heated or stirred for an adequate amount of time. Once the solution is in the indended state some of it is applied to the substrate and subsequently the substrate is spun around an axis perpendicular to its surface. This process ejects most of the solvents and ideally leaves an even and uniformly coated film. The characteristics of the film like coverage, thickness, crystallinity or surface roughness strongly depend on the spinning parameters such as acceleration, spinning speed and spinning time. However the intricacies of designing these processes are not within the scope of this thesis.

For the PTAA layer 2 mg/ml of PTAA (Xi'an Polymer Light Technology Corp., Mn=17900, Mw=33000) are dissolved in toluene (99.8 %) at 75 °C. 80 μl of the hot solution are applied to the substrate and spun at 500 rpm for 4 s with a ramping rate of 500 rpm/s and subsequently at 4500 rpm for an additional 20 s with a ramping rate of 800 rpm/s. The resulting layer is annealed on a hotplate at 110 °C for 10 minutes and let cool down to room temperature before proceeding. The perovskite solution uses a mixture of two solvents, 95 % dimethylformamide (DMF, 99.8 %) and 5 % dimethylsulfoxide (DMSO, 99.5 %). Dissolved in 1.667 ml of this mixture

are 0.9 mmol of lead acetate trihydrate ($Pb(CH_3COO)_2 \cdot 3H_2O$, >98.0 %, TCI Deutschland GmbH), 0.1 mmol of lead chloride ($PbCl_2$, >99.999 %, Sigma Aldrich Company Ltd.) and 3 mmol of methylammonium iodide (MAI, Greatcell Solar) yielding approximately 1.8 ml of solution with a concentration of 0.6 mol/l with excess MAI. The solution is stirred at room temperature over night and filtered using a 45 μm polytetrafluorethylene (PTFE) filter prior to use. The solution is heated up to 75 °C and 120 μl are applied to the substrate. In order to facilitate a more homogeneous film formation the solution is applied during spincoating, after the substrate has accelerated. The substrate is spun at 1400 rpm for 5 s with a ramping rate of 350 rpm/s and subsequently at 6000 rpm for 20 s with a ramping rate of 767 rpm/s. After spincoating the perovskite layer is annealed at 75 °C for 2 minutes. PCBM (99.5 %, Solenne BV) is dissolved at a concentration of 20 mg/ml in a solvent mixture of 50 % chlorobenzene (CB, 99.8 %) and 50 % toluene. The solution is stirred over night at 75 °C. 60 μl of the hot solution is brought onto the substrate and spun at 1200 rpm for 60 s with a ramping rate of 400 rpm/s. The finished layer is not annealed but dried at room temperature. BCP (>99.8 %, Ossila Ltd.) is dissolved in IPA at a concentration of 0.5 mg/ml and treated in an ultrasonic bath for 1 h. Then 120 μl are spincoated at 4000 rpm for 30 s with a ramping rate of 800 rpm/s.

After all layers are spun onto the substrate the ITO stripes that function as the front contacts have to be uncovered in order to be contacted. In figure 3.1 (b) the places where the spincoated layers are removed are marked by squiggly lines. The layers are removed by scratching them off using a metal pen. The last step in preparing a fully functioning cell is the thermal evaporation of the silver back contact. This is done in an evacuated evaporation chamber at 2 Å/s while parts of the substrate are masked. This leads to a pattern of the back contact which is shown in a darker grey in figure 3.1 (b). Four cells with an area of 4 mm x 4 mm are created by the overlap of the silver back contact with the ITO front contact. The two stripes of silver at the top and the bottom contact the ITO where it was laid bare from the removal of the spincoated layers. Thereby these silver stripes function as the front contacts. The dark dots at the left and the right of the ITO stripes mark the places in which the cells are usually contacted in order to conduct electrical measurements.

3.2 Characterization Methods

In this chapter the different methods that were used to characterize the PSCs are introduced. In chapter 3.2.1 current-voltage measurements are introduced, whereas in chapter 3.2.2 the luminescence measurements are illustrated.

3.2.1 Current-Voltage Characteristics

Current-voltage curves are one of the most basic yet most important measurements to characterize the performance of a solar cell. Some of the central operational characteristics can be taken from illuminated (see chapter 2.1.2) and dark current voltage curves. Current voltage curves were measured in two different setups. First they were measured in a calibrated class AAA solar simulator that closely matches the AM1.5g spectrum and is situated within a glovebox with nitrogen atmosphere. This solar simulator is based on the model WXS-90S-L2,AM1.5GMM (Wacom Electric Co., Ltd.) and employs a combination of a xenon and a halogen lamp as light sources. The measurements in this solar simulator aim to accurately reproduce the performance of a solar cell under real world solar illumination. Secondly illuminated current-voltage curves were taken simultaneously during voltage dependent photoluminescence measurements in order to be able to correlate both characterization methods.

Both setups that measure the current voltage characteristics make use of measurement boxes that samples can be put into. In these boxes the samples are contacted at the points shown in figure 3.1 (b). The contacting in conjunction with an external switch-box allows to routinely measure all four cells on a substrate as defined in a PC measurement software. The measurement parameters supplied by the PC software are implemented by a source measurement unit (SMU, Keithley SMU 2450). In the measurement box the samples are sealed and kept in the nitrogen atmosphere from the glovebox they were mounted in. Illumination is introduced into the box via a quartz glass window. Illumination losses due to the glass window are taken into account during measurement evaluation. The measurement configuration also allows for the introduction of metal masks to change the aperture of a measurement.

At the calibrated solar simulator illuminated current-voltage curves are measured as well as the current-voltage behaviour of the cell in the dark. Both measurements are conducted multiple times in a row both in forward (J_{SC} to V_{OC}) and reverse direction (V_{OC} to J_{SC}). Multiple sweeps are necessary to ensure that the solar cell is in a stable condition and no ions are moving or degradation is taking place [85, 86]. Forward and reverse sweeps are used to detect possible hysteretic behaviour which is often encountered in PSCs [73, 78].

Additionally to the current-voltage sweeps suns-V_{OC} measurements are conducted. Here the open-circuit voltage V_{OC} and the short-circuit current density J_{SC} are taken at varying illumination intensities ϕ. Since it is not trivial to change the illumination intensity of a calibrated solar simulator a setup with a white LED (Cree XLamp CXA3050, 2700 K, 100W) as the light source situated within a glovebox was used for these measurements. The spectrum of the LED does not precisely match the spectrum of solar irradiation, especially in the UV and IR regions. For current-voltage measurements conducted to quickly screen freshly processed cell batches the LED current is calibrated by comparing the J_{SC} of a reference cell at a calibrated solar simulator to that at the LED setup. For the suns-V_{OC} measurements the LED has the advantage that its irradiance is reasonably linear with the LED current I_{LED} in the relevant regime. The suns-V_{OC} measurements conducted at this setup enable us to calculate the ideality factor $n_{id,OC}$ of the cell at open circuit (see eq. 2.51).

3.2.2 Luminescence

In chapter 2.5.6 the theoretical fundamentals of luminescence measurements were introduced. While there are a multitude of measurement techniques that involve photoluminescence or electroluminescence, the setup used for this thesis was a simple steady-state luminescence experiment.

3.2.2.1 Steady-State Experimental Setup

The experimantal setup is sketched in figure 3.2. The excitation light source is a 532 nm coherent sapphire laser. The light supplied by this laser passes through two filters. The first is a blue-green BG39 filter that is used because the frequency

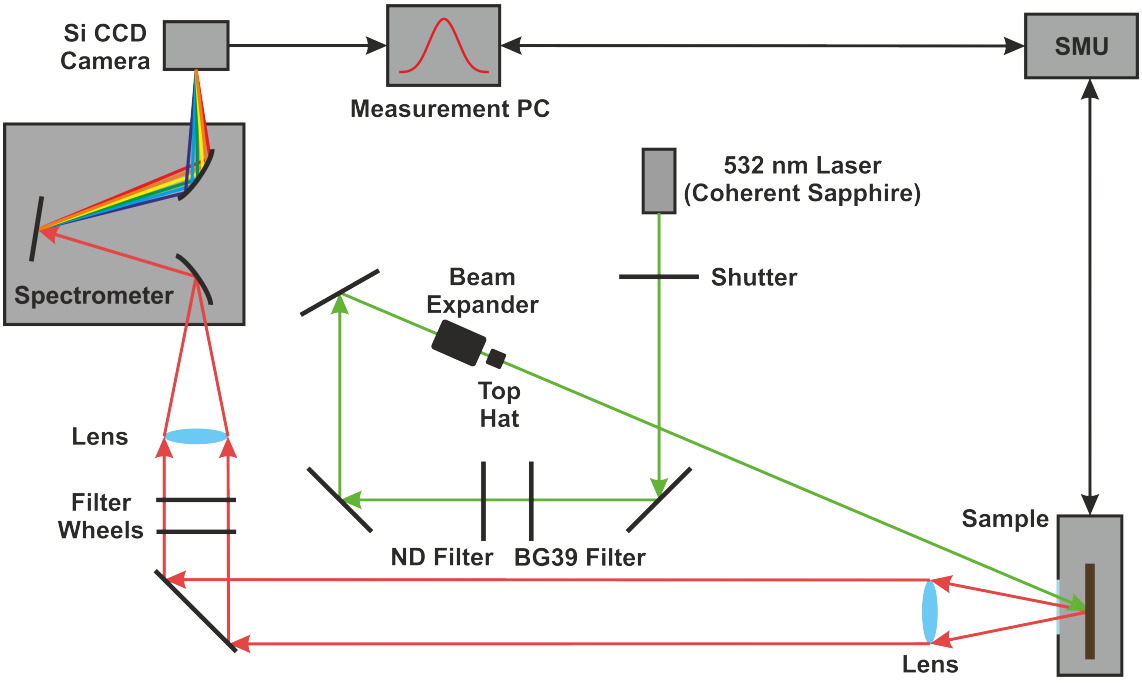

Figure 3.2: Schematic depiction of the steady-state luminescence setup. The sample is illuminated with an expanded 532 nm laser beam, the emitted luminescence is collected with a system of lenses and filters and fed into a spectrometer. The spectrometer in conjunction with the Si CCD camera measures the spectrally resolved luminescence signal and relays the data to the measurement PC. The PC additionally controls the SMU to set current or voltage while simultaneously measuring other.

doubled laser can emit residual infrared light of the fundamental wavelength 1064 nm. This infrared light is filtered out while the laser wavelength is transmitted. The second filter consists of an array of neutral-density (ND) filters that can be interchanged. These ND-filters are used to reduce the intensity of the laser beam without any spectral bias. After passing the filters the beam is guided by mirrors into a beam expander in which the diameter of the beam is increased by a factor of 7. Subsequently the beam passes through a top head beam shaper that changes the round gaussian intensity profile of the laser beam into a quadratic profile with a homogeneous intensity distribution. After the beam shaper the quadratic beam profile has an area of approximately 5.3 mm $\times$ 5.3 mm able to fully illuminate the cell area of a PSC as processed according to chapter 3.1 (see figure 3.1 (b)).

Once the laser reaches the sample, part of the illumination is absorbed, exciting

charge carriers and inducing photoluminescence. The luminescence photons are emitted and collected by a lens to form a parallel beam. This beam passes two filter wheels where edge filters can be set to filter out reflected laser light (532 nm filters). Behind the filter wheels an additional lens focuses the luminescence beam into a spectrometer (Andor Shamrock 303). The spectrometer utilizes a setup of two concave mirrors and an optical grating to filter light of a narrow wavelength range from the beam. This way the luminescence signal can be spectrally scanned, the light is subsequently coupled into an Andor Si (deep depletion) CCD camera (iDus Series) where the light intensity is measured and relayed to to the measurement PC. There the spectrally resolved luminescence spectrum is saved and can be evaluated.

3.2.2.2 Voltage-Dependent Luminescence

The majority of luminescence measurements are performed on films of a singular material as opposed to a fully processed solar cell. In this thesis, however, I am measuring the luminescence properties of full perovskite solar cells that are mounted in a measurement box that shields them from the ambient air and contacts all cells on the substrate. I am therefore able to apply a voltage or current bias to the cell via an SMU (Keithley SMU 2400). Unlike most luminescence measurements I can then measure the luminescence signal not only at open circuit, but during a full current-voltage sweep. This is what I have done for this thesis.

The cell was mounted within the measurement box and introduced into the laser beam path. The substrate is masked such that only one of the four cells on the substrate is illuminated with a square aperture of 3 mm $\times$ 3 mm. Measurements are performed at eight different illumination intensities adjusted via the ND filters. For each illumination intensity six consecutive current-voltage sweeps were performed without interruption, alternating between forward sweeps and reverse sweeps, starting with a forward sweep. Each sweep is split into two voltage regimes. In the low voltage regime (-0.1 V to 0.9 V) measurements are taken with a spacing of 0.1 V, since the luminescence signal hardly changes and in order to reduce scanning time and strain on the cell. In the high voltage regime (>0.9 V) Measurements are performed at an increment of 0.02 V in order to more precisely monitor the cell behaviour around the open-circuit voltage. The V_{OC} of the cell at any given

illumination intensity is determined beforehand and the upper voltage regime is terminated slightly above V_{OC} in order to not overexpose the Si CCD camera due to a high generation of electroluminescence. Forward and reverse scans are performed in order to check for hysteresis effects and multiple sweeps were performed in order to fully activate the cell and detect possible degradation.

At each of the specified voltages a luminescence spectrum was taken. In order for the charge carriers and potentially moving ions to equilibrate before each spectrum is taken, illumination and voltage are held for 500 ms. Figure 3.3 shows the semilogarithmic plots of the normalized spectra taken at each voltage specified above during the six sweeps performed at a constant illumination intensity. While the spectral information is not relevant to the evaluation of the data performed in this thesis, it does give insight into potential error sources during the measurements. If an additional unwanted light source were to impact the data acquisition the shape of the spectra could be altered. The 174 spectra shown in figure 3.3 however show very little changes in shape with applied voltage. The same is the case for all further illumination intensities that are investigated.

The integration time that is necessary for a measurement naturally depends on the luminescence intensity. If the integration time is too low the measurement signal will not be strong enough and will be tainted by background noise. If the integration time is too high the measurement time is unnecessarily inflated and the CCD camera will be overexposed. Additionally to these constraints each set of voltage sweeps generates luminescence signals of significantly different magnitudes. Therefore the integration time has to be chosen in a way that all luminescence intensities can be properly detected while keeping all measurements comparable. Since the illumination intensity was varied by a factor of 20 in total, the integration time had to be adjusted to the corresponding illumination. In table 3.1 the utilized illumination intensities are displayed in relative values together with the respective integration times used.

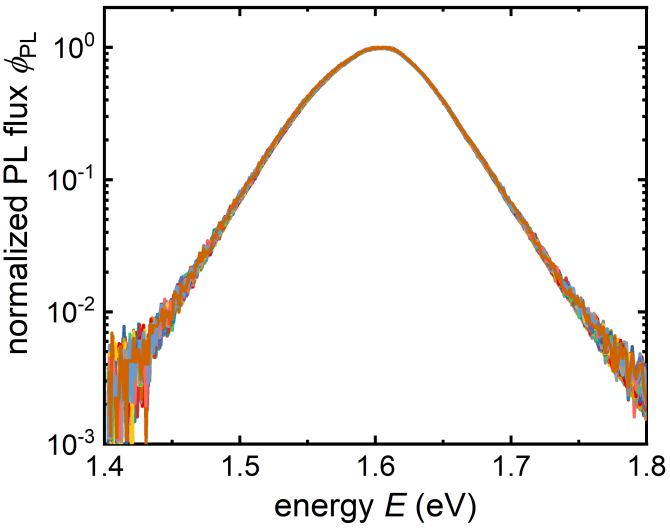

Figure 3.3: 174 normalized photoluminescence spectra taken during six consecutively measured current-voltage sweeps of a perovskite solar cell (see chapter 3.1). The sweeps were performed from -0.2 V to 1.26 V and in reverse in alternating order at a constant illumination intensity. The spectra were taken at different voltages during the sweeps spanning the entire voltage range.

Table 3.1: Relative illumination intensities used for voltage dependent luminescence measurements with the corresponding integration time of the Si CCD camera. Illumination intensities are normalized to the highest illumination, which generates a short-circuit current density J_{SC} closest to that of solar irradiation.

Illumination intensity ϕ (a.u.)	**Integration time t_{int} (s)**
1	0.2
0.735	0.2
0.459	0.2
0.278	0.2
0.163	2
0.087	2
0.061	2
0.050	4

3.2.2.3 Evaluation of Voltage Dependent Luminescence

After the luminescence spectra have been measured they need to be evaluated. This evaluation is done with a MATLAB script. Additionally to the spectra at various illumination intensities ϕ and externally applied voltages V_{ext} dark spectra ϕ_{dark} were taken for each integration time used. The corrected luminescence spectra

$$\phi_{\mathrm{corrected}}(\lambda) = \frac{\phi_{\mathrm{illum}}(\lambda) - \phi_{\mathrm{dark}}(\lambda)}{C(\lambda)t} \tag{3.1}$$

are calculated by subtracting the dark spectra from the illuminated spectra and dividing by the intergration time t and the calibration factor $C(\lambda)$. The calibration factor $C(\lambda)$ spectrally corrects the signal of the Si CCD camera. It accounts for absorption and reflection errors stemming from the camera and the optical components of the measurement setup. The calibration factors were calculated from an intensity profile taken of a calibrated light source with a known spectrum. After these corrections the spectra are converted to an energy axis and the maximum photon fluxes are extracted. These photon fluxes will be used to calculate the internal voltage V_{int} of the device. Equation 3.11 that is used for these calculations will be introduced in the following chapter.

3.2.2.4 Ruling out Measurement Errors

Expectedly, solar cells in short-circuit conditions exhibit significantly lower luminescence fluxes ϕ_{PL} than the same cell does at open-voltage or even higher biases. This raises the question whether luminescence spectra taken at and around short circuit may be influenced by undesired light sources. This consideration is made even more important due to the fact that in the measurement setup used for the luminescence measurements the laser illumination of the samples is incident at an angle of approximately 35° as can be seen in figure 3.2. In figure 3.4 possible paths for the illumination are illustrated more closely. The laser light represented by the green arrows arrives at the sample at an angle. The mask sketched in black shields the substrate except for the aperture of 3 mm × 3 mm, which is smaller than the cell area defined by the front and back contacts of 4 mm × 4 mm. The light that passes the aperture of the mask may enter the glass substrate of the sample and

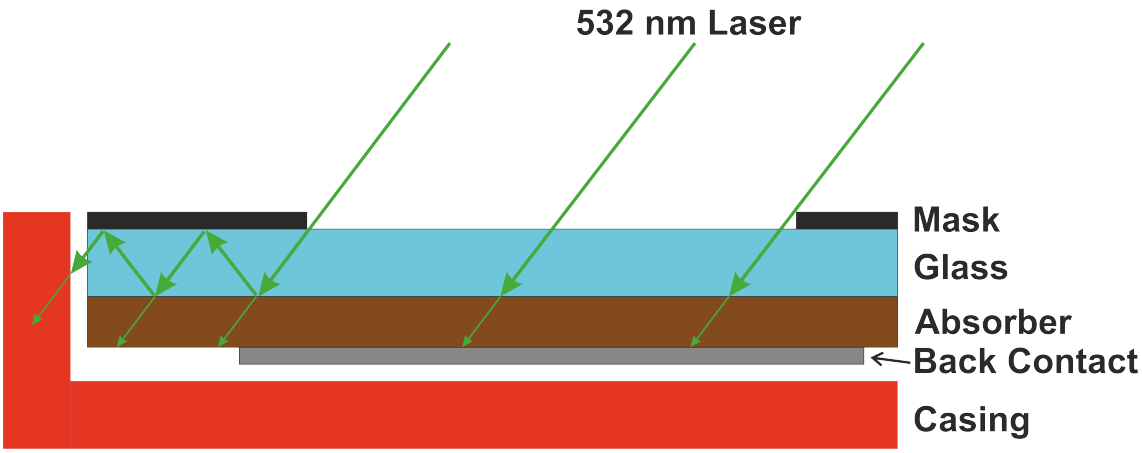

Figure 3.4: Schematic depiction of light guiding during luminescence measurements. The laser light impinges on the substrate at an angle and will partially enter the perovskite absorber generation photoluminescence. Some of the light however will be reflected at the absorber's surface and will reach areas outside the defined cell area. Some light will leave the substrate altogether and is absorbed by the measurement box casing. For simplicity refraction is not taken into account.

subsequently the perovskite absorber (additional layers not shown for simplicity). The laser light may be partially reflected at both the air-glass interface as well as the glass-perovskite interface leading to a light guiding effect within the glass as sketched in figure 3.4. This may lead to laser light being coupled into the bulk perovskite outside of the cell area defined by the overlap of the front and back contacts as well as the red polymer casing of the measurement cube. Luminescence signals from both materials could in theory be guided back along the same path and supply a significant part of the luminescence signal at low voltages.

In order to rule out any contribution stemming from the measurement box casing, the luminescence spectrum of the bare red plastic was taken. In figure 3.5 a normalized version of this spectrum is shown together with two spectra taken during the luminescence measurements discussed in this thesis. It is clearly visible that the maximum of the box casing signal (red curve) is far away from the perovskite maximum, while a small local maximum exists closer to it. The measurement data shown represent spectra of the highest illumination intensity at maximum voltage (blue curve) and the lowest illumination intensity at minimum voltage (grey curve). The spectral shape of the data has not changed and therefore a significant part of

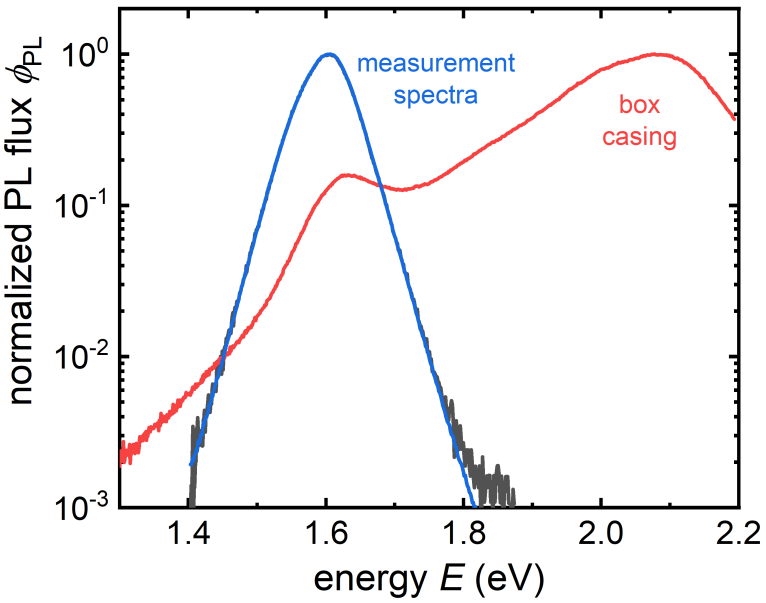

Figure 3.5: Normalized luminescence spectrum of the red plastic casing of a measurement box (red curve) compared to two luminescence spectra taken during data acquisition. The measurement data are represented by the normalized spectra of the highest illumination intensity at maximum voltage (blue curve) and the lowest illumination intensity at minimum voltage (grey curve).

the signal stemming from the box casing can be ruled out.

A more pressing concern however is the illumination of bulk perovskite outside of the cell area defined by the overlap of the front and back contacts. As mentioned before, we see significantly higher luminescence signals coming from a cell in open circuit as opposed to a cell around short-circuit conditions. However this is only the case in the contacted region since areas of the bulk perovskite that are not contacted can accordingly not be at short circuit. Charge carriers generated in these regions of the substrate generated by stray laser light are not extracted and therefore generate a luminescence signal corresponding to a cell in open circuit. As mentioned before, this signal could be guided within the glass or the absorber towards the aperture of the mask and significantly influence the luminescence signal coupled out of the substrate at lower voltages. In order to combat this effect the uncontacted regions

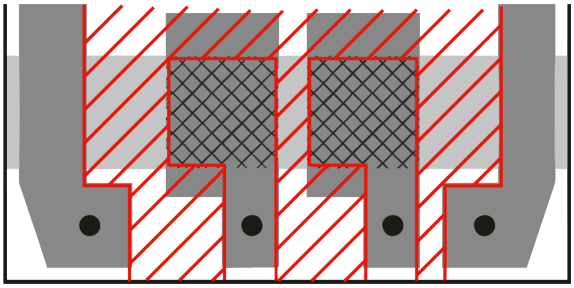

Figure 3.6: Schematic representation of the removal of the active layers a substrate by laser ablation. The hatched area represents the spaces where material was removed, at the edges of the evaporated silver contacts (dark grey) it extends 50 μm into the contact.

of the cell substrate were removed by laser ablation. In order to remove the layers a frequency tripled Nd:YVO_4 UV-laser (Rofin-Sinar Technologies Inc., Model RSY 20 E / THG) was used. The laser has a pulse duration of 6 ns, a pulse rate of 15 kHz, a focus length of 90 mm and was used with a power of approximately 6 mW. Material is removed in lines with a spacing of 15 μm between lines. The axis velocity for each line is 300 mm/s which in combination with the pulse rate leads to a spacing of 20 μm between laser ablation spots within a line. The diameter of the ablation performed by a single laser pulse is approximately 30-35 μm leading to a uniform removal of all layers processed in the lab. Figure 3.6 shows an illustration of one half of a substrate as used for this thesis. The regions hatched in red were removed by laser ablation leaving only the front contacts to the left and right, as well as the active cell area and a contacting strip. Wherever the lasered area reaches the silver contact (dark grey) it cuts into that area by 50 μm. The same removal pattern is applied on the other half of the substrate as well.

This way the influence of perovskite outside of the cell area is significantly reduced. Perovskite in permanent open-circuit conditions only remains below the front contact strips (where it was not removed by scratching), below the small contact strip for each cell and below the cells that are not currently measured. Further experiments were carried out to exclude possible influences of these areas as well. Substrates were measured with all perovskite lasered away except for a single cell with contacting strip and one back contact stripe. Furthermore substrates with an unpatterned ITO front contact were examined excluding the influence of the contact strip of the examined cell. All of these efforts did not significantly influence

the measurement data enabling us to conclude that the data presented in this thesis is not corrupted by measurement inaccuracies stemming from stray light.

3.3 Drift-Diffusion Simulations with ASA

This chapter introduces the numerical device simulations, which were used in this thesis to model the behaviour of perovskite solar cells and to reproduce the data gathered by the measurements described above. The software employed for the simulations is the commercial one dimensional numerical device simulator *Advanced Semiconductor Analysis* (ASA) [139]. This program was developed at the Technical University of Delft and was specifically designed to simulate thin-film solar cells. It is comprised of two components, the optical and the electrical simulation. In order to carry out its tasks the software needs a multitude of parameters to function. In order to supply the necessary parameters to the ASA software a framework was created in the programming environment MATLAB. Subsequently MATLAB was also utilized to process and evaluate the data ASA provides. In the following the input and output parameters for both the optical and the electrical calculations as well as the theoretical foundations will be introduced.

3.3.1 Optical simulation

The aim of the optical simulation is to calculate a spatially resolved optical generation rate $G_{\mathrm{opt}}(x)$ within a stack of layers. In order to do this ASA first requires a sequence of layers defined by the device architecture. For a generic PSC in a *p-i-n*-architecture this could be glass / PTAA (HTL) / perovskite / PCBM (ETL) / Ag. Layers are ordered starting from the direction the light is impinging from. Generally the way the incident light is coupled from one layer in the stack into another is dependent on the angle of incidence θ_0 and the complex refractive indices N_0 and N_1 of the two optical media respectively. Since we only consider cases of light entering the cell perpendicular to its surface, the angular dependencies will not be discussed here. The complex refractive index $N = n_{\mathrm{r}} - ik$ is made up of a real part n_{r}, which I will in the following refer to as the refractive index, as well as the

extinction coefficient k. When light impinges onto an optical interface of two media with differing complex refractive indices N, part of it will be reflected and part of it will be transmitted into the second medium. At normal incidence the reflectance R and the transmittance T can be calculated using the Fresnel equations

$$r = \frac{N_0 - N_1}{N_0 + N_1}, \tag{3.2a}$$

$$t = \frac{2N_0}{N_0 + N_1}. \tag{3.2b}$$

with the complex Fresnel amplitude coefficients r and t [140]. Using these coefficients the reflectance

$$R = |r|^2 = \left| \frac{N_0 - N_1}{N_0 + N_1} \right|^2 \tag{3.3}$$

and the transmittance

$$T = \left| \frac{N_1}{N_0} \right| |t|^2 = 4 \frac{|N_0 N_1|}{|N_0 + N_1|^2} \tag{3.4}$$

can be determined. The above equations are solved using *GenPro3* [141], which is part of ASA. The model takes into account reflective losses as well as interference effects arising from light being reflected at internal reflection within the device and at the rear of the device. It is possible to additionally take into account light scattering and haze effects at interfaces. These effects will not be considered in this thesis since the interfaces in the examined cells should be relatively smooth.

Once light is coupled into a layer of the solar cell stack it is absorbed. How quickly the incident light is absorbed depends on its wavelength and the absorption coefficient $\alpha(\lambda)$ of the medium. The absorption coefficient α is related to the exctinction coefficient k via $\alpha = 4\pi k/\lambda$. The approach typically used to calculate the absorption profile of photons ins the Lamber-Beer absorption formula, which assumes an exponential reduction of the photon flux ϕ dependent on the absorption coefficient α. The photon flux ϕ at a depth x within a medium is then defined as

$$\phi(x, \lambda) = \phi_0(\lambda) \exp(-\alpha(\lambda) x), \tag{3.5}$$

where ϕ_0 is the incident photon flux density at the surface of the respective medium. This reduction of photon flux ϕ can be related to the spectral generation rate

$$g(x,\lambda) = \phi_0(\lambda)\alpha(\lambda)\exp(-\alpha(\lambda)x), \tag{3.6}$$

assuming a generation of exactly one electron-hole pair per absorbed photon. Finally the optical generation rate G_{opt} relevant for the electrical simulation can be calculated by integrating the spectral generation rate via

$$G_{\mathrm{opt}}(x) = \int_0^\infty g(x,\lambda)d\lambda. \tag{3.7}$$

In summary, in order for ASA to calculate the optical generation rate G_{opt} in the layer stack, it requires a list of the layers said layer stack is comprised of, their respective thicknesses d, refractive indices $n_{\mathrm{r}}(\lambda)$ and extinction coefficients $k(\lambda)$. Additionally the spectrally resolved incoming photon flux ϕ is necessary for the calculations. Utilizing the layer thicknesses d and a user defined spacing ASA creates a spatial grid of points where both the optical and electrical calculations will be carried out. Refractive indices n_{r} and extinction coefficients k are supplied in file form. They are obtained from modelling transmittance and reflectance measurements of corresponding single layers of the applied materials with the software SCOUT [142]. Additionally the high wavelength values of the extinction coefficient k of perovskites were determined from photoluminescence measurements in order to precisely reproduce the absorption edge. The resulting optical data is shown in figure 3.7.

ASA allows for the spectrum of the incident light to be supplied in form of a file (e.g. the AM1.5g spectrum of the sun), it can also be set to a single wavelength emulating a laser beam as used in PL measurements. Analogously it is possible to omit the optical simulation altogether in favor of a user defined generation rate G. This can be supplied in form of a file or the generation rate across the electrically simulated layers can simply be set to a fixed value. The latter is useful when trying to simulate generic situations in order to understand the basic behaviour of a solar cell manufactured in a specific architecture.

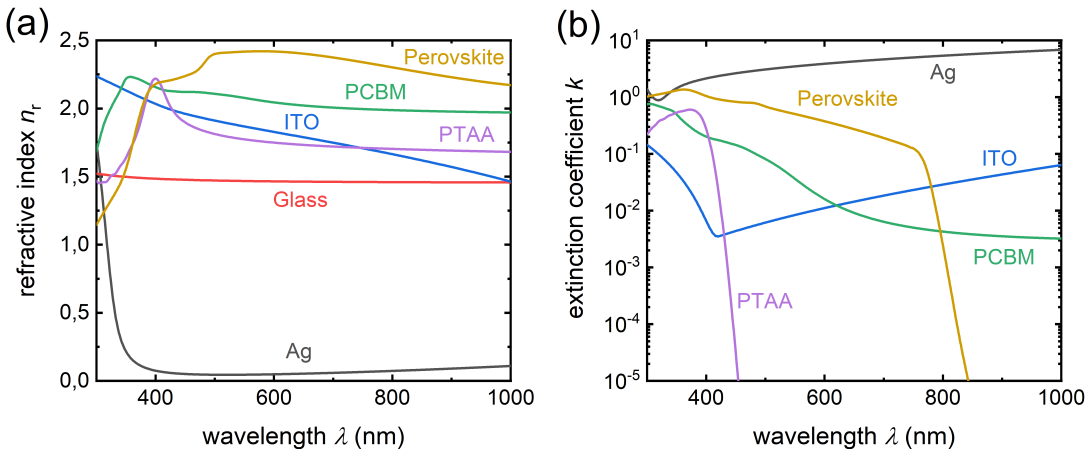

Figure 3.7: (a) Refractive index n_r and (b) extinction coefficient k as a function of wavelength λ for relevant films and materials used in the processing of the solar cells examined in this thesis as well as the simulations thereof.

3.3.2 Electrical Simulation

The theoretical basis for the electrical drift-diffusion simulations was introduced in chapter 2.4. There we derived a system of three coupled partial differential equations only dependent on the free charge carrier densities and the electrostatic potential (see equations 2.17, 2.19a and 2.19b). In order to simplify these equations we will consider the simulated layer stack in steady-state where $\frac{\partial n}{\partial t} = \frac{\partial p}{\partial t} = 0$. This turns the original set of partial differential equations into a set of ordinary differential equations given by

$$\frac{d^2\varphi}{dx^2} = -\frac{\rho}{\epsilon_0 \epsilon}, \tag{3.8a}$$

$$G - R = -D_\mathrm{n}\frac{d^2 n}{dx^2} - \mu_\mathrm{n}\frac{d}{dx}\left(\frac{d\varphi}{dx}n\right), \tag{3.8b}$$

$$G - R = -D_\mathrm{p}\frac{d^2 p}{dx^2} - \mu_\mathrm{p}\frac{d}{dx}\left(\frac{d\varphi}{dx}p\right). \tag{3.8c}$$

In order to solve the equations above suitable boundary conditions are required. In the case of the solar cells simulated in this thesis the boundaries are given by the metallic contacts at front and back. The interfaces can be represented as Schottky contacts where the position of the Fermi level depends on an effective barrier height

φ_b. The height of this barrier at the metal-semiconductor interface is given by the difference between the work function of the metal φ_m and the electron affinity of the semiconductor χ, which defines the position of the conduction band edge E_C. Therefore the boundary conditions for the Poisson equation can be defined as

$$\varphi(x=0) = -\varphi_\mathrm{b,f}, \tag{3.9a}$$

$$\varphi(x=d) = \varphi_\mathrm{b,b}, \tag{3.9b}$$

where d is the thickness of the characterized stack and $\varphi_\mathrm{b,f/b}$ are the barrier heights at the front and the back respectively. The boundary conditions for the continuity equations are defined by the surface recombination velocities of the respective charge carriers at the interfaces. They can be written as

$$J_\mathrm{n}(x=0) = qS_\mathrm{n,0}\Delta n(0), \tag{3.10a}$$

$$J_\mathrm{n}(x=d) = qS_\mathrm{n,d}\Delta n(d), \tag{3.10b}$$

$$J_\mathrm{p}(x=0) = qS_\mathrm{p,0}\Delta p(0), \tag{3.10c}$$

$$J_\mathrm{p}(x=d) = qS_\mathrm{p,d}\Delta p(d), \tag{3.10d}$$

with $\Delta n/p$ as the excess charge carrier concentration of free carriers and $S_\mathrm{n/p,0/d}$ as the surface recombination velocities of electrons and holes at the respective contacts.

With the boundary conditions introduced the mathematical problem is fully described. In order for the simulation software to deliver the equilibrium solutions for charge carrier concentrations, recombination rates or current-voltage curves it needs to be supplied with the necessary parameters.

The generic band diagram is supplied by the band gaps E_g of all simulated semiconductor layers and their respective electron affinities χ, additionally their thicknesses d were already introduced when generating the evaluation grid for the optical simulation. The effective densities of states N_V and N_C for the valence band and the conduction band respectively are necessary as well as the doping densities for acceptors N_A and donators N_D. For the boundary conditions the effective barrier heights at the contacts $\varphi_\mathrm{b,f/b}$ as well as the respective surface recombination velocities $S_\mathrm{n/p,0/d}$ have to be supplied. In order to account for recombination losses the

mobilities of charge carriers $\mu_{\mathrm{n/p}}$ and their lifetimes $\tau_{\mathrm{n/p}}$ are needed, as well as the semiconductor temperature T and the coefficient for radiative recombination k_{rad}. For the Poisson equation the relative permittivities ϵ of the employed materials are required. Finally an external series resistance R_{s} is taken into account as well as a parallel resistance R_{p}.

All of the parameters mentioned above are provided to ASA through the MATLAB framework. With them ASA is able to calculate charge carrier concentrations and currents for different voltage biases and illumination conditions. Therefore it can calculate current-voltage characteristics of the simulated layer stack both under illumination as well as in the dark. It supplies the band energies as well as the charge carrier concentrations and recombination rates spatially resolved along the x-axis perpendicular to the layer surfaces.

The charge carrier concentrations within the perovskite layer can then be used to calculate the splitting of the QFLs or the internal voltage V_{int} [97, 143]. Since at open circuit there is no current flowing the internal voltage needs to equal the external voltage or $V_{\mathrm{int}} = V_{\mathrm{ext}} = V_{\mathrm{OC}}$. For the internal voltage V_{int} at differing externally applied voltages this can be used as a reference point. Using equation 2.43 the luminescence emission fluxes can be compared and a relation for the internal voltage

$$V_{\mathrm{int}}(\phi) = \frac{k_{\mathrm{B}}T}{q} \ln\left(\frac{\phi}{\phi_{\mathrm{OC}}}\right) + V_{\mathrm{OC}} \tag{3.11}$$

can be found, with ϕ_{OC} as the luminescence flux at open circuit [144]. Note that this equation simply requires relative luminescence intensities and the open-circuit voltage V_{OC} to be measured, no calibration of the illumination flux is necessary for these calculations.

4 Interpretation of Simulated Current-Voltage and Luminescence Data

Any experimental methods applied to a solar cell are used with the intention to gain information about its behaviour or fundamental properties. Current-voltage and luminescence based measurements are some of the most basic and most frequently used characterization techniques in the field of photovoltaics. Therefore it is important to have an understanding of what information can be taken from these measurements both in isolation and in combination. The measurements discussed in this chapter can yield insight into the recombination mechanisms in the cell, the properties of the contacts and the distribution of the electric field. Especially the latter is oftentimes not well understood for thin-film solar cells. In order to interpret measurement results of the mentioned methods, simulations have been conducted for six different generic layer stacks employing the simulation software ASA. To ensure as much comparability as possible all stacks have the same thickness of 550 nm and use the same simulation parameters where possible and sensible. The parameters used for the simulations are displayed in table 4.1. For some simulations parameters deviate from the ones in the table, however this will be specified in the following illustrations of the simulated cases.

4.1 Band Diagrams of Generic Simulation Cases

Table 4.1: List of parameter values used for the ASA simulations of the six solar cell stacks presented in this chapter.

Absorber	
band gap E_g	1.6 eV
electron affinity E_A	4 eV
effective density of states CB N_C	$2 \cdot 10^{18}$ cm^{-3}
effective density of states VB N_V	$2 \cdot 10^{18}$ cm^{-3}
charge carrier mobility μ	100 cm^{2}V^{-1}s^{-1}
charge carrier lifetime τ	10^{-7} s
radiative recombination coefficient k_{rad}	$5 \cdot 10^{-11}$ cm^{3}s^{-1}
relative permittivity ϵ	30
Contact Layers (Stacks 3-6)	
band gap ETL/HTL E_g	1.8 eV
electron affinity ETL E_A	4.1 eV
electron affinity HTL E_A	3.7 eV
effective density of states CB N_C	$1 \cdot 10^{19}$ cm^{-3}
effective density of states VB N_V	$1 \cdot 10^{19}$ cm^{-3}
charge carrier mobility μ	10^{-2} cm^{2}V^{-1}s^{-1}
charge carrier lifetime τ	10^{-7} s
radiative recombination coefficient k_{rad}	$1 \cdot 10^{-12}$ cm^{3}s^{-1}
relative permittivity ϵ	3
External Parameters	
external series resistance R_s	2 Ωcm^2
parallel resistance R_p	$1 \cdot 10^{10}$ Ωcm^2
temperature T	300 K
effective barrier height front $\phi_{b,f}$	0 eV
effective barrier height back $\phi_{b,b}$	0 eV
surface recombination velocity front S_f	0 ms^{-1}
surface recombination velocity back S_b	0 ms^{-1}

1. *pn*-junction

   The *pn*-junction was briefly introduced in chapter 2.1.4 as the charge separation mechanism in crystalline silicon solar cells. The difference in thickness between crystalline silicon solar cells and PSCs is usually two to three orders of magnitude, which has to be taken into account when comparing the two. Copper indium gallium selenide (CIGS) cells also employ a similar architecture at thicknesses of a few micrometers. One way to create a *pn*-junction is to bring two layers of the same semiconductor with opposite dopants into contact. Figure 4.1 (a) shows the band diagram of such a simulated *pn*-junction solar cell in the dark at short circuit. It consists of a moderately doped 500 nm thick *p*-layer ($N_\mathrm{A} = 10^{17}$ cm^{-3}) on the left combined with a highly doped *n*-layer ($N_\mathrm{D} = 10^{19}$ cm^{-3}) with a thickness of 50 nm on the right. Note that unlike specified in table 4.1 the effective densities of states in the bands are $N_\mathrm{C} = N_\mathrm{V} = 1 \cdot 10^{19}$ cm^{-3} for this simulation. The high doping in the *n*-layer fixes the band positions and the conduction band and valence band are almost completely flat. Between the two layers the so-called space charge region (SCR) has formed. This region is depleted of charge carriers that have diffussed away from the SCR to equilibrate the spatial imbalance in charge carrier concentrations created by the dopants.

   Figure 4.1 (b) depicts the same absorber in the dark with an applied voltage. The voltage applied leads to a splitting of the QFLs and the electric field at the *pn*-junction is reduced. Figures (c) and (d) show the cell with charge carriers being created at short circuit and at the open-circuit voltage V_OC respectively. This situation emulates charge carrier generation through illumination, however the optical simulation within ASA was not used. Instead a constant generation rate $G = 2.2 \cdot 10^{21}$ cm^{-3}s^{-1} across the whole absorber was implemented in order to exclude optical effects from this basic approach. For simplicity in the following simulations with a nonzero generation rate G will still be referred to as illuminated or under illumination. At short circuit under illumination the QFLs are almost flat in large parts of the *p*-layer as well as almost all of the *n*-layer, while there are still very few charge carriers within the SCR. This means that the majority of recombination events will

take place in the field free bulk of the *n*- and *p*-layers. At open circuit the QFLs are again flat and no current is flowing.

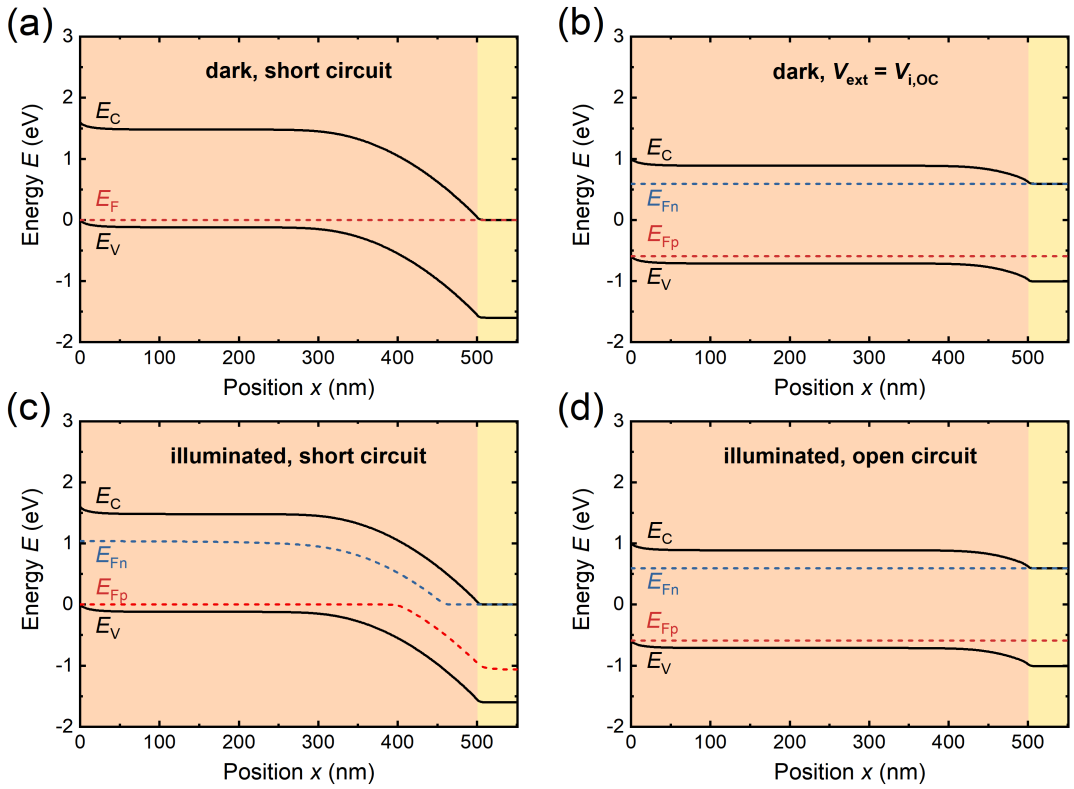

Figure 4.1: Band diagram of a simulated *pn*-type solar cell under different bias conditions. The valence band energy E_V and the conduction band energy E_C are displayed together with the QFLs for electrons E_{Fn} and holes E_{Fp} respectively. Applied bias conditions are (a) $V_{ext} = 0$ V and (b) $V_{ext} = V_{i,OC}$ for the cell in the dark as well as (c) $V_{ext} = 0$ V and (d) $V_{ext} = V_{i,OC}$ for the cell at a constant generation rate $G = 2.2 \cdot 10^{21}$ cm^{-3}s^{-1}. $V_{i,OC}$ refers to the open-circuit voltage under illumination conditions.

2. *pin*-junction

In contrast to the *pn*-junction the *pin*-junction utilizes a third intrinsic layer between two rather heavily doped layers. This kind of architecture is used in thin-film technologies such as amorphous silicon solar cells and organic solar cells. Figure 4.2 shows the band diagrams for the simulated *pin*-type solar cell. The layer stack is comprised of the undoped *i*-layer spanning 500 nm with two symmetrical contact layers at the front and the back with a thickness of 25 nm each. Both the *p*-layer and the *n*-layer are equally doped

at $N_A = N_D = 5 \cdot 10^{18}$ cm^{-3}. As was the case for the *pn*-junction, the effective densities of states in the bands are $N_C = N_V = 1 \cdot 10^{19}$ cm^{-3} for this simulation as well. Initially it is obvious, that the built-in field drops off almost entirely over the intrinsic absorber layer. Due to the high doping densities the *n*-layer and the *p*-layer have flat bands and pin the Fermi-levels of the charge carrier types supplied by their respective dopants.

Under illumination at short circuit (fig. 4.2 (c)) the majority of the charge carriers drift towards the contacts and only a small concentration of charge carriers remains in the middle of the *i*-layer. There we find an area where the QFLs are parallel to the bands and charge carrier concentration is constant. At open circuit (fig. 4.2 (d)) the field in the intrinsic layer is reduced and the bands are slightly bent due to the doped contact layers. The charge carrier concentrations across the *i*-layer are changing with the position within the absorber.

3. Symmetrical undoped contact layers

   In the above two cases we have assumed material characteristics of each layer to be equal except for its doping concentration. In perovskite solar cells and other thin film technologies, the ETL and HTL are usually not produced from the same material as the absorber and therefore have very different properties from the absorber itself. They are also not necessarily doped as mentioned in chapter 2.1.4. In this case the electric field distribution is not defined by the doping densities but by the relative permittivities ϵ of the materials involved. The simulated layer stack employs the same order of layers as the *pin*-junction but the characteristics of the *p*-layer and the *n*-layer are different. They now exhibit a higher band gap and worse transport properties (see table 4.1). Especially these weak transport properties of the transport layers are an unusual trait of some PSCs. There are also offsets of 0.1 V between the transport layers and the intrinsic absorber. The contact layers in these cells are not only different in their electrical properties but also in their absorbing characteristics. They are usually chosen with the goal to minimize parasitic absorption and therefore absorb significantly less incoming radiation generating small amounts of charge carriers. In the simulation the

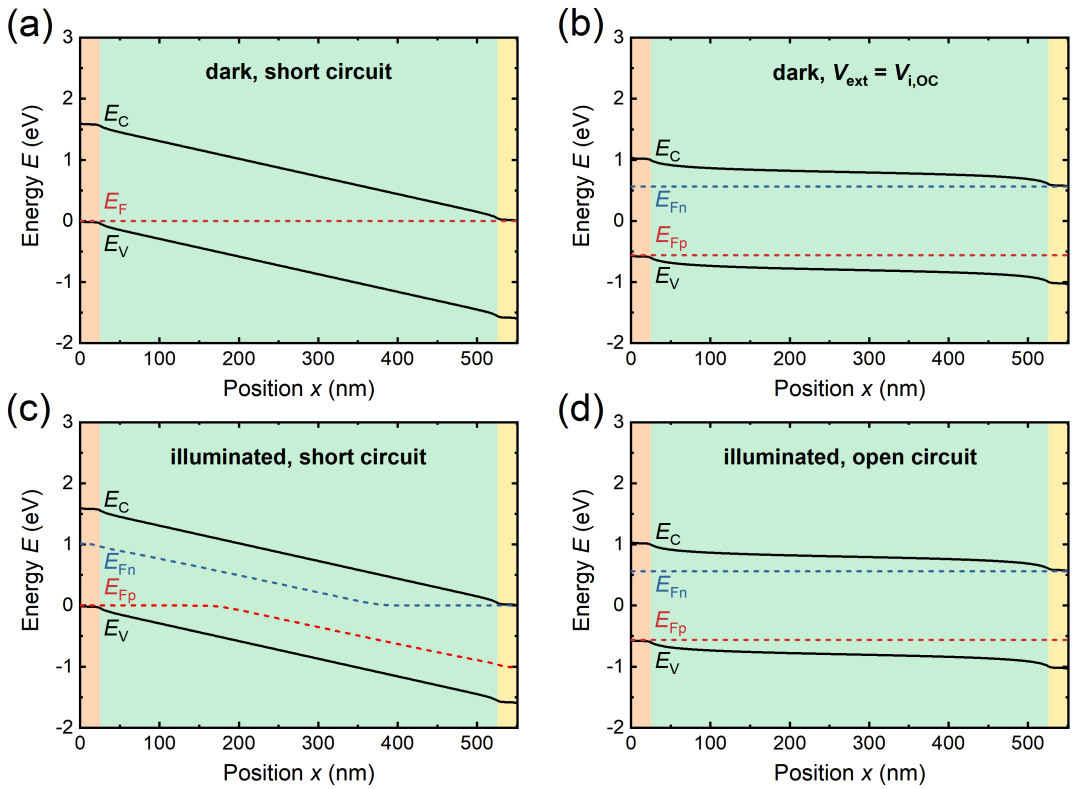

Figure 4.2: Band diagram of a simulated *pin*-type solar cell under different bias conditions. The valence band energy E_V and the conduction band energy E_C are displayed together with the QFLs for electrons E_{Fn} and holes E_{Fp} respectively. Applied bias conditions are (a) $V_{ext} = 0$ V and (b) $V_{ext} = V_{i,OC}$ for the cell in the dark as well as (c) $V_{ext} = 0$ V and (d) $V_{ext} = V_{i,OC}$ for the cell at a constant generation rate $G = 2.2 \cdot 10^{21}$ cm^{-3}s^{-1}. $V_{i,OC}$ refers to the open-circuit voltage under illumination conditions.

contact layers are idealized as generating no charge carriers at all. In order to keep short-circuit currents of all simulations comparable the generation rate $G = 2.42 \cdot 10^{21}$ cm^{-3}s^{-1} in the absorber was increased by a factor determined by the ratio of the thickness of the layer stack divided by the absorber thickness ($d_{stack}/d_{absorber} = 550$ nm$/500$ nm $= 1.1$). The resulting band diagrams are depicted in figure 4.3. Due to the relative permittivity ϵ being significantly higher in the absorber, as is the case for perovskite solar cells, a significant amount of the built-in potential drops across the transport layers. Under illumination at short circuit (fig. 4.3 (c)) majority carriers accumulate in the *p*-layer and the *n*-layer due to their inferior transport capabilities. The con-

centrations of the respective majority carriers is also slightly increased in the absorber close to the interfaces with the transport layers while the concentration of minority carriers is reduced. Aside from this effect the charge carrier concentrations across the absorber are almost equal across its entire thickness. At open circuit (fig. 4.3 (b) and (d)) all remaining electric field drops off in the transport layers and the charge carrier concentration in the absorber is more or less constant.

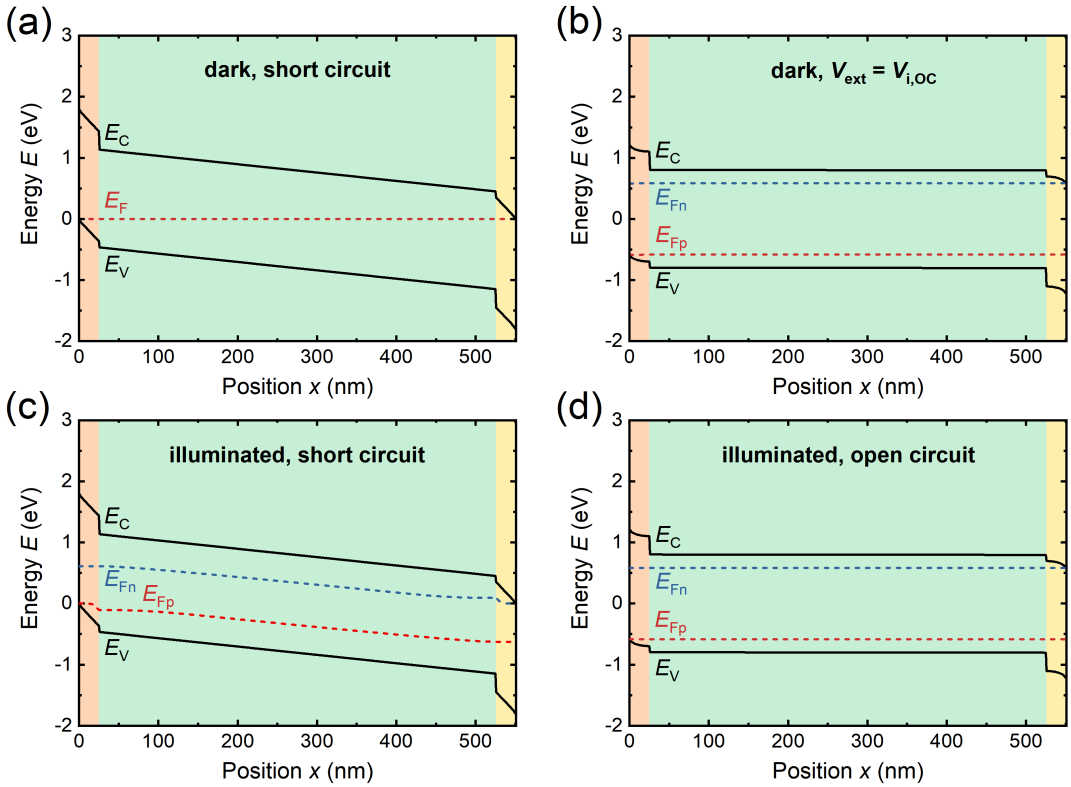

Figure 4.3: Band diagram of a simulated solar cell with a layer stack similar to a PSC with symmetrical transport layers under different bias conditions. The valence band energy E_V and the conduction band energy E_C are displayed together with the QFLs for electrons E_{Fn} and holes E_{Fp} respectively. Applied bias conditions are (a) $V_{ext} = 0$ V and (b) $V_{ext} = V_{i,OC}$ for the cell in the dark as well as (c) $V_{ext} = 0$ V and (d) $V_{ext} = V_{i,OC}$ for the cell at a constant generation rate $G = 2.2 \cdot 10^{21}$ cm^{-3}s^{-1}. $V_{i,OC}$ refers to the open-circuit voltage under illumination conditions.

4. Asymmetrical undoped contact layers

   In the PSCs examined in this thesis not only are the transport layers not

heavily doped, they are not symmetrical either. In order to illustrate the changes to the behaviour of a cell the fourth generic layer stack simulated utilizes the same parameters as the one with symmetrical undoped contact layers. The only difference is, that the 500 nm thick intrinsic absorber is bordered by a 5 nm thick p-type layer and a 45 nm thick n-type layer. As in the previous case the charge carriers are only generated in the absorber at an increased rate G for comparability. The resulting band diagrams are shown in figure 4.4. Most of the built-in potential drops across the thicker n-layer. Additionally the charge carrier concentrations in the intrinsic layer are changed significantly. Both in the dark and in the illuminated case at short circuit (fig. 4.3 (a) and (c)) the hole concentration is higher in the absorber than the concentration of electrons. At open circuit (fig. 4.3 (b) and (d)) the effect is less pronounced but still visible. Analogously to the symmetrical case discussed before the majority carrier concentrations in the transport layers are increased significantly due to their worse transport characteristics compared to the absorber. Due to the thin HTL this increased concentration extends far into the absorber at the front side, while this accumulation is reduced at the rear.

5. Symmetrical undoped contact layers with screened field

   An important property of perovskite solar cells is the movement of free ionic charges within the layer stack [85, 86]. This movement of ions can lead to the often encountered hysteretic effects during current-voltage measurements but has been detected in largely hysteresis-free cells as well. The impact of the movement of the ions is strongly tied to the speed at which the movement takes place and an equilibrium state can be reached. In the measurements conducted for this thesis I aimed to take all measurements in such a state of equilibration. As in all systems striving to equilibrate the ionic charges move along the electric field thereby reducing it. If sufficient ionic charges are present in the absorber the electric field built up in the absorber may be screened entirely. In order to simulate this electric field screening with minor effort the relative permittivity of the intrinsic absorber was increased to an arbitrarily high value ($\epsilon = 10000$) for the symmetrical case of undoped contact

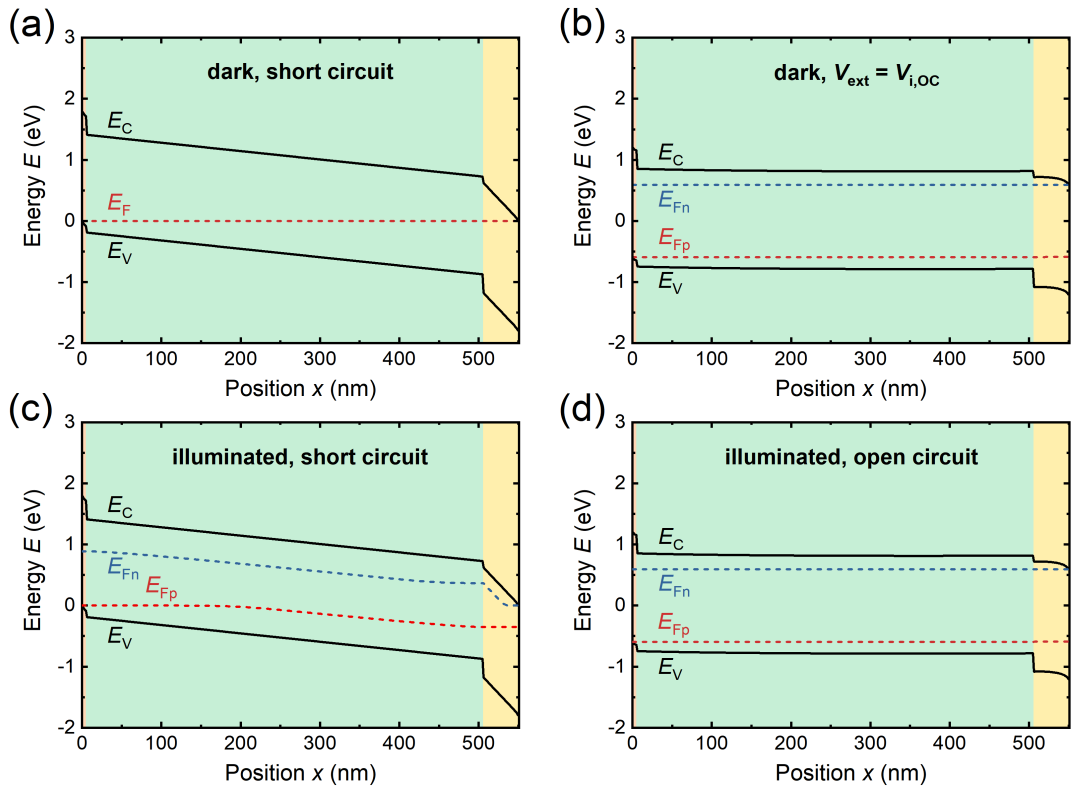

Figure 4.4: Band diagram of a simulated solar cell with a layer stack similar to a PSC with asymmetrical transport layers under different bias conditions. The valence band energy E_V and the conduction band energy E_C are displayed together with the QFLs for electrons E_{Fn} and holes E_{Fp} respectively. Applied bias conditions are (a) $V_{ext} = 0$ V and (b) $V_{ext} = V_{i,OC}$ for the cell in the dark as well as (c) $V_{ext} = 0$ V and (d) $V_{ext} = V_{i,OC}$ for the cell at a constant generation rate $G = 2.2 \cdot 10^{21}$ cm^{-3}s^{-1}. $V_{i,OC}$ refers to the open-circuit voltage under illumination conditions.

layers presented above as simulation case 3. The resulting band diagrams are shown in figure 4.5. The band diagrams behave anologously to the ones in case 3 with the exception of the electric field that is now almost completely screened from the absorber as intended. The built-in voltage drops off in equal part at the front and the back transport layer.

6. Asymmetrical undoped contact layers with screened field

   The same field screening effect that was applied to the symmetrical case is also applied to the asymmetrical architecture. The resulting band diagrams can be

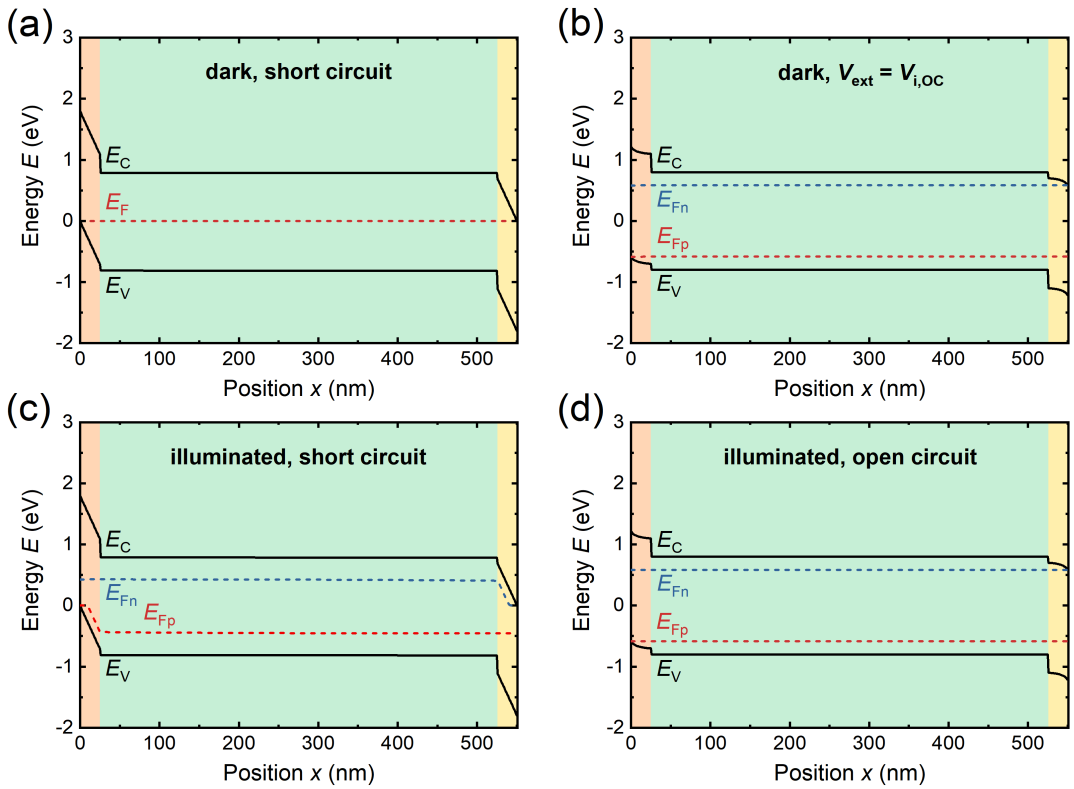

Figure 4.5: Band diagram of a simulated solar cell with a layer stack similar to a PSC with symmetrical transport layers and a screened electrical field within the absorber under different bias conditions. The valence band energy E_V and the conduction band energy E_C are displayed together with the QFLs for electrons E_{Fn} and holes E_{Fp} respectively. Applied bias conditions are (a) $V_{ext} = 0$ V and (b) $V_{ext} = V_{i,OC}$ for the cell in the dark as well as (c) $V_{ext} = 0$ V and (d) $V_{ext} = V_{i,OC}$ for the cell at a constant generation rate $G = 2.2 \cdot 10^{21}$ cm^{-3}s^{-1}. $V_{i,OC}$ refers to the open-circuit voltage under illumination conditions.

seen in figure 4.6. Here the field is also screened from the absorber and now almost exclusively drops off at the ETL. In the absorber the concentration of holes is still significantly higher both at short circuit as well as in open-circuit conditions. In figure 4.6 (c) we can see that the charge carrier concentration in the HTL is basically the same as it is in the absorber whereas it is different in the ETL. Here the concentration of holes as the minority carriers reduces from the absorber-ETL interface towards the ETL-contact interface. When the illuminated cell is at open circuit (figure 4.6 (d)), both transport layers have the same constant charge carrier densities as the absorber.

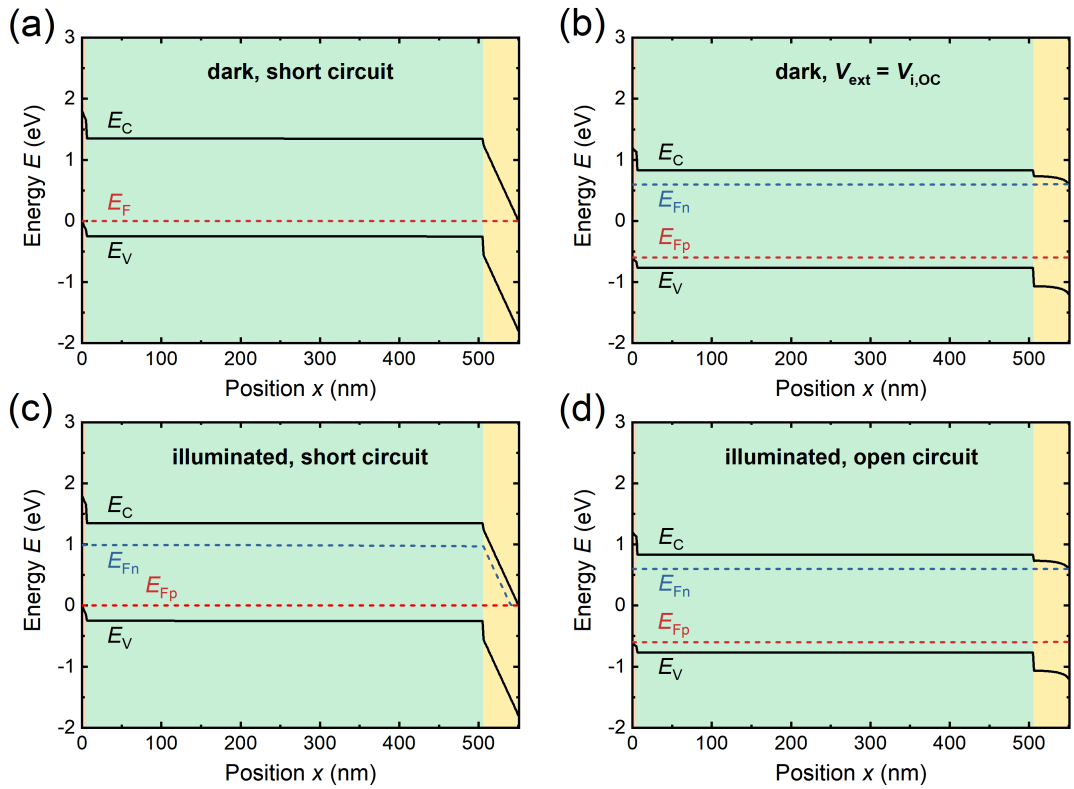

Figure 4.6: Band diagram of a simulated solar cell with a layer stack similar to a PSC with asymmetrical transport layers and a screened electrical field within the absorber under different bias conditions. The valence band energy E_V and the conduction band energy E_C are displayed together with the QFLs for electrons E_{Fn} and holes E_{Fp} respectively. Applied bias conditions are (a) $V_{ext} = 0$ V and (b) $V_{ext} = V_{i,OC}$ for the cell in the dark as well as (c) $V_{ext} = 0$ V and (d) $V_{ext} = V_{i,OC}$ for the cell at a constant generation rate $G = 2.2 \cdot 10^{21}$ cm^{-3}s^{-1}. $V_{i,OC}$ refers to the open-circuit voltage under illumination conditions.

Now I have introduced the six simulation cases that will be examined to compare their current-voltage and luminescence characteristics. In the following we will take a look at the behaviour of the measurements for these cases and what we can learn about the characteristics of such solar cells. In turn this will enable us to draw conclusions from measurement data in order to decide what the band diagram of the measured cell might look like.

4.2 The Classical Ideality Factor

Several approaches of measuring and calculating an ideality factor n_{id} of a solar cell have been introduced in chapter 2.5.7. Two of the most common ways of going about the determination of ideality factors are derived from the dark current-voltage curve or the suns-V_{OC} characteristics of a cell. First we will take a look at one of the simplest ways to access an ideality factor, the dark current-voltage characteristic of a solar cell utilizing equation 2.50. This semilogarithmic dark current-voltage characteristic is shown in figure 4.7 (a) for all six simulation cases. Most of the curves show a similar slope in the relevant region between 0.3 - 1 V with the asymmetric undoped contact case with a screened field being the obvious exception. This case and the *pn*-case also show some noise at low voltages stemming from the numerical simulations.

In order to evaluate the slope of the semilogarithmic dark current-voltage plot the dark ideality factor was calculated using equation 2.50. The result of this calculation is the voltage dependent dark ideality factor as displayed in figure 4.7 (b). For the interpretation of these dark ideality factor values it is important to understand how they are connected to recombination mechanisms and resistive effects. While table 2.1 assigns an ideality factor value to a recombination mechanism in a specific injection situation, this statement is only valid locally. The dark ideality factors shown in figure 4.7 (b) however are a superposition of the ideality factors across the entire layer stack. Since the charge carrier concentrations at the boundaries (the interfaces between transport layers and external contacts) are always in low level injection with opposite majority carrier types every ratio of n to p inbetween those LLI characteristics is represented in the layer stack as long as the bands are continuous. Step-like functions of the bands at interfaces may interrupt this continuum of charge carrier density ratios. Accordingly to the variety of these ratios, all manners of ideality factors are represented in a cell stack and the measured or simulated superposition ideality factor depends on the local recombination rates and therefore on the charge carrier concentrations. In order to better understand the behaviour of the ideality factor derived from the dark current-voltage characteristic of the simulated cells figure 4.8 shows the spatially resolved recombination rates within the layer stacks of all examined cases at 0.3 V and 1 V.

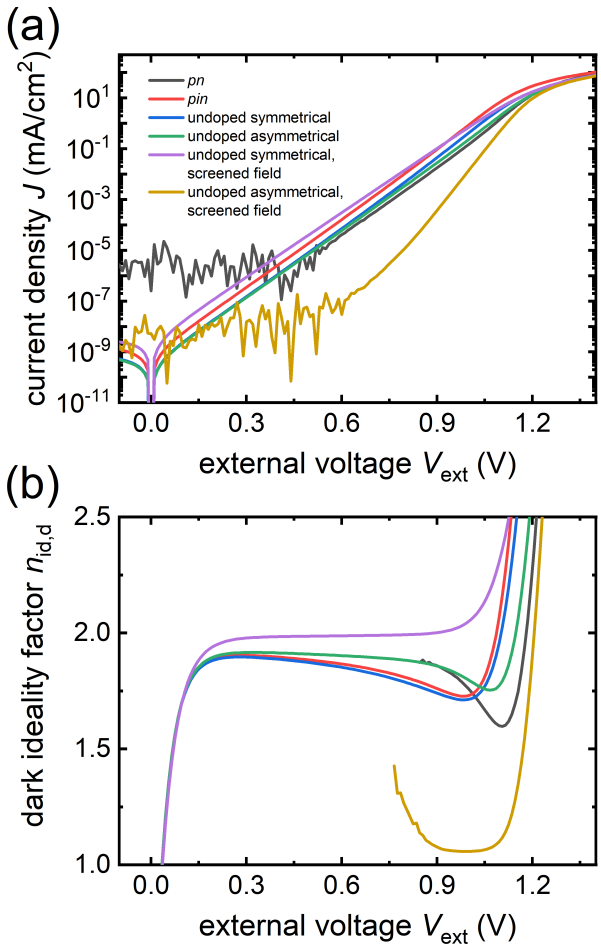

Figure 4.7: (a) Dark current-voltage curves generated from simulating generic solar cell stacks and (b) the dark ideality factor $n_{\mathrm{id,d}}$ derived from these dark current-voltage curves according to equation 2.50.

The ideality factors are similar for most simulated cases as was to be expected from examination of the dark current-voltage curves. Between 0.3 - 1 V most values are close to a value of $n_{\mathrm{id,d}} = 2$. Note that the curves for the two cases showing noisy dark current-voltage characteristics were partly masked because the noise leads to an erratic behaviour of the ideality factor data. The curve corresponding to the cell with a *pn*-junction shows a reduction of $n_{\mathrm{id,d}}$ with increasing voltage dipping to a minimum at around 1.1 V. This is due to the behaviour of a *pn*-junction often necessitating a representation of the data in a two diode model [145]. At lower voltages the recombination is dominated by the *pn*-junction fixing the ideality factor

to 2 as can be seen in figure 4.8 (a), which shows a maximum of the recombination in the junction. At higher voltages the p-doped bulk as well as the n-doped layer, where the ideality factor is closer to 1, start to gain a higher influence. Recombination per volume in the junction is still higher than the bulk but the higher thickness of the bulk enables it to significantly influence the ideality factor. In this case the effect is not very pronounced however and the superposition of the recombination only dips to an ideality factor of about 1.6. At higher voltages the series resistance R_s dominates the charge carrier losses and the ideality factors diverge, no longer yielding information about recombination processes.

The most idealized $n_\mathrm{id,d}$ curve is exhibited by the cell employing symmetrical undoped contacts with a screened electrical field. For this case over the vast majority of the absorber $n = p$ for all voltages. This means that SRH dominated recombination leads to an ideality factor of $n_\mathrm{id,d} = 2$ which is exactly what the simulation yields. Figure 4.8 (e) shows the homogeneous distribution of the recombination rate corroborating this interpretation.

The curves for the *pin*-type cell and the symmetrical cell without field screening show a similar behaviour but with a slight decrease towards higher voltages. This decrease can be attributed to the change in charge carrier distribution within the absorber of the cell. The ideality factors below 2 are again generated by the superposition of ideality factors in the center of the absorber ($n = p$, $n_\mathrm{id,d} = 2$) and towards the edges ($n > p$; $n < p$; $n_\mathrm{id,d} < 2$). As figures 4.8 (b) and (c) show, recombination is highest in the center of the absorber for both cases and at both examined voltages, yielding an ideality factor close to $n_\mathrm{id,d} = 2$. Towards higher voltages the discrepancy in recombination at the center of the absorber and towards the contacts is reduced leading to a higher influence of the latter regions on the superposition of the ideality factors and the reduction that can be seen in figure 4.7 (b).

The ideality factor curve of the asymmetrical case without field screening shows a similar trend to that exhibited by the *pn*-cell with a slight dip towards higher voltages. This happens because at lower voltages the point along the position-axis at which $n = p$ can still be found within the absorber yielding an ideality factor of $n_\mathrm{id,d} = 2$. In figure 4.8(d) this point corresponds to the maximum in the red curve. With increased voltage this point is driven out of the absorber with bands flattening.

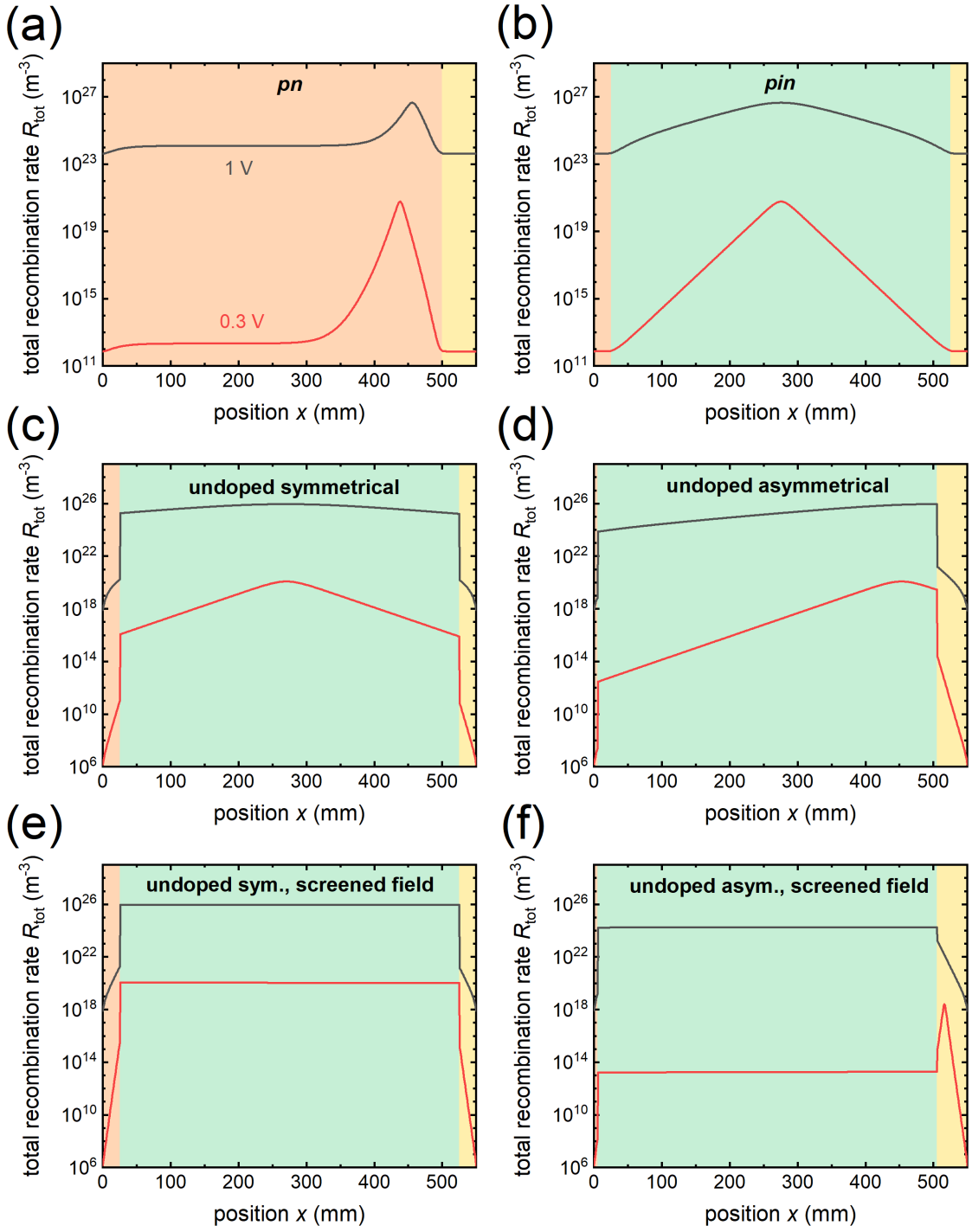

Figure 4.8: Spatially resolved total recombination rates R_{tot} at 0.3 V (red curves) and at 1 V (grey curves) for the simulations of (a) a *pn*-type solar cell, (b) a *pin*-type solar cell, (c) a cell employing symmetric undoped contacts, (d) a cell employing asymmetric undoped contacts, (e) a cell employing symmetric undoped contacts with a screened field in the absorber and (f) a cell employing asymmetric undoped contacts with a screened field in the absorber.

It is actually lost in the step-like function at the interface between the absorber and the HTL. Therefore at higher voltages we have $n < p$ in all of the bulk as well as a higher influence of the absorber region closer to the ETL with higher charge carrier asymmetries, reducing the ideality factor.

The most striking deviation in ideality factor can be seen for the last case with asymmetric contacts and a screened field. This situation leads to an ideality factor that is almost $n_{\mathrm{id,d}} = 1$ between 0.8 - 1.1 V. Looking at the band diagrams in figure 4.6, we can see that for all voltages the hole concentration in the absorber is higher than the concentration of electrons. Accordingly the ideality factor stemming from SRH recombination is around 1 (see table 2.1). In figure 4.8 (f) we see that this configuration shows by far the lowest recombination rates in the absorber of all considered cases. This is the case due to the low level injection state of the bulk reducing recombination. The recombination maximum is actually situated in the ETL, even though its band gap is larger than the band gap of the absorber. The maximum point again marks the position where $n = p$, it was driven out of the absorber due to the screening of the field. This is why the dark ideality factor of this cell is closer to 2 at lower voltages even if it is only indicated in figure 4.7 (b) by the increase from 0.9 V towards lower voltages before the data is cut off. With increased voltage, recombination in the absorber regains its dominance, pinning the ideality factor to a value close to 1 due to the asymmetry in charge carrier densities.

As mentioned in chapter 2.5.7 the ideality factor derived from the dark current-voltage characteristic of a cell suffers from the influences of resistive losses. This is the case because a current induced by the applied voltage is flowing in the cell, which is influenced by both the series resistance R_{s} and the parallel resistance R_{p}. A better solution to measure - or in this case simulate - the ideality factor is to derive it from cell parameters taken at open circuit. Since under these conditions no net current is flowing, resistive effects are eliminated. In order to determine this ideality factor, the open-circuit voltage V_{OC} is taken as a function of illumination flux ϕ (for the simulations the generation rate G is varied) and then the results are evaluated using equation 2.51. This method yields the same results as taking the photoluminescence flux ϕ_{PL} of a cell at open circuit for varying incident illumination fluxes ϕ and calculating $n_{\mathrm{id,PL}}$ using equation 2.53. The resulting open-circuit ideality factors

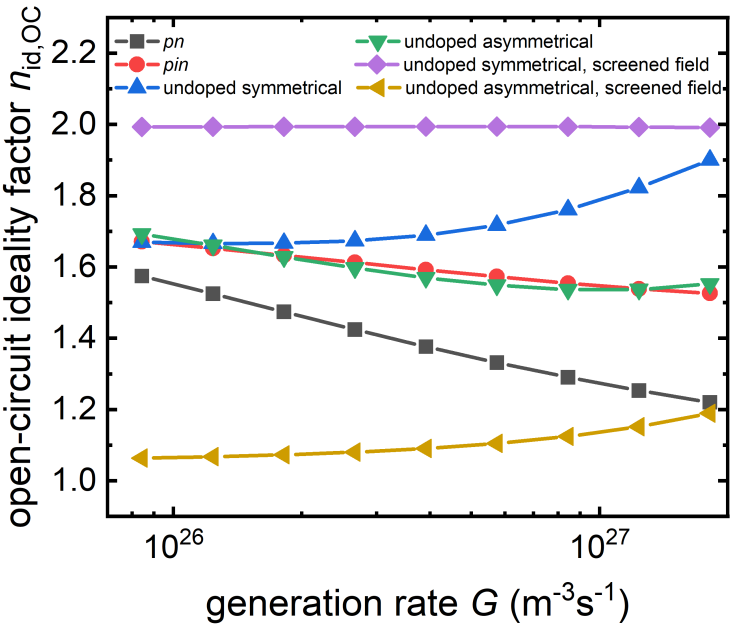

Figure 4.9: Ideality factor $n_{\mathrm{id,OC}}$ at open-circuit conditions calculated from generic solar cell stack simulations for varying generation rates G.

$n_{\mathrm{id,OC}}$ are shown in figure 4.9. Unlike the curves shown in figure 4.7 (b) the open-circuit ideality factor $n_{\mathrm{id,OC}}$ is not depicted as a function of the externally applied voltage but as a function of the generation rate G. For moderately high values such as those chosen here, this generation rate G is proportional to the illumination intensity ϕ impinging on a real solar cell.

When comparing the values of the open-circuit ideality factor $n_{\mathrm{id,OC}}$ to those determined from the dark current-voltage curves whe see similar trends. In order to interpret them I again visualized the spatially resolved recombination rates as can be seen in figure 4.10. This time the cells were under illumination with variable generation rates that correspond to the data points shown in figure 4.9 (grey lines). The highest value for the open-circuit ideality factor still corresponds to the symmetrically contacted cell with a screened electric field. It does not matter how many charge carriers are generated, the carrier concentration in the absorber will be equal for electrons and holes and therefore the open-circuit ideality factor is constant as well. In figure 4.10 (e) we see that the recombination rate is homogeneous across

the absorber for all illumination intensities.

The same architecture without a screened electric field exhibits slightly lower values for $n_{\mathrm{id,OC}}$, which is caused by the electric field across the absorber. This electric field leads to asymmetries in electron and hole concentrations across the absorber which increase towards the contacts. The more charge carriers are created, the higher the V_{OC} becomes, flattening the bands in the absorber. Therefore the open-circuit ideality factor increases with the generation rate G as the charge carrier concentrations in the absorber trend towards a situation where $n = p$. The flattening of the bands leads to a homogenization of the recombination rates, which can be seen in figure 4.10 (c).

The *pin*-type cell shows a similar band diagram to the case of undoped symmetrical contacts. However, here the highly doped contact layers pin the QFLs and keep the bands in the absorber from fully flattening as they do for the undoped contacts. Therefore the asymmetry in charge carrier concentrations is more pronounced and lower values for the open-circuit ideality factor are achieved. Additionally, for the *pin*-cell recombination also takes place within the transport layers, even though it is limited by the concentration of minority carriers. In figure 4.10 (b) we see that recombination at open circuit is dominated by the center of the bulk absorber where $n = p$. With increasing generation rate G the recombination bias towards this central area of the cell is reduced with the contacts and the bulk adjacent to them gaining more relevance. This leads to the gradual reduction of $n_{\mathrm{id,OC}}$ that can be observed in figure 4.9 (b).

The curve for the cell with asymmetrical undoped contacts without field screening shows similar values to the *pin*-type cell. It does however exhibit two competing trends, first leading to a reduction of $n_{\mathrm{id,OC}}$ at lower generation rates and then to a slight increase towards higher values of G. The initial reduction can again be attributed to the region of the absorber in proximity to the HTL. Here the discrepancy in charge carrier densities is highest, leading to both a low open-circuit ideality factor and lower recombination rates. With increasing illumination intensity, more minority carriers are introduced into this region of the cell increasing its impact on the open-circuit ideality factor which is in turn reduced. The increase in recombination towards the HTL can be witnessed in figure 4.10 (d). Finally with higher

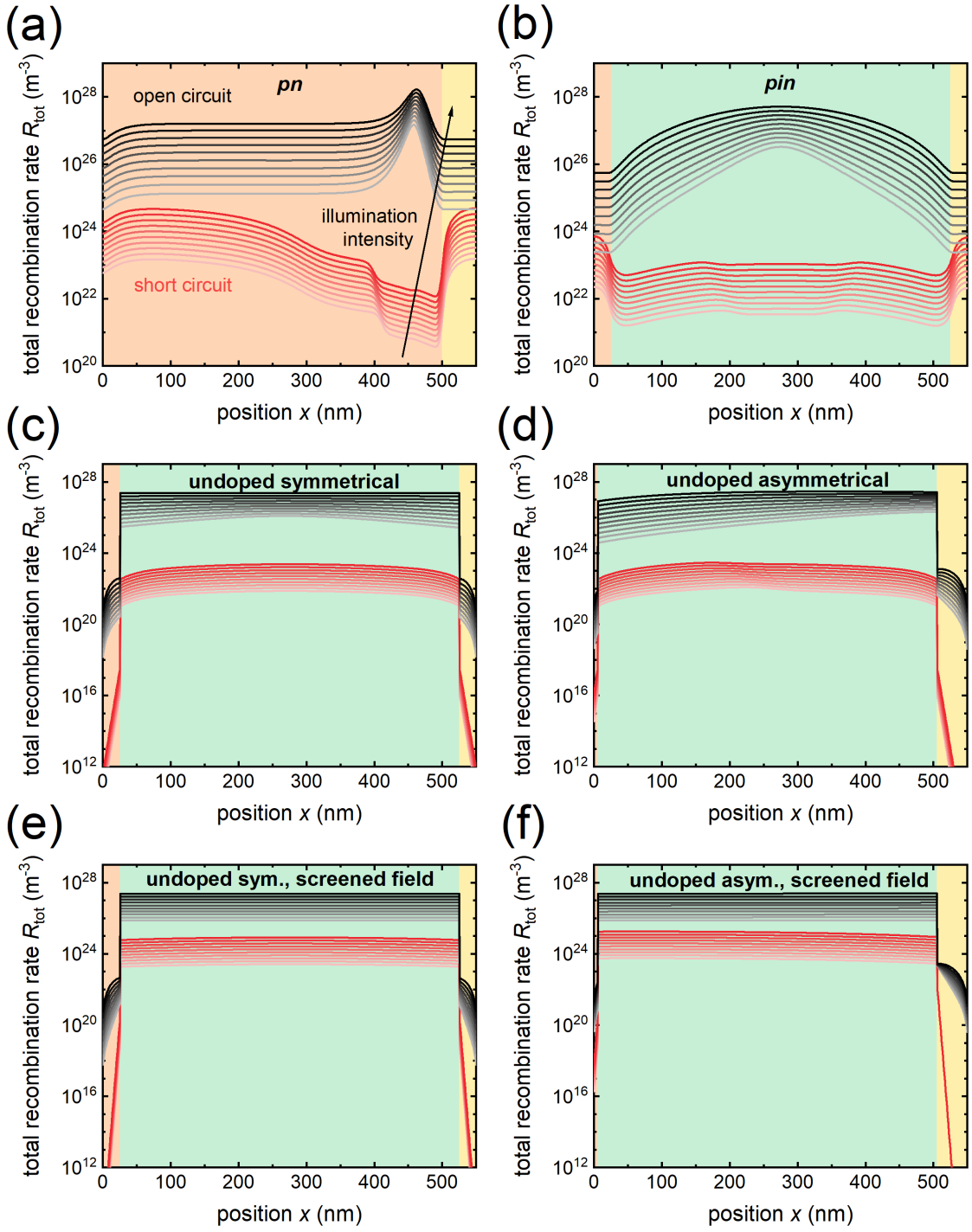

Figure 4.10: Spatially resolved total recombination rates R_{tot} under illumination at short circuit (red curves) and at open circuit (grey curves) for the simulations of (a) a *pn*-type solar cell, (b) a *pin*-type solar cell, (c) a cell employing symmetric undoped contacts, (d) a cell employing asymmetric undoped contacts, (e) a cell employing symmetric undoped contacts with a screened field in the absorber and (f) a cell employing asymmetric undoped contacts with a screened field in the absorber. Recombination rates are displayed for logarithmically varied generation rates G as indicated in panel (a), corresponding to the data shown in figure 4.9.

illumination intensities or generation rates the inequality of carrier concentrations is reduced in the entire absorber, slightly increasing the open-circuit ideality factor towards higher values of G.

One of the strongest trends in $n_{\mathrm{id,OC}}$ can be observed for the *pn*-type solar cell with the ideality factor at open circuit reducing from 1.6 to 1.2 across the simulated generation rate variation. This can again be attributed to the two competing recombination centers, the *p*-doped bulk and the junction. For lower illumination intensities - analogously to the lower voltages in the dark current-voltage curves - recombination in the junction is dominant which yields an open-circuit ideality factor closer to 2. However, even at the lower end of the simulated generation rates, the bulk already has a significant impact on $n_{\mathrm{id,OC}}$. Towards higher generation rates recombination in the bulk is increased as can be seen in figure 4.10 (a), leading to a further reduction in the open-circuit ideality factor.

Finally, the cell with asymmetrical undoped contacts and a screened field across the absorber yields the lowest $n_{\mathrm{id,OC}}$. At all generation rates the bands in the absorber are flat and figure 4.10 (f) shows that recombination rates in the absorber are spatially unvaried. Since the asymmetrical contact layers caused a situation where $n < p$ across the absorber the open-circuit ideality factor is close to 1. It slightly increases with the generation rate G as the asymmetry in charge carrier concentrations is reduced.

The ideality factors determined from the slope of the dark current voltage as well as the dependency of the open-circuit voltage V_{OC} on illumination intensity ϕ were discussed in combination in this chapter and summed up as 'classical' ideality factors. In order to understand the similarities and discrepancies between the two, the results shown in figures 4.7 (b) and 4.9 were combined in figure 4.11 for comparison. It is evident that for all cases shown the ideality factors are similar at lower voltages but diverge towards higher values. This is the case because unlike the ideality factors taken at open circuit, the dark ideality factors are calculated with a current flowing in the cell. Since the simulations employ an external series resistance R_{s} this reduces the extracted current influencing the slope of the dark current-voltage curve and subsequently increasing the ideality factor derived from this slope. Thus the external series resistance R_{s} causes the divergence of the ideal-

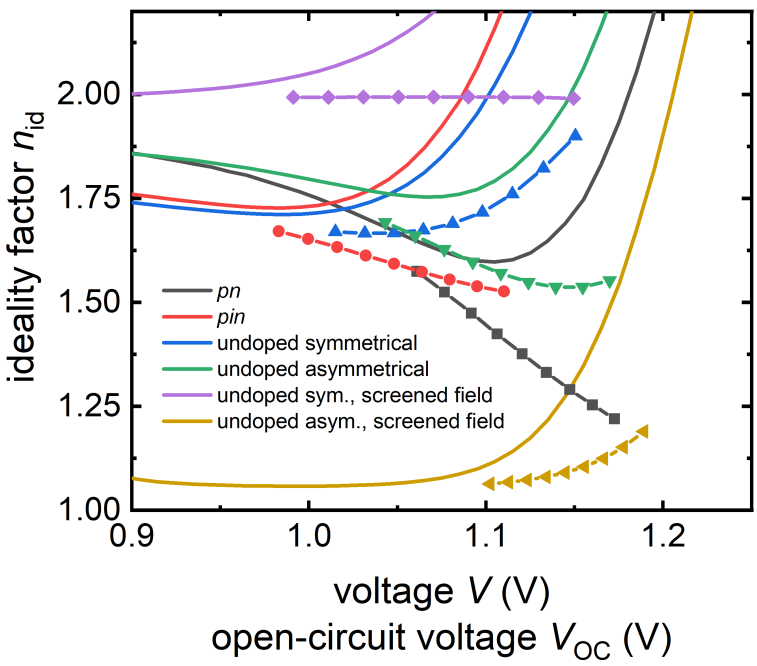

Figure 4.11: Ideality factors derived from dark current voltage characteristics ($n_{id,d}$, solid lines) in comparison to ideality factors at open-circuit conditions for varying generation rates G ($n_{id,OC}$, lines with symbols) calculated from generic solar cell stack simulations.

ity factor $n_{id,d}$ taken from the dark current-voltage characteristic towards infinity as can be observed in figure 4.11. If we remove the series resistance R_s from the simulations this influence is gone and the curves for both methods of determining the ideality factor are congruent. The respective curves were not added to the figure for clarity. This comparison underlines the validity of both methods for calculation of the ideality factor and the necessity to understand where they can be applied. Additionally the advantage of the determination of the ideality factor without current flow in the cell is confirmed.

4.3 Ideality Factor at Short Circuit

Analysis of the ideality factor from dark current-voltage curves or suns-V_{OC} measurements has been mentioned as fairly standard procedure. Something that is not usually considered is the dependency of charge carrier accumulation within a solar

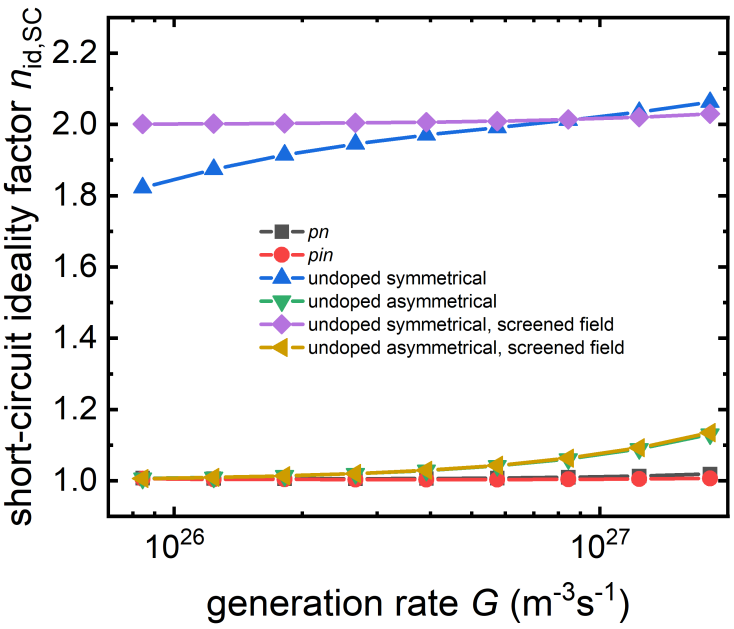

Figure 4.12: Ideality Factor at short-circuit conditions calculated from generic solar cell stack simulations for varying generation rates G.

cell with varied illumination intensity, especially at short circuit. This dependency can grant insights into the distribution of the electric field as well as the charge carrier distribution within a cell at short circuit. In this thesis I will define a short-circuit ideality factor $n_{\mathrm{id,SC}}$ via equation 2.53, or more specifically

$$n_{\mathrm{id,SC}} = \frac{q}{k_{\mathrm{B}}T}\frac{dV_{\mathrm{int,0}}}{d\ln(\phi)}. \tag{4.1}$$

It is determined from the change in luminescence intensity and the resulting internal voltage at short circuit $V_{\mathrm{int,0}}$ with respect to the illumination intensity of a cell. As this ideality factor is not taken at open circuit, naturally a current will be flowing within the cell and therefore resistive effects can not be excluded. However these resistances are part of what can be examined when looking at the short-circuit ideality factor. In an idealized solar cell with no series resistance and an infinitely high charge carrier mobility-lifetime product $\mu\tau$ all charge carriers that are generated within a solar cell would be extracted as a usable current. This would mean that no charge carriers would remain in the absorber of the cell able to recombine and

contribute to a luminescence signal. If we are able to measure a luminescence signal at short circuit this means that the cell is not actually ideal and charge carriers that could not be extracted are recombining. The intensity of the luminescence signal then grants insight into the amount of charge carriers that remain in the absorber. In figure 4.12 the short-circuit ideality factor $n_{\mathrm{id,SC}}$ is plotted against the generation rate G for all investigated simulation cases. Right away it is striking to see that the values for all six cases are pinned to either one of the extrema of 1 or 2. In order to comprehend the behaviour of $n_{\mathrm{id,SC}}$ the spatially resolved recombination rates at short circuit are shown in figure 4.10 as well (red lines).

The short-circuit ideality factor of the *pn*-type cell is almost 1 due to the majority of charge carriers residing in the bulk of the *p*-type layer or in the *n*-type layer with holes and electrons as the majority carriers respectively. As figure 4.10 (a) shows these regions of the cell exhibit the highest recombination rates, dominating $n_{\mathrm{id,SC}}$. This situation is mostly unchanged with an increased generation rate G marked with only a very slight increase in short-circuit ideality factor, which can be attributed to an equilibration of the ratios of the charge carrier densities in the doped layers.

The $n_{\mathrm{id,SC}}$ for the *pin*-type cell is similarly pinned to a value of 1. At short circuit the recombination mainly takes place in the highly doped transport layers as figure 4.10 (b) shows. This pins the short-circuit ideality factor to a value of 1, it changes even less with increased generation rate than it did for the *pn*-cell.

The only cases exhibiting short-circuit ideality factors around 2 are the cells with symmetrical undoped contact layers. For the case without field screening $n_{\mathrm{id,SC}}$ is slightly lower due to charge carrier asymmetries close to the transport layers. These asymmetries also lead to the recombination rates being reduced close to the transport layers as figure 4.10 (c) shows. With higher generation rates G, charge carrier ratios trend towards high level injection ($n = p$) and the short-circuit ideality factor is increased.

For the same architecture with a screened electric field in the absorber the ideality factor is once more pinned to $n_{\mathrm{id,SC}} = 2$ due to the flat bands yielding $n = p$ across the entire absorber (see figure 4.10 (e)).

For the asymmetrically contacted cells the short-circuit ideality factor is con-

sistently close to 1, both with and without field screening. In order to understand this behaviour of the $n_{\mathrm{id,SC}}$, we take a look at the current density $J_{\mathrm{n/p}}$ of electrons and holes in the transport layers. In chapter 2.8 we derived equation 2.65 which enables us to understand $J_{\mathrm{n/p}}$ as a function of the internal voltage V_{int}, the external voltage V_{ext} and a prefactor. This prefactor is what we call the extraction current $J_{\mathrm{extr,n/p}}$ and is defined in equation 2.66. If we take equation 2.65 under short-circuit conditions it simplifies to

$$J_{\mathrm{SC}} = J_{\mathrm{extr,n}} \left[\exp\left(\frac{q V_{\mathrm{int,n}}}{k_{\mathrm{B}} T} \right) - 1 \right], \tag{4.2}$$

here $J_{\mathrm{n}} = J_{\mathrm{SC}}$ since we assume the current density through both transport layers to be equal to the current that can be externally measured at the cells contacts. This can in turn be solved to yield an expression for $V_{\mathrm{int,n}}$ at short circuit

$$V_{\mathrm{int,n}} = \frac{k_{\mathrm{B}} T}{q} \ln\left(\frac{J_{\mathrm{SC}}}{J_{\mathrm{extr,n}}} + 1 \right) \tag{4.3}$$

and subsequently according to the definition of $V_{\mathrm{int,n}}$ and $V_{\mathrm{int,p}}$ (see figure 2.23) we arrive at

$$V_{\mathrm{int}} = V_{\mathrm{int,n}} + V_{\mathrm{int,p}} = \frac{k_{\mathrm{B}} T}{q} \ln\left[\left(\frac{J_{\mathrm{SC}}}{J_{\mathrm{extr,n}}} + 1 \right) \left(\frac{J_{\mathrm{SC}}}{J_{\mathrm{extr,p}}} + 1 \right) \right]. \tag{4.4}$$

This equation can grant valuable insight into the ideality factor $n_{\mathrm{id,SC}}$ at short circuit, since it shows the dependency of V_{int} on the extraction currents $J_{\mathrm{extr,n/p}}$. From chapter 2.8 we remember that a high gradient of the QFL in a transport layer coincides with a low value for J_{extr}, while a low gradient leads to a high value. If there is a high gradient of the majority carrier QFL present in both transport layers the corresponding extraction current densities $J_{\mathrm{extr,n/p}}$ will be significantly lower than the J_{SC} term leading the latter to dominate both terms in the logarithm in equation 4.4. Since J_{SC} is linearly dependent on the illumination intensity ϕ this leads to an ideality factor at short circuit of $n_{\mathrm{id,SC}} = 2$. The ideality factor can anologously be determined depending on the configuration of QFL gradients in the transport layers, the corresponding ideality factors are listed in table 4.2.

This means that in order for the ideality factor at short circuit not to be equal

Table 4.2: Relation of the extraction current densities $J_{\mathrm{extr,n/p}}$ to the short-circuit current density J_{SC} and the resulting ideality factors at short circuit $n_{\mathrm{id,SC}}$.

$J_{\mathbf{extr,n}}$	$J_{\mathbf{extr,p}}$	$n_{\mathbf{id,SC}}$
$\ll J_{\mathrm{SC}}$	$\ll J_{\mathrm{SC}}$	2
$\gg J_{\mathrm{SC}}$	$\ll J_{\mathrm{SC}}$	1
$\ll J_{\mathrm{SC}}$	$\gg J_{\mathrm{SC}}$	1

to one of the extreme values 1 or 2, the condition $J_{\mathrm{SC}} \approx J_{\mathrm{extr}}$ has to be met for one of the contacts.

In order to test this theory the extraction current densities $J_{\mathrm{extr,n/p}}$ at both transport layers have been evaluated as a function of the external voltage V_{ext} for all four cases employing undoped transport layers. This was done for generation rates G corresponding to 1 sun and 0.1 sun illumination. The resulting curves can be seen in figure 4.13. The curves for the two evaluated generation rates G only differ very slightly from one another (changes in the third to fourth significant digit) and can therefore not be discerned in the graphs. In all panels the grey and red curves relate to the extraction current density of the electrons at the ETL ($J_{\mathrm{extr,n}}$) and of the holes at the HTL ($J_{\mathrm{extr,p}}$), respectively. The extraction current densities were calculated in two different ways. The solid lines depict the result of resolving equation 2.65 for J_{extr} and calculating it as a function of $V_{\mathrm{int,n/p}}$ and $J_{\mathrm{n/p}}$ (which as stated above is assumed to be equal to J_{SC}). The dashed lines are the result of calculating $J_{\mathrm{extr,n/p}}$ from equation 2.66 in dependency of the potential difference between the edges of the transport layers. In all graphs shown in figure 4.13 we see that the results for both calculations are very similar at low to medium voltages but slightly diverge towards higher voltages. This is the case because at higher voltages the assumption of flat bands in the transport layers from chapter 2.8 no longer holds. Aside from that however, the model developed in chapter 2.8 describes the simulation data very well. Note that all curves were simulated with the same parameters as introduced in section 4.1 except for the external series resistance R_{s} which was set to zero. With inclusion of the series resistance the model would still hold up well but the solid curves would be slightly shifted upwards at low to medium voltages as J_{SC} would be reduced by a small margin.

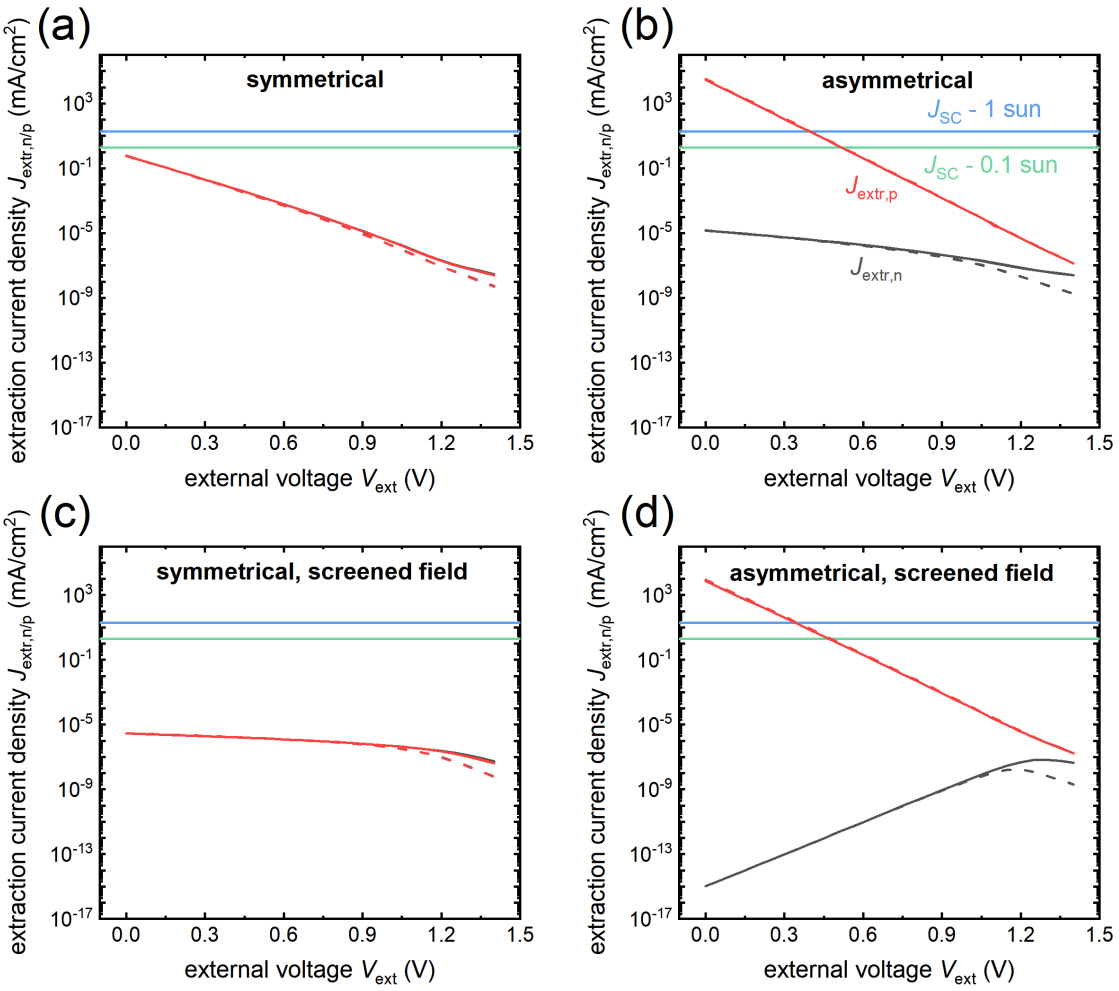

Figure 4.13: Extraction current densities calculated for the simulations of solar cells employing undoped transport layers with (a) symmetrical transport layers, (b) asymmetrical transport layers, (c) symmetrical transport layers and field screening and (d) asymmetrical transport layers and field screening. The extraction current density $J_{\mathrm{extr,n}}$ for electrons across the ETL is shown in grey and the extraction current density $J_{\mathrm{extr,p}}$ for holes across the HTL is displayed in red. Current densities calculated according to equation 2.65 and equation 2.66 are displayed by solid lines and dashed lines respectively. The simulations were conducted at generation rates G corresponding to 1 sun and 0.1 sun illumination. Since for both values of G the results are nearly identical, they can not be distinguished in the figures. The short-circuit current densities J_{SC} for 1 sun and 0.1 sun are shown for reference in blue and green respectively.

In the symmetrical case, both with and without field screening, the extraction current densities are equal at both contacts (figure 4.13 (a) and (c)). Slight deviations at high voltages are caused by numerical errors in the simulation. The field-screened case exhibits considerably lower values for J_{extr} caused by the increased field in the transport layers. For the asymmetrical case the curves deviate significantly with $J_{\mathrm{extr,n}}$ showing lower values than $J_{\mathrm{extr,p}}$ as was to be expected due to the distribution of the electric field and the gradient of the QFLs in the ETL (figure 4.13 (b) and (d)). With field screening the values are significantly decreased for the ETL that now sees the majority of the electric field within the cell. The curve for the HTL however is mostly unchanged.

We are now able to put these results into context with the short-circuit ideality factor $n_{\mathrm{id,SC}}$ and use them to interpret the values seen for both the symmetrically and the asymmetrically contacted cells. We simply need to take a look at the values for $J_{\mathrm{extr,n/p}}$ at short circuit and apply the rules from table 4.2. The first case of the symmetric cell is actually the most interesting as at short circuit it exhibits the value closest to J_{SC} ($J_{\mathrm{extr,n/p}}(0\ \mathrm{V}) \approx 0.6\ \mathrm{mA/cm^2}$). This is lower than both values of J_{SC} displayed in figure 4.13 (a) and leads to an ideality factor close to 2 which corroborates the results from figure 4.12. The value is however close enough to J_{SC} that changes of the illumination intensity ϕ will cause $n_{\mathrm{id,SC}}$ to change as well (see figure 4.12). This is not the case because the values for J_{extr} are changing (as mentioned above, these changes are insignificant), but because at lower illumination intensities J_{SC} is reduced moving closer to the short-circuit value of J_{extr}. For the symmetric case with a screened field $J_{\mathrm{extr,n/p}}$ is considerably smaller with several orders of magnitude between J_{extr} at short circuit and J_{SC}, pinning the ideality factor to 2 and showing no dependency on the generation rate G.

The asymmetric case however yields a value of J_{extr} significantly larger than J_{SC} at the HTL and one significantly smaller at the ETL. This is the case both with and without field screening and pins the ideality factor at 1, which is again in agreement with the curves in figure 4.12. With higher generation rate G, J_{SC} is increased reducing the gap to the extraction current density at the HTL which leads to the slight increase observed for $n_{\mathrm{id,SC}}$ in figure 4.12. This is the case for both cells with and without field screening in the absorber. The slightly lower $J_{\mathrm{extr,p}}$

value at short circuit for the cell with a screened field accordingly leads to a higher $n_{\mathrm{id,SC}}$. Overall the short-circuit ideality factor of the idealized simulations shows much clearer trends towards values of either 1 or 2 than the open-circuit ideality factor does. This can be understood by applying our new model, which we can use to demonstrate the rather specific conditions that have to be met by a thin-film solar cell in order to exhibit a short-circuit ideality factor between the two extremes. The values for J_{extr} have to be close to J_{SC} for both contact layers, which for our simulations was only the case for our perfectly symmetrical architectures without doping.

4.4 Voltage Dependent Behaviour of Current and Luminescence Data

So far we have mostly considered the ideality factor, determined from the data gathered through simulations. However there is also a lot of information to be gained by looking at the voltage dependent behaviour of this data, both for the current under illumination as well as the luminescence. Both of these aspects will be examined in the following.

4.4.1 Illuminated Current-Voltage Characteristics

Possibly the centerpiece of photovoltaic efficiency screening of a solar cell is the illuminated current-voltage curve. As introduced in chapter 2.1.2 the current voltage curve allows for the determination of some of the most fundamental performance metrics of a solar cell such as the open-circuit voltage V_{OC}, the short-circuit current density J_{SC}, the maximum power density P_{max} and the fill factor FF. In figure 4.14 the illuminated current-voltage curves corresponding to the six simulation cases are displayed. Since all cells are simulated in an idealized state without significant extraction barriers, all cells yield similar current-voltage characteristics with slight deviations from each other. Since the generation rate integrated over the whole stack is the same for all simulations the J_{SC} is similar as well.

The performance metrics that were mentioned above are listed in table 4.3

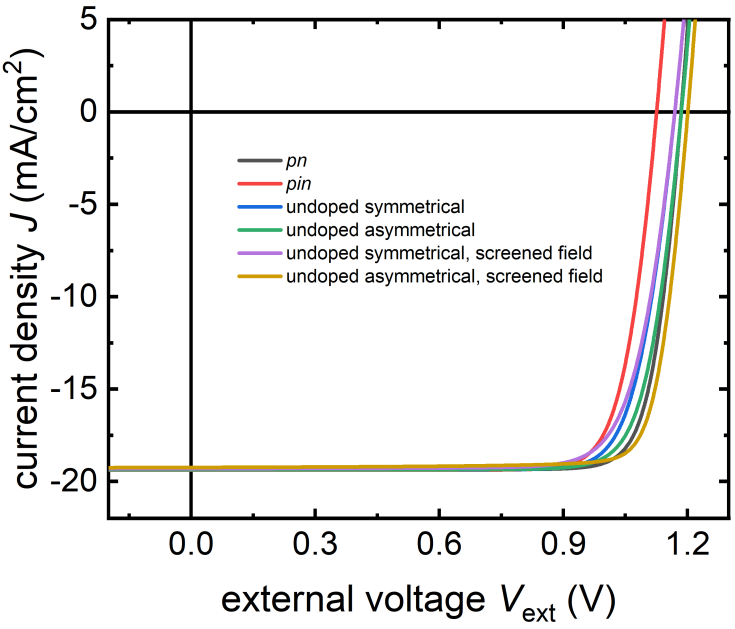

Figure 4.14: Illuminated current-voltage curves generated from simulating generic solar cell stacks in comparison to measurement data.

for each cell. At first we will take a look at the short-circuit current densities J_{SC}. While the differences are small enough to necessitate considering changes in the range of 0.01 mA/cm^2, they can still give information about the charge carrier extraction from the cell. Since I omitted an optical simulation for this chapter of the thesis and the generation rate G is constant, optical losses do not have to be taken into consideration. This means that all changes in J_{SC} stem from differing charge extraction characteristics and the resulting recombination losses. Looking at the values for J_{SC} we see that the value for the *pin*-type cell is higher than the current extracted from the *pn*-cell. While the *pn*-cell relies on the depletion region at the junction for charge separation the *pin*-cell has an electric field that extends across the entire absorber. This facilitates a more efficient separation of electrons and holes and a faster transport towards the contacts. Therefore charge carriers will be extracted quicker and are less likely to recombine, which would result in a reduction of the extracted current. In the *pn*-cell there is a large region within the *p*-type bulk that is field-free and therefore not aiding in charge carrier extraction,

Table 4.3: Characteristic values of the simulated illuminated current-voltage curves.

	$J_{\mathbf{SC}}[\frac{\mathbf{mA}}{\mathbf{cm}^2}]$	$V_{\mathbf{OC}}$ [V]	$P_{\mathbf{max}}[\frac{\mathbf{mW}}{\mathbf{cm}^2}]$	FF [%]
pn	19.37	1.18	19.2	83.6
pin	19.39	1.13	17.8	81.6
undoped symmetrical	19.37	1.17	18.3	80.9
undoped asymmetrical	19.37	1.19	18.7	81.6
undoped sym., screened field	19.31	1.17	17.8	78.9
undoped asym., screened field	19.24	1.20	19.4	83.9

making losses to recombination more likely.

The values for both the symmetric and the asymmetric case of undoped contact layers without electric field screening are similar to that of the *pn*-type cell and lower than that of the *pin*-cell. It has to be taken into account however, that the generation profile is somewhat different (no generation in the transport layers but increased generation in the absorber to facilitate an equal amount of total generation) so these values are not entirely comparable. In comparison to the *pin* simulation the electric field in the absorber is lower but the transport layers now contain some of this drop off of the electric potential. Additionally the charge carrier mobilities μ in the transport layers are significantly lower hindering charge carrier extraction. Overall these conditions lead to a slight decrease in J_{SC} compared to the *pin*-case. Between the symmetric and the asymmetric case almost no differences in J_{SC} can be observed.

However, significantly lower values for the J_{SC} are found for the same simulations introducing the field screening in the absorber. J_{SC} is reduced by 0.06 mA/cm^2 in the symmetric case and by 0.13 mA/cm^2 in the asymmetric case. The reductions can be explained by a combination of the bad transport properties of the ETL and HTL as well as the flat bands in the absorber. Charge carriers are no longer drifting towards the respective contacts they are supposed to be extracted at and are therefore accumulating and recombining within the absorber, thus reducing J_{SC}. The effect is more pronounced for the cell employing asymmetric contact layers because in the equilibrated state of the cell fewer holes are situated in the thin hole transport layer and instead remain within the absorber. This increases

the equilibrium charge carrier concentration within the absorber leading to higher recombination losses and subsequently a reduced J_{SC}. Note that the concentration of electrons in the absorber is largely unchanged in comparison to the symmetric case with the amount being extracted limited by the charge carrier mobility in the electron transport layer.

While the changes in short-circuit current density are rather small and can hardly be seen by eye in figure 4.14, the differences in open-circuit voltage V_{OC} are a lot more striking. Here we can observe the opposite trend that was exhibited by the J_{SC} values in many cases. While the *pin*-type cell had the most efficient charge carrier extraction and therefore the highest short-circuit current, its V_{OC} is significantly lower than that produced by the other simulated cells. This is explained by the reduced charge carrier concentrations within the cell due to the more efficient extraction. The splitting of the QFLs that we have interpreted before as an internal voltage V_{int} of the cell sets a limit for the externally observed voltage V_{ext}. V_{int} will always be lower than V_{ext} for voltages lower than V_{OC} which is the point where both internal and external voltage are equal. Worse extraction properties of a cell signify the necessity for a higher externally applied voltage to reach the same charge carrier concentrations at the contacts as are present within the bulk. In the case of the *pin*-type cell charges are extracted from the bulk quite well and therefore only a small V_{OC} is necessary to equilibrate the QFL splitting across the device.

The *pn*-type cell has a higher QFL splitting due to charge carriers remaining in the field-free *p*-type bulk and therefore has a significantly higher V_{OC} than the *pin*-cell.

The cells with the undoped, low-mobility contact layers have to again be considered seperately due to the changed generation distribution. They show higher open-circuit voltages than the *pin*-cell and are close to the *pn*-cell at 1.17 V and 1.19 V for the symmetrical case and the asymmetrical case respectively. As mentioned in conjunction with the J_{SC} values this can be attributed to the low electric field within the absorber and the reduced charge carrier mobilities μ in the transport layers. While J_{SC} remained largely unchanged between the symmetrical and the asymmetrical simulation we do see a change here. While the extraction through the HTL is more efficient in the asymmetric case, the ETL becomes the limiting factor

requiring a higher voltage to equilibrate the QFL splitting.

Upon examination of the V_{OC} values of the field-screened simulations we see, that it remained largely unchanged in the symmetrical case whereas it increased for the asymmetrical case. The increase can once more be attributed to the reduced charge carrier extraction capabilities of the cell in the field-screened setup as mentioned above.

Finally we will have a look at the fill factors FF. The fill factors are generally quite similar and all cells exhibit values around 80 %. As was elucidated in chapter 2.3, changes in the fill factor are usually caused by resistive effects and are dependent on changes of the ideality factor. A higher ideality factor ($n_{\mathrm{id}} > 1$) relates to an increase of the recombination at the MPP which subsequently reduces V_{MPP} and FF [146, 147]. The resistances causing these effects can be twofold, either incited by an external series resistance $R_{\mathrm{s,ext}}$ caused by the contacting infrastructure or by an internal series resistance $R_{\mathrm{s,int}}$ stemming from finite mobilies of charge carriers within the absorber and transport layers. Since the external contribution to the series resistance was kept constant for all simulations (see table 4.1) any changes to the FF can be attributed to internal characteristics of the cells. Note, that the effects of small changes to the series resistance will usually only manifest itself in the illuminated current-voltage curve towards higher voltages. Therefore the changes in open-circuit voltage have a significant influence on the FF as well, making the interpretation of data more difficult. This leads to the illuminated current-voltage characteristic of the *pn*-cell exhibiting a higher FF than the *pin*-cell even though both cells have the same charge carrier mobilities μ.

4.4.2 Internal Voltage Calculated from Photoluminescence

The second set of data for which we examine the voltage dependent behaviour is the internal voltage V_{int} calculated from a potential photoluminescence signal of the simulated cells. V_{int} was determined according to equation 3.11 from the voltage dependent luminescence flux in comparison to the luminescence flux at open circuit. These luminescence fluxes are in turn dependent on the charge carrier concentrations in the absorber material (for the *pn*-case and the *pin*-case in all layers). Accordingly

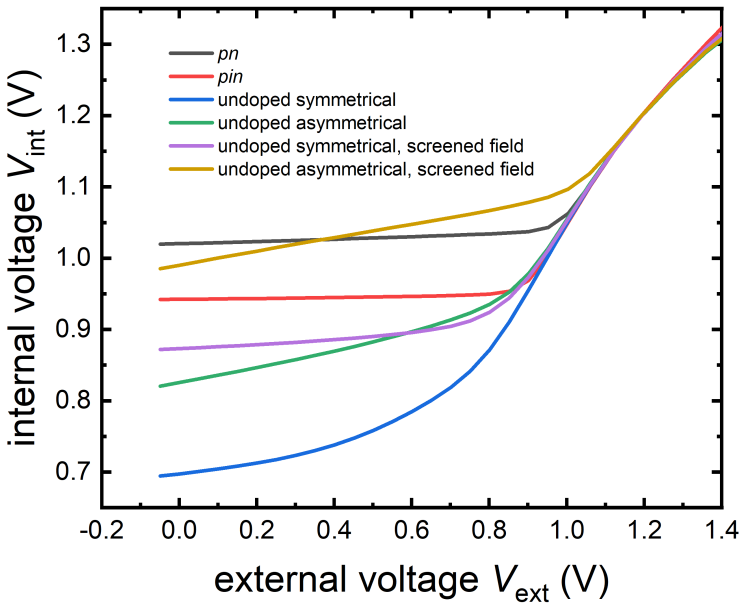

Figure 4.15: Internal voltage curves generated from simulating generic solar cell stacks in comparison to measurement data.

the internal voltage V_{int} is a measure for the concentration of unextracted charge carriers within the absorber. The behaviour of this internal voltage in dependency to the externally applied voltage V_{ext} is shown for all simulated solar cell architectures in figure 4.15.

Right away we can see that all curves show a similar trend at higher voltages since their open-circuit voltages are rather close to each other. At the same time at lower voltages both the shape of the curves as well as the absolute values show large discrepancies. It has to be noted however that even for the lowest curve an internal voltage of $V_{\text{int}} \approx 0.7$ V is left at short circuit signifying a significant amount of charge carriers remaining in the bulk of the cell.

First we will have a look at the *pn*-type cell. Remarkably the $V_{\text{int}}(V_{\text{ext}})$ characteristic for this cell is almost entirely flat for $0\ V < V_{\text{ext}} < 0.9\ V$ and only afterwards does it increase towards V_{OC}. The values for the internal voltage are also constantly higher than 1 V. This is the case because most of the charge carriers are situated in the *p*-doped bulk of the absorber dominating recombination and accordingly lu-

minescence. The charge carrier concentration in this region of the cell does not change with the applied voltage because of the flat bands caused by the doping of the material. This screens the field from the bulk of the absorber keeping charge carrier concentrations unchanged. The same applies to the highly n-doped rear of the cell. The slow increase in V_{int} in the lower voltage regime can be attributed to a slow rise in charge carrier concentration and subsequently recombination in the junction. At high voltages the junction is flattened and more charge carriers are pressed into the cell rapidly increasing V_{int}. With further increasing voltages the internal voltage will increase as well with the increase eventually being limited by the series resistance R_{s} of the cell.

The $V_{\mathrm{int}}(V_{\mathrm{ext}})$ characteristic of the *pin*-cell is rather similar to the behaviour of the *pn*-type cell but in the lower voltage regime V_{int} is reduced. The flatness of this regime can again be explained by highly doped areas of the cell dominating recombination. In this case the p-doped and n-doped regions at the front and the back respectively are facilitating this behaviour. The doping again screens the externally applied field keeping recombination, luminescence and internal-voltage mostly constant. The gradual change in V_{int} is attributed to the slowly increasing charge-carrier concentrations in the intrinsic bulk layer also indicated by the resulting increase in recombination. The overall reduced V_{int} value can be explained by the smaller spatial dimensions of the parts of the cell dominating recombination. At higher voltages again more charge carriers are forced into the cell finally increasing V_{int} once more.

For the cells employing undoped contact layers and no field screening, a different situation presents itself. Regions dominating recombination are not as clear-cut as in the previous two cases and rather subject to change with respect to the applied voltage. In order to understand these changes, especially at lower voltages, band diagrams and charge-carrier concentrations are shown in figure 4.16. Panel (a) shows the band diagrams for the symmetrical case without field screening for external voltages varied between $V_{\mathrm{ext}} = 0\ \mathrm{V} - 0.6\ \mathrm{V}$. The corresponding charge-carrier concentrations across the cell are shown in panel (b). In figure 4.10 (c) we saw that for this case recombination is almost homogeneous across the absorber and slightly reduced towards the interfaces with the transport layers due to diverging densities

of electrons and holes. When applied, the external voltage reduces the field in the absorber (see figure 4.16 (a)), slowing charge carrier extraction and therefore increases V_{int}. This can be seen in the corresponding curve in figure 4.15 as well, the internal voltage shows a clear increase with V_{ext}. In the beginning at lower external voltages this increase is not as steep. Here the reduction of the electric field in the absorber and the transport layers exacerbates the accumulation of charge carriers at the interfaces (see figure 4.16 (b)). The accumulation on both sides increases and extends further into the bulk, leading to a faster increase in V_{int}. Eventually the accumulation region extends across the entire absorber and a further increase in external voltage increases charge carrier concentrations across the entire thickness of the absorber. At higher voltages the curve behaves the same as the two discussed before.

Taking a look at the the symmetrical case with a screened field in the absorber, we see that the screening of the field has a significant impact on the shape of the $V_{\mathrm{int}}(V_{\mathrm{ext}})$ curve. The V_{int} value at short circuit is significantly increased with respect to the cell without field screening and the slope at low voltages is reduced considerably. Since the electric field is screened from the absorber and into the transport layers, charge carriers are removed less efficiently. As shown in figure 4.16 (d) this leaves more of them in the absorber at short circuit. Since the permittivity was increased in the absorber, a change in the external voltage does not significantly change the field in the absorber. This is supposed to emulate the effect of ionic charges redistributing and thereby keeping the absorber field-free. Since the field in the absorber does not change significantly, the increase in V_{int} is slowed as well. The increase that can be seen in the curve stems from the decrease of the field within the transport layers displayed in figure 4.16 (c), further reducing charge carrier extraction. Most of the newly unextracted charge carriers however accumulate in the transport layers which is why V_{int} is only slowly increasing.

In the asymmetric case without field screening, a higher amount of charge carriers as compared to the symmetrical cell remains in the bulk increasing luminescence and V_{int}. This can also be seen in the $V_{\mathrm{int}}(V_{\mathrm{ext}})$ characteristic as the internal voltage at short circuit is increased with respect to the symmetrical case. In this cell recombination is dominated by the increased density of charge carriers towards

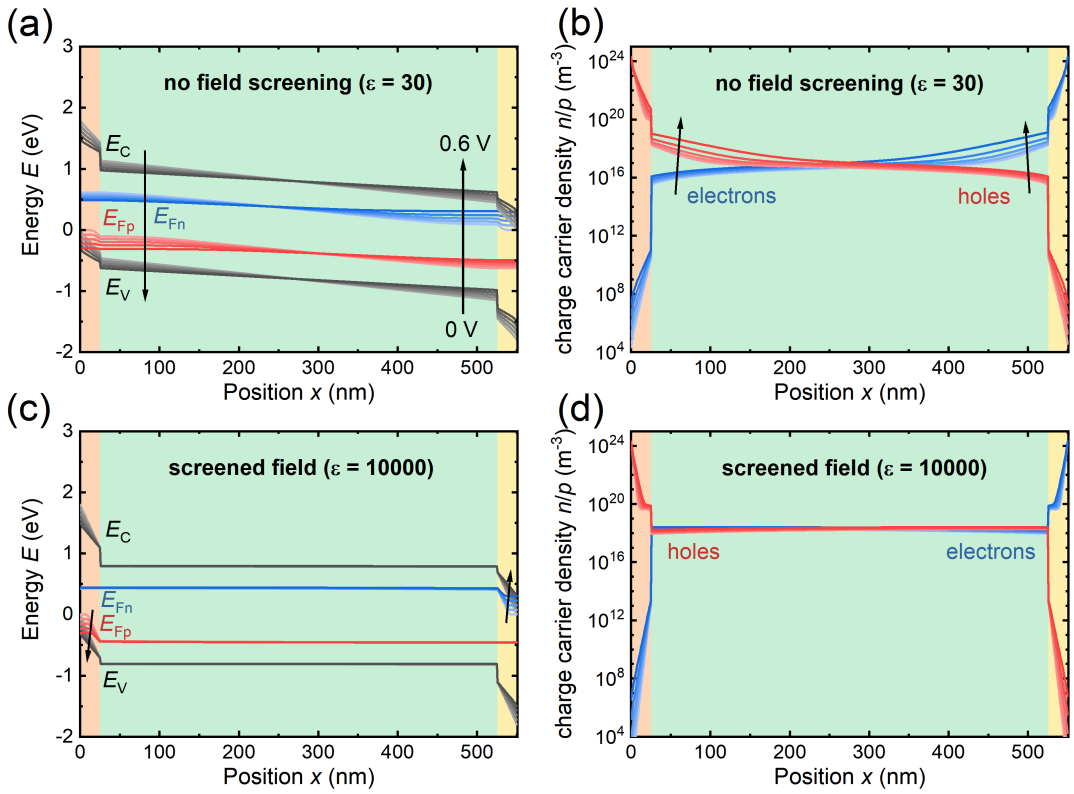

Figure 4.16: (a) Band diagrams and (b) charge-carrier concentrations in a simulated cell employing symmetric undoped transport layers and no field screening. All data is shown for externally applied voltages $V_{\mathrm{ext}} = 0\ \mathrm{V} - 0.6\ \mathrm{V}$ with lighter colors corresponding to lower voltages. (c) Band diagrams and (d) charge-carrier concentrations for the same cell architecture with field screening in the absorber. The external voltage is varied anologously.

the HTL at the front (see figure 4.17 (b)). This accumulation of charge carriers is again exacerbated by an applied external voltage dominating the anologous effect at the ETL on the other side of the device. The increase in V_{int} with respect to V_{ext} is rather linear, comparable to that observed for the *pn*-cell and the *pin*-cell. This is the case because the accumulation region dominates recombination (see figure 4.10 (d)) and therefore the internal voltage. The slope of the $V_{\mathrm{int}}(V_{\mathrm{ext}})$ curve is increased in comparison to the *pn*-cell and the *pin*-cell, because the charge carrier concentration in the region dominating recombination is influenced more strongly by V_{ext} than the doped semiconductors are. This is also corroborated by the overall reduced level of V_{int}. In summary, the increase of V_{int} is dominated by the increase

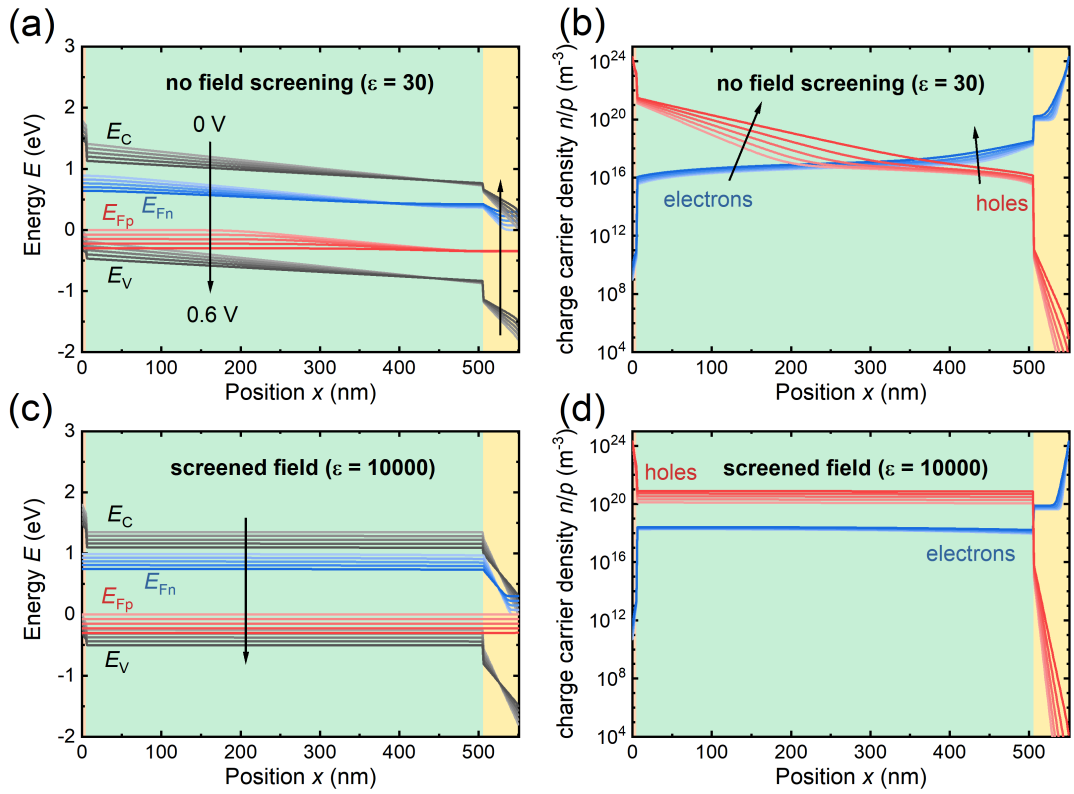

Figure 4.17: (a) Band diagrams and (b) charge-carrier concentrations in a simulated cell employing asymmetric undoped transport layers and no field screening. All data is shown for externally applied voltages $V_{\text{ext}} = 0\ \text{V} - 0.6\ \text{V}$ with lighter colors corresponding to lower voltages. (c) Band diagrams and (d) charge-carrier concentrations for the same cell architecture with field screening in the absorber. The external voltage is varied anologously.

in charge carrier concentration at the HTL interface, resulting in the shape of the curve seen in figure 4.15.

In the asymmetric case with field screening, the initial V_{int} value at short circuit is increased by a similar margin with respect to the unscreened cell as was the case for the symmetrical simulations. The increase with V_{ext} however is just as steep as it was without a screening of the electric field. This is the case because while the amount of electrons within the absorber only increases minimally with V_{ext}, the concentration of holes is increased drastically (see figure 4.17 (d)). In the symmetric simulation including field screening, additional unextracted charge carriers would reside in the transport layers. In the asymmetric cell this is only the case for the

electrons (see figure 4.17 (c)), whereas the holes are pushed into the absorber since the HTL is so thin. This way V_{int} keeps increasing linearly with V_{ext} even with a screened electric field within the absorber.

4.5 Conclusion

In this chapter we have looked at a number of different basic characterization methods used to evaluate solar cells of varying types and functionalities. I have presented simulations of different solar cell stacks and gave insight into the behaviour of the resulting measurement data with respect to the cell archetypes. For each of the measurements and data evaluations some cells were exhibiting similar results while others were distinctly different. It is usually not possible to use a single measurement technique in order to specify the band diagram or the electric field distribution of a solar cell. When all of these techniques are combined however, a more complete picture can be formed granting more detailed insights into the inner workings of an investigated cell. Therefore the understanding that was gained in this chapter will be applied to measurements of real solar cells in the following chapter of this thesis and will be the foundation for their interpretation.

5 Measurements and Simulations of Voltage Dependent Luminescence Data

5.1 First Measurements and Exclusion of Error Sources

In the previous chapter we looked at simulations of the current-voltage behaviour, the ideality factors and the internal voltage V_{int} derived from voltage dependent luminescence measurements for various different thin-film solar cell architectures. In this chapter we will have a look at measurements conducted on perovskite solar cells and put them into context with simulations in an effort to form a model of the device that is able to explain all of the results. The main focus will be put onto the results of luminescence measurements with respect to illumination intensity ϕ and externally applied voltage V_{ext}. As was introduced in chapter 2.1.6, PSCs often show transient behaviour under illumination and voltage bias and the cells examined for this thesis were no exception. Therefore the measurement procedure had to be adapted to these circumstances as was already partially outlined in chapter 3.2.2.

All cells measured were previously activated by illuminated voltage sweeps. These prebiased samples were then measured in the steady-state photoluminescence setup and voltage sweeps were performed simultaneously tracking luminescence ϕ_{PL} and current density J. The luminescence spectra were evaluated as outlined in chapter 3.2.2 and the internal voltage V_{int} is calculated according to equation 3.11. Surprisingly first measurements of as-processed samples yielded an internal voltage

almost entirely constant at low voltages up to 1 V. The grey curves in figure 5.1 correspond to a measurement of a cell simply mounted in a measurement device contacting the cells and introduced into the luminescence measurement setup. This quick and simple approach left numerous possible errors that had to be ruled out in order to confidently interpret the gathered data. The first thought that springs to mind when examining the grey curves is that there may be a secondary light source impinging on the detector eclipsing the possibly significantly lower luminescence signal of a solar cell at short circuit or close to it. The source supplying this erroneous signal would have to emit in the same wavelength as the perovskite absorber as only the peak values of the luminescence spectra were evaluated in the internal voltage data. Therefore stray laser light could be ruled out and the central remaining question whether additional regions of the perovskite coated substrate the cell was situated on supplied a signal that did not originate from the cell itself. The considerations taken have been outlined before in chapter 3.2.2.4, figure 5.1 elucidates the impact the efforts taken had on the measurement data.

The sample measured consisted of four cells on a singular substrate on half of which all spincoated layers were removed by laser ablation as shown in figure 3.6. This gave me the opportunity to measure cells with and without surrounding perovskite absorber material at open circuit on a single substrate. Additionally to removing surrounding material by laser ablation a mask could be used to define the aperture of the measurement to 3×3 mm^2. In figure 5.1 external voltage sweeps of the internal voltage V_{int} are shown for the lasered cells with (blue curves) and without a mask (red curves). Dark curves relate to forward sweeps while the lighter curves represent reverse sweeps of the external voltage. We see a significant difference between the level of the internal voltage for the lasered cell as opposed to the unlasered device. Removing the surrounding perovskite led to a decrease in the luminescence signal at low to medium voltages. At high voltages the signals are similar due to higher amounts of charge carriers being introduced into the system via the externally applied voltage. The change in luminescence signal at lower voltages leads me to conclude that a portion of the signal did indeed stem from activation of the laser-ablated regions and luminescence generated outside of the cell area being coupled into the detector. When comparing the curves pertaining to the masked and unmasked measurements of the lasered cell we see an additional

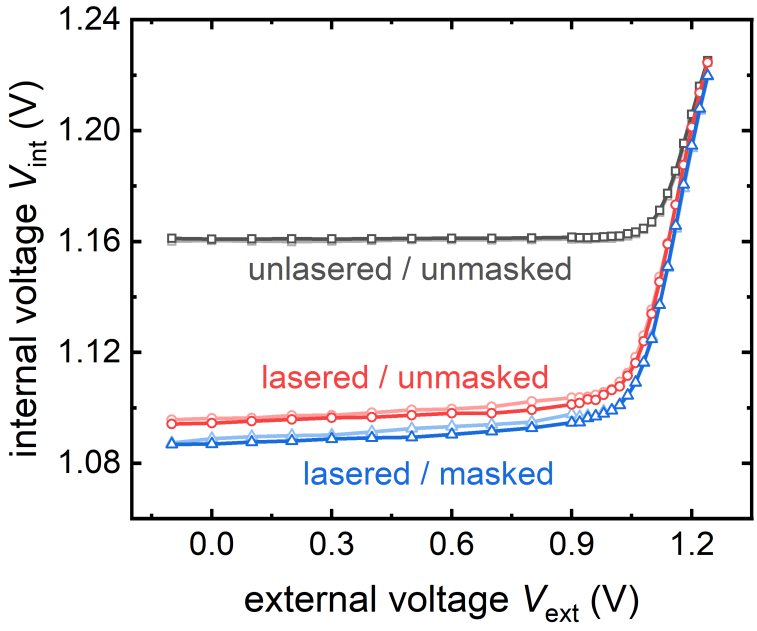

Figure 5.1: Comparison of the internal voltage in dependency on the external voltage measured under varied conditions. All measurements were carried out on cells situated on the same substrate. The data for the grey curves was taken from a cell surrounded by uncontacted perovskite and no mask was used to define the aperture of the measurement. The red and the blue curves correspond to a cell where the surrounding perovskite was removed by laser ablation with a mask applied during the measurement of the latter but not the former. Dark curves indicate voltage sweeps in forward direction, while the light curves relate to sweeps in reverse direction.

small reduction in the luminescence signal and subsequently the internal voltage V_{int}. This can be attributed to less laser light reaching the glass substrate and potentially illuminating uncontacted perovskite, especially the stripe left on the substrate for contacting of the cell. Note that cell functionality was monitored by current-voltage measurements conducted before and after the laser ablation process in order to rule out any degradation of the cell introduced in the process.

While the level of luminescence between short circuit and about 1 V did change significantly, the overall shape of the $V_{\mathrm{int}}(V_{\mathrm{ext}})$ characteristic was only slightly changed. The low-voltage regime is less flat for the lasered cell as opposed to the unlasered device but the measurements still suggest a high amount of charge carriers

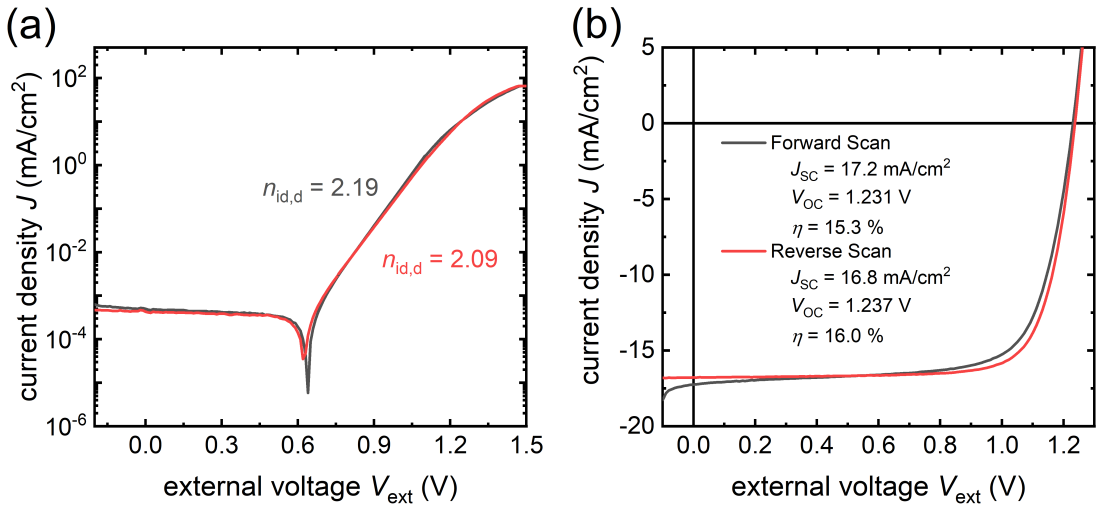

Figure 5.2: (a) Dark current-voltage curves and (b) illuminated current-voltage curves measured at a AAA solar simulator in forward (grey curve) and reverse direction (red curve). The dark ideality factor $n_{\mathrm{id,d}}$ was calculated from the slope of the linear regime of the dark current-voltage curve at 0.7-1.1 V.

remaining in the bulk of the absorber even at short circuit. The influence of lasering and masking the samples was however demonstrated and both procedures were used as standard protocol for all measurements presented in this thesis. Including the additional experiments outlined in chapter 3.2 I am able to confidently state that the values for the internal voltage V_{int} determined from the luminescence measurements stem from the cells investigated.

5.2 Interpretation of a Full Data Set

With the established measurement procedures I was able to measure a full set of current-voltage, luminescence and ideality factor data. In the following I will show one of these sets for one sample. Figure 5.2 shows the current-voltage characteristic measured at a AAA solar simulator (a) in the dark and (b) under 1 sun illumination. Both measurements were conducted in forward and reverse directions, the former is displayed in grey, while the latter is shown in red. For the dark measurements the current-voltage curves show slight differences between the sweep directions, caused by hysteretic effects. Additionally the measurements exhibit a shift of the minimum

from 0 V to over 0.6 V due to prebiasing as discussed in chapter 2.1.6. Fitting the slope of the linear regime of the curves yields a dark ideality factor of $n_{\mathrm{id,d}} = 2.19$ for the sweep in forward direction and $n_{\mathrm{id,d}} = 2.19$ for the reverse. The illuminated current-voltage curves in panel (b) show mild hysteresis as well. The characteristic values are stated in the figure. The cell was produced in a procedure similar to the one described by Liu et al. [148], the process is described in chapter 3.1.

With the current-voltage characteristics determined at the solar simulator the sample was sufficiently preconditioned to carry out the measurements at the photoluminescence setup. As described before, voltage sweeps were carried out both in forward and reverse direction at different intensities of the illuminating 532 nm laser while current density J and luminescence signal ϕ_{PL} were measured simultaneously. In order to allow for the sample to equilibrate with the conditions of each measurement and to be able to detect possible degradation taking place, six voltage sweeps were performed at each illumination intensity, alternating between reverse and forward sweeps three times each. In figure 5.3 (b) the resulting current voltage curves are shown, sweeps in forward direction are shown in dark colors while sweeps in reverse direction are shown in light colors. The measurements were conducted as indicated by the protocol shown in panel (a). All curves shown are the last ones measured at each respective illumination intensity. It is evident that the cell still exhibits moderate hysteresis comparable to the hysteresis shown at the solar simulator. Aside from that there is no apparent degradation taking place. In panel (c) the corresponding values for the internal voltage V_{int} are shown with the arrow indicating the increase in illumination intensity. Again there are two curves for each illumination intensity pertaining to a forward (dark) and reverse sweep (light). For the most part the curves for a single illumination intensity do not show large discrepancies. The differences that can be observed see the values for the internal voltage drop a little lower for the reverse sweeps. This is in agreement with the current-voltge curves as a lower internal voltage signifies less charge carriers remaining in the bulk of the cell and the reverse voltage sweeps exhibit a higher current J of extracted charge carriers. In the following only one type of curve will be examined for each illumination intensity, since the efficiency shown is slightly higher the reverse sweep data was chosen for closer evaluation.

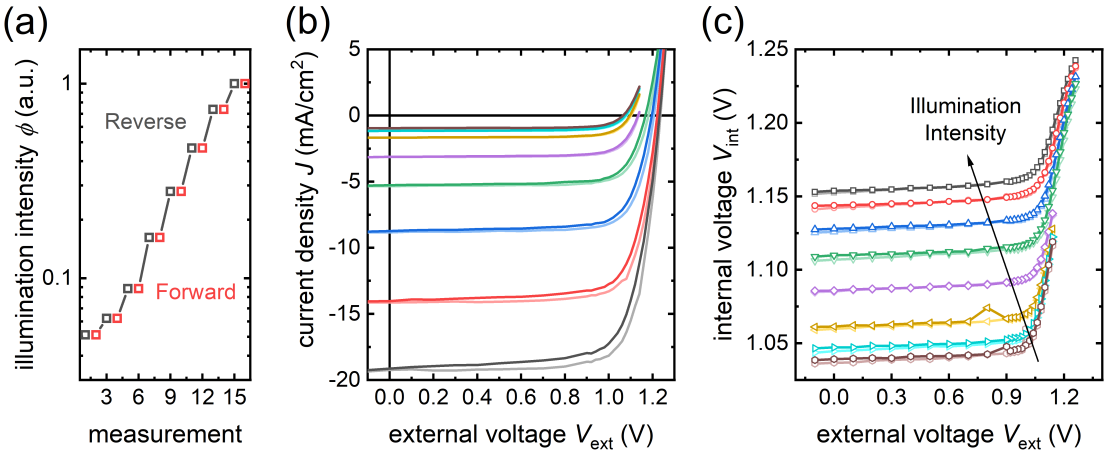

Figure 5.3: (a) Measurement chronology of data shown in panels (b) and (c). Reverse and forward voltage sweeps were measured consecutively for ascending illumination intensities ϕ. (b) Current-voltage curves measured at the photoluminescence setup under laser illumination of varied intensity simultaneously to (c) the internal voltage V_{int} determined from PL measurements as a function of the externally applied voltage V_{ext}. In both panels dark curves correspond to voltage sweeps in forward direction while light curves pertain to measurements in reverse direction.

The aformentioned six voltage sweeps at a single illumination intensity were all measured consecutively. After they were finished the setup was set to the next illumination intensity in line. In order to facilitate the strongest prebiasing of the cell at the start, the highest illumination intensity was chosen as the initial value and was subsequently reduced. This way the illumination intensity was varied from the highest value to the lowest and then back up to the highest in order to rule out any degradation effects and prebiasing errors possibly caused by the sweep direction (see chapter 2.1.6) and the significantly longer measurements times (a full set of data was acquired over a time of several hours). This chronology of the measurements in shown in figure 5.4 (a). In panel (b) the current-voltage curves are shown for the initial measurements at descending illumination intensity (dark curves) and the subsequent data at ascending laser intensity (light curves). All curves shown are the final reverse sweeps of their respective measurement set. In panel (c) the corresponding curves for the internal voltage V_{int} are displayed. In most cases both the current-voltage curves as well as the V_{int} curves show little discrepancy between the up sweep and the down sweep of the illumination intensity. The largest

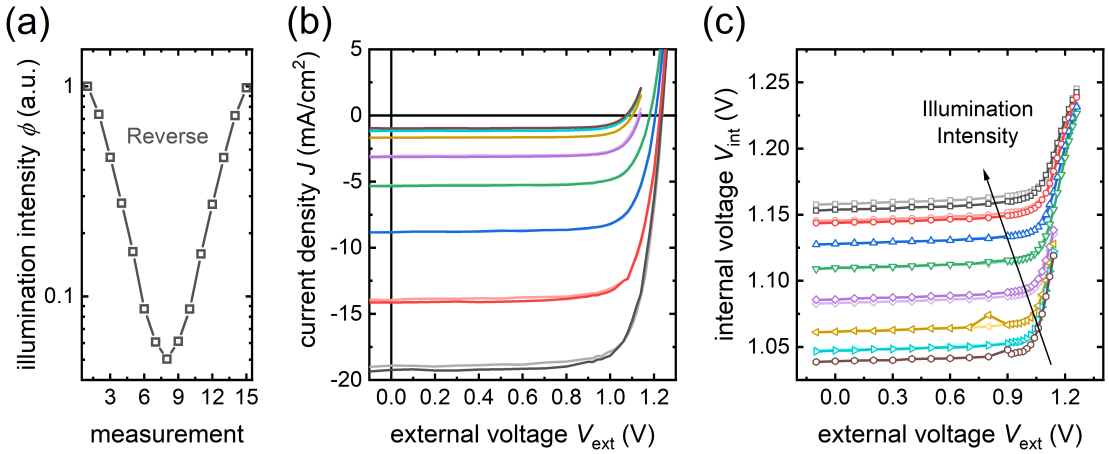

Figure 5.4: (a) Measurement chronology of data shown in panels (b) and (c). All voltage sweeps were measured in reverse direction. (b) Current-voltage curves measured at the photoluminescence setup under laser illumination of varied intensity simultaneously to (c) the internal voltage V_{int} determined from PL measurements as a function of the externally applied voltage V_{ext}. The curves were consecutively measured with descending illumination intensity ϕ (dark curves) and subsequently with ascending illumination intensity (light curves). The curve for the lowest illumination intensity ϕ was only measured once and therefore has no equivalent in a lighter color. All curves shown were measured in reverse direction.

mismatches are observed for the highest illumination intensity and to a lesser extent to the second highest intensity. This can be attributed to an insufficient activation of the cell in the first measurement cycles leading to a reduced internal voltage and accordingly to and increased short-circuit current. The same can be observed for the second highest illumination intensity. Therefore when further analyzing the data and trying to fit simulations to it, I will focus on the curves measured at ascending illumination intensity. Still these results show a remarkable stability of the cell and good reproducibility of the measured data.

From the voltage dependent luminescence data we can now analogously to chapters 4.2 and 4.3 calculate the ideality factor according to equation 2.53. In order to do this the relative illumination intensity ϕ was plotted in arbitrary units versus the internal voltage V_{int} at a certain externally applied voltage V_{ext}. The resulting graphs are shown in figure 5.5. Panel (a) shows ϕ in dependency to the internal voltage at short circuit $V_{\mathrm{int,0}}$, data points are taken from the measurements

displayed in figure 5.4 (b) and sweep from high values of ϕ to low values (grey curve) and back to the starting value (red curve). A linear fit through the values at ascending ϕ indicated by the blue line allows us to calculate the ideality factor at short circuit $n_{\mathrm{id,SC}} = 1.55$ from its slope. This result is a little surprising since we have learned in chapter 4.3 that $n_{\mathrm{id,SC}}$ is usually either very close to 1 or to 2 and only very specific conditions allow it to considerably diverge from these two extrema. This will significantly complicate the simulations attempting to recreate these measurements in the following section. There are a few peculiarities to note in the data seen here. The first thing to note is that for most illumination intensities the data points for the descending sweep of ϕ are closely matched by the data points collected during the ascending sweep. Exceptions to this rule are the two highest illumination intensities showing a considerable deviation at the highest value and a smaller, yet still visible discrepancy at the second highest value of ϕ. This matches the observations made in figure 5.4 (b), however these aberrations do not influence the calculated value of the ideality factor $n_{\mathrm{id,SC}}$ since it was only calculated for the red curve. The second peculiarity of the data is a slight step-like bend in the data between the fourth and fifth highest values for ϕ. This can be explained by a change in integration time of the measurement procedure as documented in table 3.1. Between the two data points in question the integration time was changed by a factor of 10 from 0.2 s to 2 seconds creating two regimes of measurement data. The change of integration time was necessary in order to retain a suitable signal to noise ratio for all measurements conducted, it was kept constant in the two regimes visible in order to retain optimal comparability between data sets. The effect on the data in figure 5.5 (a) was weak enough that the ideality factor $n_{\mathrm{id,SC}}$ could justifiably be determined by a linear regression of the entire data set.

In figure 5.5 (b) the illumination intensity ϕ is shown versus the open-circuit voltage V_{OC}. Here a linear regression can yield the ideality factor at open circuit $n_{\mathrm{id,OC}}$. However it is evident that the small bend that was visible in panel (a) is amplified at open circuit. The change of the integration time has a significant impact on the open-circuit voltage V_{OC}. This is unsurprising since Liu et al. have shown in a publication about PSCs similar to the one evaluated for this thesis that the open-circuit voltage shows transient behaviour reducing V_{OC}, especially in the first seconds of a measurement [148]. The same transient reduction in V_{OC} was

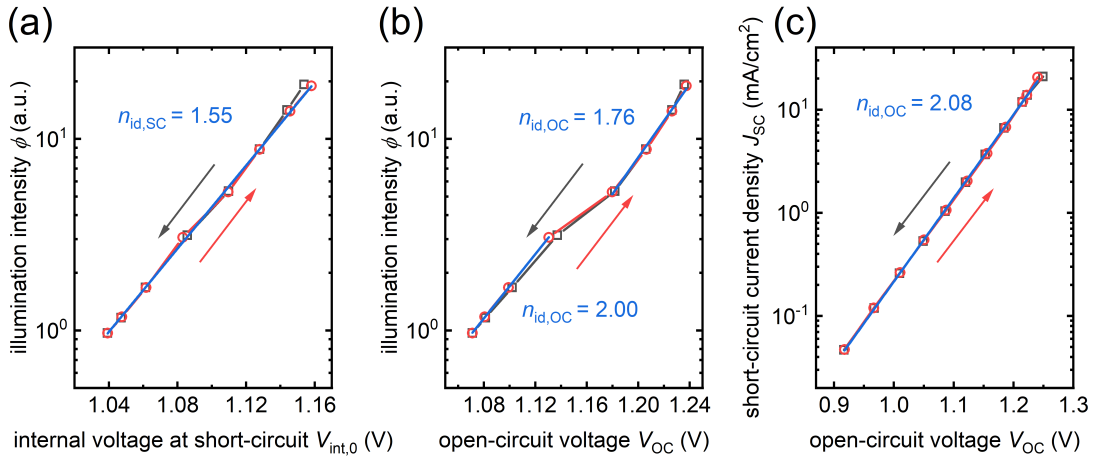

Figure 5.5: (a) Semi-logarithmic plot of the illumination intensity as a function of the corresponding internal voltage at short circuit $V_{\mathrm{int},0}$ with the short-circuit ideality factor $n_{\mathrm{id,SC}}$ as determined by the slope of the data. (b) Analogous plot versus the open-circuit voltage V_{OC} with the open-circuit ideality factor $n_{\mathrm{id,OC}}$ determined from the slope. (c) Suns-Voc data measured using a white-light LED and the open-circuit ideality factor $n_{\mathrm{id,OC}}$ taken from the slope. All data sets consist of consecutively measured sweeps of descending (grey curves) and arscending illumination intensities ϕ. Linear fits were conducted for ascending ϕ and are marked by blue lines.

reported by Calado et al. as well [116]. This is why every measurement is preceded by a 500 ms equilibration time, however this can not fully negate the effect and longer equilibration times would be both impractical and harmful to the solar cells functionality. At open circuit the bend in the data does not allow for a linear fit of all data points, the ideality factor $n_{\mathrm{id,OC}}$ was therefore determined seperately for both regimes. At low illumination intensities ϕ it is around 2.00 while higher intensities yield an ideality factor of 1.76.

Finally in figure 5.5 (c) we can see the results of a suns-V_{OC} measurement conducted using a white-light LED. Here the short-circuit current density J_{SC} is displayed as a function of the open-circuit voltage V_{OC}, exhibiting a rather linear dependency. As was the case with the data sets in panels (a) and (b) the illumination intensity was reduced from the maximum value to the minimum value and then increased back up in order to exclude any transient effects tainting the measurement results. A small activation effect can be observed for the first data point at the

maximum illumination intensity ϕ stemming from insufficient prebiasing of the cell. Aside from that we can confidently carry out a linear regression of the data, resulting in an ideality factor at open circuit of $n_{\mathrm{id,OC}} = 2.08$. This value coincides reasonably well with the results found at the photoluminescence setup.

5.3 Simulation of Measured Data Using ASA

In the previous section the measurement data was presented. In order to gain a deeper understanding of the inner workings of our solar cell we now want to find a simulation that is ideally able to explain the full data set with a single set of simulation parameters. In order to approach this task, the first step is naturally to start with what we know. The materials used in our cells were either characterized in our group or their characteristics can be found elsewhere in literature. These parameters can be used to run first simulations. In table 5.1 the parameters used for this preliminary simulation can be found in conjunction with the values found in literature and the respective publication. Note that for some of the parameters such as the densities of states for the polymer transport layers no literature values are properly documented and others, such as the electron affinity of PCBM, literature values are ambiguous and show large discrepancies. Therefore not all values are shown with a reference from literature and sensible assumptions were made.

Table 5.1: Parameter values used for a first simulation using values found in literature and determined in the work group. The used values are stated side by side with the parameters found in literature and the respective source.

Parameter	Simulation	Literature	Source
band gap E_g	1.6 eV	1.6 eV	[148]
E_A perovskite	3.83 eV	3.83 eV	[148]
N_C perovskite	$2 \cdot 10^{18}$ cm^{-3}	$2.21 \cdot 10^{18}$ cm^{-3}	[149]
N_V perovskite	$2 \cdot 10^{18}$ cm^{-3}	$2.21 \cdot 10^{18}$ cm^{-3}	[149]
μ perovskite	20 cm^{2}V^{-1}s^{-1}	20 cm^{2}V^{-1}s^{-1}	[149]
τ perovskite	10^{-5} s	10^{-5} s	[148]
k_{rad} perovskite	$5 \cdot 10^{-11}$ cm^{3}s^{-1}	$1.4 \cdot 10^{-11} - 1.4 \cdot 10^{-10}$ cm^{3}s^{-1}	[150]
ϵ perovskite	30	33.5	[151]
E_g PCBM	2 eV	1.7 - 2.4 eV	[152, 153]
E_A PCBM	3.83 eV	3.62 - 4.3 eV	[154]
N_C PCBM	$2 \cdot 10^{19}$ cm^{-3}		
N_V PCBM	$2 \cdot 10^{19}$ cm^{-3}		
μ PCBM	10^{-3} cm^{2}V^{-1}s^{-1}	10^{-3} cm^{2}V^{-1}s^{-1}	[155]
ϵ PCBM	3	3.82	[156]
E_g PTAA	3 eV	2.97 - 3.4 eV	[157]
E_A PTAA	2.23 eV	1.8 - 2.23 eV	[157]
N_C PTAA	$2 \cdot 10^{18}$ cm^{-3}		
N_V PTAA	$2 \cdot 10^{18}$ cm^{-3}		
μ PTAA	10^{-2} cm^{2}V^{-1}s^{-1}	$10^{-3} - 10^{-2}$ cm^{2}V^{-1}s^{-1}	[158]
ϵ PTAA	3	2.5 - 4	[158]
μ interface PCBM	10^{-3} cm^{2}V^{-1}s^{-1}		
τ interface PCBM	$3 \cdot 10^{-8}$ s		
μ interface PTAA	10^{-3} cm^{2}V^{-1}s^{-1}		
τ interface PTAA	$3 \cdot 10^{-8}$ s		
R_s	2 Ωcm^2		
R_p	$5 \cdot 10^5$ Ωcm^2		
T	300 K		
$\phi_{b,f}$	0 eV		
$\phi_{b,b}$	0 eV		

The simulations conducted to fit the measurement data are similar to those shown in chapter 4, but with a few differences. The thicknesses of the layers in the simulated cell are adjusted to the layers fabricated in our laboratory, the perovskite has a thickness of 350 nm, the PCBM acting as the ETL is 40 nm thick and the PTAA acting as the HTL has a thickness of 10 nm. Additionally to these three layers of the solar cell stack there are two additional layers acting as the interfaces between the bulk perovskite and the ETL and the HTL respectively. They are each 5 nm thick and they will in the following be referred to as the PCBM interface and the PTAA interface. The band gap for the PCBM interface is equal to the difference between the valence band energy E_V of the perovskite and the conduction band energy E_C of the PCBM. Anologously the band gap for the PTAA interface is equal to the difference between the valence band energy E_V of the PTAA and the conduction band energy E_C of the bulk perovskite. This setup for the interface layers means that in accordance with equation 2.31 a misalignment of the bands between the bulk and the transport layers leads to a reduction of the interface band gap subsequently increasing interface recombination. These two additional layers allow to consider interface recombination in the simulation.

In contrast to the simulations in chapter 4 there is no constant generation rate G within the absorber but the optical simulation introduced in chapter 3.3.1 is used. The simulations utilizes monochromatic laser illumination with a wavelength of 532 nm like the laser used in the photoluminescence setup. For the optical simulations the interfaces are treated belonging to the perovskite absorber.

With this adapted method of simulating our perovskite solar cells and taking into account characteristic values close to those found in literature or in-house measurements, the simulations were conducted. The first goal was to closely match the current-voltage behaviour both in the dark as well as under illumination and additionally the corresponding ideality factor at open circuit $n_\mathrm{id,OC}$. Figure 5.6 shows the band diagrams of the simulation using the values in table 5.1. Panels (a) and (b) show the band diagrams in the dark at 0 V and V_OC respectively, panels (c) and (d) show the band diagrams under the highest simulated illumination und the same biases. We see that the realistic value for the permittivity $\epsilon = 30$ in the perovskite leaves the field in the absorber unscreened and at short circuit the QFLs are not

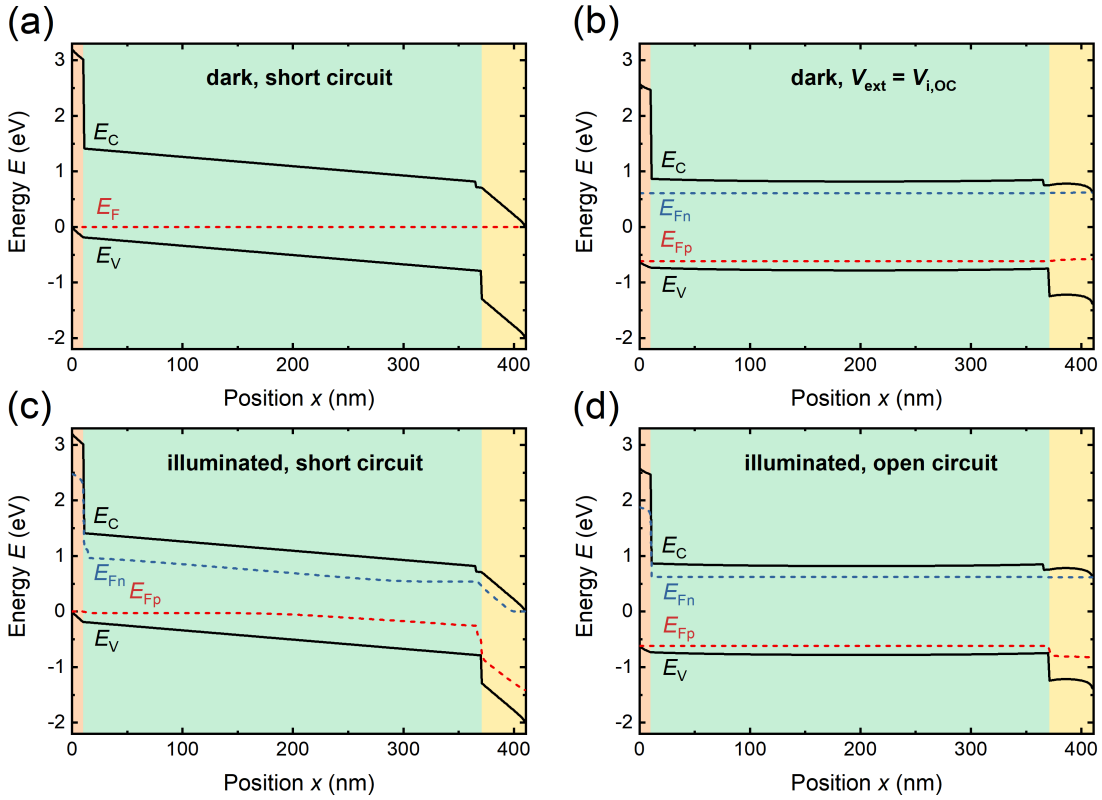

Figure 5.6: Band diagram of a simulated cell mostly utilizing parameters found in literature. The valence band energy E_V and the conduction band energy E_C are displayed together with the QFLs for electrons E_{Fn} and holes E_{Fp} respectively. Applied bias conditions are (a) $V_{ext} = 0$ V and (b) $V_{ext} = V_{i,OC}$ for the cell in the dark as well as (c) $V_{ext} = 0$ V and (d) $V_{ext} = V_{i,OC}$ for the cell under illumination by 532 nm laser light. $V_{i,OC}$ refers to the open-circuit voltage under illumination conditions. Illumination intensity is the highest value investigated in this chapter.

parallel and their splitting varies across the absorber.

In figure 5.7 we now see the results of the simulation in comparison to the measurement data, for each measurement type the measurements are indicated by symbols, while the simulations is shown as solid lines. In panel (a) we see the dark current-voltage characteristic, the shift of the measurement data as explained in chapter 2.1.6 is striking. Since the simulation does not take ionic movement into account this shift was not reproduced by the simulation, the slope and the resulting ideality factor $n_{id,d}$ however close match the measurements. In panel (b) we see the illuminated current-voltage curves for the four highest illumination intensities

ϕ that were utilized for the measurements. We see that the simulations match the measured data well with respect to the short-circuit current density J_{SC}, the open-circuit voltage V_{OC}, as well as the fill factor FF.

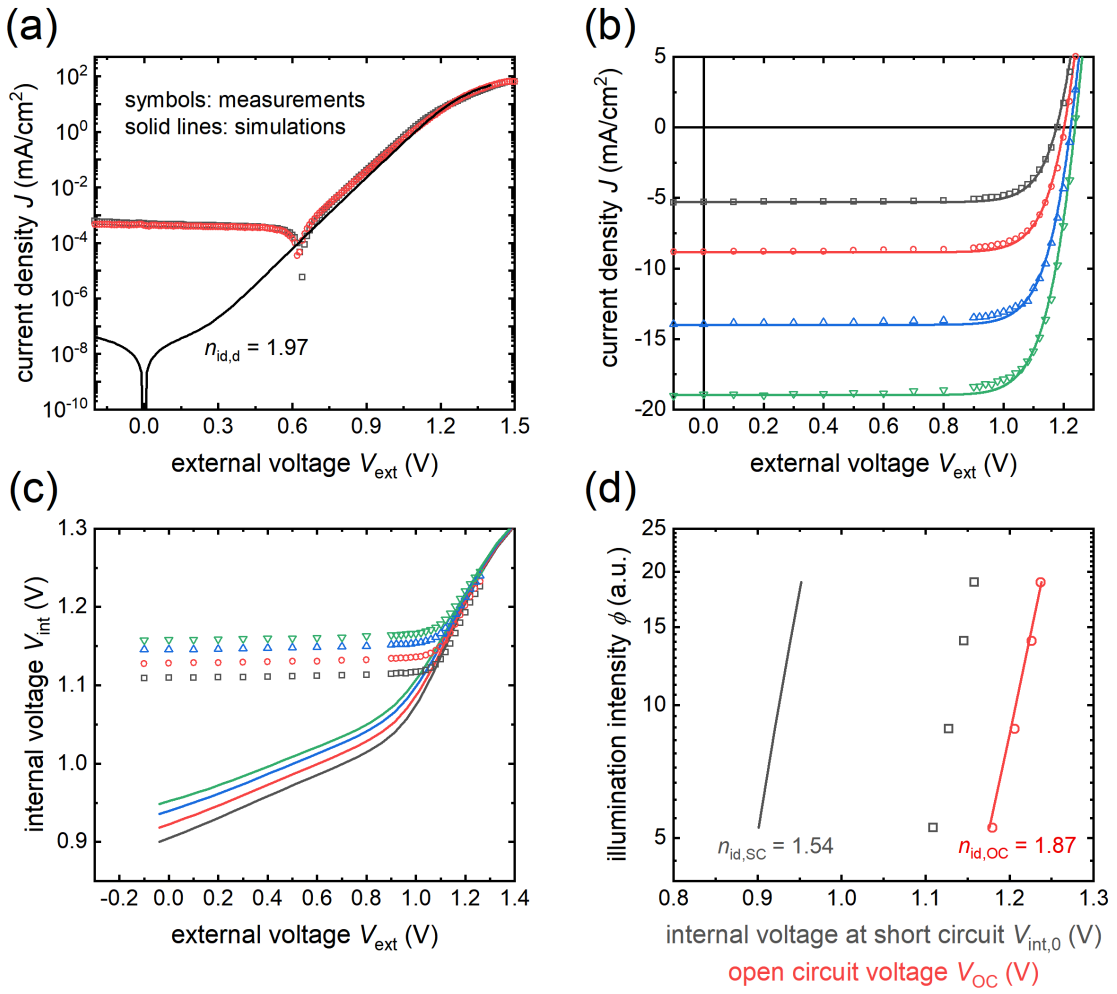

Figure 5.7: Simulations mostly utilizing parameters found in literature in comparison to measurement results. Simulations do not take field screening effects due to ion migration into account. (a) Simulated dark current-voltage curve (solid black line) in comparison to measured sweeps in forward (grey symbols) and reverse (red symbols) direction. (b) Illuminated current voltage curves and (c) internal voltage V_{int} versus external voltage V_{ext} for the four highest illumination intensities ϕ both simulated (solid lines) and measured (symbols). (d) Illumination intensity ϕ versus the internal voltage at short circuit $V_{\mathrm{int,0}}$ and the open-circuit voltage V_{OC} for the determination of the ideality factors $n_{\mathrm{id,SC}} = 1.54$ and $n_{\mathrm{id,OC}} = 1.87$, respectively. Simulations are represented by solid lines, measurements by symbols, the ideality factors shown relate to the simulations.

So far the parameters chosen for this initial simulation closely match the measurements. However figure 5.7 (c) shows the internal voltage V_{int} versus external

voltage V_{ext} characteristic of the simulation in comparison to the measured cell and here we see a big discrepancy. Since the simulation mostly resembles the asymmetric cell without field screening from chapter 4, the $V_{\mathrm{int}}(V_{\mathrm{ext}})$ curve shows a similar behaviour as well. The favourable conduction properties of the perovskite in conjunction with the aid of the electric field leads to an efficient extraction of charge carriers at short circuit. Therefore the internal voltage V_{int} induced by charge carriers remaining in the absorber is significantly reduced as compared to the measurement results. An increasing externally applied voltage V_{ext} reduces the field in the absorber, hinder charge carrier extraction and increases V_{int}. However it does not reach the high values found in the measurements until the external voltage is close to open circuit.

When we take a look at the ideality factors in figure 5.7 (d), we see that the simulation values for the ideality factor at open circuit closely match those from the measurements. This is unsurprising since the illuminated current-voltage curves from the simulations closely matched the measurements, including the open circuit. The ideality factor $n_{\mathrm{id,OC}} = 1.87$ from the simulation is slightly higher than the ideality factor calculated from the measurements in the same regime of ϕ, but these differences are not very significant. The curve for the simulated ideality factor at short circuit is moved to lower voltages as the onset of the simulated $V_{\mathrm{int}}(V_{\mathrm{ext}})$ curves is significantly lower than the measured data. The slope however is strikingly similar to that of the measurements and yields almost the same ideality factor $n_{\mathrm{id,SC}} = 1.54$. This is again a diversion from the model presented in chapter 2.8. The model only seems to apply to cells with flat quasi-Fermi levels in the absorber. Since the simulation shows significant fluctuations of the QFLs in the absorber it does not apply and the ideality factor can be between 1 and 2.

Overall this first attempt of simulating the measurement data has shown, that the current-voltage characteristic as well as the ideality factor at open circuit $n_{\mathrm{id,OC}}$ can be matched by simulations without too much effort. The $V_{\mathrm{int}}(V_{\mathrm{ext}})$ however requires a more sophisticated approach as it can not be explained by this set of parameters.

When attempting to approach the behaviour of the internal voltage V_{int} with respect to the externally applied voltage V_{ext}, the most important feature of the

measured data is the flat regime at lower to intermediate voltages. Here the internal voltage shows very little change at a quite significant level. In chapter 4.4.2 we have already found rather simple cell constructions yielding such a behaviour of the $V_{\mathrm{int}}(V_{\mathrm{ext}})$ curve (see figure 4.15). Both the *pn*-type cell and the *pin*-type cell exhibited a similar behaviour. In the former case this was caused by the doping of both the thick *p*-layer and the thinner *n*-layer with a higher concentration of dopants. The doping of these layers created large volumes in the cell where the bands are flat and unchanged by the external voltage V_{ext}. The same is true for the *pin*-type cell, here the highly doped layers at either side of the intrinsic *i*-layer form small volumes of field-free absorber material. While these two layers only account for a small percentage of the whole cell volume they dominate recombination du to the increased density of charge carriers. The third case that exhibits a flattened regime in the $V_{\mathrm{int}}(V_{\mathrm{ext}})$ curve at low to intermediate voltages is the symmetrical cell with an architecture resembling a perovskite solar cell and a screened field in the absorber. The field screening is achieved by setting the permittivity ϵ_{per} in the absorber to an arbitrarily high value simulating the field screening caused by a redistribution of ionic defects. This sort of field screening also makes the charge carrier concentrations in the absorber less dependent on the external voltage V_{ext}, however the curve is not quite as flat because changes in the field distribution in the transport layers still significantly influences the extraction of charge carriers from the absorber. However it could be flattened by reducing the charge carrier mobilities μ_{pero} in the absorber.

These findings from chapter 4 show us that there are certain requirements for a simulation reproducing the $V_{\mathrm{int}}(V_{\mathrm{ext}})$ measurements:

1. A volume within the solar cell where the electric field is mostly independent from the external voltage V_{ext} at low to intermediate values.
2. This volume needs to dominate radiative recombination.

As indicated by my discussion of previous results above, we can either achieve the screening of an externally applied field by doping the absorber (as it is the only layer relevant for the luminescence signal) or by increasing the permittivity ϵ_{pero} in the absorber emulating the effect of redistributing ionic defects. First we will consider the case of a doped perovskite absorber. While the $CH_3NH_3PbI_3$

perovskite used in the measured cell is not extraneously doped a compositionally induced doping has been discussed before [159]. Since the perovskite layers were processed with an excess of CH_3NH_3I, this could lead to a slight n-doping of the layer. Additionally the chlorine used in processing could act as a dopant [160]. Note that we do not generally assume the perovskite in the measured cell to be doped and the following simulations are rather a means to show how the $V_{\mathrm{int}}(V_{\mathrm{ext}})$ behaviour of the measured cell can be simulated. In figure 5.8 we see band diagrams under differing illumination and voltage conditions for a cell with an acceptor density $N_{\mathrm{A}} = 10^{17}$ cm^{-3} in the absorber (all simulation parameters are shown in table A.1). In panels (a) and (c) we see the band diagrams at short circuit in the dark and under illumination respectively. In both cases the bands are rather flat with a small downward bend towards the PCBM. This is caused by charge carriers leaving the absorber and residing in the PCBM transport layer, which is not the case in the thinner PTAA layer. In the illuminated case we see the QFL for the electrons E_{Fn} also follow this drop. The band diagrams in open circuit (panels (b) and (d)) show entirely flat bands as well as QFLs. We can see an asymmetry in charge carrier density with holes as the majority carriers in all four situations. This is of course induced by the doping of the perovskite.

In figure 5.9 we can now see the resultant characteristics of these simulations in context with the measured data. In panel (a) we see the simulated dark current-voltage curve in comparison to measurement data and straight away it does not match. The slope in the upper part of the curve (1 V - 1.2 V) yields an ideality factor $n_{\mathrm{id,d}} = 1.15$. The simulated dark current-voltage curve being dissimilar to the measurement data will be the case for a lot of simulations. This may be explained by the disparities in both ionic and electronic conductivity in perovskite under differing illumination conditions [161]. Kim et al. have shown that the conductivity can change over multiple orders of magnitude with illumination intensity ϕ. Since I am not able to simulate these effects (especially towards lower voltages), the mismatch between simulation and experimental data will be present for most upcoming data sets. The dark current-voltage curves will however still be shown for reference.

Figure 5.9 (b) shows the illuminated current-voltage curves for corresponting to the measurements of the four highest illumination intensities. We see that the

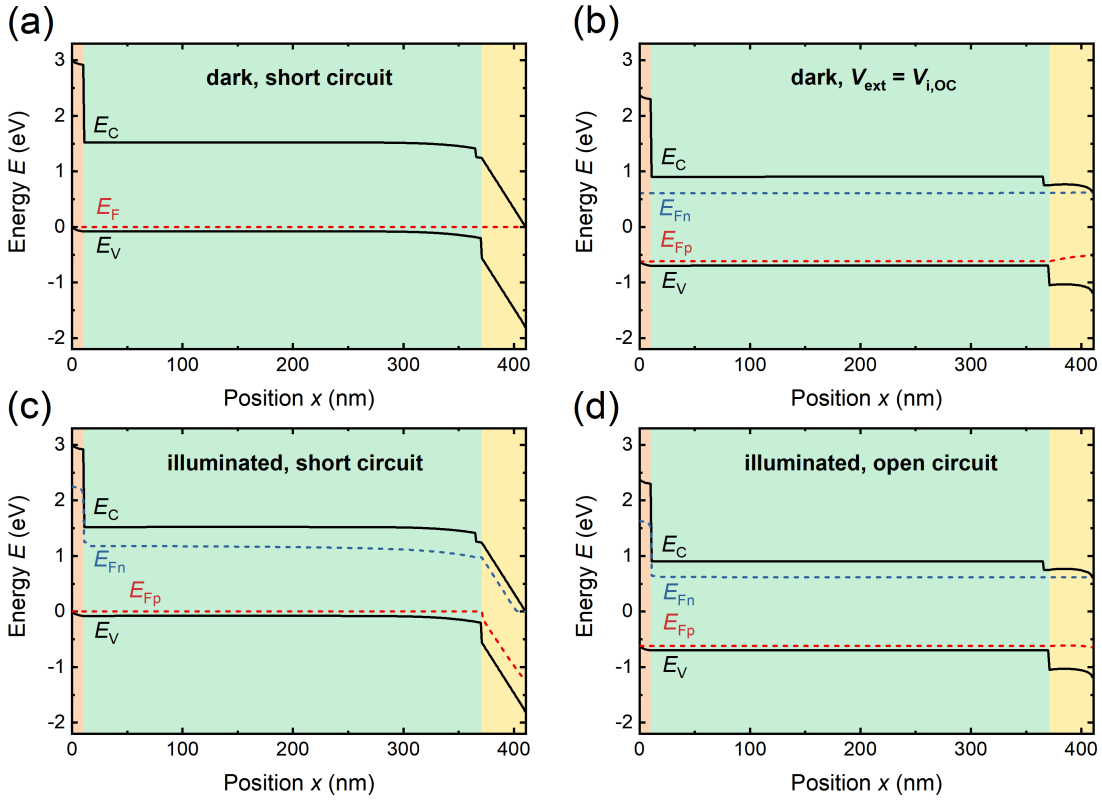

Figure 5.8: Band diagram of a simulated cell utilizing a perovskite absorber with an acceptor density $N_A = 10^{17}$ cm^{-3}. The valence band energy E_V and the conduction band energy E_C are displayed together with the QFLs for electrons E_{Fn} and holes E_{Fp} respectively. Applied bias conditions are (a) $V_{ext} = 0$ V and (b) $V_{ext} = V_{i,OC}$ for the cell in the dark as well as (c) $V_{ext} = 0$ V and (d) $V_{ext} = V_{i,OC}$ for the cell under illumination by 532 nm laser light. $V_{i,OC}$ refers to the open-circuit voltage under illumination conditions. Illumination intensity is the highest value investigated in this chapter.

short-circuit current density J_{SC} is matched in all cases, while the fill factor FF and the open-circuit voltage V_{OC} are slightly off. In panel (c) we can see the internal voltage V_{in} curves. First we will take a look at the green curve pertaining to the highest illumination intensity ϕ and the corresponding measurement data. It is evident that the simulation closely matches the measurement, both curves show the characteristic flat regime up to roughly $V_{ext} = 1$ V. This is the case because the charge carrier concentrations in the absorber only undergoes minimal changes due to the external voltage. Additionally to the independence from V_{ext}, the level of the internal voltage at short circuit $V_{int,0} = 1.16$ V is rather higher matching the

measurement data. This can be attributed to the high amount of charge carriers supplied by the dopants. Once we take a look at the $V_{\mathrm{int}}(V_{\mathrm{ext}})$ curves for the other simulated illumination intensities we see that they do not match the measurement results at all. They keep the same shape of the curve but the level of the flat regime is off with respect to the measured data. This is a clear indication that the ideality factor at short circuit $n_{\mathrm{id,SC}}$ as introduced in chapter 4.3 is too low in the simulations.

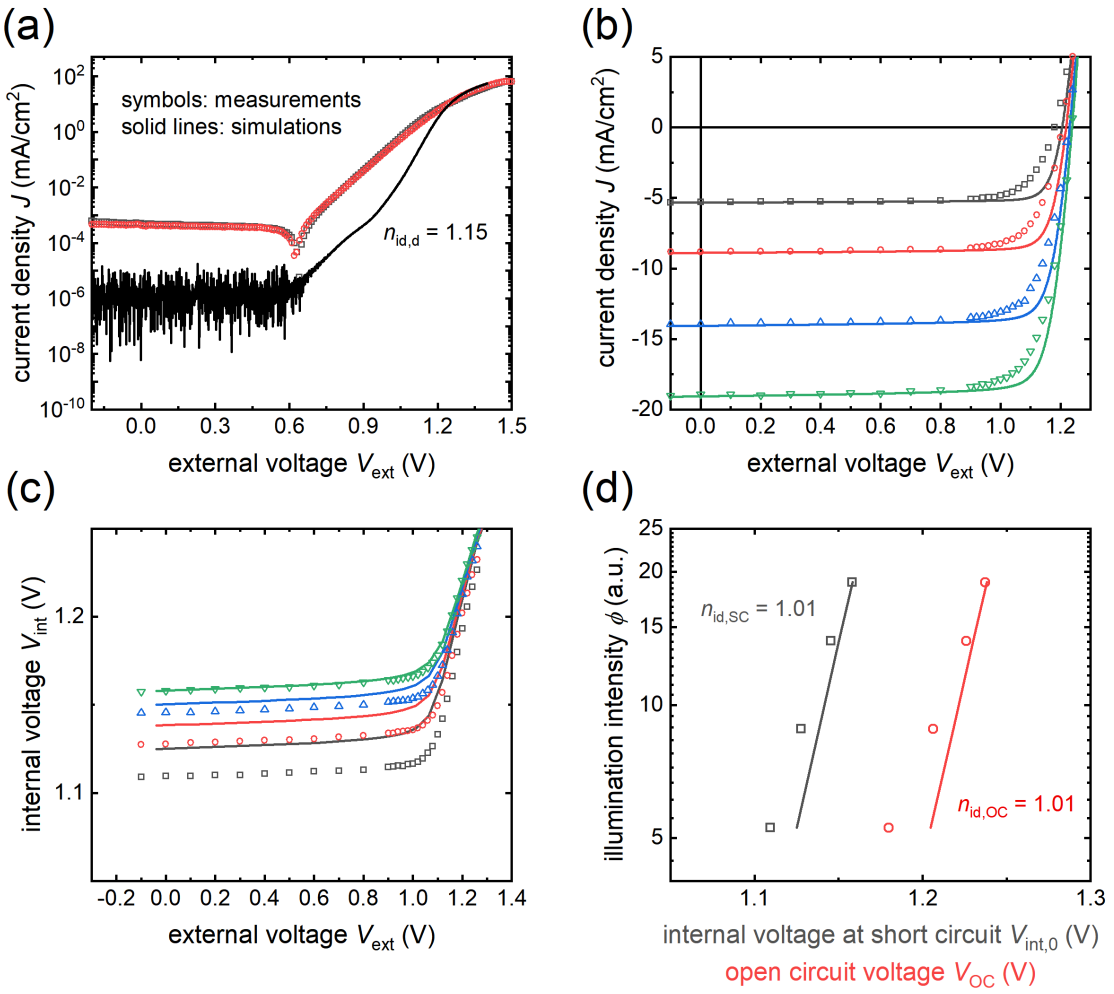

Figure 5.9: Simulations of a cell utilizing a perovskite absorber with an acceptor density $N_A = 10^{17}$ cm^{-3}. (a) Simulated dark current-voltage curve (solid black line) in comparison to measured sweeps in forward (grey symbols) and reverse (red symbols) direction. (b) Illuminated current voltage curves and (c) internal voltage V_{int} versus external voltage V_{ext} for the four highest illumination intensities ϕ both simulated (solid lines) and measured (symbols). (d) Illumination intensity ϕ versus the internal voltage at short circuit $V_{int,0}$ and the open-circuit voltage V_{OC} for the determination of the ideality factors $n_{id,SC} = 1.01$ and $n_{id,OC} = 1.01$, respectively. Simulations are represented by solid lines, measurements by symbols, the ideality factors shown relate to the simulations.

In figure 5.9 (d) the internal voltage at short circuit $V_{int,0}$ and at open circuit, which is per definition V_{OC}, are shown with respect to the illumination intensity. Since the simulation fit the measured $V_{int}(V_{ext})$ curve at the highest illumination

intensity ϕ the corresponding data points in this panel are also matched. However going from there it is evident that the slope of the simulated lines is significantly higher than the measurement data. From this slope we can once again calculate the ideality factors at short circuit $n_{\mathrm{id,SC}}$ and at open circuit $n_{\mathrm{id,OC}}$, both of which are at about 1.01. This should come as little surprise since the doping of the perovskite absorber clearly created an asymmetry of charge carriers within. Therefore recombination adheres to low level injection properties, reducing the ideality factor to 1. While this was always to be expected for the short-circuit case, the additional charge-carriers at open circuit could have offset this asymmetry, however in this case the doping concentration was too high for that to happen. In order to demonstrate the effect of the doping density N_{A} on the simulated cell additional simulations were run varying the acceptor density $N_{\mathrm{A}} = 10^{15} - 10^{17}$ cm^{-3}. The resulting characteristics are shown in figure A.1. The reduction of the density of dopants leads to a reduction of the internal voltage at low to intermediate voltage regime of the $V_{\mathrm{int}}(V_{\mathrm{ext}})$ curve ceases to be flat. At the same time the ideality factors both in short circuit and in open circuit are increased because the absorber is no longer consistently in LLI. At the same time J_{SC} is increased and V_{OC} is reduced.

We have seen that it is possible to explain the behaviour of the $V_{\mathrm{int}}(V_{\mathrm{ext}})$ curve with a doping of the perovskite absorber. However it is unclear whether a doping of the perovskite can realistically be this high and furthermore it pins the ideality factors to a value close to 1 which does not coincide with my measurement results. Therefore we will have to take a look at simulations that do not rely on this kind of doping. As mentioned before a second approach to achieve a flat regime in the $V_{\mathrm{int}}(V_{\mathrm{ext}})$ curve is to screen the electric field from the absorber via an increase of the relative permittivity ϵ_{pero} in the absorber to an arbitrarily high value. As it turns out however, this condition is not sufficient to generate the $V_{\mathrm{int}}(V_{\mathrm{ext}})$ curve that we desire. If the mobility-lifetime product $\mu\tau$ in the perovskite absorber is too high, charge carriers will still be able to diffuse out of it. In this case the electric field in the transport layers will significantly influence the extraction of charge carriers subsequently making the internal voltage dependent on the externally applied voltage. This means that additionally to increasing the permittivity of the absorber, its transport properties have to be substantially reduced in order to reproduce the accumulation of charge carriers in the absorber seen in the measurements.

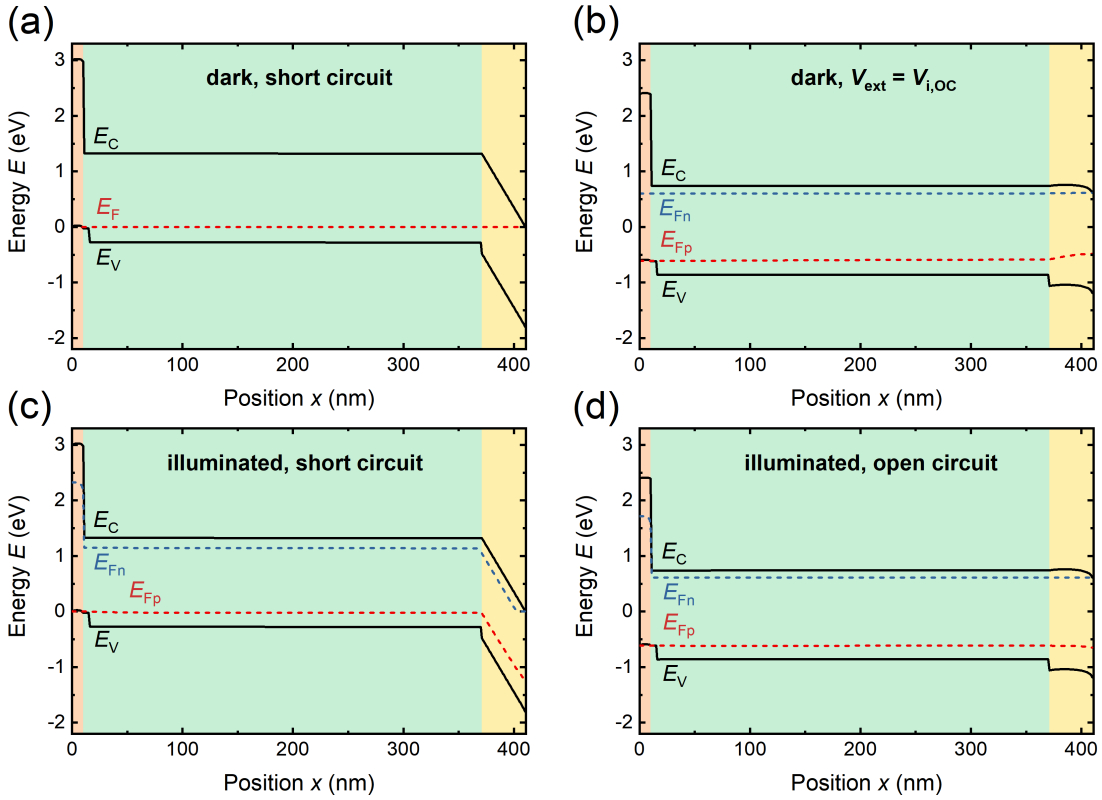

Figure 5.10: Band diagram of a simulated cell utilizing a perovskite absorber with an electric field screened due to ionic movement. The valence band energy E_V and the conduction band energy E_C are displayed together with the QFLs for electrons E_{Fn} and holes E_{Fp} respectively. Applied bias conditions are (a) $V_{ext} = 0$ V and (b) $V_{ext} = V_{i,OC}$ for the cell in the dark as well as (c) $V_{ext} = 0$ V and (d) $V_{ext} = V_{i,OC}$ for the cell under illumination by 532 nm laser light. $V_{i,OC}$ refers to the open-circuit voltage under illumination conditions. Illumination intensity is the highest value investigated in this chapter.

In the following we will take a look at a simulated cell that achieves the flat bands in the absorber by means of increasing the relative permittivity ϵ_{pero} in the absorber while simultaneously reducing its charge-carrier transport capabilities. The corresponding simulation parameters can be found in table A.2. Additionally to the field screening the hole transport layer has been doped.

Figure 5.10 shows the band diagrams under different illumination and voltage biases for a simulated cell that is able to reproduce the $V_{int}(V_{ext})$ measurement results without doping in the absorber but including an increased permittivity in the absorber. It is evident that the bands are entirely flat under all shown circumstances,

the electric field has been screened from the absorber and differences in potential can only be observed in the transport layers. In panel (a) we can see that the Fermi level E_{F} at short circuit in the dark is closer to the valence band indicating an excess of holes in the absorber. This is the case because the PTAA hole transport layer is doped for this simulation to control the ideality factor at short circuit $n_{\mathrm{id,SC}}$. The doping also to a certain extent causes the electric field to be screened from the PTAA layer as well, exacerbating the field in the PCBM layer. In all cases except for figure 5.10 (a) however we see that there is actually a majority of electrons in the absorber as indicated by the QFLs. This is the case because the extraction properties are significantly different for electrons and holes respectively. At the interface between absorber and ETL the conduction band energies E_{C} are perfectly aligned providing no aid in charge carrier extraction and the conducting properties of the PCBM layer are worse compared to the PTAA layer transporting holes. Furthermore the large offsets between the valence band energies E_{V} of the absorber and the HTL lead to an increased recombination at the interface. All of these asymmetries change the charge carrier densities in the absorber and enable us to control the ideality factor at open circuit $n_{\mathrm{id,OC}}$.

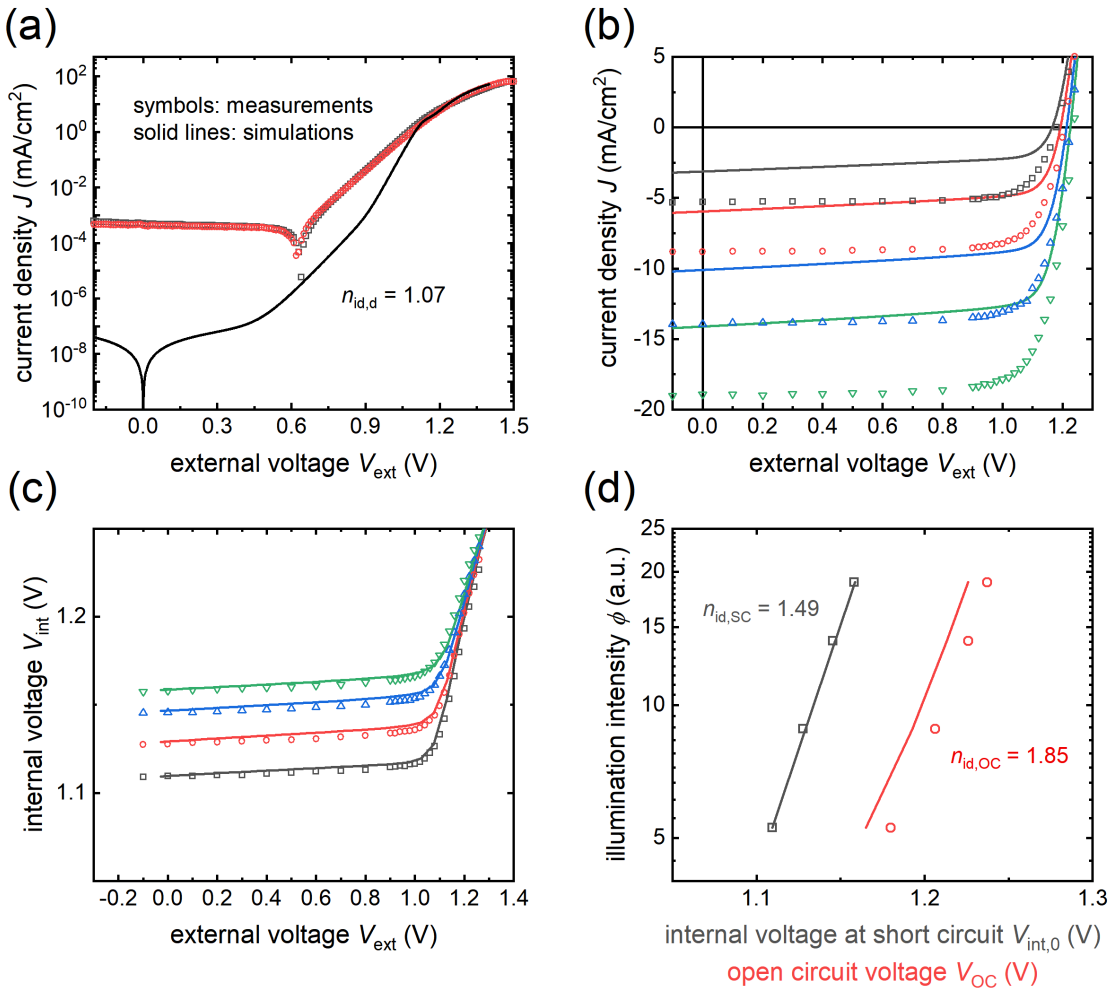

Figure 5.11: Simulations of a cell utilizing a perovskite absorber with an electric field screened due to ionic movement. (a) Simulated dark current-voltage curve (solid black line) in comparison to measured sweeps in forward (grey symbols) and reverse (red symbols) direction. (b) Illuminated current voltage curves and (c) internal voltage V_{int} versus external voltage V_{ext} for the four highest illumination intensities ϕ both simulated (solid lines) and measured (symbols). (d) Illumination intensity ϕ versus the internal voltage at short circuit $V_{\mathrm{int,0}}$ and the open-circuit voltage V_{OC} for the determination of the ideality factors $n_{\mathrm{id,SC}} = 1.01$ and $n_{\mathrm{id,OC}} = 1.01$, respectively. Simulations are represented by solid lines, measurements by symbols, the ideality factors shown relate to the simulations.

In figure 5.11 we can now see the characteristics of the simulated cell in comparison to the measured data. In panel (a) we can again see the dark current-voltage curve not reproducing the measured curves except for the highest voltage regions

where it is limited by the series resistance R_s. This can again be interpreted to be caused by the incongruency between the transport properties of the perovskite absorber in the dark and unter illumination. Panel (b) shows the illuminated current-voltage curves for the simulations and the measurements and straight away it is evident, that there is a large mismatch here. Because matching the $V_{int}(V_{ext})$ curves via the lack of electric field in the absorber necessitates rather limited transport properties in the absorber, charge carriers are not efficiently extracted, significantly reducing the short-circuit current density J_{SC}. While simply increasing the charge carrier liefetimes τ in the perovskite absorber may seem like a solution to this issue, this would simultaneously increase V_{int} at low voltages and significantly reduce the ideality factors both at short circuit and open circuit. The bad transport properties can additionally be seen by the slope exhibited in the low to intermediate voltage range in the illuminated current-voltage curve.

However if we take a look at the $V_{int}(V_{ext})$ curves shown in figure 5.11 (c) we see a very good agreement between the simulation and the measured data. Both the level of the internal voltage at short circuit $V_{int,0}$ as well as the flatness of the low to intermediate voltage regime are remarkably similar to the behaviour exhibited by the measurement data. Additionally this is the case for all four illumination intensities shown in the figure. This then translates over to the ideality factors determined in panel (d). All data points for $V_{int,0}$ closely match the measurement data and accordingly the short-circuit ideality factor $n_{id,SC} = 1.49$ is very similar as well. When evaluating the ideality factor at open circuit $n_{id,OC} = 1.85$, we see that there is a slight offset between simulation and measured data, the slope however is very similar leading to a comparable ideality factor at V_{OC} as well. Overall this simulation rather closely matches the measurement data with the caveat that the extraction properties are so unfavourable that the illuminated current-voltage curve is unreasonably distorted.

Now we have taken a look at two methods to achieve the proper shape of the $V_{int}(V_{ext})$ curve exhibited by my measurements. However, while we have an explanation why the dark current-voltage curve may not be properly reproduced, both approaches have additional shortcomings. The method to achieve a good fit of the $V_{int}(V_{ext})$ curve by doping the perovskite is able to reproduce the illuminated

current-voltage curve, but pins the ideality factors to a value close to 1. The method that screens the field from the absorber by an increased permittivity ϵ_{pero} on the other hand is able to properly reproduce the ideality factors, but necessitates reduced conduction properties within the cell unrealistically limiting the short-circuit current density J_{SC}. Now the task becomes finding a set of parameters that are able to simultaneously match all of these properties as they were measured on real cells. I have shown two starting points for a search for this set of parameters, in the following however I will omit the option of doping the perovskite absorber. As mentioned before it is rather unlikely that the perovskite used in the cell is doped to the simulated extent and furthermore the pinning of the ideality factors to values close to 1 is almost impossible to resolve without compromising on the fit of the $V_{\mathrm{int}}(V_{\mathrm{ext}})$ curve. As the simulations involving an increased dielectric permittivity ϵ_{pero} have shown the ideality factors can be controlled a lot better in the framework presented therein.

In the following I will use the set of parameters shown in table A.2 as a starting point to vary the most crucial characteristics influencing the solar cell behaviour. Note that using this kind of starting point strongly predetermines the influence any given parameters can and will have. I will make efforts to elucidate the relevance of a parameter in as universal a matter as possible.

The first characteristic value of the simulation we will take a look at is the dielectric permittivity ϵ_{pero} in the absorber of the cell. In figure A.2 we can see the same data as shown for the previous simulations for a variation of $\epsilon_{\mathrm{pero}} = 10 - 10000$. Higher values yield a stronger field screening effect and it is evident that both the low short-circuit current density J_{SC} (panel (b)) and the flat regime in the $V_{\mathrm{int}}(V_{\mathrm{ext}})$ curve (panel (c)) are strongly influenced by this effect. In the context of the given set of parameters the field screening reduces J_{SC} while increasing the internal voltage V_{int}. Additionally the field screening keeping the charge carriers in the perovskite absorber increases V_{OC}. In panel (d) we see the ideality factors at short circuit $n_{\mathrm{id,SC}}$ and at open circuit $n_{\mathrm{id,OC}}$ as a function of the varied ϵ_{pero}. While an accumulation of holes at the HTL interface leads to a low $n_{\mathrm{id,OC}}$ for low field screening, the value becomes higher with increasing values of ϵ_{pero} as more charge carriers remaining in the absorber partly level the asymmetry in charge carriers introduced by the doping

of the PTAA layer. At the same time the ideality factor at short circuit is slightly reduced. Overall this variation shows that the field screening in the absorber in the context of the other parameters is necessary in order to reproduce the measured $V_{\mathrm{int}}(V_{\mathrm{ext}})$ curve. At the same time however it has detrimental effects on the current-voltage curve and significantly influences the ideality factors.

Next we will consider the p-type doping of the PTAA hole transport layer, the importance of which has thus far not been fully clarified. In figure A.3 the influence of a variation of the acceptor density $N_{\mathrm{A,PTAA}} = 10^{17} - 10^{19}$ cm^{-3} in the PTAA layer is shown. An increase of the doping concentration is shown to reduce the J_{SC} of the simulated cell. This reduction of J_{SC} is caused by an increase of the density of holes p as the minority carriers. An increase of p reduces the ratio p/n ($p < n$) and thus increases the recombination rate R in accordance with equation 2.29. The increased recombination rate in turn reduces J_{SC}. Simultaneously the V_{OC} is slightly increased due to a flattening of the bands in the HTL, which slows charge extraction. The internal voltage V_{int} is increased with additional doping as the dopants provide charge carriers that diffuse into the perovskite absorber and disperse across its entire thickness. This effect is in addition to the slowing of charge carrier extraction increasing the concentration of charge carriers remaining in the absorber. These effects lead to an elevation of the level of the flat regime in the $V_{\mathrm{int}}(V_{\mathrm{ext}})$ curve due to the increase of the density of dopants in the PTAA layer. The shape of the curve however only changes slightly. At the same time the ideality factors are influenced significantly. At short circuit the ideality factor is close to 2 with only slight doping and it decreases as the doping concentration increases. In order to understand this effect we have to take a look at equations 2.66 and 4.4. The doping of the HTL decreases the electric field F in the HTL, which in turn increases $J_{\mathrm{extr,p}}$ (see equation 2.66). With this increase V_{int} shifts from a quadratic correlation to J_{SC} towards a linear correlation (see equation 4.4). This shift manifests in a change of the ideality factor at short circuit $n_{\mathrm{id,sc}}$, which is reduced with increasing doping concentrations of the HTL. Once a critical value of the doping density is reached however, charge carrier extraction in the HTL is reduced to the point that the cell efficiency is significantly reduced and the ideality factors diverge to higher values. Overall we can see that in the effort of matching the measured data the p-type doping of the PTAA layer can be utilized as a tool to

influence the ideality factor without significantly changing the other properties of the cell as long as the doping density is not increased too far.

In a further step we will take a look at the band offsets at the interfaces between the perovskite absorber and the transport layers. As mentioned before these offsets significantly influence the efficiency with which charge carriers are extracted from the perovskite absorber. In figure A.4 we see the influence of the variation of the valence band offset $\Delta E_{\mathrm{V}} = 0 - 0.4$ eV at the absorber-PTAA interface. It is evident that the variation of this offset has strong implications for the functionality of the simulated cell which have to be carefully analyzed. Since the doping of the PTAA layer screens the electric field from the HTL, a situation where the bands are aligned, ergo the offset is 0 eV, sees the short-circuit current density J_{SC} reduced to a very low value. Accordingly the internal voltage V_{int} is increased to extremely high values. Increasing ΔE_{V} improves the charge carrier extraction eventually reducing the internal voltage and improving the extracted current density. At the same time V_{OC} is reduced. Eventually (in this case at roughly $\Delta E_{\mathrm{V}} = 0.25$ eV) the illuminated current-voltage curve shows a favourable fill factor FF and the $V_{\mathrm{int}}(V_{\mathrm{ext}})$ curve matches the measured data. Further increasing the band offset will lead to a loss of potential energy reducing the open-circuit voltage V_{OC}. Simultaneously the internal voltage is further reduced. Finally the ideality factors can be evaluated for all these developments. Initially when the conduction band energies are aligned the recombination is dominated by the bulk of the perovskite absorber. Since the doping of the PTAA layer leads to an increase in hole concentration in the absorber the resulting LLI conditions yield an ideality factor close to 1 both in short circuit and in open circuit. When the offset is introduced and increased the extraction of holes from the absorber is improved and recombination at the interface is increased due to a reduction of the energy gap between the conduction band in the absorber and the valence band in the HTL. The increased recombination at the interface reduces the hole concentration in the absorber and eventually compensates the additional holes introduced due to the PTAA-doping. This results in an ideality factor close to 2 for both open circuit and short circuit. A further increase in the band offsets leads to an exacerbation of the interface recombination which eclipses the influence of the PTAA doping leading to reduced ideality factors. However here we see a divergence between the ideality factors at short circuit and in open circuit. The

$n_{\mathrm{id,SC}}$ is reduced sooner than the $n_{\mathrm{id,OC}}$. This opens a window in which the ideality factors differ as could be observed in the measurement data. This window is created by the two competing recombination sites in the bulk and at the interface. It can be shaped or shifted by the variation of different simulation parameters but is necessary to control the ideality factors of the simulated solar cell.

In figure A.5 we see the influence of a variation of the conduction band offset $\Delta E_{\mathrm{C}} = 0 - 0.2$ eV at the absorber-PCBM interface. At the initial value of 0 eV the bands are aligned for both layers neither blocking the extraction of charge carriers nor forming a barrier for their reintroduction. With an increase of the offset charge carrier extraction is improved leading an increase in J_{SC} and a decrease of charge carriers remaining in the absorber. Correspondingly the level of the flat V_{int} regime is reduced, as is the open-circuit voltage V_{OC}. Further increasing the offset of the bands will, anologously to the perovskite-PTAA interface, amplify the effects on both the internal voltage and the open-circuit voltage, as well as significantly reduce the cells efficiency due to the loss of potential energy at the interface. When considering the ideality factors we see that $n_{\mathrm{id,SC}}$ is mostly unaffected by the changes, whereas $n_{\mathrm{id,OC}}$ is significantly increased. This is the case because the increased extraction and recombination of electrons counteracts the asymmetry of charge carriers in the absorber introduced by the band offsets at the PTAA-perovskite interface. At offsets $\Delta E_{\mathrm{C}} = 0.2$ eV and higher the losses in V_{OC} reduce $n_{\mathrm{id,OC}}$.

We have already discussed the necessity for limited transport of charge carriers from the perovskite absorber towards the contacts for the internal voltage V_{int} to remain as high at short circuit as it is in the measured data. In figure A.6 we see the impact of a variation of the charge carrier mobility $\mu_{\mathrm{pero}} = 0.1 - 100$ cm^2/Vs in the perovskite asorber on the simulated solar cell behaviour. Straight away the results are rather logical. A higher charge carrier mobility in the absorber leads to a more efficient extraction of charge carriers. Correspondingly the extracted current is increased while the amount of charge carriers remaining in the bulk absorber is reduced. This reduction per definition leads to a decrease of the internal voltage that eventually saturates as can be seen in panel (c). Not only does the overall level of the flat part of the $V_{\mathrm{int}}(V_{\mathrm{ext}})$ curve decrease with an increasing value of μ_{pero}, but it also develops an increased slope. This shows that increasing the charge carrier mobility

in the absorber does improve the illuminated current voltage characteristic of the cell but simultaneously creates a mismatch in the $V_{\mathrm{int}}(V_{\mathrm{ext}})$ curve. The changes in the internal voltage influence the ideality factors shown in panel (d) as well. While the ideality factor at short circuit $n_{\mathrm{id,SC}}$ is slightly reduced, the ideality factor at open circuit significantly increases to values even exceeding 2. This can be attributed to a more efficient extraction of electrons that have a higher probability of entering the ETL despite the aligned conduction band energies. This in turn reduces the asymmetry of charge carrier concentrations in the absorber increasing the ideality factor.

The second material property of the bulk perovskite dictating the charge carrier density within is the charge carrier lifetime τ_{pero}. Figure A.7 shows the impact of a variation of $\tau_{\mathrm{pero}} = 10^{-7} - 10^{-4}$ s. As was the case for the charge carrier mobility an increase of the charge carrier lifetime significantly improves the illuminated current voltage curve as evidenced by panel (b). The simulated curves approach the measured data with an increase in τ_{pero} and match J_{SC} rather well from a value of approximately $3 \cdot 10^{-7}$ s upwards. Simultaneously the increased lifetime leads to a larger number of charge carriers remaining in the absorber which in turn increases the internal voltage. In panel (c) it is clearly visible that the shape of the $V_{\mathrm{int}}(V_{\mathrm{ext}})$ curve does not change but the level of its flat regime is increased. This increase eventually saturates. Finally we can take a look at the impact of the charge carrier lifetime variation on the ideality factors. At short circuit the impact is rather small with only the lowest simulated values for τ_{pero} visibly impacting $n_{\mathrm{id,SC}}$. The open-circuit ideality factor $n_{\mathrm{id,OC}}$ however sees a significant drop with an increase of the charge carrier lifetime. This drop coincides with the values for τ_{pero} that lead to a significant reduction of J_{SC}. This is the case because as the lifetime is increased, recombination in the absorber is reduced. This leads to the recombination at the interface between the HTL and the absorber to dominate and since there are a majority of holes at this interface the ideality factor $n_{\mathrm{id,OC}}$ is reduced.

With the previous variation we noticed the relevance of the interface recombination at the border between the perovskite absorber and the PTAA layer functioning as the HTL. The recombination properties of this interface are important for the simulations as well. The charge carrier mobility does not have a signif-

icant impact as the layer used to simulate the interface recombination is rather thin at 5 nm. The charge carrier lifetime however strongly influences the cells behaviour. In figure A.8 we see the impact of a variation of the charge carrier lifetime $\tau_{\mathrm{int,PTAA}} = 10^{-8} - 10^{-5}$ s at the absorber-PTAA interface. For the illuminated current voltage curve and the $V_{\mathrm{int}}(V_{\mathrm{ext}})$ curve the behaviour is quite similar to that induced by the variation of τ_{pero}. A higher charge carrier lifetime at the interface increases J_{SC} as well as the level of the flat $V_{\mathrm{int}}(V_{\mathrm{ext}})$ regime. Additionally it also significantly impacts the open-circuit voltage V_{OC}, which is reduced along with J_{SC}. The most striking difference to the influence of τ_{pero} can be seen for the ideality factors that show opposite trends. With increased charge carrier lifetime in the interface the ideality factor at open circuit $n_{\mathrm{id,OC}}$ is significantly increased. The increased charge carrier lifetime at the interface reduces the recombination losses and increases the hole concentration in the absorber, reducing the asymmetry and accordingly increasing the ideality factor. Meanwhile $n_{\mathrm{id,SC}}$ is only slightly increased with $\tau_{\mathrm{int,PTAA}}$.

In the context of the parameter set used for the simulations shown in figure 5.11 the parameter variations shown are the most crucial to control the results we are concerned about. There are further parameters that can be influential for simulations in a different context however. The charge carrier mobilities in the layers representing the interfaces do not have a significant influence on the simulations as the layers are chosen to be rather thin. The same is true for the charge carrier mobility μ_{PTAA} in the PTAA hole transport layer, the low thickness of the layer makes the mobility insignificant. If it were to be reduced to a value that affects the simulation, the cell functionality would rapidly collapse. The charge carrier lifetime τ_{PTAA} in the PTAA layer is of no significance either since its high band gap energy E_{g} makes recombination in this layer insignificant. While the band gap in the PCBM layer is closer to that of the perovskite, recombination is not significant in the context of the parameters used either and the charge carrier lifetime τ_{PCBM} in this layer does not impact any of the relevant parameters. The same is true for the charge carrier mobility μ_{PCBM} in the ETL, a variation does not impact cell functionality except for very low values where the diode properties rapidly decay without yielding any sensible simulation results. Furthermore the energetic offsets $\phi_{\mathrm{b,f}}$ and $\phi_{\mathrm{b,b}}$ between the work functions of the external metal contacts and the

bands of the transport layers were varied. They can introduce a resistive effect hampering the illuminated current voltage characteristic without enabling a better fit of the simulation with respect to the measured data. Finally while the charge carrier mobility $\mu_{\mathrm{int,PCBM}}$ does not have a considerable impact on the simulations, the charge carrier lifetime $\tau_{\mathrm{int,pcbm}}$ can be reduced to a value where recombination becomes significant at this interface as well.

The ultimate goal of varying the parameters in a set that properly replicates the $V_{\mathrm{int}}(V_{\mathrm{ext}})$ measurements was to find a set of parameters that is able to combine this fit of the $V_{\mathrm{int}}(V_{\mathrm{ext}})$ curve with an illuminated current-voltage curve and ideality factors at short circuit and open circuit that match the measurement data. Unfortunately my attempts at replicating all measured data at once were unsuccessful because the measurement results are mutually exclusive in my approach to simulating the solar cell. As was discussed above figure A.4 (d) shows a window of opportunity in which the open-circuit ideality factor $n_{\mathrm{id,OC}}$ is significantly higher than the short-circuit ideality factor $n_{\mathrm{id,SC}}$. This window is created by virtue of two recombination centres - the perovskite absorber and its interface with the PTAA hole transport layer - that both significantly contribute to the recombination of the cell as a whole. If either of the two recombination sites were to dominate recombination the ideality factor would be pinned and the independency of its value at short circuit and open circuit would be lost. This means that when changing parameters in the simulation it has to be taken into account that the recombination in the bulk absorber and at the interface have to remain similar. Recombination rates can either be high, low or anything inbetween for both recombination sites, but they can not significantly deviate. This of course considerably narrows the space in which the simulation can be adapted and leads to an impasse between two properties of the simulated cell. If the charge carrier extraction from the cell is generally bad, the internal voltage V_{int} can be reproduced as it was measured. However in this case, which corresponds to the simulations shown in figure 5.11, the short-circuit current density J_{SC} will be significantly reduced leading to a discrepancy with the measured illuminated current-voltage curves. If on the other hand the charge extraction is generally improved, the illuminated current-voltage curve will bei properly reproduced, but the high values of the internal voltage V_{int} can not be reached.

These results show that with the constraints imposed by the simulation approach used for this thesis it was not possible to reproduce the measured data. The reason for this could be inhomogeneities or other 2-dimensional effects within the perovskite absorber. If there are perovskite grain in the bulk material that are not properly electrically contacted to the rest of the absorber they may be luminescing as though they were under open-circuit conditions. This increased photoluminescing activity would then strongly influence the luminescence signal at low to intermediate voltages. This increase of the luminescence signal and subsequently of the calculated internal voltage V_{int} can not be taken into account by the simulation because the bulk is assumed to be homogeneous in the onedimensional optical approach that is used.

5.4 Conclusion

In this chapter I showed voltage dependent luminescence measurements and the internal voltage V_{int} derived from this data. These $V_{\mathrm{int}}(V_{\mathrm{ext}})$ measurements yielded ideality factors both at short circuit and open circuit that showed differing behaviour. The luminescence measurements were conducted in conjunction with dark and illuminated current-voltage curves at varied illumination intensities ϕ. I highlighted potential issues regarding the measurement protocol and outlined the approach that was taken to attain a full set of data. Subsequently I demonstrated that while simple simulations of the cell are capable of reproducing the current-voltage curves as well as the ideality factors, they did not match the $V_{\mathrm{int}}(V_{\mathrm{ext}})$ behaviour of the measured data. I then showed approaches to attain a simulation that matches this characteristic, however these approaches exhibited diverging results for either the current-voltage curves or the ideality factors. Finally that led me to conclude that with the simulating methods utilized for this thesis it was not possible to reproduce the entire set of data measured for my cells. This inability could be attributed to inhomogeneities in the cell elevating the measured internal voltage V_{int} at low to medium externally applied voltages due to insufficient contacting. Nevertheless we have seen how we can interpret my measured data and how a simulation of this data can be approached.

6 Series Resistances in Perovskite Solar Cells

Series resistances R_s are an inevitable component of a solar cell and have been accepted and understood as such for a long time. Taking resistive effects into consideration is common practice for simulations and modelling of solar cells of all technologies. A fundamental measurement used for the determination of the series resistance is the dark current-voltage characteristic $J_\mathrm{d}(V)$ of a solar cell. From a dark current-voltage curve crucial parameters such as the dark ideality factor $n_\mathrm{id,d}$, the parallel resistance R_p and the series resistance R_s can be extracted.

In chapter 2.1.5 I introduced a method to determine the series resistance R_s over a wide range of voltages by comparing different current-voltage characteristics. These characteristics are the dark current-voltage curve, which I will denote with $J_\mathrm{d}(V)$, the illuminated current-voltage curve denoted as $J_\mathrm{i}(V)$ and the suns-V_OC curve, which is generated by measuring V_OC and J_SC at varied illumination intensities ϕ. R_s can be calculated by comparing any two out of these curves as was described in chapter 2.1.5. This redundancy of differing calculation methods can yield insights into potential limitations of any of the current-voltage behaviours. This method of calculating R_s is well established for crystalline silicon solar cells but so far has only found limited attention with respect to thin film solar cells [70]. For perovskite solar cells to date no reports on the voltage dependent series resistance $R_\mathrm{s}(V)$ exist. Mundhaas et al. [162] determined the series resistance taken from a comparison of the illuminated current-voltage curve $J_\mathrm{i}(V)$ with suns-V_OC data and found a dependency of R_s on the sweep speed of the $J_\mathrm{i}(V)$-measurement. However they did not continue to examine the voltage dependencies of the series resistance more closely. However in this chapter we will take a look at this dependency. Aside

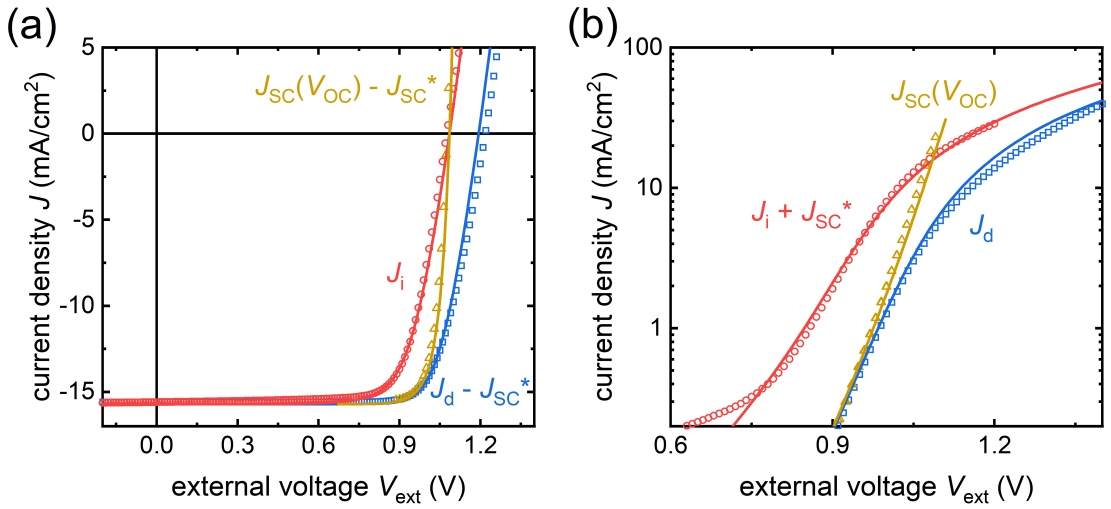

Figure 6.1: (a) Linear plot of the current-voltage characteristic of a perovskite solar cell in the dark $J_\mathrm{d}(V)$ (blue) and under one sun illumination $J_\mathrm{i}(V)$ (red) as well as its suns-V_OC curve (yellow). The curves for $J_\mathrm{d}(V)$ and suns-V_OC were moved to the fourth quadrant of the coordinate system by subtraction of the short-circuit current density J^*_SC taken from $J_\mathrm{i}(V)$. (b) Semilogarithmic plot of the same current-voltage curves. The curve for $J_\mathrm{i}(V)$ was moved to the first quadrant of the coordinate system by adding J^*_SC. In both panels measurement data are shown in the form of symbols while simulations are depicted as solid lines.

from finding insights into the effects various parameters have on the functionality of a perovskite solar cell, the voltage dependent evaluation of the series resistance allows us to separate an internal contribution to the series resistance $R_\mathrm{s,int}$ from the ohmic external part $R_\mathrm{s,ext}$. This is interesting because it allows us to disentangle ohmic resistive effects from extraction limiting factors such as limited charge-carrier mobilities and unfavourable distributions of the electric field within a solar cell (see chapter 4). This information can be utilized to optimize the design of future perovskite solar cell concepts.

6.1 Voltage Dependent Series Resistance from Current-Voltage Measurements

As was introduced in chapter 2.1.5 the series resistance of a cell can be calculated using equations 2.10a-2.10c. All of these equations are based on the voltage differences at equal current densities of two curves. Especially when comparing $J_\mathrm{d}(V)$ to the suns-V_OC curve this difference can be quite small. This means that small fluctuations of the measurement values can lead to substantial errors in the resulting values for the series resistance. As was explained in chapter 2.1.6, PSCs can exhibit quite substantial fluctuations of measurement data caused by hysteretic behaviour due to ionic movement. In order to limit this kind of influence, a sample fabricated by coevaporation exhibiting negligible amounts of hysteresis was measured (for processing see appendix A.2). In figure 6.1 (a) a set of measured data consisting of $J_\mathrm{d}(V)$, $J_\mathrm{i}(V)$ and suns-V_OC is shown with symbols. Optoelectronic simulations were conducted using ASA, the simulation parameters are listed in table 6.1 and the resulting curves are depicted as solid lines. In figure 6.1 (b) the same curves are shown in a semilogarithmic plot. In the linear graph we see, that the simulations for the dark and the illuminated curves show a similar behaviour at high voltages, the voltage discrepancy between both curves is rather constant. However, this is not the case for the measured data, here the curves diverge slightly. This finding corroborates what we found in chapter 5; the current-voltage behaviour of PSCs in the dark is significantly different from the behaviour under illumination. The simulations are able to replicate the illuminated curve well, whereas the simulation of the dark curve slightly diverges from the measured data at high voltages. The same can be seen in the semilogarithmic plot in figure 6.1 (b). Here we also see that the simulation for the illuminated current-voltage curve does not fit the measurement data for values lower than 0.75 V. However, this is not an issue for the observations and conclusions in this chapter, because I will not consider the series resistance for lower voltages in the calculations.

Finally we see that in the semilogarithmic plot the suns-V_OC is asymptotic to the dark current-voltage curve. This is easily understood when considering that the illumination intensity ϕ is reduced towards lower voltages, closing in on the

dark conditions $J_d(V)$ is measured under. The suns-V_{OC} curve intersects $J_i(V)$ at one-sun illumination. The main desirable characteristic of the suns-V_{OC} curve is its independence from ohmic series resistances.

In figure 6.2 we can now see the voltage dependent series resistance $R_s(V)$ as determined by equations 2.10a-2.10c in a semi-logarithmic plot. The analysis of the data is confined to a regime of higher voltages because the suns-V_{OC} characteristic can not be measured to an indefinitely low illumination intensity ϕ. However here the measurements shown as data points show an interesting behaviour. The series resistance calculated from the comparison of $J_i(V)$ to the suns-V_{OC} curve (orange circles) shows higher values towards lower voltages ($\approx$ 0.9 V). When the voltage is increased, the series resistance is reduced and then saturates. I interpret this effect as a possibility to distinguish between the voltage independent ohmic external series resistance $R_{s,ext}$ and the voltage dependent non-ohmic internal series resistance $R_{s,int}(V)$. $R_{s,ext}$ sets a lower limit to the series resistance that can not be changed by applying a voltage to the solar cell, it is signified by the residual resistance at high voltages. From the $J_i(V)$ vs. suns-V_{OC} curve it can be estimated to about 7 Ωcm^2.

When comparing $J_d(V)$ to the suns-V_{OC} data (green squares), we witness an increase of the resistance with lower voltages as well. Eventually however the data diverge towards lower and even negative values. Naturally this is not a physical effect, but caused by limitations of the measurement method. As stated before and evidenced by figure 6.1 (b) the two current-voltage characteristics compared here are very similar at low voltages, amplifying measurement inaccuracies. Therefore I will focus on the series resistance values at $V > 0.95$V. The behaviour is comparable to the curve previously discussed, it is however shifted to slightly higher values of R_s and does not yet saturate to a constant value. The lowest value reached is around 8.5 Ωcm^2.

Finally the comparison between $J_d(V)$ and $J_i(V)$ (purple triangles) yields a data set over a significantly wider range of voltages as neither measurement is confined by illumination intensities. At lower voltage values the data closely matches the results of the $J_i(V)$ vs. suns-V_{OC} comparison. We can see the series resistance R_s increase further with lower voltages and eventually saturates. A saturation can

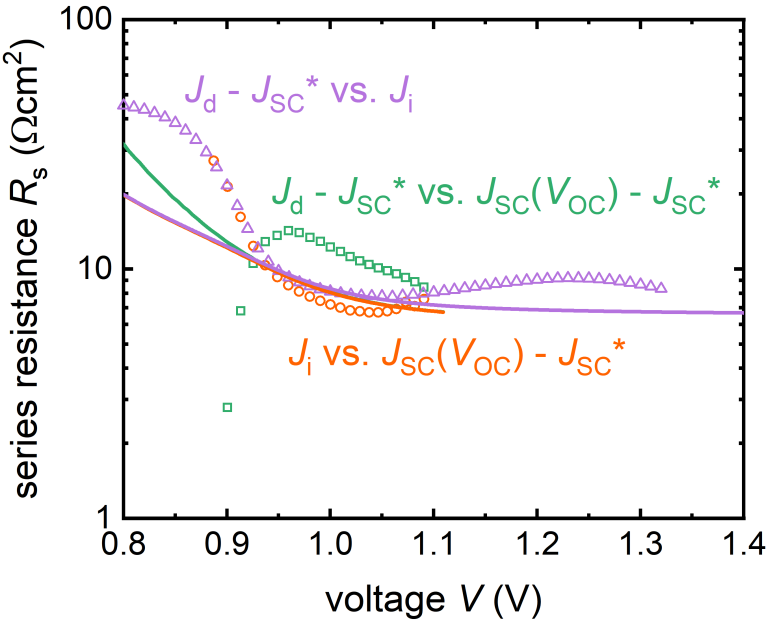

Figure 6.2: Series resistance R_s as a function of externally applied voltage V as determined from the comparison of different current-voltage characteristics. The suns-V_{OC} curve in comparison to the dark current-voltage characteristic $J_d(V)$ (green) as well as the illuminated current-voltage curve $J_i(V)$ (orange) and a comparison of the dark and the illuminated current-voltage characteristic (purple). Measurement results are shown as symbols, simulations are represented by solid lines.

also be observed at high voltages, eventually reaching a value of $R_{s,ext} = 8\ \Omega\text{cm}^2$.

Additionally to the measurement results for the series resistance R_s figure 6.2 shows the series resistances as derived from the simulations shown previously. These data sets show significantly less discrepancies between the three calculation methods than the measurement data exhibited. This emphasizes the necessity for accurate measurements in order to carry out this kind of analysis. The simulations do however fit the measurement data quite well and saturate to comparable values of the external contribution to the series resistance. A discrepancy can however be seen at lower voltages, where the increase of the series resistance is less pronounced in the simulations than it is in the measurements. As was discussed at length in chapter 5, it is far from trivial to simulate this voltage dependent behaviour, especially when a comparison between a cell in the dark and under illumination is part of the model.

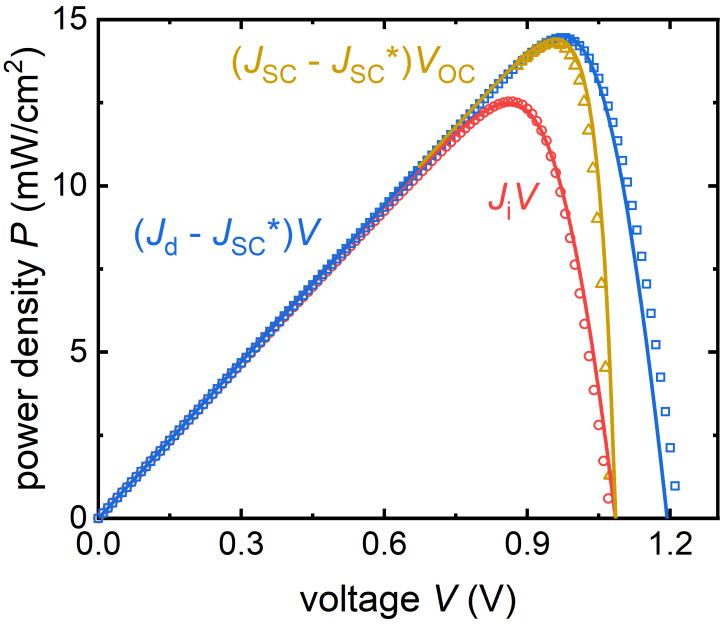

Figure 6.3: Power density P as a function of voltage V for dark (blue) and illuminated (red) current-voltage characteristics as well as the suns-V_{OC} curve (yellow). The short-circuit current density J^*_{SC} taken from $J_i(V)$ was subtracted from the $J_d(V)$ and suns-V_{OC} data before $P(V)$ was calculated. Symbols represent measured data, simulations are shown as solid lines.

The behaviour of both the voltage dependent and independent contributions to the series resistance will be examined for various cell parameters in this chapter.

When evaluating the series resistance of a real or simulated solar cell we naturally always have the functionality of the whole device and correspondingly its efficiency in mind. Accordingly it makes sense to evaluate the power density $P(V)$ that can be extracted from a solar cell in the context of its series resistance, both voltage dependent and independent. In figure 6.3 we see the power density that can be extracted as a function of the applied voltage V corresponding to the three current voltage curves shown in figure 6.1. Measurement results are once again shown as symbols, simulations as solid lines. The red curves shows the behaviour of the cell under one-sun illumination and its maximum signifies the maximum power density that can be extracted from it under standard conditions. The characteristic of the

suns-V_{OC} curve is, that it is independent from ohmic series resistances, therefore the yellow curve shows the power density P the cell could generate under one-sun illumination, if the ohmic contribution to the series resistance $R_{\mathrm{s,ext}} = 0\ \Omega\mathrm{cm}^2$. The theoretical power density generated from the dark current-voltage curve shifted by the short-circuit current density J^*_{SC} from the illuminated curve does not have a physical equivalent. It is shown for comparison and in order to illustrate the behaviour of $J_{\mathrm{d}}(V)$ with respect to the other curves.

6.2 Simulation of Parameters Impacting the Series Resistance

In the previous section we have seen, that the voltage dependent determination of the series resistance $R_{\mathrm{s}}(V)$ enables us to distinguish between ohmic and non-ohmic contributions. As a next step we are going to examine how certain parameters of the layers within a solar cell stack influence both the ohmic $R_{\mathrm{s,ext}}$ and the non-ohmic $R_{\mathrm{s,int}}$. For this we will keep all simulation parameters the same as they were for the simulations in the previous section and vary only one to observe its impact.

6.2.1 External Series Resistance

The simplest example is to vary the series resistance R_{s} as it is implemented in the simulation software ASA. Here this series resistance is assumed as an external element of the equivalent circuit and therefore acts exactly as we defined the external series resistance $R_{\mathrm{s,ext}}$. In figure 6.4 (a) we see the voltage dependent series resistance calculated as introduced in the previous chapter. The external series resistance was varied logarithmically from 1 to 10 $\Omega\mathrm{cm}^2$ as indicated by the arrow. For all values chosen we see that the method of calculation does not significantly change the outcome for voltages higher than 0.9 V. At lower values the $J_{\mathrm{d}}(V)$ versus suns-V_{OC} comparison yields considerably higher values for R_{s} than the other two methods. This can be attributed to gradients in the splitting of the quasi-Fermi levels, which are assumed to be flat in the absorber (see [70]). Whereas this assumption holds for the JV_{d} and suns-V_{OC} characteristics that are used to calculate the green curves,

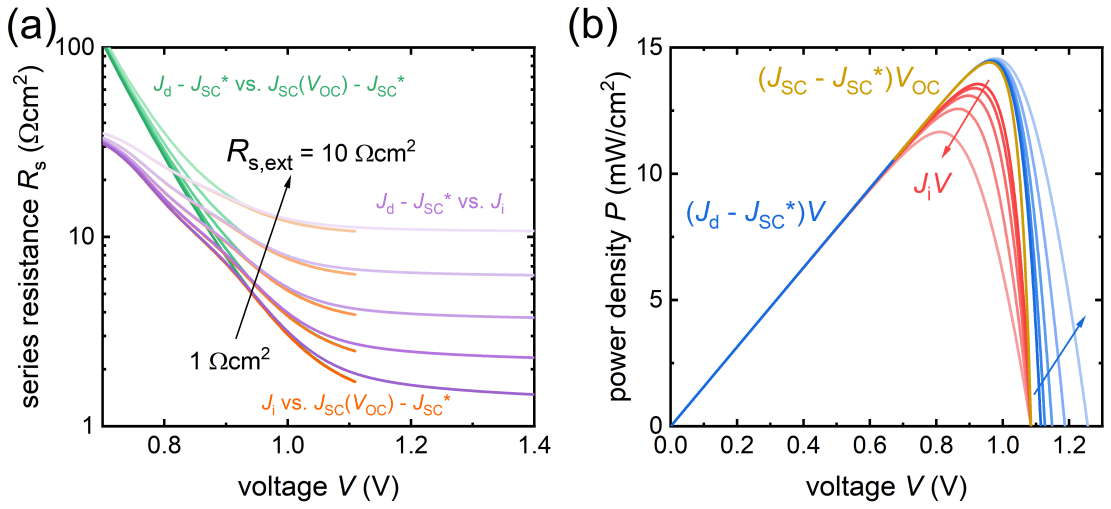

Figure 6.4: (a) Simulated series resistance R_s for varying values of the external series resistance $R_{s,ext} = 1 - 10$ Ωcm^2 implemented in the simulation. The series resistance was calculated using three different approaches comparing two current-voltage characteristics of the solar cell as denoted in the figure. (b) Power density P as a function of voltage derived from the dark current-voltage curve $J_d(V)$ (blue), the illuminated current-voltage curve $J_i(V)$ (red) and the suns-V_{OC} curve (yellow). All curves are shown for the same variation of $R_{s,ext}$, arrows indicating the same directional change of the parameter as indicated in panel (a).

the JV_i data is determined utilizing significantly non-flat QFL splittings at low voltages. This leads to a reduced calculated series resistance R_s at low voltages as can be observed for the purple and orange curves. Towards higher voltages the JV_d versus $J_i(V)$ curves and the $J_i(V)$ versus suns-V_{OC} curves also diverge slightly. However both show a similar trend and equilibrate towards a value similar to the external series resistance set in the simulation. The $J_d(V)$ versus $J_i(V)$ curve for the lowest value set reaches $R_{s,ext}(1.4\text{ V}) = 1.47$ Ωcm^2, whereas the highest value only lets it go down to $R_{s,ext}(1.4\text{ V}) = 10.7$ Ωcm^2. This corroborates our interpretation of the saturation point of the voltage dependent series resistance curves as the ohmic external series resistance $R_{s,ext}$. At lower voltages the series resistance increases, however here the curves for the varied external component converge as it becomes less and less significant. As would be expected, the non-ohmic internal contribution to the series resistance $R_{s,int}$ remains unchanged.

In figure 6.4 (b) we see the power density curves for the three current-voltage characteristics examined. The first thing to notice is that the suns-V_{OC} curve remains unchanged for all values of $R_{\mathrm{s,ext}}$ as the V_{OC} is independent from any series resistive effects. There are nonzero changes due to a reduction in J_{SC}, however these are insignificantly small. The power density curve relating to the illuminated current-voltage characteristic is reduced by the increasing series resistance as it reduces the fill factor FF and subsequently the power that can be extracted at the maximum power point. J_{SC} and V_{OC} remain largely unchanged. The curves relating to $J_{\mathrm{d}}(V)$ see a slight increase of the maximum power density due to an increased V_{OC} and a simultaneously unchanged J_{SC}. The slope of the right flanks of the curves relating to $J_{\mathrm{d}}(V)$ and $J_{\mathrm{i}}(V)$ are the same due to the constant series resistance that defines the distance between them.

6.2.2 Absorber Charge Carrier Mobilities

Now that we have understood how the external series resistance impacts the curves for the voltage dependent series resistance and the power density, we can take a look at a parameter that influences the internal component of the series resistance $R_{\mathrm{s,int}}$. In figure 6.5 (a) we see the voltage dependent series resistance for different values of the charge carrier mobility μ_{pero} in the perovskite absorber. The mobility was varied logarithmically from 100 $\mathrm{cm}^2/\mathrm{Vs}$ down to 1 $\mathrm{cm}^2/\mathrm{Vs}$. The first thing to notice is that for all methods of R_{s} calculation the curves converge at an external series resistance of approximately $R_{\mathrm{s,ext}} = 7\ \Omega\mathrm{cm}^2$. This means that a change of the charge carrier mobilities in the perovskite absorber does not lead to an increase in the ohmic resistance exhibited by the cell. At lower voltages however the series resistance is significantly increased. The slope of the R_{s}-increase is roughly constant for all values of μ_{pero}, but it is shifted towards higher voltages for reduced charge carrier mobilities. This means that a reduction of μ_{pero} necessitates a higher externally applied voltage to reduce the series resistance to the external ohmic minimum. This shift of the R_{s}-slope can be observed for all calculation methods.

In panel (b) of figure 6.5 we see again see the curves of the voltage dependent power density P. As was the case for the external series resistance before, an increase of the internal series resistance reduces the maximum power density output of the

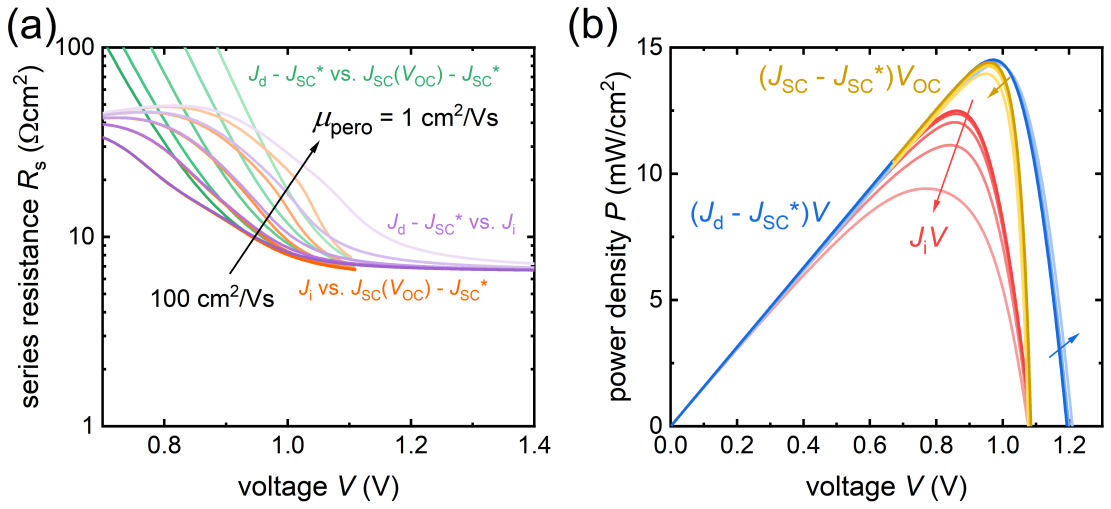

Figure 6.5: (a) Simulated series resistance R_s for varying values of the charge carrier mobility in the perovskite absorber $\mu_{pero} = 100 - 1$ cm^2/Vs. The series resistance was calculated using three different approaches comparing two current-voltage characteristics of the solar cell as denoted in the figure. (b) Power density P as a function of voltage derived from the dark current-voltage curve $J_d(V)$ (blue), the illuminated current-voltage curve $J_i(V)$ (red) and the suns-V_{OC} curve (yellow). All curves are shown for the same variation of μ_{pero}, arrows indicating the same directional change of the parameter as indicated in panel (a).

cell under illumination (red curves). Noticeably for this case the suns-V_{OC} curves show a change as well. Due to the weaker transport properties of the absorber the open-circuit voltage is reduced as well which in turn impacts the suns-V_{OC} curve. This shows that while the suns-V_{OC} characteristic is mostly unchanged due to ohmic series resistances, non-ohmic contributions due to for example transport limitations can impact it. It is also noteworthy that the power density curves derived from the dark current-voltage characteristic are almost unchanged. This shows again, that the behaviour of the cell in the dark is rather disconnected from the illuminated view. The slight shift of the right-hand side of the curve relates to an increase of the series resistance at voltages as high as V_{OC}.

6.2.3 Transport Layer Charge Carrier Mobilities

Not only the charge carrier mobilities in the perovskite absorber can inhibit the extraction of charge carriers, it can also be hindered by low mobilities in the transport layers. In order to evaluate the influence of a transport layer we will first take a look at the electron conducting layer, which in my experiments was formed by PCBM. To emulate the effect of a screened field in the absorber, the simulations were conducted both at a plausible value of the perovskite permittivity $\epsilon_{\mathrm{pero}} = 30$ as a well as an arbitrarily high value chosen to be $\epsilon_{\mathrm{pero}} = 10000$. As was the case in the previous chapters, this high value is used to screen as much of the electric field from the absorber as possible, emulating the effect of moving ionic defects rearranging to the same effect. In figure 6.6 (a) we can see the variation of the series resistance when decreasing the charge carrier mobility μ_{PCBM} in the ETL. Interestingly for the curves taking into account the illuminated current voltage characteristic $J_{\mathrm{i}}(V)$ (orange and purple), the voltage dependent internal component of the series resistance $R_{\mathrm{s,int}}$ is rather unchanged, their series resistances converging for lower voltages. Their lowest saturation point at high voltages however is increased by a reduction of the charge carrier mobility μ_{PCBM}. This means that in the examined cell configuration the ETL acts like a resistor, its resistance being modulated by the charge carrier mobility. Any externally applied voltage will to a considerable extent be absorbed by the bulk perovskite, while the field in the ETL is not changed as much. However a change of the electric field in the ETL is still taking place, which is why the R_{s}-curves do look different from the ones in figure 6.4 (a). There is a discrepancy in the slope at intermediate voltages indicating a weak underlying non-ohmic resistance effect.

The ohmic behaviour of the series resistance induced by a change of the ETL mobilities is reflected in the power density P curves in figure 6.6 (b). As was the case for the variation of the external series resistance $R_{\mathrm{s,ext}}$, the suns-V_{OC} curve is almost unaffected by the changes as it is independent from ohmic series resistances. However the fill factor of the illuminated characteristic $J_{\mathrm{i}}(V)$ is reduced subsequently reducing its power density output. The curves relating to $J_{\mathrm{d}}(V)$ again show an increase in V_{OC} caused by the reduced fill factor FF of the cell.

In order to compare the situation described above to a cell with a screened electric field in the absorber the same simulations were run with an increased per-

mittivity in the perovskite of $\epsilon_{\text{pero}} = 10000$. The resulting values for the series resistance R_{s} are shown in figure 6.6 (c). Here we see that the situation has changed significantly. The settling point of the series resistance towards higher voltages still increases with a reduction of the charge carrier mobility in the PCBM layer indicating an ohmic behaviour. However at intermediate voltages (0.85 - 1.15 V) the curves have undergone remarkable changes. All curves show a significant increase of the series resistance towards lower voltages. This means that if the electric field is screened from the absorber the transport layers can induce non-ohmic resistances in the solar cell. In other words, even if the diffusion lengths in the perovskite absorber are very high, significantly exceeding the thickness of the layer, there can still be diffusive collection losses due to limited charge carrier mobilities in the transport layers. In this case the losses are modulated by the externally applied voltage as the field screening in the absorber and the low thickness of the HTL push all the potential changes into the ETL. Therefore the voltage strongly changes the field in the ETL, reducing the transport losses within.

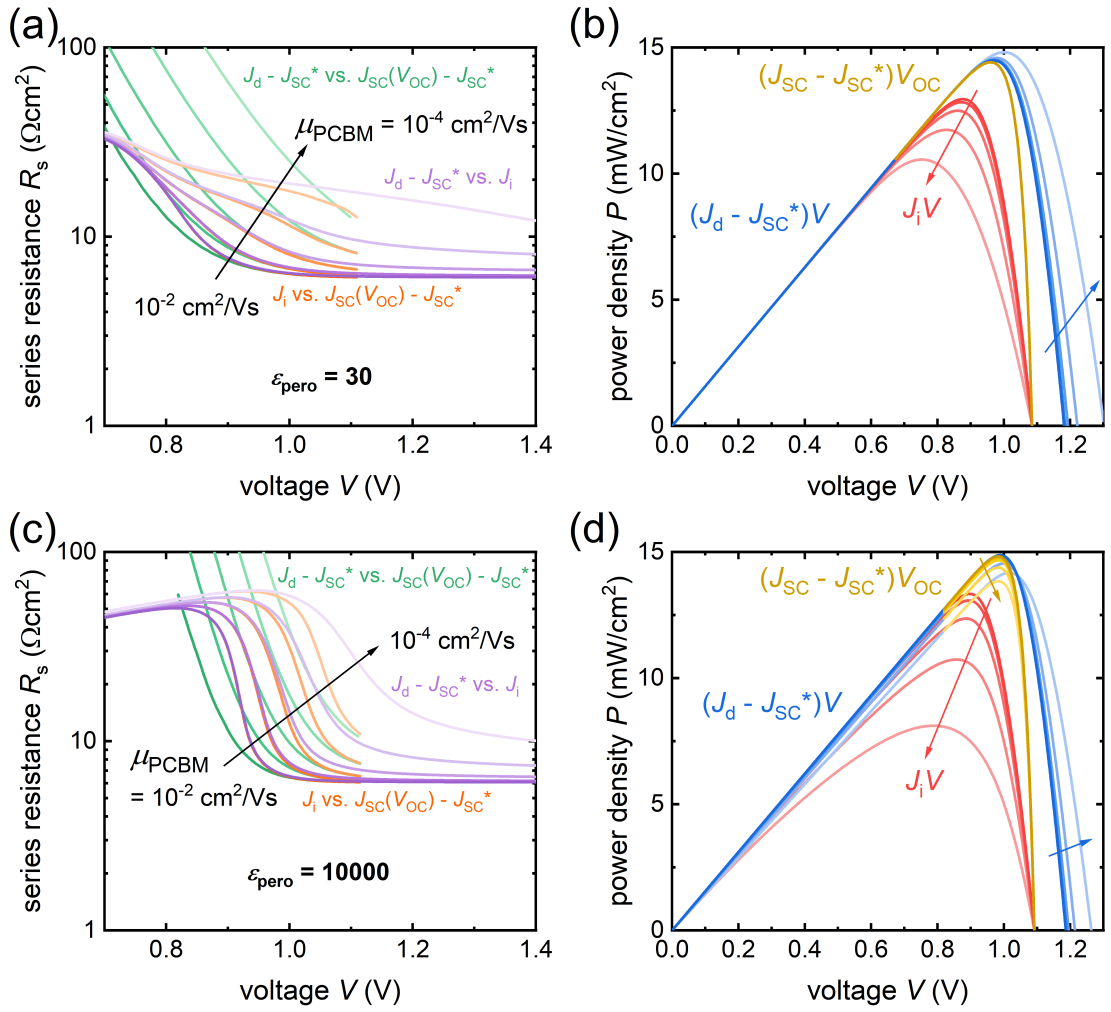

Figure 6.6: (a) Simulated series resistance R_s for varying values of the charge carrier mobility in the PCBM electron transport layer $\mu_\mathrm{PCBM} = 10^{-2} - 10^{-4}$ cm^2/Vs with a low permittivity in the perovskite absorber layer $\epsilon_\mathrm{pero} = 30$. The series resistance was calculated using three different approaches comparing two current-voltage characteristics of the solar cell as denoted in the figure. (b) Power density P as a function of voltage derived from the dark current-voltage curve $J_\mathrm{d}(V)$ (blue), the illuminated current-voltage curve $J_\mathrm{i}(V)$ (red) and the suns-V_OC curve (yellow). All curves are shown for the same variation of μ_PCBM at the same ϵ_pero, arrows indicating the same directional change of the parameter as indicated in panel (a). Panels (c) and (d) are equivalent to (a) and (b) except for a higher permittivity $\epsilon_\mathrm{pero} = 10000$ screening the field from the absorber.

This is also reflected by the power density curves shown in figure 6.6 (d). The curves for the illuminated case $J_\mathrm{i}(V)$ are affected significantly stronger than they

were in the previous case. This is especially reflected by the slope of the left-hand side of the curve, which indicates the short-circuit current density J_{SC}. The reduction of this slope shows, that the effect of the transport limitation in the ETL is strong enough to reduce the current extracted from the cell. In the classical description of a diode the series resistance would not be capable of influencing J_{SC}. The reduction of J_{SC} also influences the suns-V_{OC} curve leading to a reduction of the potential power density P with lower charge carrier mobilities in the ETL.

In order to further illustrate the relationship between the difference $V_{\mathrm{d}} - V_{\mathrm{i}}$ and the series resistance R_{s}, figure 6.7 shows four band diagrams of a field screened cell. Panels (a) and (c) correspond to the highest simulated value of $\mu_{\mathrm{PCBM}} = 10^{-2}$ cm^2/Vs and panels (b) and (d) utilize the lowest simulated value (10^{-4} cm^2/Vs). (a) and (b) were simulated in the dark, (c) and (d) were simulated under one-sun illumination. For all simulations the voltage bias was chosen such that the dark and the illuminated cases yield an equal recombination current density J_{rec}. The current density for the illuminated simulation is chosen as the J_{MPP}, accordingly the current density for the dark simulation is $J = J^*_{\mathrm{SC}} - J_{\mathrm{MPP}}$.

Figure 6.7 (a) shows the band diagram of a cell with high charge carrier mobility in the PCBM in the dark. The Fermi levels are flat across the entire layer stack and therefore the external voltage is practically identical to the splitting of the QFLs. In panel (b) the same situation is shown for a significantly lower mobility in the PCBM. Here the PCBM layer acts as a resistor for the introduction of charge carriers into the bulk perovskite. In order to inject the charge carriers into the cell a higher external voltage is necessary, leading to a gradient in E_{Fn} facilitating the electron transport. This gradient also means that there is a significant difference between the externally applied voltage and the splitting of the QFLs.

Figure 6.7 (c) depicts the band diagram for the same cell as (a) under illumination. Here we see a gradient of E_{Fn} in the PCBM but in the opposite direction to the one seen in panel (b). This gradient is necessary to extract the generated electrons from the absorber. Accordingly the external voltage is lower than the QFL splitting. This effect is amplified significantly by a decrease of the PCBM mobility as can be seen in (d). The gradient in the PCBM layer is increased as well as the difference between external voltage and QFL splitting. These gradients in the PCBM are the

cause of the voltage dependent contributions to the series resistance seen in figure 6.6 (c) and they are modulated by the charge carrier mobility in the PCBM layer. The differences in V_{ext} between the upper and the lower panels in figure 6.7 are used to calculate the series resistance via equation 2.10a.

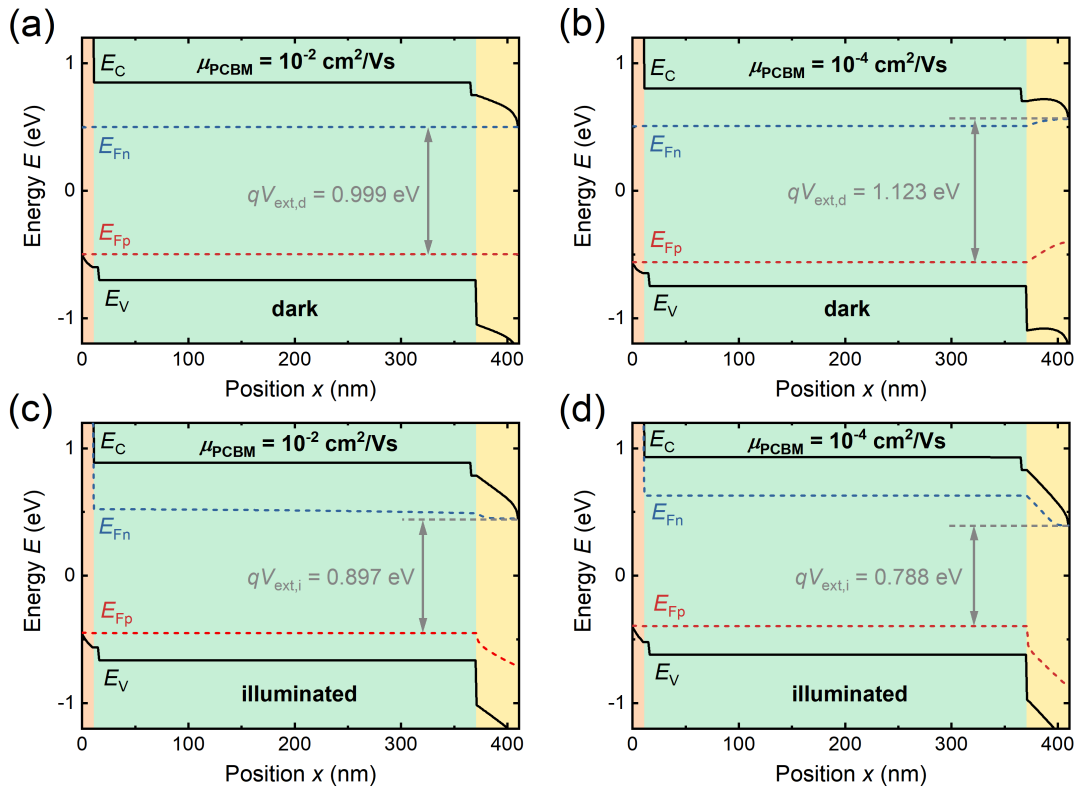

Figure 6.7: Simulated band diagrams corresponding to the simulations shown in this chapter utilizing charge carrier mobilities in the PCBM layer of (a, c) 10^{-2} cm^2/Vs and (b,d) 10^{-2} cm^2/Vs. Panels (a) and (b) represent band diagrams in the dark at a current $J = J_{\mathrm{MPP}} - J_{\mathrm{SC}}$. Panels (c) and (d) show band diagrams under illumination at the maximum power point. The difference in voltage corresponds to the one used in equation 2.10a to calculate R_{s}.

In figure 6.8 (a) we see the changes in series resistance induced by a variation of the charge carrier mobilities μ_{PTAA} in the hole transport layer which in my experiments consists of PTAA. Since the layer is quite thin, even mobilites as low as 10^{-4} cm^2/Vs do not have a significant impact on charge extraction and series resistance R_{s}. Once the charge carrier mobilities reach a critical point however they create

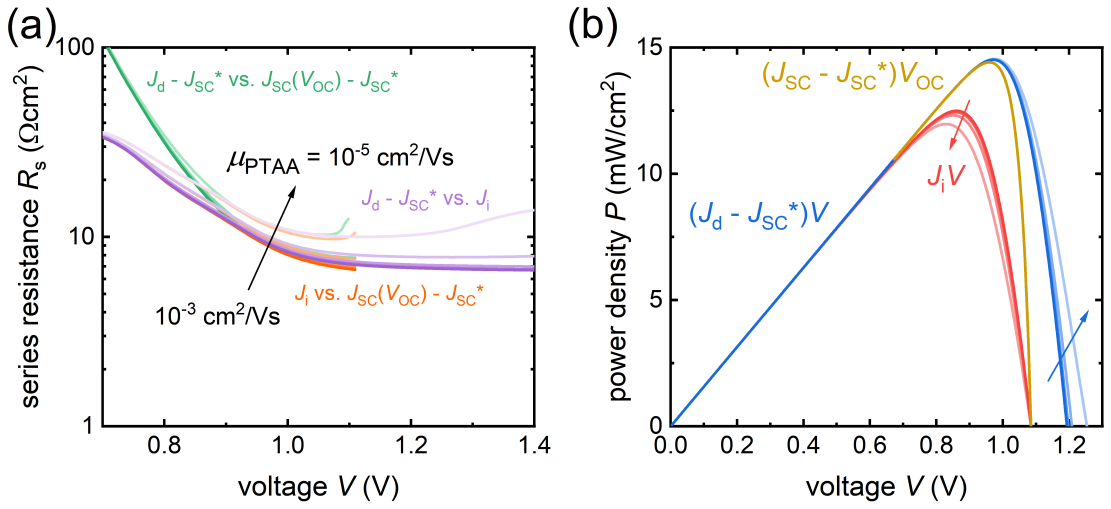

Figure 6.8: (a) Simulated series resistance R_s for varying values of the charge carrier mobility in the PTAA hole transport layer $\mu_\mathrm{PTAA} = 10^{-3} - 10^{-5}$ cm^2/Vs. The series resistance was calculated using three different approaches comparing two current-voltage characteristics of the solar cell as denoted in the figure. (b) Power density P as a function of voltage derived from the dark current-voltage curve $J_\mathrm{d}(V)$ (blue), the illuminated current-voltage curve $J_\mathrm{i}(V)$ (red) and the suns-V_OC curve (yellow). All curves are shown for the same variation of μ_PTAA, arrows indicating the same directional change of the parameter as indicated in panel (a).

an ohmic resistive effect quickly reducing the functionality of the simulated cell. In the figure we see that eventually the external series resistance at high voltages is rapidly increasing. In panel (b) we can see the corresponding reduction of the power density P from the illuminated solar cell, while the suns-V_OC characteristic is unchanged. Except for the reduced influence on the cell as a whole the HTL functions anologously to the ETL discussed before. In the case of a screened electric field in the absorber this effect will not change significantly as the non-ohmic contribution to the series resistance will be dominated by the thicker ETL.

In summary we have learned that the influence of the transport layer charge carrier mobilities on the series resistance R_s is strongly influenced by the overall field distribution within the solar cell as a whole. If the electric field in a transport layer is largely unchanged with the external voltage, its resistive influence will be mostly of ohmic nature, whereas ionic movement can cause a significant voltage

dependence in the series resistance caused. In this case the charge carrier mobilities in the transport layers can cause significant non-ohmic effects to the series resistance R_s.

6.2.4 Electric Field Screening

Next we will have a look at the effect of the increase of the dielectric permittivity in the perovkite absorber ϵ_pero on the cell as a whole. We will do this for two cases, the basic case from approximating the measurement data with a charge carrier mobility in the absorber of $\mu_\mathrm{pero} = 100\mathrm{cm}^2/\mathrm{Vs}$ and secondly with a reduced value of $mu_\mathrm{pero} = 1\mathrm{cm}^2/\mathrm{Vs}$. Figure 6.9 (a) shows the change in series resistance R_s for the case with a high charge carrier mobility in the absorber. We can see that for all methods of calculation the slope of the series resistance increases significantly and is moved towards higher voltages. However the ohmic contribution to the series resistance at high voltages is slightly reduced. When we take a look at the power density P curves in panel (b) we see a rather surprising development. The power density that can be taken from the illuminated cell at the MPP is only slightly reduced and the MPP for the suns-V_OC curve and the curve relating to $J_\mathrm{d}(V)$ is even increased. This is the case because there are two competing processes taking place. On the one hand the electric field is screened from the perovskite absorber, slightly hindering charge carrier extraction. Since the diffusion lengths of charge carriers within the bulk absorber are very high, they can still be extracted rather efficiently. Therefore the field screening only reduces the short-circuit current density J_SC slightly as evidenced by the left-hand slope of the P-curve. At the same time the screened electric field is moved to the low charge carrier mobility ETL, improving charge extraction. This leads to a slightly increased open-circuit voltage V_OC subsequently increasing the power density P.

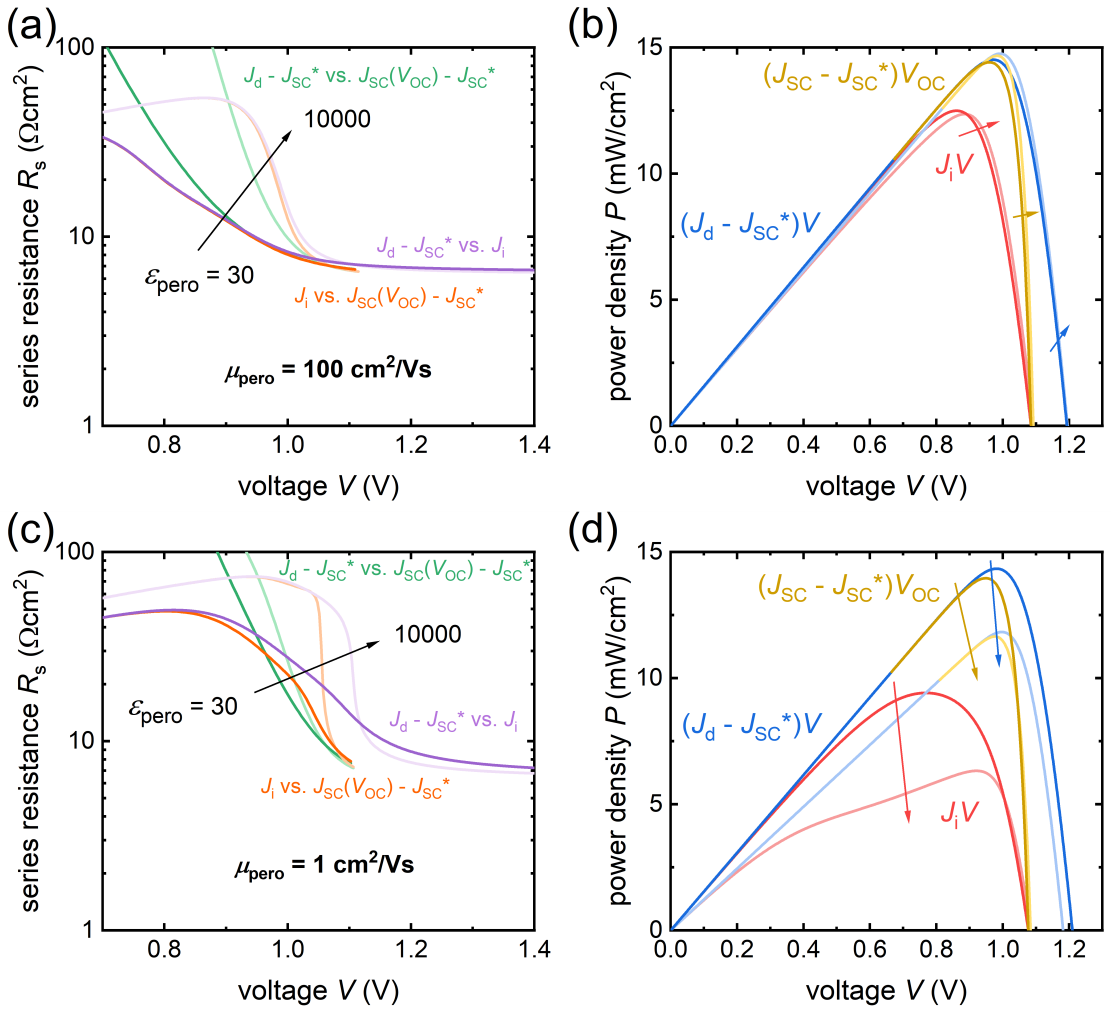

Figure 6.9: (a) Simulated series resistance R_s for a literature value of the dielectric permittivity in the perovskite absorber $\epsilon_{pero} = 30$ as well as an arbitrarily high value $\epsilon_{pero} = 10000$ screening the field from the absorber. The charge carrier mobility in the absorber is set to $\mu_{pero} = 100$ cm^2/Vs. The series resistance was calculated using three different approaches comparing two current-voltage characteristics of the solar cell as denoted in the figure. (b) Power density P as a function of voltage derived from the dark current-voltage curve $J_d(V)$ (blue), the illuminated current-voltage curve $J_i(V)$ (red) and the suns-V_{OC} curve (yellow). All curves are shown for the same values of ϵ_{pero}, arrows indicating the same directional change of the parameter as indicated in panel (a). Panels (c) and (d) are equivalent to (a) and (b) except for a lower charge carrier mobility in the absorber $\mu_{pero} = 1$ cm^2/Vs.

If we now take a look at the series resistances in figure 6.9 (c) for the case

of a reduced μ_{pero}, a different situation presents itself. The slope of the series resistance is significantly increased and moved to higher voltages. While we still see a decrease of the ohmic contribution to the series resistance at high voltages, the voltage dependent series resistance is strongly amplified. In panel (d) we see that the output power density of the cell is significantly reduced due to the field screening in the absorber. While the increased field in the transport layers still leads to an increase in the open-circuit voltage V_{OC}, the short-circuit current density J_{SC} is severely reduced due to charge carriers unable to diffuse out of the absorber. This reduction of J_{SC} also leads to a reduction of the maximum power density P that can be extracted from the $R_{\mathrm{s,ext}}$-independent suns-V_{OC} characteristic as the non-ohmic resistive effect of the limited charge carrier mobility μ_{pero} in the perovkite is exacerbated.

Overall we have seen that the influence of field screening induced by ionic defect redistribution can have vastly differing effects on a perovskite solar cell depending on the material properties of the cell. If the perovskite absorber shows remarkably good conducting properties, it may actually aid the functionality of the cell by diverting the electric field to the low mobility transport layers. If the conducting properties of the absorber are limited however, the screening of the field can substantially limit the functionality of the cell by introducing a strong internal series resistance $R_{\mathrm{s,int}}$.

6.2.5 Extraction Offsets

Finally we will take a look at the extraction offsets that can be present at both the front contact and the back contact of a solar cell. These boundary conditions refer to the offset between the bands in the transport layers carrying the respective majority carriers and the work function φ_{m} of the metal contact. Here we are looking at offsets where the work function in the metal contact is electrically favourable to the transport layer easing the extraction of charge carriers. The effect of such an offset is twofold, it reduces the density of majority carriers in the transport layers and it reduces the electric field within the transport layer by reducing the energy difference between the band energy in the absorber and the metal work function φ_{m}.

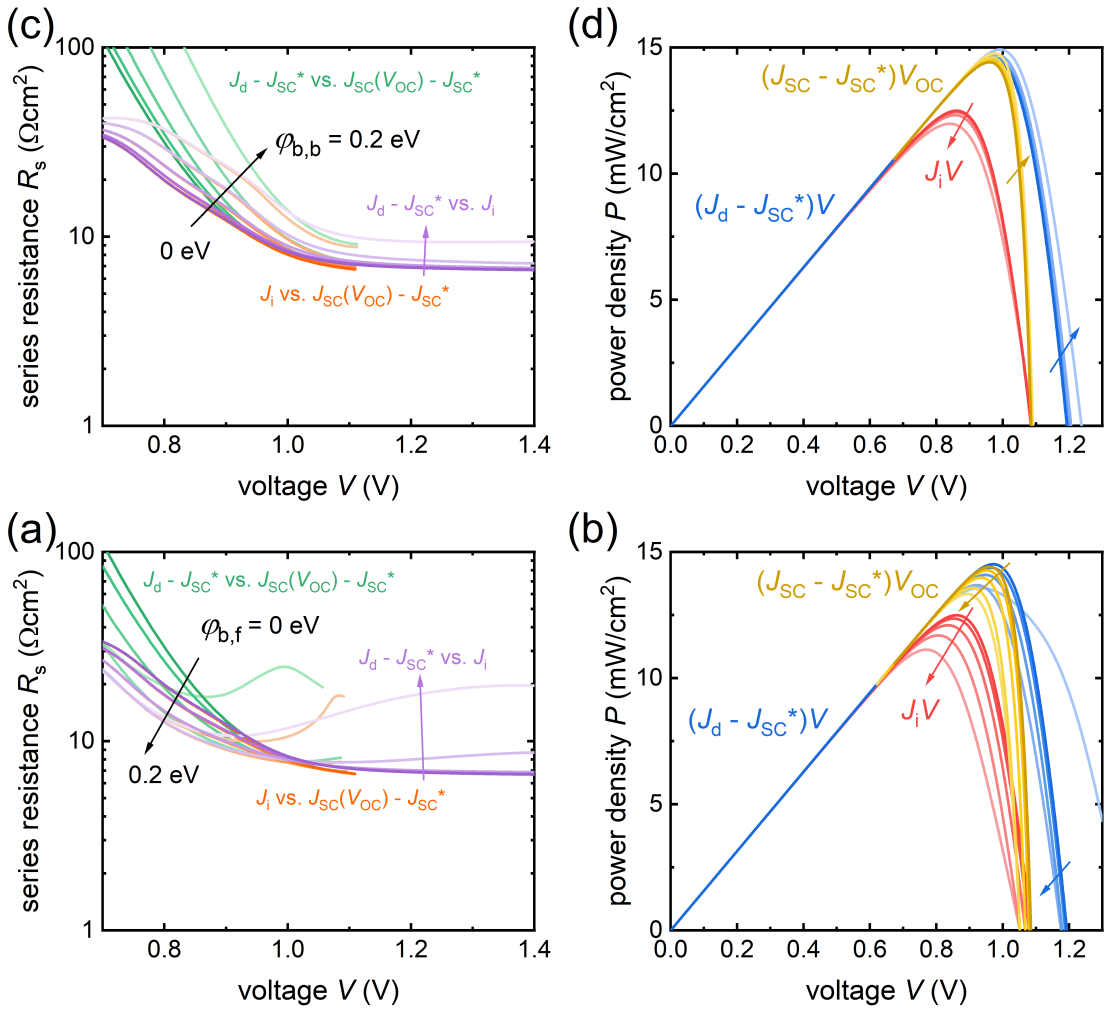

Figure 6.10: (a) Simulated series resistance R_s for varying values of the extraction barrier $\varphi_{b,b} = 0 - 0.2$ eV at the front contact of the cell. The series resistance was calculated using three different approaches comparing two current-voltage characteristics of the solar cell as denoted in the figure. (b) Power density P as a function of voltage derived from the dark current-voltage curve $J_d(V)$ (blue), the illuminated current-voltage curve $J_i(V)$ (red) and the suns-V_{OC} curve (yellow). All curves are shown for the same values of ϵ_{pero}, arrows indicating the same directional change of the parameter as indicated in panel (a). Panels (c) and (d) show the same results for a variation of the extraction barrier $\varphi_{b,b} = 0 - 0.2$ eV at the back of the cell.

In figure 6.10 (a) we see the voltage dependent series resistance for a variation of the extraction offset $\varphi_{b,f}$ at the frontside of the solar cell which in this case pertains to the PTAA hole transport layer. Here we see two different effects for the nonohmic

contribution to the series resistance and the ohmic contribution at high voltages. At lower voltages the series resistance is reduced by an increase in the offset at the contact because charge extraction is improved. Since the PTAA layer is rather thin this also leads to the hole concentration in the absorber being reduced because charge extraction is accelerated. Therefore the voltage-dependent series resistance is reduced. Meanwhile at low values of $\varphi_{\mathrm{b,f}}$ the ohmic part of the series resistance is almost unchanged. This aligns with the behaviour we saw for the change of the charge carrier mobility μ_{PTAA} in figure 6.8 (a). At higher values of $\varphi_{\mathrm{b,f}}$ however the ohmic series resistance sharply increases. This is the point where the electric field in the HTL is fully compensated and the offset towards the metal work function φ_{m} induces a barrier hampering extraction. This subsequently rapidly reduces charge extraction and increases the series resistance R_{s}.

In figure 6.10 (b) we can see the effect on the power density P of these changes. While charge extraction is slightly improved by the offset it also significantly reduces the open-circuit voltage V_{OC}. Not only does this lead to a reduction of the power density under illumination, but it also reduces the maximum of the curves relating to the suns-V_{OC} curves. The curves pertaining to the $J_{\mathrm{d}}(V)$ simulations show a similar trend for the V_{OC} with it spiking in the end due to the formation of an extraction barrier.

When we consider the same sort of extraction offset at the backside of the cell by increasing the value for $\varphi_{\mathrm{b,b}}$, we see a different trend of the series resistance as shown in figure 6.10 (c). In this case both the non-ohmic and the ohmic contributions increase with an increasing offset. This is the case because the PCBM layer functioning as the ETL at the back is significantly thicker than the HTL and therefore has a much stronger negative impact on charge extraction. Here an increasing extraction offset $\varphi_{\mathrm{b,b}}$ only manifests itself in a reduction of majority carriers close to the metal interface. However the reduction of the electric field in the PCBM layer has a significantly higher impact on the cell amplifying the resistive effects of the layer. As a result more charge carriers remain the the absorber than for the increase of the extraction offset. The additional deterioration of the conduction properties of the ETL lead to a reduction in the internal series resistance $R_{\mathrm{s,int}}$ and at higher values it also increases the ohmic series resistance. This is again in line with the

impact of the charge carrier mobility μ_{PCBM} shown in figurea 6.6 (a) and (c).

In figure 6.10 (d) we see the changes to the power density curves corresponding to the variation of $\varphi_{\mathrm{b,b}}$. We see that the reduction in efficiency for an illuminated cell is actually significantly lower. While the extracted current is reduced this effect is partly compensated by an increase of the open-circuit voltage V_{OC} due to the increased density of charge carriers remaining in the cell. For the curves relating to the suns-V_{OC} characteristic this increase in open-circuit voltage even leads to a slight increase of its maximum power density P, the V_{OC} increases anologously for the curves corresponding to $J_{\mathrm{d}}(V)$.

Overall we find that the influence of the offsets at the metal contacts can have significantly different impacts on the series resistance R_{s} as well as the cell functionality. The negative effects can be strongly modulated by the transport layer characteristics.

6.3 Voltage Dependent Series Resistance Derived from Luminescence Measurements

Aside from comparing current-voltage characteristics of a solar cell there are of course further methods to determine the series resistance R_{s}. In chapters 4 and 5 I have discussed the characteristics of the internal voltage V_{int} of a perovskite solar cell in relation to the externally applied voltage V_{ext}. This characteristic was also measured for the cell examined in this chapter, the resulting data is shown in figure 6.11 (a). The cell exhibits a lower internal voltage at short circuit $V_{\mathrm{int,0}}$ than the cell shown inf chapter 5, but the general behaviour with respect to the external voltage V_{ext} is very similar. From the relationship between the internal and the external voltage we can calculate the series resistance as

$$R_{\mathrm{s}}(V_{\mathrm{ext}}) = \frac{V_{\mathrm{int}} - V_{\mathrm{ext}}}{J}, \tag{6.1}$$

as Rau et al. did for CIGS-type cells [144]. This way we assume the series resistance R_{s} to be the retarding factor inhibiting the internal voltage V_{int} to be fully usable externally. The voltage dependent series resistance R_{s} resulting from this calculation

is shown in a semilogarithmic plot in figure 6.11 (b). The first observation we make is that at all illumination intensities the series resistance increases strongly towards low voltages. Secondly we see that the series resistance R_s is significantly reduced with increased illumination intensity. This shows that the series resistance is not only dependent on the voltage applied to the cell, but on the illumination intensity as well. This is easily understood considering the logarithmic dependency of the internal voltage on the illumination intensity ϕ as defined in equation 3.11. However the short-circuit current density J_SC as well as the current density for all low to intermediate voltages is linearly dependent on the illumination intensity ϕ. This leads to a dependency for the series resistance $R_\mathrm{s} \propto \ln(\phi)/\phi$ elucidating the cause for the improvement of the series resistance due to increased illumination intensity ϕ. The change in series resistance therefore also depends on the short-circuit ideality factor $n_\mathrm{id,SC}$. If we take a look at higher external voltages we see, that the series resistance again saturates at a minimum value which remains rather constant. Since the measurement data is only taken up to voltages of about 1.1 V not curves were able to fully saturate leading to slight offsets in the levels for the external series resistance $R_\mathrm{s,ext}$. However the trend towards a shared minimum value is visible and the results from the luminescence-based determination of the series resistance is in accordance with the methods previously discussed in this chapter.

6.4 Conclusion

In this chapter I discussed several different methods of calculating the series resistance R_s of a solar cell and applied these methods to perovskite solar cells. Transcending the simple derivation from the slope of the dark current-voltage curve, I calculated R_s from the comparison of three different current-voltage characteristics as well as a comparison between the internal voltage V_int and the external voltage V_ext. With these methods I was able to calculate the series resistance as a function of the externally applied voltage and differentiate between a voltage independent external component $R_\mathrm{s,ext}$ of the series resistance as well as a voltage dependent internal contribution $R_\mathrm{s,int}$. I then showed by the means of simulations which parameters influence these two components of the series resistance. While external ohmic resis-

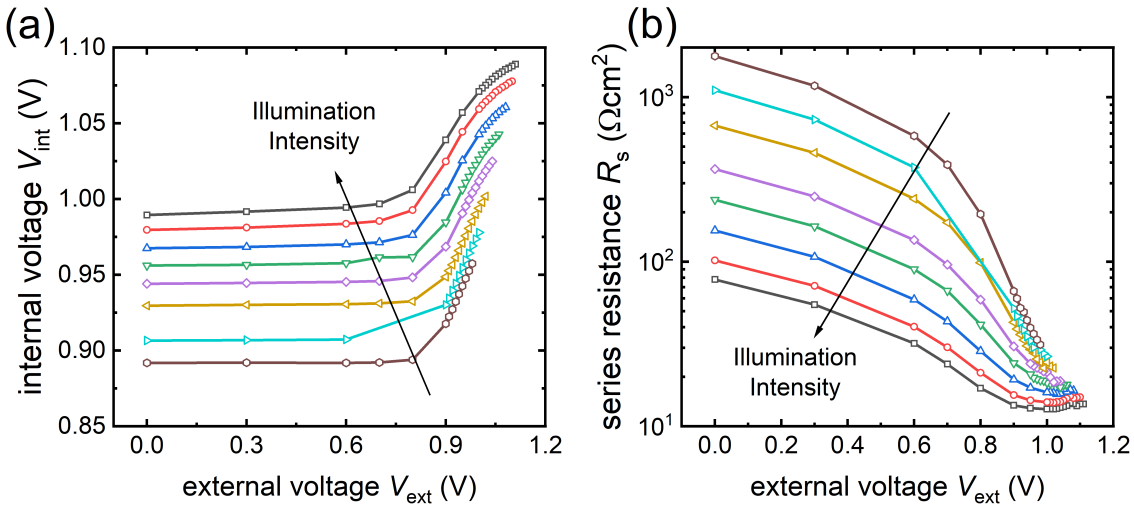

Figure 6.11: (a) The internal voltage V_{int} calculated from photoluminescence measurements shown as a function of the external voltage applied to the solar cell. The curves relate to different illumination intensities ϕ as indicated by the arrow. (b) The voltage dependent series resistance R_{s} calculated from the relation of the internal voltage to the external voltage.

tors expectedly contributed to the voltage independent component, charge carrier mobilities in the absorber as well as the transport layers determined the voltage dependent part. I elucidated how these parameters interact with the electric field in the solar cell and the screening thereof by changing the permittivity of the absorber. Finally I discussed the influence of energetic offsets at the interfaces between transport layers and metal contacts and how their influence is governed by the properties of the transport layers.

Table 6.1: Parameter values used for the simulations shown in this chapter.

Parameter	**Simulation**
band gap E_g	1.55 eV
E_A perovskite	4 eV
N_C perovskite	$2 \cdot 10^{18}$ cm^{-3}
N_V perovskite	$2 \cdot 10^{18}$ cm^{-3}
μ perovskite	100 cm^{2}V^{-1}s^{-1}
τ perovskite	$2 \cdot 10^{-8}$ s
k_{rad} perovskite	$5 \cdot 10^{-11}$ cm^{3}s^{-1}
ϵ perovskite	30
E_g PCBM	1.8 eV
E_A PCBM	4.1 eV
N_C PCBM	$2 \cdot 10^{19}$ cm^{-3}
N_V PCBM	$2 \cdot 10^{19}$ cm^{-3}
μ PCBM	10^{-3} cm^{2}V^{-1}s^{-1}
ϵ PCBM	3
E_g PTAA	3 eV
E_A PTAA	2.45 eV
N_C PTAA	$2 \cdot 10^{18}$ cm^{-3}
N_V PTAA	$2 \cdot 10^{18}$ cm^{-3}
μ PTAA	10^{-3} cm^{2}V^{-1}s^{-1}
ϵ PTAA	3
μ interface PCBM	1 cm^{2}V^{-1}s^{-1}
τ interface PCBM	$3 \cdot 10^{-7}$ s
μ interface PTAA	1 cm^{2}V^{-1}s^{-1}
τ interface PTAA	$3 \cdot 10^{-7}$ s
R_s	6 Ωcm^2
R_p	$5 \cdot 10^3$ Ω
T	300 K
$\phi_{b,f}$	0 eV
$\phi_{b,b}$	0 eV

7 Conclusion and Outlook

The main goal of this work was to gain insights into the extraction and recombination of charge carriers in perovskite solar cells. To this end I started out by conducting electrical simulations of generic cell architectures as they are used in thin-film solar cells. This way I was able to understand the impact of different layer stacks on the band diagram, especially with respect to the doping density and field screening effects due to mobile ionic defects. The field screening induced by the redistribution of the ionic defects was emulated by increasing the dielectric permittivity ϵ. The simulations of the various cell compositions yielded current voltage behaviour in the dark and under illumination as well as the internal voltage $V_{\mathrm{int}}(V_{\mathrm{ext}})$ as a measure of the density of charge carriers remaining in the bulk absorber. From these characteristic curves I was able to both calculate the ideality factor at open-circuit $n_{\mathrm{id,OC}}$ as well as a newly defined ideality factor at short-circuit $n_{\mathrm{id,SC}}$. The behaviour of all of the aforementioned characteristics of the simulated cells was interpreted yielding a foundation for the understanding of full measured sets of this kind of data. The ideality factors were also evaluated in the framework of a theory founded on the extraction current densities J_{extr} in the transport layers. While these calculations granted insights into the dependendy of the ideality factors on the transporting properties and the electric field distribution within a solar cell, they were only valid for cells with flat bands in the absorber. In the future this theory can be expanded to include the transport characteristics in the absorber in order to interpret ideality factors n_{id} in a larger array of situations.

Afterwards a full set of current-voltage curves, internal voltage determined from luminescence measurements and ideality factors was presented. I elucidated the aspects that have to be taken into consideration during the planning stage and during the implementation of the voltage dependent luminescence measurements

necessary to determine the internal voltage V_{int}. Most noteworthy for these measurements was the behaviour of the $V_{\mathrm{int}}(V_{\mathrm{ext}})$ curve, because the internal voltage was remarkably high at short-circuit and remained almost constant up to about 0.9 V. Subsequently efforts were taken to match the measured $V_{\mathrm{int}}(V_{\mathrm{ext}})$ in the context of the full data set with ASA simulations. A simple simulation based on parameters taken from literature as well as sensible estimations yielded results that were able to replicate the current-voltage curves and the ideality factors at short-circuit and open-circuit rather well. However the $V_{\mathrm{int}}(V_{\mathrm{ext}})$ curve was not reproduced, most importantly the high amount of charge carriers remaining in the bulk under short-circuit conditions was not achieved. I then proceeded to demonstrate two ways of fitting the measured internal voltage data by either doping the perovskite absorber or screening the electric field from the absorber by increasing the dielectric permittivity ϵ_{pero}. While this enabled me to reproduce the internal voltage measurements, I was unable to do so while simultaneously matching all other measured characteristics. Parameter variations showed that having to recombination sites with similar total recombination rates created a window in which the ideality factors at short-circuit and at open-circuit diverged as could be witnessed in the measurement data. In order to stay within this window the two recombination sites could only be altered in conjunction leading to two possible simulation scenarios. In the first scenario charge carriers are prevented from leaving the absorber, yielding a high internal voltage but reducing the extracted short-circuit current density J_{SC}. In the second scenario charge carriers are extracted more efficiently leading to a close reproduction of the illuminated current-voltage curve, in the meantime however the internal voltage is significantly reduced with respect to the measured values. This leads me to conclude that the full set of measurements can not be matched by the kind of simulations utilized for this thesis.

A reason for the mismatch between simulations and measurements may lie in inhomogeneities within the measured cell. If for example single grains of the perovskite layers are not properly contacted to the rest of the cell they may luminesce as though they were under open-circuit conditions, significantly increasing the luminescence signal at low to medium voltages. Further simulation efforts could be conducted including mobile charges representing ionic defects. Additionally further measurements can be conducted on cells of varying processing conditions in order

to evaluate the influence of processing on the behaviour of the resulting cells.

Finally I took a look at the series resistance R_s in perovskite solar cells. I introduced multiple different methods for the calculation of the series resistance from current-voltage measurements as well as from voltage dependent photoluminescence data. From the comparison of current-voltage curves measured under different illumination biases I was able to calculate the series resistance R_s as a function of the externally applied voltage V_ext. The resulting curves showed that the series resistance is not a constant value as would be expected from an ohmic resistor, but that it is higher at low voltages and is reduced towards a higher external bias. I concluded that the series resistance is comprised of two components, an ohmic external contribution $R_\mathrm{s,ext}$ that is independent from any voltage bias and a non-ohmic internal contribution $R_\mathrm{s,int}(V)$ that is modulated by the externally applied voltage. I then proceeded to show how various parameters such as charge carrier lifetimes τ, charge carrier mobilities μ, and energetic offsets influence both parts of the series resistance R_s. Additionally I evaluated how the influence of these parameters was altered if the electric field was screened from the absorber by an increased value of the dielectric permittivity ϵ_pero. While the simulations yielded close insights into the behaviour of the series resistance, in the future additional cells with differing processing conditions and materials can be measured and evaluated in a similar fashion in order to determine the influence of material properties and processing conditions on the series resistance and subsequently on the functionality of perovskite solar cells.

A Appendix

A.1 Variations of Simulation Parameters

Table A.1: Parameter values used for the simulations of a solar cell utilizing a perovskite absorber with an acceptor density $N_A = 10^{17}$ cm^{-3} displayed in figure 5.8 and 5.9.

Parameter	**Simulation**
band gap E_g	1.6 eV
E_A perovskite	4 eV
N_C perovskite	$2 \cdot 10^{18}$ cm^{-3}
N_V perovskite	$2 \cdot 10^{18}$ cm^{-3}
μ perovskite	30 cm^{2}V^{-1}s^{-1}
τ perovskite	10^{-8} s
k_{rad} perovskite	$5 \cdot 10^{-11}$ cm^{3}s^{-1}
ϵ perovskite	30
N_A perovskite	10^{17} cm^{-3}
E_g PCBM	1.8 eV
E_A PCBM	4.155 eV
N_C PCBM	10^{19} cm^{-3}
N_V PCBM	10^{19} cm^{-3}
μ PCBM	10^{-3} cm^{2}V^{-1}s^{-1}
ϵ PCBM	3
E_g PTAA	3 eV
E_A PTAA	2.6 eV
N_C PTAA	$2 \cdot 10^{18}$ cm^{-3}
N_V PTAA	$2 \cdot 10^{18}$ cm^{-3}
μ PTAA	10^{-1} cm^{2}V^{-1}s^{-1}
ϵ PTAA	3
μ interface PCBM	1 cm^{2}V^{-1}s^{-1}
τ interface PCBM	$3 \cdot 10^{-3}$ s
μ interface PTAA	10^{-3} cm^{2}V^{-1}s^{-1}
τ interface PTAA	$3 \cdot 10^{-7}$ s
R_s	2 Ωcm^2
R_p	$5 \cdot 10^5$ Ωcm^2
T	300 K
$\phi_{b,f}$	0 eV
$\phi_{b,b}$	0 eV

Table A.2: Parameter values used for the simulations of a cell utilizing a perovskite absorber with an electric field screened due to ionic movement displayed in figures 5.10 and 5.11.

Parameter	**Simulation**
band gap E_g	1.6 eV
E_A perovskite	4 eV
N_C perovskite	$2 \cdot 10^{18}$ cm^{-3}
N_V perovskite	$2 \cdot 10^{18}$ cm^{-3}
μ perovskite	0.2 cm^{2}V^{-1}s^{-1}
τ perovskite	10^{-7} s
k_{rad} perovskite	$5 \cdot 10^{-11}$ cm^{3}s^{-1}
ϵ perovskite	10000
E_g PCBM	1.8 eV
E_A PCBM	4 eV
N_C PCBM	$1 \cdot 10^{19}$ cm^{-3}
N_V PCBM	$1 \cdot 10^{19}$ cm^{-3}
μ PCBM	10^{-3} cm^{2}V^{-1}s^{-1}
ϵ PCBM	3
E_g PTAA	3 eV
E_A PTAA	2.35 eV
N_C PTAA	$2 \cdot 10^{18}$ cm^{-3}
N_V PTAA	$2 \cdot 10^{18}$ cm^{-3}
μ PTAA	10^{-1} cm^{2}V^{-1}s^{-1}
ϵ PTAA	3
N_A PTAA	$5 \cdot 10^{18}$ cm^{-3}
μ interface PCBM	10^{-3} cm^{2}V^{-1}s^{-1}
τ interface PCBM	10^{-7} s
μ interface PTAA	10^{-3} cm^{2}V^{-1}s^{-1}
τ interface PTAA	10^{-7} s
R_s	2 Ωcm^2
R_p	$5 \cdot 10^5$ Ωcm^2
T	300 K
$\phi_{b,f}$	0 eV
$\phi_{b,b}$	0 eV

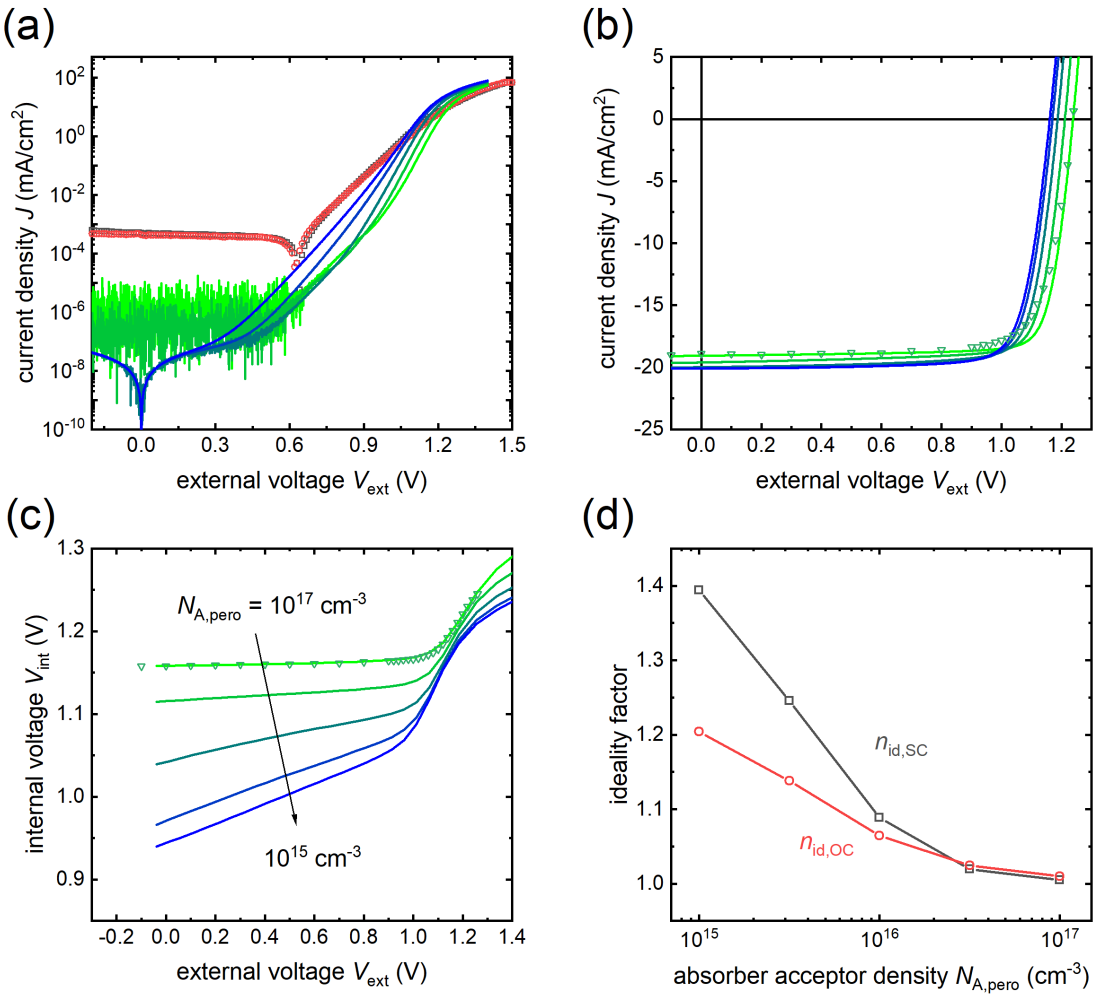

Figure A.1: Simulations of a cell utilizing a doped perovskite absorber in comparison to measurement values. Simulations use a variation of the acceptor density $N_{\mathrm{A,pero}} = 10^{15} - 10^{17}$ cm^{-3} in the perovskite absorber. (a) Simulated dark current-voltage curves (solid green lines) in comparison to measured sweeps in forward (grey symbols) and reverse (red symbols) direction. (b) Illuminated current voltage curves and (c) internal voltage V_{int} versus external voltage V_{ext} for the highest illumination intensity ϕ both simulated (solid lines) and measured (symbols). (d) Ideality factors at short-circuit $n_{\mathrm{id,SC}}$ and at open-circuit $n_{\mathrm{id,OC}}$ as a function of the acceptor density $N_{\mathrm{A,pero}}$ in the perovskite absorber. Simulation parameters can be found in table A.1.

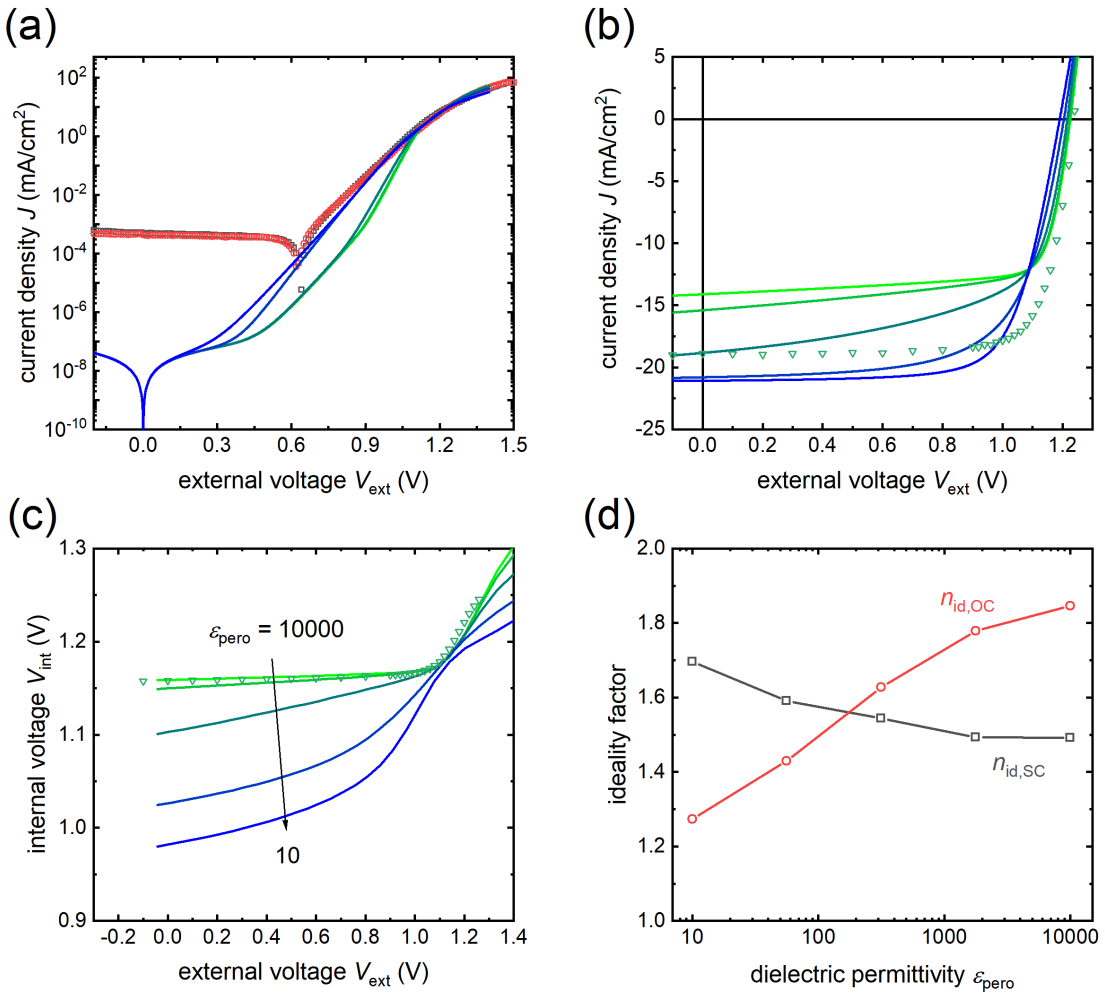

Figure A.2: Simulations of a cell utilizing an absorber with a screened electric field in comparison to measurement values. Simulations use a variation of the dielectric permittivity $\epsilon_{\text{pero}} = 10 - 10000$ eV in the perovskite absorber. (a) Simulated dark current-voltage curves (solid green lines) in comparison to measured sweeps in forward (grey symbols) and reverse (red symbols) direction. (b) Illuminated current voltage curves and (c) internal voltage V_{int} versus external voltage V_{ext} for the highest illumination intensity ϕ both simulated (solid lines) and measured (symbols). (d) Ideality factors at short-circuit $n_{\text{id,SC}}$ and at open-circuit $n_{\text{id,OC}}$ as a function of the dielectric permittivity ϵ_{pero} in the perovskite absorber. Simulation parameters can be found in table A.2.

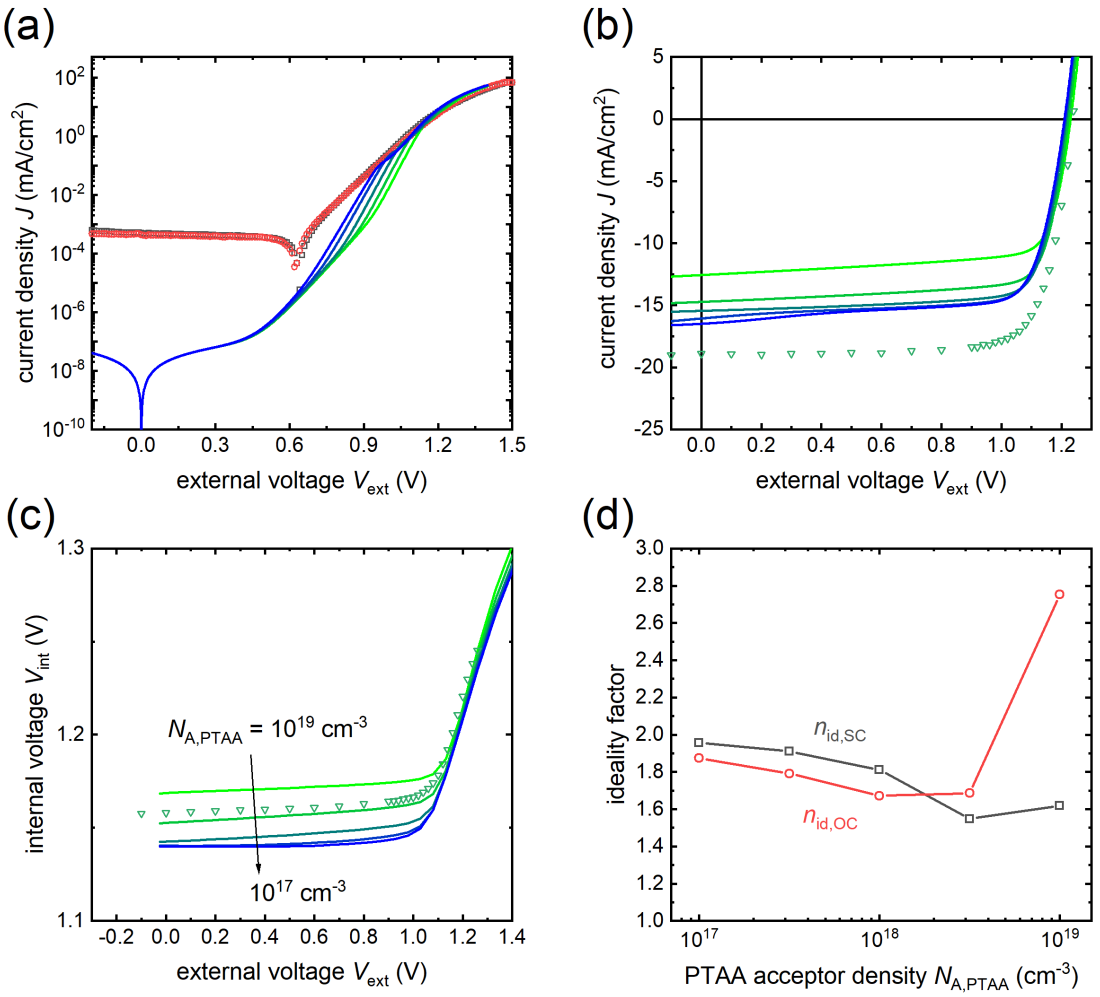

Figure A.3: Simulations of a cell utilizing an absorber with a screened electric field in comparison to measurement values. Simulations use a variation of the acceptor density $N_{\mathrm{A,PTAA}} = 10^{17} - 10^{19}$ cm^{-3} in the PTAA layer. (a) Simulated dark current-voltage curves (solid green lines) in comparison to measured sweeps in forward (grey symbols) and reverse (red symbols) direction. (b) Illuminated current voltage curves and (c) internal voltage V_{int} versus external voltage V_{ext} for the highest illumination intensity ϕ both simulated (solid lines) and measured (symbols). (d) Ideality factors at short-circuit $n_{\mathrm{id,SC}}$ and at open-circuit $n_{\mathrm{id,OC}}$ as a function of the acceptor density $N_{\mathrm{A,PTAA}}$ in the PTAA layer. Simulation parameters can be found in table A.2.

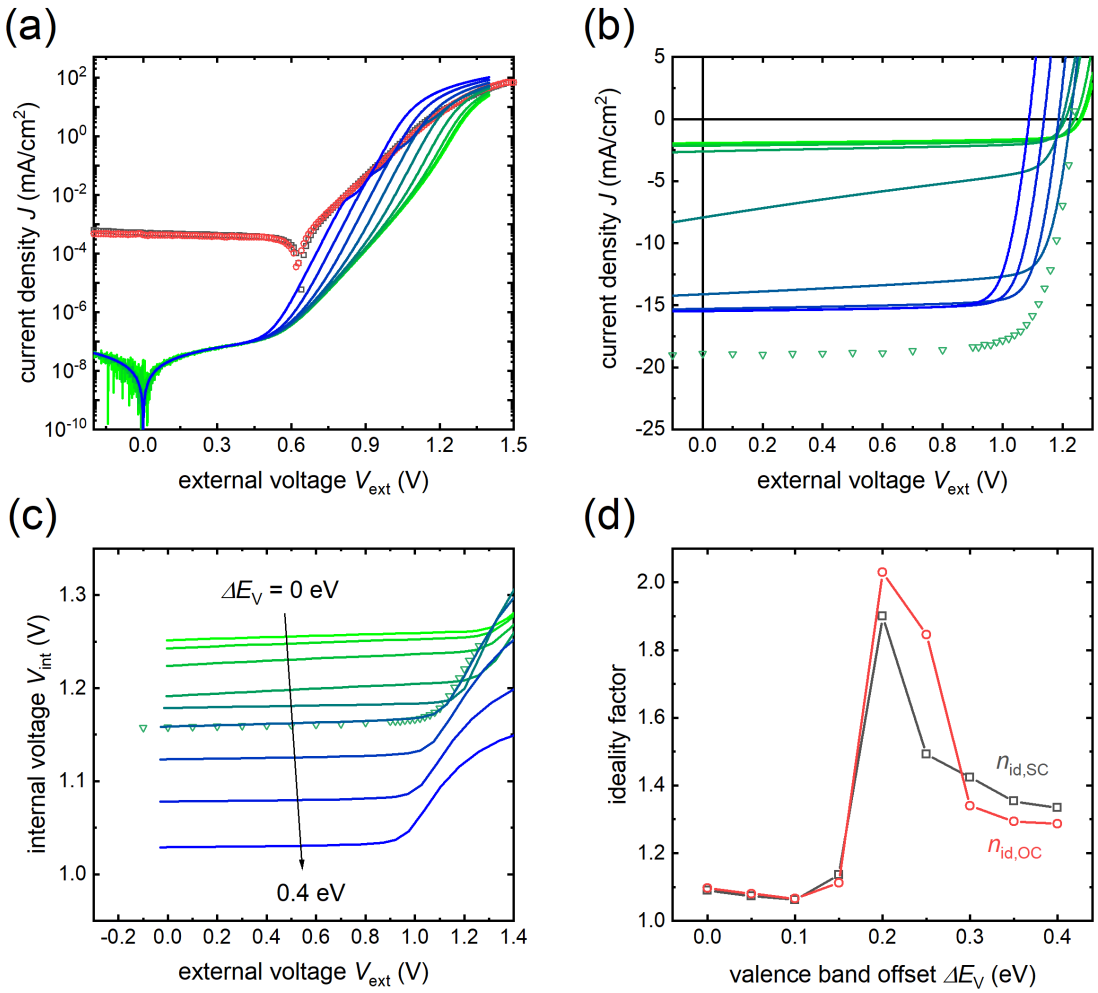

Figure A.4: Simulations of a cell utilizing an absorber with a screened electric field in comparison to measurement values. Simulations use a variation of the valence band offset $\Delta E_\mathrm{V} = 0 - 0.4$ eV at the absorber-PTAA interface. (a) Simulated dark current-voltage curves (solid green lines) in comparison to measured sweeps in forward (grey symbols) and reverse (red symbols) direction. (b) Illuminated current voltage curves and (c) internal voltage V_int versus external voltage V_ext for the highest illumination intensity ϕ both simulated (solid lines) and measured (symbols). (d) Ideality factors at short-circuit $n_\mathrm{id,SC}$ and at open-circuit $n_\mathrm{id,OC}$ as a function of the valence band offset ΔE_V at the absorber-PTAA interface. Simulation parameters can be found in table A.2.

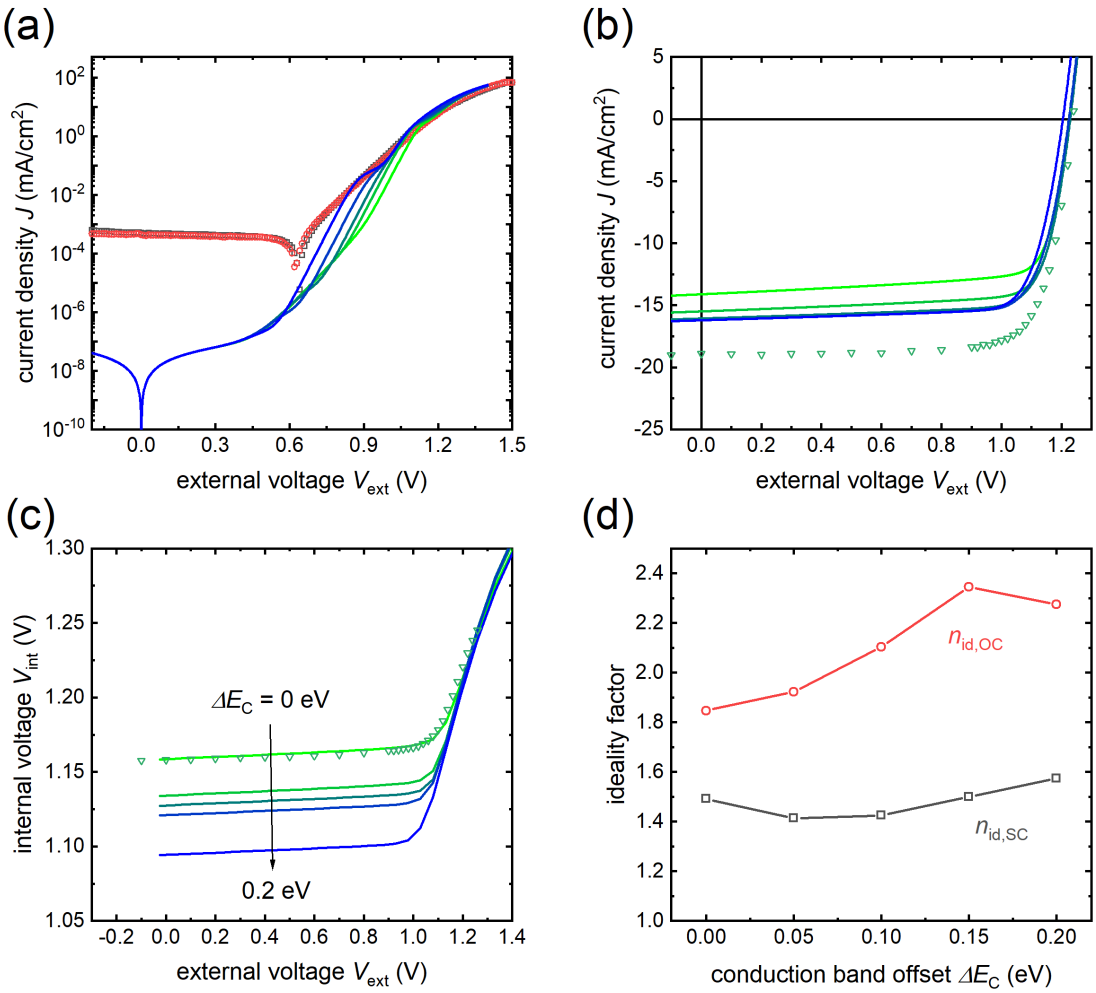

Figure A.5: Simulations of a cell utilizing an absorber with a screened electric field in comparison to measurement values. Simulations use a variation of the conduction band offset $\Delta E_C = 0 - 0.2$ eV at the absorber-PCBM interface. (a) Simulated dark current-voltage curves (solid green lines) in comparison to measured sweeps in forward (grey symbols) and reverse (red symbols) direction. (b) Illuminated current voltage curves and (c) internal voltage V_{int} versus external voltage V_{ext} for the highest illumination intensity ϕ both simulated (solid lines) and measured (symbols). (d) Ideality factors at short-circuit $n_{id,SC}$ and at open-circuit $n_{id,OC}$ as a function of the conduction band offset ΔE_C at the absorber-PCBM interface. Simulation parameters can be found in table A.2.

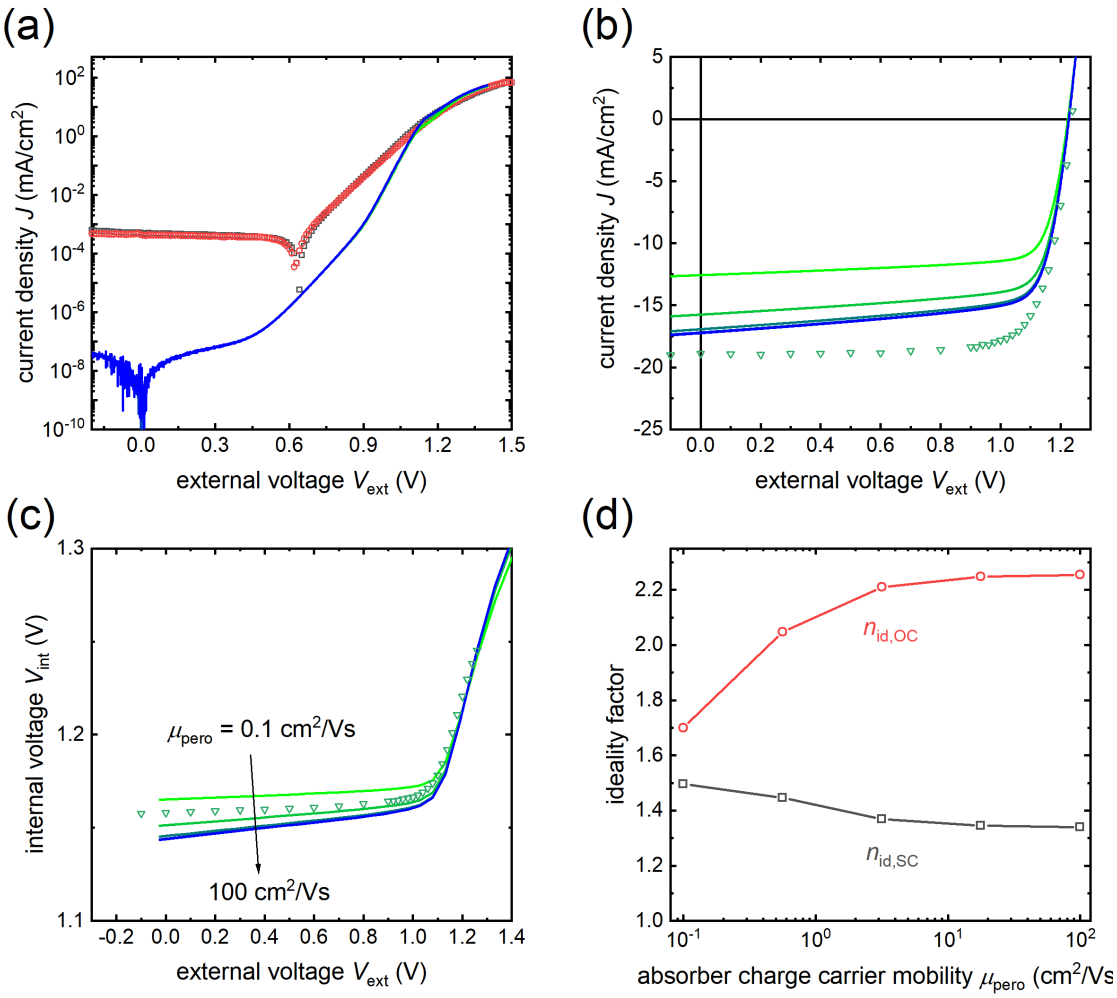

Figure A.6: Simulations of a cell utilizing an absorber with a screened electric field in comparison to measurement values. Simulations use a variation of the charge carrier mobility $\mu_{\mathrm{pero}} = 0.1 - 100$ cm^2/Vs in the perovskite absorber. (a) Simulated dark current-voltage curves (solid green lines) in comparison to measured sweeps in forward (grey symbols) and reverse (red symbols) direction. (b) Illuminated current voltage curves and (c) internal voltage V_{int} versus external voltage V_{ext} for the highest illumination intensity ϕ both simulated (solid lines) and measured (symbols). (d) Ideality factors at short-circuit $n_{\mathrm{id,SC}}$ and at open-circuit $n_{\mathrm{id,OC}}$ as a function of the charge carrier mobility μ_{pero} in the perovskite absorber. Simulation parameters can be found in table A.2.

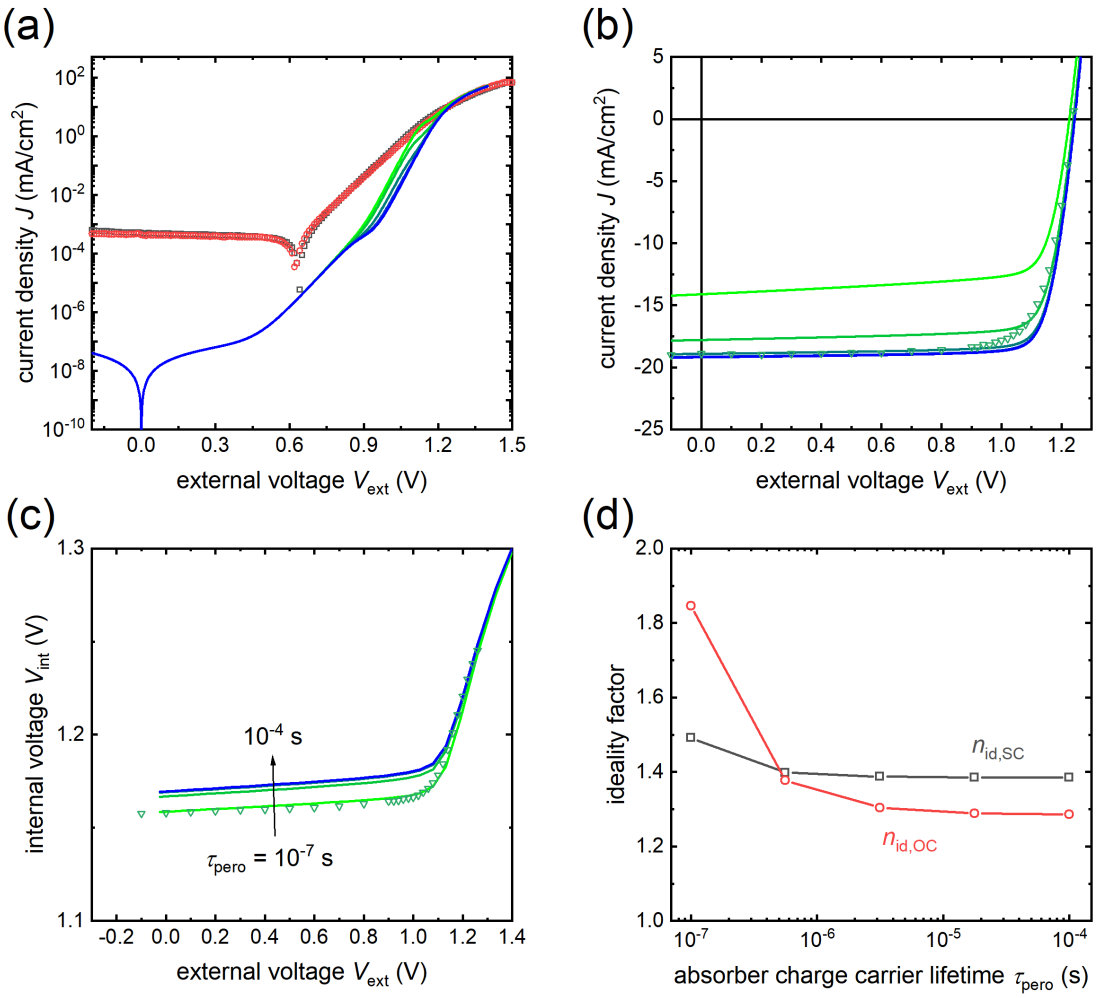

Figure A.7: Simulations of a cell utilizing an absorber with a screened electric field in comparison to measurement values. Simulations use a variation of the charge carrier lifetime $\tau_{\mathrm{pero}} = 10^{-7} - 10^{-4}$ s in the perovskite absorber. (a) Simulated dark current-voltage curves (solid green lines) in comparison to measured sweeps in forward (grey symbols) and reverse (red symbols) direction. (b) Illuminated current voltage curves and (c) internal voltage V_{int} versus external voltage V_{ext} for the highest illumination intensity ϕ both simulated (solid lines) and measured (symbols). (d) Ideality factors at short-circuit $n_{\mathrm{id,SC}}$ and at open-circuit $n_{\mathrm{id,OC}}$ as a function of the charge carrier lifetime τ_{pero} in the perovskite absorber. Simulation parameters can be found in table A.2.

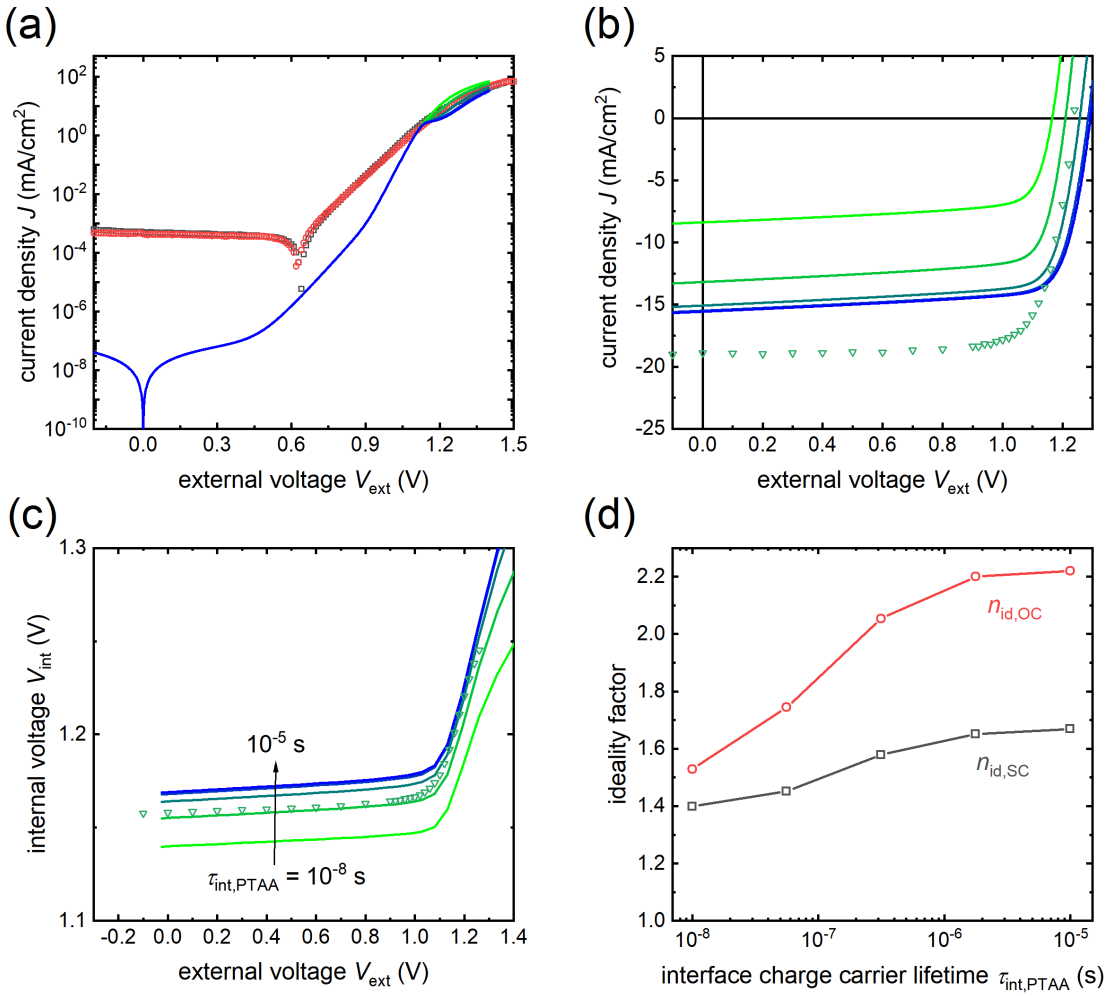

Figure A.8: Simulations of a cell utilizing an absorber with a screened electric field in comparison to measurement values. Simulations use a variation of the charge carrier lifetime $\tau_{\mathrm{int,PTAA}} = 10^{-8} - 10^{-5}$ s at the absorber-PTAA interface. (a) Simulated dark current-voltage curves (solid green lines) in comparison to measured sweeps in forward (grey symbols) and reverse (red symbols) direction. (b) Illuminated current voltage curves and (c) internal voltage V_{int} versus external voltage V_{ext} for the highest illumination intensity ϕ both simulated (solid lines) and measured (symbols). (d) Ideality factors at short-circuit $n_{\mathrm{id,SC}}$ and at open-circuit $n_{\mathrm{id,OC}}$ as a function of the charge carrier lifetime $\tau_{\mathrm{int,PTAA}}$ at the absorber-PTAA interface. Simulation parameters can be found in table A.2.

A.2 Processing of Coevaporated Cells

The coevaporated sample utilized in chapter 6 is fabricated in a similar architecture to the one shown in figure 3.1. The main differences are the use of poly(3,4-ethylenedioxythiophene) polystyrene sulfonate (PEDOT:PSS) and Poly(4-butylphenyl-diphenyl-amine) (Poly-TPD) for the hole transporting layer instead of PTAA and the different method of processing the perovskite film.

Commercially bought 20 mm × 20 mm glass substrates with pre-patterned ITO (Zhuhai Kaivo Optoelectronic Co., Ltd.) are cleaned in an ultrasonic bath with soap (Hellmanex III), acetone and isopropyl alcohol (IPA, purity of 99.5 %) for 10 minutes at a time. The cleaned substrates are dried and subsequently treated with oxygen plasma for 12 minutes. Immediately following the oxygen plasma treatment the samples are moved to a fume hood, where 150 μl of a PEDOT:PSS dispersion (1.3 - 1.7 wt% in water, M121 AI 4083, Ossila Ltd.) are applied the substrates through a 0.45 μm polytetrafluoroethylene (PTFE) filter and a syringe. The substrates are then spun in a spincoater at 5000 rpm for 60 s with a ramping rate of 5000 rpm/s and subsequently annealed in ambient air on a hotplate at 110 °C for 10 minutes. The samples are then transferred to a glovebox filled with nitrogen (N_2). Inside the glovebox Poly-TPD (>99 %, 1-Material Inc.) is dissolved at a ratio of 4 mg/ml in chlorobenzene and stirred at room temperature. 120 μl of the solution is brought onto the substrates and spincoated at 4000 rpm for 60 s with a ramping rate of 800 rpm/s. The resulting layers are then dried at room temperature for 30 minutes.

The coevaporated $MAPbI_3$ perovskite layer was deposited in a coevaporation chamber (CreaPhys GmbH) by evaporating MAI and PbI_2 powders (see supporting information in [163]). After the samples were introduced to the chamber, it was pumped down to a base pressure of 10^{-6} mbar. Both materials were evaporated from current-heated, ceramic crucibles. The deposition rates for the two materials were monitored by two sensors situated about 25 cm above each source, while a third sensor close to the substrate measured the combined deposition rate. The crucibles are first manually heated to 80 °C and 200 °C for MAI and PbI_2 respectively. The deposition rates were then controlled by using the software SQC-310Comm (Inficon AG). The software controls the heating power output by both crucibles in order to facilitate deposition rates of 0.1 Å/s for MAI and 0.3 Å/s for PbI_2. When the desired

deposition rates are reached the substrate shutter is opened until a thickness of 300 nm for the resulting layer is reached. Afterwards the substrate shutter is closed and the crucibles are cooled before the substrates are removed from the deposition chamber for further processing.

After coevaporation is concluded the samples are moved back to the nitrogen-filled glovebox where the final processing steps are taken. PCBM (99.5 %, Solenne BV) is dissolved at a concentration of 20 mg/ml in chlorobenzene (CB, 99.8 %). The solution is stirred over night at 75 °C. 120 μl of the solution is brought onto the substrate and spun at 1200 rpm for 60 s with a ramping rate of 400 rpm/s. The finished layer is not annealed but dried at room temperature for 30 minutes. BCP (>99.8 %, Ossila Ltd.) is dissolved in IPA at a concentration of 0.5 mg/ml and treated in an ultrasonic bath for 1 h. Then 120 μl are spincoated at 4000 rpm for 30 s with a ramping rate of 800 rpm/s. Before the silver back contact is evaporated onto the sample, the front contact has to be uncovered by scratching with a metal pen (see chapter 3.1). Then the contact is processed in an evacuated evaporation chamber at 2 Å/s while parts of the substrate are masked. The samples are then ready to be measured.

References

[1] United Nations, *The World at Six Billion: Introduction*. 1999.

[2] U.S. Census Bureau, *U.S. and World Population Clock*. Sept. 2019.

[3] P. Gerland, A. E. Raftery, H. Ševčíková, N. Li, D. Gu, T. Spoorenberg, L. Alkema, B. K. Fosdick, J. Chunn, N. Lalic, G. Bay, T. Buettner, G. K. Heilig, and J. Wilmoth, "World population stabilization unlikely this century," *Science*, vol. 346, pp. 234–237, Oct. 2014.

[4] M. Z. Jacobson, "Review of solutions to global warming, air pollution, and energy security," *Energy & Environmental Science*, vol. 2, no. 2, pp. 148–173, 2009.

[5] V. Masson-Delmotte, P. Zhai, H.-O. Pörtner, D. Roberts, J. Skea, P. R. Shukla, A. Pirani, W. Moufouma-Okia, C. Péan, R. Pidcock, S. Connors, J. B. R. Matthews, Y. Chen, X. Zhou, M. I. Gomis, E. Lonnoy, T. Maycock, M. Tignor, and T. Waterfield, *IPCC, 2018: Summary for Policymakers. In: Global Warming of 1.5°C. An IPCC Special Report on the impacts of global warming of 1.5°C above pre-industrial levels and related global greenhouse gas emission pathways, in the context of strengthening the global response to the threat of climate change, sustainable development, and efforts to eradicate poverty.*

[6] *AR5 Climate Change 2013: The Physical Science Basis — IPCC*.

[7] O. Hoegh-Guldberg, P. J. Mumby, A. J. Hooten, R. S. Steneck, P. Greenfield, E. Gomez, C. D. Harvell, P. F. Sale, A. J. Edwards, K. Caldeira, N. Knowlton, C. M. Eakin, R. Iglesias-Prieto, N. Muthiga, R. H. Bradbury, A. Dubi, and M. E. Hatziolos, "Coral Reefs Under Rapid Climate Change and Ocean Acidification," *Science*, vol. 318, pp. 1737–1742, Dec. 2007.

[8] P. J. Webster, G. J. Holland, J. A. Curry, and H.-R. Chang, "Changes in Trop-

ical Cyclone Number, Duration, and Intensity in a Warming Environment," *Science*, vol. 309, pp. 1844–1846, Sept. 2005.

[9] A. Dai, "Drought under global warming: a review," *Wiley Interdisciplinary Reviews: Climate Change*, vol. 2, no. 1, pp. 45–65, 2011.

[10] A. A. Khasnis and M. D. Nettleman, "Global Warming and Infectious Disease," *Archives of Medical Research*, vol. 36, pp. 689–696, Nov. 2005.

[11] Fraunhofer ISE, "Photovoltaics Report," p. 47, Mar. 2019.

[12] Fraunhofer ISE, "Recent Facts about Photovoltaics in Germany," May 2019.

[13] Fraunhofer Institute for Solar Energy Systems, *Current and Future Cost of Photovoltaics*. 2015.

[14] D. M. Chapin, C. S. Fuller, and G. L. Pearson, "Solar energy converting apparatus," Feb. 1957.

[15] M. A. Green, "Third generation photovoltaics: Ultra-high conversion efficiency at low cost," *Progress in Photovoltaics: Research and Applications*, vol. 9, no. 2, pp. 123–135, 2001.

[16] L. Meng, Y. Zhang, X. Wan, C. Li, X. Zhang, Y. Wang, X. Ke, Z. Xiao, L. Ding, R. Xia, H.-L. Yip, Y. Cao, and Y. Chen, "Organic and solution-processed tandem solar cells with 17.3% efficiency," *Science*, vol. 361, pp. 1094–1098, Sept. 2018.

[17] NREL, *Best Research-Cell Efficiency Chart*. Mar. 2020.

[18] K. Yoshikawa, H. Kawasaki, W. Yoshida, T. Irie, K. Konishi, K. Nakano, T. Uto, D. Adachi, M. Kanematsu, H. Uzu, and K. Yamamoto, "Silicon heterojunction solar cell with interdigitated back contacts for a photoconversion efficiency over 26%," *Nature Energy*, vol. 2, p. 17032, May 2017.

[19] M. A. Green, E. D. Dunlop, D. H. Levi, J. Hohl-Ebinger, M. Yoshita, and A. W. Y. Ho-Baillie, "Solar cell efficiency tables (version 54)," *Progress in Photovoltaics: Research and Applications*, vol. 27, no. 7, pp. 565–575, 2019.

[20] J. Gong, S. B. Darling, and F. You, "Perovskite photovoltaics: life-cycle assessment of energy and environmental impacts," *Energy & Environmental Science*, vol. 8, no. 7, pp. 1953–1968, 2015.

[21] I. Celik, Z. Song, A. J. Cimaroli, Y. Yan, M. J. Heben, and D. Apul, "Life Cycle Assessment (LCA) of perovskite PV cells projected from lab to fab," *Solar Energy Materials and Solar Cells*, vol. 156, pp. 157–169, Nov. 2016.

[22] Q. Lin, A. Armin, R. C. R. Nagiri, P. L. Burn, and P. Meredith, "Electro-optics of perovskite solar cells," *Nature Photonics*, vol. 9, pp. 106–112, Feb. 2015.

[23] D. B. Mitzi, K. Chondroudis, and C. R. Kagan, "Organic-inorganic electronics," *IBM Journal of Research and Development*, vol. 45, pp. 29–45, Jan. 2001.

[24] C. C. Stoumpos, C. D. Malliakas, and M. G. Kanatzidis, "Semiconducting Tin and Lead Iodide Perovskites with Organic Cations: Phase Transitions, High Mobilities, and Near-Infrared Photoluminescent Properties," *Inorganic Chemistry*, vol. 52, pp. 9019–9038, Aug. 2013.

[25] Y. Rong, Y. Ming, W. Ji, D. Li, A. Mei, Y. Hu, and H. Han, "Toward Industrial-Scale Production of Perovskite Solar Cells: Screen Printing, Slot-Die Coating, and Emerging Techniques," *The Journal of Physical Chemistry Letters*, vol. 9, pp. 2707–2713, May 2018.

[26] Y. Rong, Y. Hu, A. Mei, H. Tan, M. I. Saidaminov, S. I. Seok, M. D. McGehee, E. H. Sargent, and H. Han, "Challenges for commercializing perovskite solar cells," *Science*, vol. 361, p. eaat8235, Sept. 2018.

[27] F. Di Giacomo, S. Shanmugam, H. Fledderus, B. J. Bruijnaers, W. J. H. Verhees, M. S. Dorenkamper, S. C. Veenstra, W. Qiu, R. Gehlhaar, T. Merckx, T. Aernouts, R. Andriessen, and Y. Galagan, "Up-scalable sheet-to-sheet production of high efficiency perovskite module and solar cells on 6-in. substrate using slot die coating," *Solar Energy Materials and Solar Cells*, vol. 181, pp. 53–59, July 2018.

[28] Z. Li, T. R. Klein, D. H. Kim, M. Yang, J. J. Berry, M. F. A. M. v. Hest, and K. Zhu, "Scalable fabrication of perovskite solar cells," *Nature Reviews Materials*, vol. 3, pp. 1–20, Mar. 2018.

[29] Y. Deng, X. Zheng, Y. Bai, Q. Wang, J. Zhao, and J. Huang, "Surfactant-controlled ink drying enables high-speed deposition of perovskite films for efficient photovoltaic modules," *Nature Energy*, vol. 3, pp. 560–566, July 2018.

[30] J.-P. Correa-Baena, M. Saliba, T. Buonassisi, M. Grätzel, A. Abate, W. Tress, and A. Hagfeldt, "Promises and challenges of perovskite solar cells," *Science*, vol. 358, pp. 739–744, Nov. 2017.

[31] W. R. Mateker and M. D. McGehee, "Progress in Understanding Degradation Mechanisms and Improving Stability in Organic Photovoltaics," *Advanced Materials*, vol. 29, no. 10, p. 1603940, 2017.

[32] K. Domanski, E. A. Alharbi, A. Hagfeldt, M. Grätzel, and W. Tress, "Systematic investigation of the impact of operation conditions on the degradation behaviour of perovskite solar cells," *Nature Energy*, vol. 3, pp. 61–67, Jan. 2018.

[33] F. Giustino and H. J. Snaith, "Toward Lead-Free Perovskite Solar Cells," *ACS Energy Letters*, vol. 1, pp. 1233–1240, Dec. 2016.

[34] Z. Shi, J. Guo, Y. Chen, Q. Li, Y. Pan, H. Zhang, Y. Xia, and W. Huang, "Lead-Free Organic–Inorganic Hybrid Perovskites for Photovoltaic Applications: Recent Advances and Perspectives," *Advanced Materials*, vol. 29, no. 16, p. 1605005, 2017.

[35] G. Rose, *De novis quibusdam fossilibus quae in montibus Uraliis inveniuntur*. Schade, 1839.

[36] M. Huijben, G. Rijnders, D. H. A. Blank, S. Bals, S. V. Aert, J. Verbeeck, G. V. Tendeloo, A. Brinkman, and H. Hilgenkamp, "Electronically coupled complementary interfaces between perovskite band insulators," *Nature Materials*, vol. 5, pp. 556–560, July 2006.

[37] K. Miyano, T. Tanaka, Y. Tomioka, and Y. Tokura, "Photoinduced Insulator-to-Metal Transition in a Perovskite Manganite," *Physical Review Letters*, vol. 78, pp. 4257–4260, June 1997.

[38] C. Zener, "Interaction between the d-Shells in the Transition Metals. II. Ferromagnetic Compounds of Manganese with Perovskite Structure," *Physical Review*, vol. 82, pp. 403–405, May 1951.

[39] D. W. Murphy, S. Sunshine, R. B. van Dover, R. J. Cava, B. Batlogg, S. M. Zahurak, and L. F. Schneemeyer, "New superconducting cuprate perovskites," *Physical Review Letters*, vol. 58, pp. 1888–1890, May 1987.

[40] D. Weber, "CH3NH3PbX3, ein Pb(II)-System mit kubischer Perowskitstruktur / CH3NH3PbX3, a Pb(II)-System with Cubic Perovskite Structure," *Zeitschrift für Naturforschung B*, vol. 33, no. 12, pp. 1443–1445, 2014.

[41] V. M. Goldschmidt, "Die Gesetze der Krystallochemie," *Naturwissenschaften*, vol. 14, pp. 477–485, May 1926.

[42] C. Li, X. Lu, W. Ding, L. Feng, Y. Gao, and Z. Guo, "Formability of ABX3 (X = F, Cl, Br, I) halide perovskites," *Acta Crystallographica Section B: Structural Science*, vol. 64, pp. 702–707, Dec. 2008.

[43] G. Kieslich, S. Sun, and A. K. Cheetham, "An extended Tolerance Factor approach for organic–inorganic perovskites," *Chemical Science*, vol. 6, no. 6, pp. 3430–3433, 2015.

[44] W. Li, Z. Wang, F. Deschler, S. Gao, R. H. Friend, and A. K. Cheetham, "Chemically diverse and multifunctional hybrid organic–inorganic perovskites," *Nature Reviews Materials*, vol. 2, p. 16099, Mar. 2017.

[45] J. H. Noh, S. H. Im, J. H. Heo, T. N. Mandal, and S. I. Seok, "Chemical Management for Colorful, Efficient, and Stable Inorganic–Organic Hybrid Nanostructured Solar Cells," *Nano Letters*, vol. 13, pp. 1764–1769, Apr. 2013.

[46] E. T. Hoke, D. J. Slotcavage, E. R. Dohner, A. R. Bowring, H. I. Karunadasa, and M. D. McGehee, "Reversible Photo-Induced Trap Formation in Mixed-Halide Hybrid Perovskites for Photovoltaics," *Chemical Science*, vol. 6, pp. 613–617, 2015.

[47] D. P. McMeekin, G. Sadoughi, W. Rehman, G. E. Eperon, M. Saliba, M. T. Hörantner, A. Haghighirad, N. Sakai, L. Korte, B. Rech, M. B. Johnston, L. M. Herz, and H. J. Snaith, "A mixed-cation lead mixed-halide perovskite absorber for tandem solar cells," *Science*, vol. 351, pp. 151–155, Jan. 2016.

[48] J. L. Knutson, J. D. Martin, and D. B. Mitzi, "Tuning the Band Gap in Hybrid Tin Iodide Perovskite Semiconductors Using Structural Templating," *Inorganic Chemistry*, vol. 44, pp. 4699–4705, June 2005.

[49] D. B. Mitzi, C. A. Feild, W. T. A. Harrison, and A. M. Guloy, "Conducting tin halides with a layered organic-based perovskite structure," *Nature*, vol. 369, pp. 467–469, June 1994.

[50] C. R. Kagan, D. B. Mitzi, and C. D. Dimitrakopoulos, "Organic-Inorganic Hybrid Materials as Semiconducting Channels in Thin-Film Field-Effect Transistors," *Science*, vol. 286, pp. 945–947, Oct. 1999.

[51] A. Kojima, K. Teshima, Y. Shirai, and T. Miyasaka, "Organometal Halide Perovskites as Visible-Light Sensitizers for Photovoltaic Cells," *Journal of the American Chemical Society*, vol. 131, pp. 6050–6051, May 2009.

[52] M. M. Lee, J. Teuscher, T. Miyasaka, T. N. Murakami, and H. J. Snaith, "Efficient Hybrid Solar Cells Based on Meso-Superstructured Organometal Halide Perovskites," *Science*, vol. 338, pp. 643–647, Nov. 2012.

[53] H.-S. Kim, C.-R. Lee, J.-H. Im, K.-B. Lee, T. Moehl, A. Marchioro, S.-J. Moon, R. Humphry-Baker, J.-H. Yum, J. E. Moser, M. Grätzel, and N.-G. Park, "Lead Iodide Perovskite Sensitized All-Solid-State Submicron Thin Film Mesoscopic Solar Cell with Efficiency Exceeding 9%," *Scientific Reports*, vol. 2, p. 591, Aug. 2012.

[54] N. J. Jeon, H. Na, E. H. Jung, T.-Y. Yang, Y. G. Lee, G. Kim, H.-W. Shin, S. I. Seok, J. Lee, and J. Seo, "A fluorene-terminated hole-transporting material for highly efficient and stable perovskite solar cells," *Nature Energy*, vol. 3, pp. 682–689, Aug. 2018.

[55] M. Yuan, L. N. Quan, R. Comin, G. Walters, R. Sabatini, O. Voznyy, S. Hoogland, Y. Zhao, E. M. Beauregard, P. Kanjanaboos, Z. Lu, D. H. Kim, and E. H. Sargent, "Perovskite energy funnels for efficient light-emitting diodes," *Nature Nanotechnology*, vol. 11, pp. 872–877, Oct. 2016.

[56] K. Lin, J. Xing, L. N. Quan, F. P. G. d. Arquer, X. Gong, J. Lu, L. Xie, W. Zhao, D. Zhang, C. Yan, W. Li, X. Liu, Y. Lu, J. Kirman, E. H. Sargent, Q. Xiong, and Z. Wei, "Perovskite light-emitting diodes with external quantum efficiency exceeding 20 per cent," *Nature*, vol. 562, pp. 245–248, Oct. 2018.

[57] F. Deschler, M. Price, S. Pathak, L. E. Klintberg, D.-D. Jarausch, R. Higler, S. Hüttner, T. Leijtens, S. D. Stranks, H. J. Snaith, M. Atatüre, R. T. Phillips, and R. H. Friend, "High Photoluminescence Efficiency and Optically Pumped Lasing in Solution-Processed Mixed Halide Perovskite Semiconductors," *The Journal of Physical Chemistry Letters*, vol. 5, pp. 1421–1426, Apr. 2014.

[58] B. R. Sutherland and E. H. Sargent, "Perovskite photonic sources," *Nature Photonics*, vol. 10, pp. 295–302, May 2016.

[59] U. Rau, "Reciprocity relation between photovoltaic quantum efficiency and electroluminescent emission of solar cells," *Physical Review B*, vol. 76, Aug. 2007.

[60] U. Rau, "Superposition and Reciprocity in the Electroluminescence and Photoluminescence of Solar Cells," *IEEE Journal of Photovoltaics*, vol. 2, pp. 169–172, Apr. 2012.

[61] C. A. Gueymard, D. Myers, and K. Emery, "Proposed reference irradiance spectra for solar energy systems testing," *Solar Energy*, vol. 73, pp. 443–467, Dec. 2002.

[62] T. Kirchartz, K. Ding, and U. Rau, "Fundamental Electrical Characterization of Thin-Film Solar Cells - Introduction," in *Advanced Characterization Techniques for Thin Film Solar Cells*, pp. 43–49, John Wiley & Sons, July 2016. Google-Books-ID: Y6CtDAAAQBAJ.

[63] D. E. Carlson and C. R. Wronski, "Amorphous silicon solar cell," *Applied Physics Letters*, vol. 28, pp. 671–673, June 1976.

[64] R. A. Street, *Technology and Applications of Amorphous Silicon*. Springer Science & Business Media, June 2013.

[65] T. Kirchartz, J. Bisquert, I. Mora-Sero, and G. Garcia-Belmonte, "Classification of solar cells according to mechanisms of charge separation and charge collection," *Physical Chemistry Chemical Physics*, vol. 17, no. 6, pp. 4007–4014, 2015.

[66] S. Colella, E. Mosconi, P. Fedeli, A. Listorti, F. Gazza, F. Orlandi, P. Ferro, T. Besagni, A. Rizzo, G. Calestani, G. Gigli, F. De Angelis, and R. Mosca, "MAPbI3-xClx Mixed Halide Perovskite for Hybrid Solar Cells: The Role of Chloride as Dopant on the Transport and Structural Properties," *Chemistry of Materials*, vol. 25, pp. 4613–4618, Nov. 2013.

[67] H. Choi, J. Jeong, H.-B. Kim, S. Kim, B. Walker, G.-H. Kim, and J. Y. Kim, "Cesium-doped methylammonium lead iodide perovskite light absorber for hybrid solar cells," *Nano Energy*, vol. 7, pp. 80–85, July 2014.

[68] O. Breitenstein, "An Alternative One-Diode Model for Illuminated Solar Cells," *IEEE Journal of Photovoltaics*, vol. 4, pp. 899–905, May 2014. Conference Name: IEEE Journal of Photovoltaics.

[69] O. Breitenstein, "An Alternative One-Diode Model for Illuminated Solar Cells," *IEEE Journal of Photovoltaics*, vol. 4, pp. 899–905, May 2014.

[70] T. C. M. Müller, B. E. Pieters, U. Rau, and T. Kirchartz, "Analysis of the series resistance in *pin* -type thin-film silicon solar cells," *Journal of Applied Physics*, vol. 113, p. 134503, Apr. 2013.

[71] U. Rau, P. O. Grabitz, and J. H. Werner, "Resistive limitations to spatially inhomogeneous electronic losses in solar cells," *Applied Physics Letters*, vol. 85, pp. 6010–6012, Dec. 2004. Publisher: American Institute of Physics.

[72] M. Wolf and H. Rauschenbach, "Series resistance effects on solar cell measurements," *Advanced Energy Conversion*, vol. 3, pp. 455–479, Apr. 1963.

[73] H. J. Snaith, A. Abate, J. M. Ball, G. E. Eperon, T. Leijtens, N. K. Noel, S. D. Stranks, J. T.-W. Wang, K. Wojciechowski, and W. Zhang, "Anomalous Hysteresis in Perovskite Solar Cells," *The Journal of Physical Chemistry Letters*, vol. 5, pp. 1511–1515, May 2014. Publisher: American Chemical Society.

[74] W. Tress, N. Marinova, T. Moehl, S. M. Zakeeruddin, M. Khaja Nazeeruddin, and M. Grätzel, "Understanding the rate-dependent J – V hysteresis, slow time component, and aging in CH 3 NH 3 PbI 3 perovskite solar cells: the role of a compensated electric field," *Energy & Environmental Science*, vol. 8, no. 3, pp. 995–1004, 2015.

[75] B. C. O'Regan, P. R. F. Barnes, X. Li, C. Law, E. Palomares, and J. M. Marin-Beloqui, "Optoelectronic Studies of Methylammonium Lead Iodide Perovskite Solar Cells with Mesoporous TiO2: Separation of Electronic and Chemical Charge Storage, Understanding Two Recombination Lifetimes, and the Evolution of Band Offsets during J–V Hysteresis," *Journal of the American Chemical Society*, vol. 137, pp. 5087–5099, Apr. 2015. Publisher: American Chemical Society.

[76] W. Xu, H. Cho, Y.-H. Kim, Y.-T. Kim, C. Wolf, C.-G. Park, and T.-W. Lee, "Organometal Halide Perovskite Artificial Synapses," *Ad-*

vanced Materials, vol. 28, no. 28, pp. 5916–5922, 2016. eprint: https://onlinelibrary.wiley.com/doi/pdf/10.1002/adma.201506363.

[77] R. S. Sanchez, V. Gonzalez-Pedro, J.-W. Lee, N.-G. Park, Y. S. Kang, I. Mora-Sero, and J. Bisquert, "Slow Dynamic Processes in Lead Halide Perovskite Solar Cells. Characteristic Times and Hysteresis," *The Journal of Physical Chemistry Letters*, vol. 5, pp. 2357–2363, July 2014. Publisher: American Chemical Society.

[78] E. L. Unger, E. T. Hoke, C. D. Bailie, W. H. Nguyen, A. R. Bowring, T. Heumüller, M. G. Christoforo, and M. D. McGehee, "Hysteresis and transient behavior in current–voltage measurements of hybrid-perovskite absorber solar cells," *Energy & Environmental Science*, vol. 7, pp. 3690–3698, Oct. 2014. Publisher: The Royal Society of Chemistry.

[79] C. Eames, J. M. Frost, P. R. F. Barnes, B. C. O'Regan, A. Walsh, and M. S. Islam, "Ionic transport in hybrid lead iodide perovskite solar cells," *Nature Communications*, vol. 6, p. 7497, June 2015. Number: 1 Publisher: Nature Publishing Group.

[80] A. K. Jena, A. Kulkarni, M. Ikegami, and T. Miyasaka, "Steady state performance, photo-induced performance degradation and their relation to transient hysteresis in perovskite solar cells," *Journal of Power Sources*, vol. 309, pp. 1–10, Mar. 2016.

[81] S. van Reenen, M. Kemerink, and H. J. Snaith, "Modeling Anomalous Hysteresis in Perovskite Solar Cells," *The Journal of Physical Chemistry Letters*, vol. 6, pp. 3808–3814, Oct. 2015. Publisher: American Chemical Society.

[82] S. Meloni, T. Moehl, W. Tress, M. Franckevičius, M. Saliba, Y. H. Lee, P. Gao, M. K. Nazeeruddin, S. M. Zakeeruddin, U. Rothlisberger, and M. Graetzel, "Ionic polarization-induced current–voltage hysteresis in CH 3 NH 3 PbX 3 perovskite solar cells," *Nature Communications*, vol. 7, p. 10334, Feb. 2016. Number: 1 Publisher: Nature Publishing Group.

[83] T.-Y. Yang, G. Gregori, N. Pellet, M. Grätzel, and J. Maier, "The Significance of Ion Conduction in a Hybrid Organic–Inorganic Lead-Iodide-Based Perovskite Photosensitizer," *Angewandte*

Chemie, vol. 127, no. 27, pp. 8016–8021, 2015. eprint: https://onlinelibrary.wiley.com/doi/pdf/10.1002/ange.201500014.

[84] Y. Shao, Y. Fang, T. Li, Q. Wang, Q. Dong, Y. Deng, Y. Yuan, H. Wei, M. Wang, A. Gruverman, J. Shield, and J. Huang, "Grain boundary dominated ion migration in polycrystalline organic–inorganic halide perovskite films," *Energy & Environmental Science*, vol. 9, pp. 1752–1759, May 2016. Publisher: The Royal Society of Chemistry.

[85] Y. Yuan and J. Huang, "Ion Migration in Organometal Trihalide Perovskite and Its Impact on Photovoltaic Efficiency and Stability," *Accounts of Chemical Research*, vol. 49, pp. 286–293, Feb. 2016. Publisher: American Chemical Society.

[86] P. Calado, A. M. Telford, D. Bryant, X. Li, J. Nelson, B. C. O'Regan, and P. R. F. Barnes, "Evidence for ion migration in hybrid perovskite solar cells with minimal hysteresis," *Nature Communications*, vol. 7, pp. 1–10, Dec. 2016. Number: 1 Publisher: Nature Publishing Group.

[87] Z. Li, C. Xiao, Y. Yang, S. P. Harvey, D. H. Kim, J. A. Christians, M. Yang, P. Schulz, S. U. Nanayakkara, C.-S. Jiang, J. M. Luther, J. J. Berry, M. C. Beard, M. M. Al-Jassim, and K. Zhu, "Extrinsic ion migration in perovskite solar cells," *Energy & Environmental Science*, vol. 10, pp. 1234–1242, May 2017. Publisher: The Royal Society of Chemistry.

[88] N. Tessler and Y. Vaynzof, "Insights from Device Modeling of Perovskite Solar Cells," *ACS Energy Letters*, vol. 5, pp. 1260–1270, Apr. 2020. Publisher: American Chemical Society.

[89] O. Almora, I. Zarazua, E. Mas-Marza, I. Mora-Sero, J. Bisquert, and G. Garcia-Belmonte, "Capacitive Dark Currents, Hysteresis, and Electrode Polarization in Lead Halide Perovskite Solar Cells," *The Journal of Physical Chemistry Letters*, vol. 6, pp. 1645–1652, May 2015. Publisher: American Chemical Society.

[90] G. Garcia-Belmonte and J. Bisquert, "Distinction between Capacitive and Noncapacitive Hysteretic Currents in Operation and Degradation of Perovskite Solar Cells," *ACS Energy Letters*, vol. 1, pp. 683–688, Oct. 2016. Publisher:

American Chemical Society.

[91] W. Shockley and H. J. Queisser, "Detailed Balance Limit of Efficiency of p-n Junction Solar Cells," *Journal of Applied Physics*, vol. 32, pp. 510–519, Mar. 1961.

[92] G. Kirchhoff, "Über das Verhältnis zwischen dem Emissionsvermögen und dem Absorptionsvermögen der Körper für Wärme und Licht," *Annalen der Physik*, vol. 185, no. 2, pp. 275–301, 1860.

[93] P. W. Bridgman, "Note on the Principle of Detailed Balancing," *Physical Review*, vol. 31, pp. 101–102, Jan. 1928.

[94] K. T. Butler, J. M. Frost, and A. Walsh, "Band alignment of the hybrid halide perovskites CH 3 NH 3 PbCl 3 , CH 3 NH 3 PbBr 3 and CH 3 NH 3 PbI 3," *Materials Horizons*, vol. 2, no. 2, pp. 228–231, 2015. Publisher: Royal Society of Chemistry.

[95] J. P. C. Baena, L. Steier, W. Tress, M. Saliba, S. Neutzner, T. Matsui, F. Giordano, T. Jesper Jacobsson, A. R. S. Kandada, S. M. Zakeeruddin, A. Petrozza, A. Abate, M. Khaja Nazeeruddin, M. Grätzel, and A. Hagfeldt, "Highly efficient planar perovskite solar cells through band alignment engineering," *Energy & Environmental Science*, vol. 8, no. 10, pp. 2928–2934, 2015. Publisher: Royal Society of Chemistry.

[96] J. M. Ball and A. Petrozza, "Defects in perovskite-halides and their effects in solar cells," *Nature Energy*, vol. 1, pp. 1–13, Oct. 2016. Number: 11 Publisher: Nature Publishing Group.

[97] M. Stolterfoht, P. Caprioglio, C. M. Wolff, J. A. Márquez, J. Nordmann, S. Zhang, D. Rothhardt, U. Hörmann, Y. Amir, A. Redinger, L. Kegelmann, F. Zu, S. Albrecht, N. Koch, T. Kirchartz, M. Saliba, T. Unold, and D. Neher, "The impact of energy alignment and interfacial recombination on the internal and external open-circuit voltage of perovskite solar cells," *Energy & Environmental Science*, vol. 12, pp. 2778–2788, Sept. 2019. Publisher: The Royal Society of Chemistry.

[98] M. A. Green, "Solar cell fill factors - General graph and empirical expressions," *Solid State Electronics*, vol. 24, p. 788, Aug. 1981.

[99] E. Fermi, "Sulla quantizzazione del gas perfetto monoatomico," *Rendiconti Lincei*, vol. 145, 1926.

[100] P. A. M. Dirac and R. H. Fowler, "On the theory of quantum mechanics," *Proceedings of the Royal Society of London. Series A, Containing Papers of a Mathematical and Physical Character*, vol. 112, pp. 661–677, Oct. 1926. Publisher: Royal Society.

[101] S. M. Sze and K. K. Ng, *Physics of Semiconductor Devices*. John Wiley & Sons, Nov. 2006. Google-Books-ID: o4unkmHBHb8C.

[102] T. Kirchartz, T. Markvart, U. Rau, and D. A. Egger, "Impact of Small Phonon Energies on the Charge-Carrier Lifetimes in Metal-Halide Perovskites," *The Journal of Physical Chemistry Letters*, vol. 9, pp. 939–946, Mar. 2018.

[103] S. D. Stranks, G. E. Eperon, G. Grancini, C. Menelaou, M. J. P. Alcocer, T. Leijtens, L. M. Herz, A. Petrozza, and H. J. Snaith, "Electron-Hole Diffusion Lengths Exceeding 1 Micrometer in an Organometal Trihalide Perovskite Absorber," *Science*, vol. 342, pp. 341–344, Oct. 2013. Publisher: American Association for the Advancement of Science Section: Report.

[104] S. D. Stranks, V. M. Burlakov, T. Leijtens, J. M. Ball, A. Goriely, and H. J. Snaith, "Recombination Kinetics in Organic-Inorganic Perovskites: Excitons, Free Charge, and Subgap States," *Physical Review Applied*, vol. 2, p. 034007, Sept. 2014. Publisher: American Physical Society.

[105] T. Unold and L. Gütay, "Photoluminescence Analysis of Thin-Film Solar Cells - Introduction," in *Advanced Characterization Techniques for Thin Film Solar Cells*, pp. 275–277, John Wiley & Sons, July 2016. Google-Books-ID: Y6CtDAAAQBAJ.

[106] P. Würfel, "The chemical potential of radiation," *Journal of Physics C: Solid State Physics*, vol. 15, pp. 3967–3985, June 1982.

[107] T. Kirchartz, L. Krückemeier, and E. L. Unger, "Research Update: Recombination and open-circuit voltage in lead-halide perovskites," *APL Materials*, vol. 6, p. 100702, Oct. 2018. Publisher: American Institute of Physics.

[108] R. T. Ross, "Some Thermodynamics of Photochemical Systems," *The Journal of Chemical Physics*, vol. 46, pp. 4590–4593, June 1967. Publisher: American

Institute of Physics.

[109] G. Smestad, M. Kunst, and C. Vial, "Photovoltaic response in electrochemically prepared photoluminescent porous silicon," *Solar Energy Materials and Solar Cells*, vol. 26, pp. 277–283, May 1992.

[110] W. van Roosbroeck and W. Shockley, "Photon-Radiative Recombination of Electrons and Holes in Germanium," *Physical Review*, vol. 94, pp. 1558–1560, June 1954. Publisher: American Physical Society.

[111] U. Rau, U. W. Paetzold, and T. Kirchartz, "Thermodynamics of light management in photovoltaic devices," *Physical Review B*, vol. 90, p. 035211, July 2014. Publisher: American Physical Society.

[112] T. Kirchartz and U. Rau, "What Makes a Good Solar Cell?," *Advanced Energy Materials*, vol. 8, no. 28, p. 1703385, 2018. eprint: https://onlinelibrary.wiley.com/doi/pdf/10.1002/aenm.201703385.

[113] O. Gunawan, T. Gokmen, and D. B. Mitzi, "Suns-VOC characteristics of high performance kesterite solar cells," *Journal of Applied Physics*, vol. 116, p. 084504, Aug. 2014. Publisher: American Institute of Physics.

[114] V. Sarritzu, N. Sestu, D. Marongiu, X. Chang, S. Masi, A. Rizzo, S. Colella, F. Quochi, M. Saba, A. Mura, and G. Bongiovanni, "Optical determination of Shockley-Read-Hall and interface recombination currents in hybrid perovskites," *Scientific Reports*, vol. 7, p. 44629, Mar. 2017. Bandieraabtest: a Cclicensetype: ccby Cgtype: Nature Research Journals Number: 1 Primaryatype: Research Publisher: Nature Publishing Group Subjectterm: Photonic devices;Solar energy and photovoltaic technology Subjectermid: photonic-devices;solar-energy-and-photovoltaic-technology.

[115] P. Caprioglio, C. M. Wolff, O. J. Sandberg, A. Armin, B. Rech, S. Albrecht, D. Neher, and M. Stolterfoht, "On the Origin of the Ideality Factor in Perovskite Solar Cells," *Advanced Energy Materials*, vol. 10, no. 27, p. 2000502, 2020. eprint: https://onlinelibrary.wiley.com/doi/pdf/10.1002/aenm.202000502.

[116] P. Calado, D. Burkitt, J. Yao, J. Troughton, T. M. Watson, M. J. Carnie, A. M. Telford, B. C. O'Regan, J. Nelson, and P. R. Barnes, "Identifying

Dominant Recombination Mechanisms in Perovskite Solar Cells by Measuring the Transient Ideality Factor," *Physical Review Applied*, vol. 11, p. 044005, Apr. 2019. Publisher: American Physical Society.

[117] T. Kirchartz and J. Nelson, "Meaning of reaction orders in polymer:fullerene solar cells," *Physical Review B*, vol. 86, p. 165201, Oct. 2012. Publisher: American Physical Society.

[118] T. Kirchartz, F. Deledalle, P. S. Tuladhar, J. R. Durrant, and J. Nelson, "On the Differences between Dark and Light Ideality Factor in Polymer:Fullerene Solar Cells," *The Journal of Physical Chemistry Letters*, vol. 4, pp. 2371–2376, July 2013. Publisher: American Chemical Society.

[119] J. Even, L. Pedesseau, J.-M. Jancu, and C. Katan, "Importance of Spin–Orbit Coupling in Hybrid Organic/Inorganic Perovskites for Photovoltaic Applications," *The Journal of Physical Chemistry Letters*, vol. 4, pp. 2999–3005, Sept. 2013.

[120] F. Brivio, K. T. Butler, A. Walsh, and M. van Schilfgaarde, "Relativistic quasiparticle self-consistent electronic structure of hybrid halide perovskite photovoltaic absorbers," *Physical Review B*, vol. 89, Apr. 2014.

[121] R. E. Brandt, V. Stevanović, D. S. Ginley, and T. Buonassisi, "Identifying defect-tolerant semiconductors with high minority-carrier lifetimes: beyond hybrid lead halide perovskites," *MRS Communications*, vol. 5, pp. 265–275, June 2015.

[122] F. Brivio, A. B. Walker, and A. Walsh, "Structural and electronic properties of hybrid perovskites for high-efficiency thin-film photovoltaics from first-principles," *APL Materials*, vol. 1, p. 042111, Oct. 2013.

[123] Y. H. Chang, C. H. Park, and K. Matsuishi, "First-Principles Study of the Structural and the Electronic Properties of the Lead-Halide-Based Inorganic-Organic Perovskites (CH3NH3)PbX3 and CsPbX3 (X = Cl, Br, I)," *Journal of the Korean Physical Society*, vol. 44, no. 4, pp. 889–893, 2004.

[124] A. Zakutayev, C. M. Caskey, A. N. Fioretti, D. S. Ginley, J. Vidal, V. Stevanovic, E. Tea, and S. Lany, "Defect Tolerant Semiconductors for Solar Energy Conversion," *The Journal of Physical Chemistry Letters*, vol. 5, pp. 1117–

1125, Apr. 2014.

[125] M.-H. Du, "Density Functional Calculations of Native Defects in CH3NH3PbI3: Effects of Spin–Orbit Coupling and Self-Interaction Error," *The Journal of Physical Chemistry Letters*, vol. 6, pp. 1461–1466, Apr. 2015. Publisher: American Chemical Society.

[126] W.-J. Yin, T. Shi, and Y. Yan, "Unusual defect physics in CH $_3$$$ NH $_3$$$ PbI $_3$$$ perovskite solar cell absorber," *Applied Physics Letters*, vol. 104, p. 063903, Feb. 2014.

[127] W.-J. Yin, T. Shi, and Y. Yan, "Unique Properties of Halide Perovskites as Possible Origins of the Superior Solar Cell Performance," *Advanced Materials*, vol. 26, no. 27, pp. 4653–4658, 2014.

[128] F. Zheng, L. Z. Tan, S. Liu, and A. M. Rappe, "Rashba Spin–Orbit Coupling Enhanced Carrier Lifetime in CH3NH3PbI3," *Nano Letters*, vol. 15, pp. 7794–7800, Dec. 2015.

[129] Z.-G. Yu, "Rashba Effect and Carrier Mobility in Hybrid Organic–Inorganic Perovskites," *The Journal of Physical Chemistry Letters*, vol. 7, pp. 3078–3083, Aug. 2016.

[130] E. Mosconi, T. Etienne, and F. De Angelis, "Rashba Band Splitting in Organohalide Lead Perovskites: Bulk and Surface Effects," *The Journal of Physical Chemistry Letters*, vol. 8, pp. 2247–2252, May 2017.

[131] X. Zhang, J.-X. Shen, and C. G. V. d. Walle, "First-Principles Simulation of Carrier Recombination Mechanisms in Halide Perovskites," *Advanced Energy Materials*, vol. n/a, no. n/a, p. 1902830.

[132] E. M. Hutter, M. C. Gélvez-Rueda, A. Osherov, V. Bulović, F. C. Grozema, S. D. Stranks, and T. J. Savenije, "Direct–indirect character of the bandgap in methylammonium lead iodide perovskite," *Nature Materials*, vol. 16, pp. 115–120, Jan. 2017.

[133] C. Motta, F. El-Mellouhi, S. Kais, N. Tabet, F. Alharbi, and S. Sanvito, "Revealing the role of organic cations in hybrid halide perovskite CH3NH3PbI3," *Nature Communications*, vol. 6, p. 7026, Nov. 2015.

[134] P. Azarhoosh, S. McKechnie, J. M. Frost, A. Walsh, and M. van Schilfgaarde,

"Research Update: Relativistic origin of slow electron-hole recombination in hybrid halide perovskite solar cells," *APL Materials*, vol. 4, p. 091501, Sept. 2016.

[135] T. Kirchartz and U. Rau, "Decreasing Radiative Recombination Coefficients via an Indirect Band Gap in Lead Halide Perovskites," *The Journal of Physical Chemistry Letters*, vol. 8, pp. 1265–1271, Mar. 2017.

[136] S. Toyoshima, K. Kuwabara, T. Sakurai, T. Taima, K. Saito, H. Kato, and K. Akimoto, "Electronic Structure of Bathocuproine on Metal Studied by Ultraviolet Photoemission Spectroscopy," *Japanese Journal of Applied Physics*, vol. 46, p. 2692, Apr. 2007. Publisher: IOP Publishing.

[137] J. Troughton, M. Neophytou, N. Gasparini, A. Seitkhan, F. H. Isikgor, X. Song, Y.-H. Lin, T. Liu, H. Faber, E. Yengel, J. Kosco, M. F. Oszajca, B. Hartmeier, M. Rossier, N. A. Lüchinger, L. Tsetseris, H. J. Snaith, S. D. Wolf, T. D. Anthopoulos, I. McCulloch, and D. Baran, "A universal solution processed interfacial bilayer enabling ohmic contact in organic and hybrid optoelectronic devices," *Energy & Environmental Science*, vol. 13, no. 1, pp. 268–276, 2020. Publisher: Royal Society of Chemistry.

[138] C. Chen, S. Zhang, S. Wu, W. Zhang, H. Zhu, Z. Xiong, Y. Zhang, and W. Chen, "Effect of BCP buffer layer on eliminating charge accumulation for high performance of inverted perovskite solar cells," *RSC Advances*, vol. 7, no. 57, pp. 35819–35826, 2017.

[139] B. E. Pieters, J. Krc, and M. Zeman, "Advanced Numerical Simulation Tool for Solar Cells - ASA5," in *2006 IEEE 4th World Conference on Photovoltaic Energy Conference*, vol. 2, pp. 1513–1516, May 2006. ISSN: 0160-8371.

[140] J. M. Bennett and H. E. Bennett, "Non-Normal-Incidence Reflection and Transmission Polarizers," in *Handbook of Optics*, p. 1100, McGraw-Hill Professional, 1995.

[141] G. Tao, M. Zeman, and J. W. Metselaar, "Accurate generation rate profiles in a-Si :H solar cells with textured TCO substrates," *Solar Energy Materials and Solar Cells*, vol. 34, pp. 359–366, Sept. 1994.

[142] W. Theiss, "SCOUT Software Package," *www.wtheiss.com*.

[143] P. Caprioglio, M. Stolterfoht, C. M. Wolff, T. Unold, B. Rech, S. Albrecht, and D. Neher, "On the Relation between the Open-Circuit Voltage and Quasi-Fermi Level Splitting in Efficient Perovskite Solar Cells," *Advanced Energy Materials*, vol. 9, no. 33, p. 1901631, 2019. eprint: https://onlinelibrary.wiley.com/doi/pdf/10.1002/aenm.201901631.

[144] U. Rau, V. Huhn, and B. E. Pieters, "Luminescence Analysis of Charge-Carrier Separation and Internal Series-Resistance Losses in Cu(In,Ga)Se_2 Solar Cells," *Physical Review Applied*, vol. 14, p. 014046, July 2020. Publisher: American Physical Society.

[145] M. Wolf, G. Noel, and R. Stirn, "Investigation of the double exponential in the current—Voltage characteristics of silicon solar cells," *IEEE Transactions on Electron Devices*, vol. 24, pp. 419–428, Apr. 1977. Conference Name: IEEE Transactions on Electron Devices.

[146] A. Vasić, M. Stojanović, P. Osmokrović, and N. Stojanović, "The Influence of Ideality Factor on Fill Factor and Efficiency of Solar Cells," *Materials Science Forum*, vol. 352, pp. 241–246, 2000. Conference Name: Trends in Advanced Materials and Processes ISBN: 9780878498598 Publisher: Trans Tech Publications Ltd.

[147] M. Leilaeioun and Z. C. Holman, "Accuracy of expressions for the fill factor of a solar cell in terms of open-circuit voltage and ideality factor," *Journal of Applied Physics*, vol. 120, p. 123111, Sept. 2016. Publisher: AIP Publishing LLCAIP Publishing.

[148] Z. Liu, L. Krückemeier, B. Krogmeier, B. Klingebiel, J. A. Márquez, S. Levcenko, S. Öz, S. Mathur, U. Rau, T. Unold, and T. Kirchartz, "Open-Circuit Voltages Exceeding 1.26 V in Planar Methylammonium Lead Iodide Perovskite Solar Cells," *ACS Energy Letters*, vol. 4, pp. 110–117, Jan. 2019.

[149] F. Staub, H. Hempel, J.-C. Hebig, J. Mock, U. W. Paetzold, U. Rau, T. Unold, and T. Kirchartz, "Beyond Bulk Lifetimes: Insights into Lead Halide Perovskite Films from Time-Resolved Photoluminescence," *Physical Review Applied*, vol. 6, p. 044017, Oct. 2016. Publisher: American Physical Society.

[150] T. Kirchartz, J. A. Márquez, M. Stolterfoht, and T. Unold,

"Photoluminescence-Based Characterization of Halide Perovskites for Photovoltaics," *Advanced Energy Materials*, vol. 10, no. 26, p. 1904134, 2020. eprint: https://onlinelibrary.wiley.com/doi/pdf/10.1002/aenm.201904134.

[151] M. Sendner, P. K. Nayak, D. A. Egger, S. Beck, C. Müller, B. Epding, W. Kowalsky, L. Kronik, H. J. Snaith, A. Pucci, and R. Lovrinčić, "Optical phonons in methylammonium lead halide perovskites and implications for charge transport," *Materials Horizons*, vol. 3, no. 6, pp. 613–620, 2016. Publisher: Royal Society of Chemistry.

[152] J. Lee, K. Vandewal, S. R. Yost, M. E. Bahlke, L. Goris, M. A. Baldo, J. V. Manca, and T. Van Voorhis, "Charge Transfer State Versus Hot Exciton Dissociation in Polymer-Fullerene Blended Solar Cells," *Journal of the American Chemical Society*, vol. 132, pp. 11878–11880, Sept. 2010. Publisher: American Chemical Society.

[153] W. C. Tsoi, S. J. Spencer, L. Yang, A. M. Ballantyne, P. G. Nicholson, A. Turnbull, A. G. Shard, C. E. Murphy, D. D. C. Bradley, J. Nelson, and J.-S. Kim, "Effect of Crystallization on the Electronic Energy Levels and Thin Film Morphology of P3HT:PCBM Blends," *Macromolecules*, vol. 44, pp. 2944–2952, Apr. 2011. Publisher: American Chemical Society.

[154] B. W. Larson, J. B. Whitaker, X.-B. Wang, A. A. Popov, G. Rumbles, N. Kopidakis, S. H. Strauss, and O. V. Boltalina, "Electron Affinity of Phenyl–C61–Butyric Acid Methyl Ester (PCBM)," *The Journal of Physical Chemistry C*, vol. 117, pp. 14958–14964, July 2013. Publisher: American Chemical Society.

[155] E. von Hauff, V. Dyakonov, and J. Parisi, "Study of field effect mobility in PCBM films and P3HT:PCBM blends," *Solar Energy Materials and Solar Cells*, vol. 87, pp. 149–156, May 2005.

[156] D. Yang, X. Zhang, K. Wang, C. Wu, R. Yang, Y. Hou, Y. Jiang, S. Liu, and S. Priya, "Stable Efficiency Exceeding 20.6% for Inverted Perovskite Solar Cells through Polymer-Optimized PCBM Electron-Transport Layers," *Nano Letters*, vol. 19, pp. 3313–3320, May 2019. Publisher: American Chemical Society.

[157] J. Endres, M. Kulbak, L. Zhao, B. P. Rand, D. Cahen, G. Hodes, and A. Kahn, "Electronic structure of the CsPbBr3/polytriarylamine (PTAA) system," *Journal of Applied Physics*, vol. 121, p. 035304, Jan. 2017. Publisher: American Institute of Physics.

[158] J. Veres, S. D. Ogier, S. W. Leeming, D. C. Cupertino, and S. M. Khaffaf, "Low-k Insulators as the Choice of Dielectrics in Organic Field-Effect Transistors," *Advanced Functional Materials*, vol. 13, no. 3, pp. 199–204, 2003. eprint: https://onlinelibrary.wiley.com/doi/pdf/10.1002/adfm.200390030.

[159] Q. Wang, Y. Shao, H. Xie, L. Lyu, X. Liu, Y. Gao, and J. Huang, "Qualifying composition dependent p and n self-doping in CH3NH3PbI3," *Applied Physics Letters*, vol. 105, p. 163508, Oct. 2014. Publisher: American Institute of Physics.

[160] S. Colella, E. Mosconi, P. Fedeli, A. Listorti, F. Gazza, F. Orlandi, P. Ferro, T. Besagni, A. Rizzo, G. Calestani, G. Gigli, F. De Angelis, and R. Mosca, "MAPbI $_{3-x}$ Cl $_{x}$ Mixed Halide Perovskite for Hybrid Solar Cells: The Role of Chloride as Dopant on the Transport and Structural Properties," *Chemistry of Materials*, vol. 25, pp. 4613–4618, Nov. 2013.

[161] G. Y. Kim, A. Senocrate, T.-Y. Yang, G. Gregori, M. Grätzel, and J. Maier, "Large tunable photoeffect on ion conduction in halide perovskites and implications for photodecomposition," *Nature Materials*, vol. 17, pp. 445–449, May 2018. Number: 5 Publisher: Nature Publishing Group.

[162] N. Mundhaas, Z. J. Yu, K. A. Bush, H.-P. Wang, J. Häusele, S. Kavadiya, M. D. McGehee, and Z. C. Holman, "Series Resistance Measurements of Perovskite Solar Cells Using Jsc–Voc Measurements," *Solar RRL*, vol. 3, no. 4, p. 1800378, 2019. eprint: https://onlinelibrary.wiley.com/doi/pdf/10.1002/solr.201800378.

[163] L. Krückemeier, B. Krogmeier, Z. Liu, U. Rau, and T. Kirchartz, "Understanding Transient Photoluminescence in Halide Perovskite Layer Stacks and Solar Cells," *Advanced Energy Materials*, vol. 11, no. 19, p. 2003489, 2021. eprint: https://onlinelibrary.wiley.com/doi/pdf/10.1002/aenm.202003489.

Abbreviations and Symbols

α	Absorption coefficient
β_{n}	Capture coefficient for electrons of a trap in in the Shockley-Read-Hall model
β_{p}	Capture coefficient for holes of a trap in in the Shockley-Read-Hall model
Δn	Excess electron concentration
Δp	Excess hole concentration
ϵ	Relative dielectric constant
ϵ_0	Dielectric constant of vacuum
ζ	Emissivity
η	Energy conversion efficiency
λ	Wavelength
μ_{C}	Chemical potential of charge carriers in the conduction band
μ_{n}	Electron mobility
μ_{p}	Hole mobility
μ_{V}	Chemical potential of charge carriers in the valence band
ν	Photon frequency
ϕ	Illumination intensity
ϕ_{em}	Emitted photon flux
ϕ_{bb}	Black body radiation
ϕ_{PL}	Spectral photoluminescence flux
ϕ_{sun}	Solar spectrum
φ	Electrostatic potential in relation to the vacuum level
ρ	Space charge density
σ_{n}	Capture cross section for electrons

σ_p	Capture cross section for holes
τ	Charge-carrier lifetime
τ_aug	Auger lifetime
τ_eff	Effective lifetime taking into account all relevant recombination mechanisms
τ_n	Electron lifetime in the Shockley-Read-Hall model
τ_p	Hole lifetime in the Shockley-Read-Hall model
τ_rad	Radiative lifetime
τ_p	Shockley-Read Hall lifetime

a	Absorptance
c	Speed of light in vacuum: $2.9979 \times 10^8\,\mathrm{m\,s^{-1}}$
C_n	Auger recombination coefficient for electrons
C_p	Auger recombination coefficient for holes
d	Thickness
D_n	Diffusion constant for electrons
D_p	Diffusion constant for holes
e_n	Emission coefficient for electrons of a trap in SRH recombination
e_p	Emission coefficient for holes of a trap in SRH recombination
E	Energy
E_C	Energy level of conduction band
E_g	Band gap energy
E_F	Energy of the Fermi level
E_Fn	Energy of the quasi-Fermi level for electrons
E_Fp	Energy of the quasi-Fermi level for holes
E_T	Energy level of a trap
E_V	Energy level of valence band
E_vac	Vacuum energy
F	Electric field
FF	Fill factor
g	Spectral generation rate
G	Generation rate
G_opt	Optical generation rate

h	Planck constant: $4.1357 \times 10^{-15}\,\mathrm{eV\,s}$
$\hbar$	Reduced Planck constant $\hbar = \mathrm{h}/(2\pi)$
J	Current density
J_0	Saturation current density
J_d	Dark current density
J_d	Emission current density
J_extr	Extraction current density, defined in equation 2.66
J_i	Illuminated current density
J_MPP	Current density at the maximum power point
J_n	Electron current density
J_p	Hole current density
J_ph	Photogenerated current density
J_rec	Recombination current density
J_sc	Short-circuit current density
k	Extinction coefficient, wave vector
k_B	Boltzmann constant: $8.6173 \times 10^{-5}\,\mathrm{eV\,K^{-1}}$
k_rad	Radiative recombination coefficient
n	Electron density
n_i	Intrinsic charge-carrier concentration
n_id	Ideality factor
n_loc	Density of localized electrons
n_r	Refractive index (real part)
n_0	Equilibrium electron concentration
N	Complex refractive index
N_A	Acceptor density
N_C	Effective density of states in the conduction band
N_D	Donator density
N_T	Trap density
N_V	Effective density of states in the valence band
p	Hole density
p_a	Probability for a photon to be parasitically absorbed
p_e	Photon outcoupling probability
p_loc	Density of localized holes

p_r	Probability of reabsorbing a photon
p_0	Equilibrium hole concentration
P_max	Maximum attainable power density of a solar cell
P_sun	Power density of the solar spectrum
q	Elementary charge: $1.6022 \times 10^{-19}\,\mathrm{C}$
$Q_\mathrm{e}^\mathrm{lum}$	External luminescence quantum efficiency
$Q_\mathrm{i}^\mathrm{lum}$	Internal luminescence quantum efficiency
R	Recombination rate
r_A	Ionic radius of molecule or atom in crystal position A
r_B	Ionic radius of molecule or atom in crystal position B
R_aug	Auger recombination rate
R_int	Interface recombination rate
R_nrad	Non-radiative recombination rate
R_p	Parallel resistance
R_rad	Radiative recombination rate
R_s	Series resistance
$R_\mathrm{s,ext}$	Ohmic external contribution to the series resistance
$R_\mathrm{s,int}$	Non-ohmic internal contribution to the series resistance
R_srh	Shockley-Read Hall recombination rate
R_surf	Surface recombination rate
R_tot	Total recombination rate
r_X	Ionic radius of molecule or atom in crystal position X
S	Surface recombination velocity
t	Time, Goldschmidt tolerance factor
T	Temperature
v_th	Thermal velocity
V	Voltage
V_bi	Built-in voltage
V_ext	Externally applied voltage
V_int	Internal Voltage, $qV_\mathrm{int} = \Delta E_\mathrm{F}$
$V_\mathrm{i,OC}$	Open-circuit voltage of a cell under illumination
V_oc	Open-circuit voltage
V_MPP	Voltage at the maximum power point

x	Position

ASA	Advanced semiconductor analysis; device simulating software
DFT	Density Functional Theory
DMF	Dimethylformamide; polar solvent
DMSO	Dimethylsulfoxide; polar solvent
DSSC	Dye sensitized solar cell
EL	Electroluminescence
ETL	Electron transport layer
EPBT	Energy payback time
FA	Formamidinium; molecule that can be a component of perovskites
GA	Guanidinium; molecule that can be a component of perovskites
HLI	High level injection
HTL	Hole transport layer
IR	Infrared (part of the light spectrum)
ITO	Indium tin oxide; transparent and conductive electrode material
LED	Light emitting diode
LLI	Low level injection
MA	Methylammonium; molecule that can be a component of perovskites
MAI	Methylammonium iodide; precursor for the fabrication of perovskites
MPP	Maximum power point
ND	Neutral density
PCBM	[6,6]-phenyl-C_{61}-butyric acid methyl ester; electron transport material
PCE	Power conversion efficiency
PEDOT:PSS	Poly(3,4-ethylenedioxythiophene) polystyrene sulfonate
PL	Photoluminescence
SQ	Thermodynamic device limit named after Shockley-Queisser
SRH	Non-radiative recombination mechanism named after Shockley-Read Hall
SCR	Space charge region

SMU	Source measurement unit
TCO	Transparent conducting oxide
UV	Ultraviolet (part of the light spectrum)

List of Publications

- **D. Grabowski**, Z. Liu, G. Schöpe, U. Rau, T. Kirchartz, "Fill Factor Losses and Deviations from the Superposition Principle in Lead-Halide Perovskite Solar Cells," *Solar RRL*, 2200507, 2022. Publisher: John Wiley & Sons, Ltd.
- B. Krogmeier, F. Staub, **D. Grabowski**, U. Rau, and T. Kirchartz, "Quantitative analysis of the transient photoluminescence of $CH_3NH_3PbI_3/PC_{61}BM$ heterojunctions by numerical simulations," *Sustainable Energy & Fuels*, vol. 2, no. 5, pp. 1027-1034, 2018. Publisher: Royal Society of Chemistry.
- P. Kaienburg, P. Hartnagel, B. E. Pieters, J. Yu, **D. Grabowski**, Z. Liu, J. Haddad, U. Rau, and T. Kirchartz, "How Contact Layers Control Shunting Losses from Pinholes in Thin-Film Solar Cells," *The Journal of Physical Chemistry C*, vol. 122, pp. 27263-27272, Dec. 2018. Publisher: American Chemical Society.
- T. Gallet, **D. Grabowski**, T. Kirchartz, and A. Redinger, "Fermi-level pinning in methylammonium lead iodide perovskites," *Nanoscale*, vol. 11, no. 36, pp. 16828-16836, 2019. Publisher: Royal Society of Chemistry.
- E. Jung, K. Budzinauskas, S. Öz, F. Ünlü, H. Kuhn, J. Wagner, **D. Grabowski**, B. Klingebiel, M. Cherasse, J. Dong, P. Aversa, P. Vivo, T. Kirchartz, T. Miyasaka, P. H. M. van Loosdrecht, L. Perfetti, and S. Mathur, "Femto- to Microsecond Dynamics of Excited Electrons in a Quadruple Cation Perovskite," *ACS Energy Letters*, vol. 5, pp. 785-792, Mar. 2020. Publisher: American Chemical Society.

Acknowledgements

While I submit this PhD thesis as my own work, it would not have been possible for me to achieve without a remarkable amount of support from a number of people. I wish to extend my sincerest gratitude to everyone who enabled me to get to this point, be their contribution large or small:

- Prof. Dr. Thomas Kirchartz for accepting me as a doctoral researcher and supporting me through his knowledge, creativity, solution-focus and time,
- Prof. Dr. Alex Redinger for kindly accepting to report on my thesis,
- Prof. Dr. Uwe Rau for immensely insightful and fruitful conversations about transport layer currents and the underlying theory,
- Dr. Benjamin Klingebiel for being an everpresent and inexhaustible source of knowledge and support in almost every fathomable situation in the institute,
- Markus Hülsbeck for supporting all sorts of luminescence measurements and helping out with his knowledge of the optical and electrical setups,
- Wilfried Reetz and Christoph Zahren for keeping the much used XRD and solar simulator setups up and running and assisting with any arising problems,
- Oliver Thimm for numerous PDS measurements and the corresponding analysis,
- Irina Kühn for helping me in my efforts of prducing properly functioning perovskite solar cells,
- Ulrike Gerhards and Dorothea Lennartz for taking a lot of chores in the chemistry lab off my hands,
- Dr. Karsten Bittkau for assisting in generating the nk-files,
- Dr. Maurice Nuys and the HITEC team for a diversified graduate school,

Acknowledgements

- Dr. Senol Öz for broadening my horizons in the field of chemistry and sharing his expertise in the processing of titanium-oxide and multi-cation perovskites,
- Dr. Jan Mock, Johanna Siekmann, Dr. Malte Köhler, Dr. Florian Staub, Dr. Pascal Kaienburg, Jinane Haddad, Lisa Krückemeier and Basita Das for conversations and time spent together both in the research context and outside of it,
- my parents. who make anything I do possible through perpetual support and care,
- my lovely wife Andrea for enduring all the stress and hardship of a PhD together with me,
- anyone joining the beloved monthly pub-quiz,
- all of my friends and colleagues from the IEK-5 I might have left out.

All of you made this experience better and I am forever grateful!